Quantum Simulation of Triangular, Honeycomb and Kagome Crystal Structures using Ultracold Atoms in Lattices of Laser Light

by

Claire K. Thomas

A dissertation submitted in partial satisfaction of the

requirements for the degree of

Doctor of Philosophy

in

Physics

in the

Graduate Division

of the

University of California, Berkeley

Committee in charge:

Professor Dan M. Stamper-Kurn, Chair
Professor Ehud Altman
Professor Angelica Stacy

Spring 2017

Quantum Simulation of Triangular, Honeycomb and Kagome Crystal Structures using Ultracold Atoms in Lattices of Laser Light

Abstract

Quantum Simulation of Triangular, Honeycomb and Kagome Crystal Structures using Ultracold Atoms in Lattices of Laser Light

by

Claire K. Thomas

Doctor of Philosophy in Physics

University of California, Berkeley

Professor Dan M. Stamper-Kurn, Chair

Ultracold atomic gases trapped at the interference of coherent beams of light constitute an artificial material. This optical lattice material may be used for controlled quantum simulations of condensed matter theories. The bulk of this dissertation concerns the construction and calibration of an optical superlattice that can form the triangular, honeycomb and kagome crystal structures. The properties and geometry of this artificial material may be dynamically changed, allowing for the experiments discussed in this thesis that would be impossible with real materials.

The use of ultracold atoms in optical lattices for quantitative tests is challenging because of the novelty of many of the techniques in the field, and because of the myriad experimental differences between these artificial materials and true materials. This thesis reports the development of a method to characterize optical lattice potentials using matter-wave diffraction. We observe an enhancement of inversion asymmetry in matter-wave diffraction from a honeycomb lattice, which we explain using a time-independent perturbative treatment of the single-particle band structure of the lattice. Our experiment also provides new insight into a commonly used detection technique.

This thesis culminates in the development and experimental realization of a quantitative test of a condensed-matter theory. The test is insensitive to the experimental differences between artificial materials and real materials. We focus on a prediction from a mean-field treatment of the Bose-Hubbard model that concerns the difference in behavior of itinerant particles on lattices that are identical but for their geometry. Using the tunable geometry of our quantum simulator, we measure the properties of ultracold atomic gases trapped in the triangular and kagome lattices under otherwise identical conditions and find that they are consistent with the mean-field scaling prediction.

to Ashley Elizabeth Harper
née le 7 Avril, 1988 – décédée le 1er Juin, 2015

dreaming up our futures
was building castles out of clouds
they were becoming all we hoped

yours was a space of healing
as bright as your smile and big as your heart
with doors open to the world

this thesis is a little piece of my cloud castle
and the world is less without yours

Contents

List of Figures

List of Tables

Acknowledgments

Before I express my gratitude to the many people that helped make this PhD possible, I want to acknowledge just a few of the benefits I've had throughout my life that helped me get to this point. I grew up with the uncommon belief that my voice deserves to be heard simply because it exists. I used this voice to interrupt classes with my questions and I used it against various instances of sexual harassment. I sometimes elected not to use my voice, because I knew I had the choice. I never felt hungry. I was never targeted by law enforcement. I never felt unsafe in my home. These unearned privileges were neither necessary nor sufficient to get a doctorate in physics, but they helped me immensely. I believe that this reflection is necessary for the betterment of our field, because awareness is the first step towards increasing diversity, and science is best understood when viewed from many angles.

It has been my honor and my pleasure to be part of an excellent team of physicists during my time at Berkeley. I want to thank Dan Stamper-Kurn for welcoming me onto this team and for his mentorship as I journeyed from student to professional. The strength of his group begins with him. Through many cycles of students and post-docs, the persistent team dynamic was to listen, to question, to suggest, to build, to dismantle and to rebuild together. I learned to always have a model for my observations, and to never be too attached to that model. In our group, everyone developed and maintained a working model of each experiment, and that made an enormous difference in my work.

The way that we spent time together encouraged casual conversation. The more perplexing observations that might have been brushed aside in formal meetings came up over lunch or on bike rides through the Berkeley hills, and while they often led nowhere, they were occasionally the seeds of discovery in our work. Dan carefully cultivated and sustained this environment; he joined us for lunches and bike rides and coffees, he listened to our questions and our theories, and he built and dismantled simple physical models at every opportunity.

Both publications reported in this thesis have seemingly complex data that are explained by the simple physical models that we built together. Dan pushed me to continue developing these models after I thought they were done, and the final products are a source of great pride. I am grateful for his persistence. Dan was also a supportive, respectful and upstanding person who fought for me when I needed it, and that meant as much to me in my growth as a scientist and in my faith in the field as any of his physics expertise.

Throughout nearly my entire PhD career I worked directly with fellow grad student Tom Barter and the achievements in these pages depended on his insight, ingenuity and vigilance. His contributions to this thesis extend beyond the technical. From the beginning, our relationship was built on an unwavering foundation of mutual respect. That made it easy to grow and develop together as both scientists and people, and I would not be the physicist that I am today were it not for his influence.

Midway through my time here at Berkeley, Tom and I had the great fortune of being joined by another graduate student, Zephy Leung. Zephy brightened the lab with his sense of humor, which was great because his diligent and hardworking nature meant that he was

lines, trees fell on buildings and welders set off fire sprinkler systems. I'm honestly not sure how all that happened in my first three years of grad school, but I'm grateful that they worked to make things go as smoothly as possible. Here I want to again thank Sydney Schreppler, this time for her efforts in working with building management and in helping put out fires (metaphorically and without sprinklers). I am also thankful to Carlos and Stephen, who made sure I had the supplies I needed for my research even when I made that task particularly challenging for them. I am thankful to Anne for making me feel personally looked after on a giant campus.

I had an excellent fellowship in grad school from the Department of Energy, for which I am grateful. I want to especially thank the program manager, Dr. Ping Ge, who was extraordinarily supportive of me both professionally and personally. The Department of Energy Office of Science Graduate Fellowship Program (DOE SCGF) was made possible in part by the American Recovery and Reinvestment Act of 2009, and was administered by ORISE-ORAU. Our work was also funded by the National Science Foundation and by the Army Research Office with funding from the DARPA OLE program.

I am fortunate to have an enormous family that supported me throughout this endeavor. I want to thank my mom, who was a constant voice of reason, support and perspective. I am also thankful to my dad and Jane, who swept me away to someplace fabulous every time I needed it most. I am grateful to my granny, whose care packages sustained me, and to the lady at the post office who always made sure they were in the most cost-effective packaging. I am thankful to my sister, Jennifer, who is a model of hard work and success.

My sister, Lucy, and brother-in-law, Barry, were role models both in science and in life, and I was extremely lucky to have their insights and support throughout this endeavor. I am grateful to my brother, Randal, and sister-in-law, Chrissie, who were always there to laugh with me, and also at me. I am thankful to Zoë, Cadence, Max and Cole, who reminded me of the wonders of the macroscopic world when I was preoccupied with the microscopic one. I am grateful to Aunt Bob, for inspiring me with stories of so many adventures. I want to thank my aunts and uncles, especially Carmen and Lew, who treated me to dinners that pulled me away from physics and away from my perspective, and Ginny and Mike, who encouraged my interests and sent cards and love from their many travels. And I want to thank the entire Arieux clan, who kept me grounded and who made sure I knew what life outside of physics grad school in Berkeley looks like.

I am thankful to Bubba, who was easy to be with and who made me feel both supported and supportive, and to all of Ashley's family who made me feel welcome in their homes and in their hearts. I am grateful to Mr. Taj, who started me on this path by accepting my alternative learning style and seeing past my youthful ennui.

I was fortunate to have an amazing network of friends who provided levity and gravity in seemingly perfect balance throughout this endeavor. Seven years is a long time, and there were many people who played an important role in this time of my life. I was so lucky to develop a close friendship with fellow grad student Nicole Duncan in our first months here.

Chapter 1

Introduction

1.1 Scene from a physics PhD

It was June of 2013 and I was alone in the lab, monitoring the experiment during a delicate process (a vacuum bake of the main chamber) while my coworkers attended a nearby conference. The fire alarm was the first sign that it would be a challenging day. The deafening sound in rhythm with blinding lights affected me less than you might imagine. I flinched but decided to stay where I was. There had been many building troubles that year, and we'd had our share of troubles in the lab (a main-chamber vacuum bake is not a good sign). I was tired of evacuating and bored with monitoring the extremely slow removal of gases from the heated vacuum chamber that occurs during a vacuum bake.

Time passed. The alarm faded into the background and I sank back into my calculations. In the periphery of my vision, I noticed a black fluid creeping under the doorway and into the lab. I looked at it in disbelief; I looked at it as though it were sentient and might crawl back into the fire sprinkler system it came from. It turns out that the water in fire sprinkler systems sits up there for a long time, so that when the sprinklers go off you are not on fire, but you are extremely dirty. There was no fire, but there was a drenched welder in the workmans closet across the hall from my lab who was having a rough day.

As I asked whether he had a sense of how much more water might be coming, Jonathan Kohler, who was the newest student in the Stamper-Kurn group, emerged from the neighboring lab. Rather than rush to the building exit, he looked at me and asked, *What do we do?* Perhaps no person has ever endeared himself to me so quickly. But alas, there was no lab protocol for a flood in Berkeley in 2013. (This oversight has been corrected.) I replied, *Email the group and grab some two by fours!* We proceeded to lift the most expensive of our electronics and laser control systems off of the floor and turn off our high voltage electronics. When we finally ran through the water to evacuate, we passed the firemen on their way downstairs. They seemed exasperated with our presence in a flooded basement.

Although we prepared for our labs to flood, I did not expect the subsequent two-day power outage. That delicate process that I had been monitoring would only last a few hours

without building electricity, and an improper shutoff could be disastrous. The post-doc and soon-to-be professor, Dr. Gyu-Boong Jo, was the first to return from the conference. He foresaw the looming power outage and politely pushed past the building managers who blocked building re-entrance. He properly shut down the vacuum pumps. Ultimately, the entire system recovered from this unfortunate series of events.

When the flood struck, I was monitoring the system through a bake out. In a bake out, we wrap the vacuum chamber in heaters and raise its temperature to about 300° F, while using pumps to remove any air or water that gets loose. It's similar to what happens in a self-cleaning oven, where food scraps are incinerated and pumped out as gas. We are left with a vacuum that has almost nothing inside, so that when we put in the atoms that we use to gain insight into the rules of quantum mechanics, we know that those atoms are alone in the system.

A bake out, once completed, never has to be done again, and every future experiment depends on its success. This bake out was my first responsibility as the senior student in my lab, and I had prepared for it obsessively. (In later chapters I will describe these preparations.) I thought that I had made contingency plans for every possibility, but a mid-summer flood in California in 2013 – in the midst of one of the most severe droughts the state has ever seen – was not on the list of potential disasters I had considered. That day I learned that I cannot plan for everything, and that I could trust my team for support and rapid problem-solving when needed.

I remember the flood like it was yesterday and, though it was nearly halfway through my time at Berkeley, it marked in many ways the beginning of this PhD. I spent many of my years alone in a basement with just one other graduate student, Thomas Barter, rebuilding an apparatus that neither of us had expected to rebuild. Later joined by Tsz-Him (Zephy) Leung, we worked tirelessly to create a machine that can elucidate the underpinnings of the physical world, and I am proud of what we built together.

With this dissertation I hope to tell you a comprehensible story in which atoms are used as well-controlled tools to understand quantum mechanics, but more importantly I hope to share a story of the endeavor of a team of people to understand the fundamental building blocks of nature and the laws that govern them, a story of the few successes that inspire us to continue through the many failures.

1.2 Overview

My work has focused on quantum simulation of condensed matter systems using ultracold atoms in a bichromatic optical lattice. In the following chapters I will discuss the two-dimensional lattice of tunable geometry in which we have studied physics of triangular, honeycomb and kagome lattice structures. We followed a prescription for building this quantum simulator – we worked to build a system that is stable, we worked to understand it in its simplest limits, and only then did we perform a complex simulation that cannot be completely described by theoretical treatments.

The work in this thesis was the subject of two manuscripts. The first involved non-interacting particles on the lattice. As I will describe, interactions are what makes quantum problems hard to solve. We performed an experiment in which we suddenly exposed a stationary cloud of atoms to an optical lattice with a honeycomb geometry. The matter-wave diffracted, resulting in sensitive crystallography of the optical lattice [1, 2].

In our second manuscript, we introduced and increased interactions among atoms in the triangular and kagome lattices. The interactions among particles on a lattice site increase as the barrier height between lattice sites increases, and the depth of an optical lattice is easily tuned by changing the intensity of the light that interferes to create the lattice. Increasing interactions of atoms in a lattice drives a phase transition between the superfluid state that is delocalized over the extent of the lattice, and the Mott insulating state, which has a fixed, integer number of particles on each site [3–7].

In this introduction, I aim to give an overview of my work that is accessible to enthusiasts, because I believe that everyone can understand something of what I've done, and that scientific research has a huge and underestimated impact on everyone's every day lives. I hope to provide insights and a coherent story that motivates the work that we have done. I will describe quantum mechanics in the simplest terms, and explain the necessity of quantum simulation and quantum computing to understand the most complex chemical and material properties. I will describe a few different approaches to such computation and simulation, and I will then describe the approach that we have taken in this work, using ultracold atoms in optical lattices. I will describe the tools that we have for manipulation and detection in such systems, and the advantages and disadvantages of this sort of simulation as it compares to other simulators as well as to the materials that we simulate. Finally, I will motivate and describe the particular lattice geometries simulated in this thesis.

1.3 Quantum mechanics

1.3.1 A quantum particle

Quantum mechanics is a set of rules that is best known for its governance of the behavior of small particles. There are a lot of misconceptions about these rules; I've spoken with people who are convinced that the particle world is a lawless land where magic abounds and human consciousness plays a mysterious role. Others have heard that there is a fundamental uncertainty in a particle's position or speed, and will suggest to me that I would be more certain if I measured more carefully. In truth, the land is not lawless, but the uncertainty is fundamental. We understand many of the rules quite well, and they are unaffected by the consciousness of the observers.

The confusion about the nature of quantum mechanics arises from our familiarity with classical mechanics – the rules that govern physics of large things, like us, at the temperatures we live in. We experience a physical world where a tennis ball is in one place at a time, and if we wanted we could calculate the trajectory it will take when thrown. You might insist that

you could not calculate the trajectory, but I maintain that you do it without thinking, every time someone throws a ball at your face. We humans have an inherent sense of classical physics, no matter how discouraging our high school courses may have been.

So we try to use that sense of physics and draw a parallel between balls and particles and we are baffled that the rules to which we have grown so accustomed no longer apply. Where a ball is described by a point in space and time, a particle is described by a function that varies in space and time, called a wavefunction. At a given time, the probability of measuring a particle in a particular place can be calculated from this wavefunction. While it may seem strange that particles cannot accurately be described as occupying a particular place at a particular time, there is nothing magical afoot. The laws of quantum mechanics are unfamiliar, but they are laws all the same. We can write down equations to describe the behavior of particles, and sometimes we can solve them. When we do solve them, the particles behave as we predict.

There is a characteristic length of a particle wavefunction, which is larger for particles of smaller mass or at lower temperature. This helps to explain why we experience a classical world. We interact with large, heavy things, made up of many many particles at room temperature. All of the matter with which we interact – marbles, tennis balls, and even humans – can be accurately described by a quantum wavefunction, but the wavelength is so small that it quantum effects are imperceptible and irrelevant to our daily experience. So the question arises, what is small? Electrons are small. In fact, the relative weight of an electron to a tennis ball is roughly the same as the relative weight of a tennis ball to the sun. An electron at room temperature has a wavefunction that is long compared to typical atomic spacings in a material, so we say that the wavefunction is delocalized over the lattice of atoms. In our work, we create a very large, delocalized wavefunction using more massive particles (atoms), which are cooled to much lower temperatures, very near absolute zero, so that their quantum wavefunctions are magnified.

A measurement of the particle will find it in just one location or state, and this is sometimes referred to as 'collapsing' the wavefunction. Many measurements of a particle will reveal its probability distribution. It is important to note that the measurement doesn't need to be recorded by a device or observed by a person in order to collapse the wavefunction. If anything in the environment interacts with a particle and carries away information about the particle's state, this will qualify as an observation and collapse the wavefunction, regardless of whether a human is there to collect the information. This presents a huge challenge to experimental studies of quantum mechanics; it is the reason that we carefully bake out the vacuum chamber in our lab. In this process, we remove nearly all the air from the environment in which we study the quantum behavior of particles so that nothing in the air will interact with the particles and measure them when we aren't looking.

The wavefunction can also describe a particle that exists in two states at the same time. This is known as *quantum superposition*. These concepts are the source of the fundamental uncertainty in a quantum mechanics. In this thesis, we explore an effect that reduces the uncertainty in a measurement (at the cost of increasing uncertainty elsewhere, because uncertainty can be moved around but never extinguished in quantum mechanics). In the

beginning of our experiment, the particles have broad wavefunctions. We introduce a lattice potential, which is an array of wells, like an egg crate. The broad particle wavefunctions mean that they are in superpositions of being in many wells of the lattice at the same time. As a result, there is an inherent uncertainty in the number of particles on any given site. We then change the conditions of the experiment, so that the uncertainty is forbidden. The superpositions cease to exist and particles become constrained to just one location. In our work, it is the interactions among particles that reduces the uncertainty in particle number on a site. To understand the nature of this reduction in uncertainty, imagine a crowd of people entering a concert hall. If the people can interact with one another, then each chair will host either zero or one person, because anyone who tried to fit more than one person in a chair would interact (badly) with one another. When the concert hall fills up, the number of people in each chair becomes more and more certain (tending to exactly one per seat). If, instead, the people did not interact and passed through one another like ghosts, then presumably they would be fine with sharing a chair. The behavior of many particles that interact can be difficult to model and understand, and this thesis concerns artificial materials in which we can specify the amount of interaction that particles have and study their behavior under different conditions.

Another curious prediction of quantum theory is that physically distinct quantum particles can be *entangled*, so that two particles may be linked and an operation on one of them (say, a detection) will affect the other. Albert Einstein, one of the most outspoken critics of quantum theory, hated this prediction most of all, calling it "spooky action at a distance." His mockery was rooted in the belief that the laws that govern the small should be understood in analogy to those that govern the large bodies of our everyday lives. The discomfort that we experience when trying to apply the familiar concepts of macroscopic physics to the smallest particles extended even to one of the most creative minds ever to have worked in the field.

1.3.2 A material: many particles

Using the laws of quantum mechanics we can write down equations to describe the behavior of a particle, but when there are many particles together, the equations can become rather complex and difficult to solve. There are roughly as many atoms in a single gram of a material as there are grains of sand on Earth, and an atom is made up of positively charged nuclei (ions) and electrons. If we need to consider all possible interactions among the particles in a material, the problem becomes very complex. Fortunately, the atoms in a material are arranged in a regular pattern, like an egg crate. We can simplify the problem by modeling the materials as electrons from each atom moving around in the egg crate-like potential created by the periodically arranged ions.

The optical and electronic properties of a material arise not from the details of the atoms that comprise it, but from the way those atoms are arranged. This is comparable to building castle walls out of legos. In Fig. 1.1 two different types of walls are shown. On the left, a wall created by directly stacking legos and lining those stacks next to one another. On the

Structures of Legos

Structures of Atoms

Weak

Strong

Soft & Opaque

Hard & Transparent
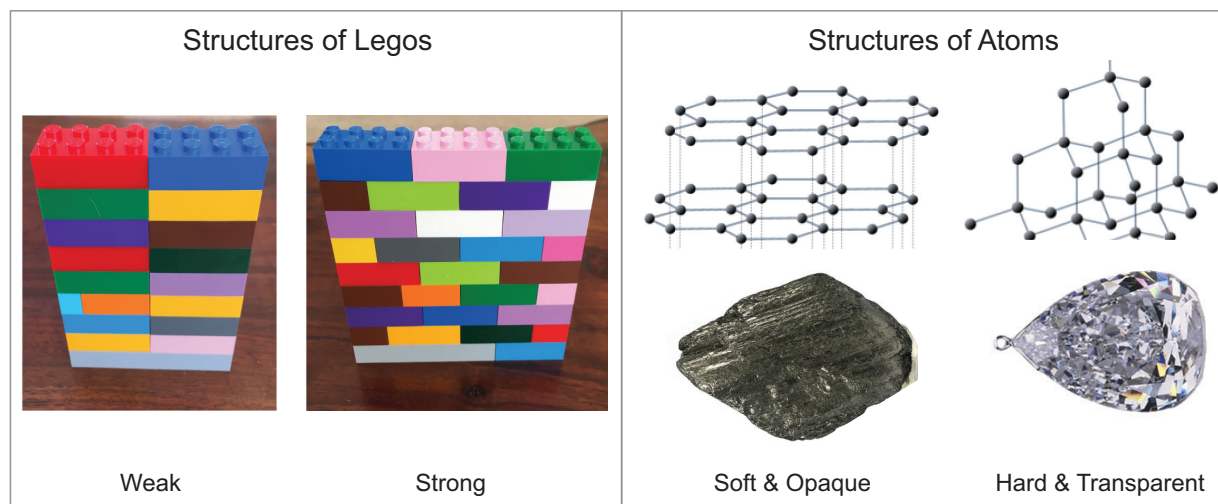
Figure 1.1: The way legos are arranged determines the properties of the resulting wall (left panel), and the way atoms are arranged determines properties of the resulting materials (right panel). Graphite and diamond are both made of carbon atoms, but the difference in the arrangement of the atoms leads to very different material properties. The arrangement of atoms in either material is shown schematically above images of the solids.

right, a wall is created by staggering the legos. The walls have different properties. The staggered wall will be stronger if the castle is under siege.

Crystalline materials are similar to the lego walls, except that the building blocks of materials are atoms rather than legos. The arrangement of the atoms determine the physical properties of the material. It will determine whether the material is conducting or insulating, whether it is transparent or opaque, and whether it gives rise to any nontrivial quantum states or quasiparticles. As an example, diamond and graphite are both made of carbon atoms, but it is quite easy to distinguish the two. The differences arise because of the arrangement of the carbon atoms.

By modeling materials as itinerant electrons on a crystalline structure, we can write down equations that are more easily solved, because we need to consider only the electrons on the crystal lattice structure. Unfortunately, this approximation isn't enough to make the problems solvable. There are still many electrons, and if the electrons interact with one another, there will be many terms. A system of 300 electrons would have 2^{300} terms in the equation, which is more than the number of particles in the visible universe. To solve this equation on a computer would require a computer the size of the known universe, and that's only a material with 300 particles.

This problem may seem intractable, but it turns out that we can make some very good approximations in condensed matter physics and understand the properties of many crystalline materials. The equations of many quantum particles (electrons) in a material are hard to solve, so we make many simplifications and approximations and reductions until we

find problems that we can solve. We make so many simplifications in understanding basic materials physics that the most remarkable thing is not that occasionally our predictions are wrong, but that they work at all.

In the simplest techniques to solving this problem, we make an enormous approximation – that the electrons do not interact with one another at all. They pass each other without notice, like strangers on the street, staring at their smartphones. They experience the periodic potential provided by the ions arranged in a crystal structure as though they were alone in the crystal. Shockingly, this approximation works quite well to predict many of the physical properties of materials.

The past century has seen many developments and great successes in quantum theory. We have described the electronic properties of materials, we have understood the mechanisms behind chemical reactions, and we have used those solutions to build the technology that we all use every day – in our pockets and on our desks are billions of components that would not have been created were it not for our understanding of the laws of quantum mechanics.

1.3.3 What is quantum simulation?

Still, there are problems in both materials physics and chemistry for which particle interactions must be more fully considered. Many methods have been developed to take interactions into account, with varying levels of computational ease or rigor. There are more sophisticated approximations in which we consider simplified particle interactions, and there are simple problems that can be fully solved on a supercomputer without approximations. But, as is always the case when a problem is simplified, there are times when the approximations don't hold. We find materials with unexpected behavior, and it always traces back to something we have neglected.

Sometimes the problems that cannot be solved relates to the interactions among the particles, which grow too complex. Other times, the challenge related more fundamentally to the geometry of the underlying lattice. The challenge for physicists is to find another way to study these problems that cannot be solved on traditional computers. The solution will be to use quantum particles to understand quantum interactions. The idea is to build an artificial material out of individual, well-controlled, quantum building blocks.

In this thesis we do exactly that. We create an artificial, well-controlled material in which we can tune the interparticle interactions with a very simple experimental knob. Motivated by the challenge of treating systems with strong interactions, we explore a phase transition that is driven by increasing interactions of lattice-trapped particles. Furthermore, motivated by the challenge concerning fundamentally complicated lattice geometries, we experimentally realize one such crystalline structure, that of the two-dimensional kagome lattice.

The first thing that is needed to perform a well-controlled quantum simulation is is a well-controlled quantum lego. The challenge is that it must be controllable, but still governed by the laws of quantum mechanics. This requires careful control over the environment. Those features that make the quantum world so strange – superposition and entanglement – break down when the particles interact with their environment. Recall when anything in the

environment interacts with a particle and carries away information about the particle's state, it qualifies as an observation and collapse the wavefunction, regardless of whether a human is there to collect the information. The quantum coherence is lost, and the system will behave like any classical system. As quantum simulators and computers grow increasingly large, the likelihood of interactions with environments grow, so that quantum coherence is hard to maintain.

1.4   Crystal structures in this thesis

In our lab, we engineer lattices of triangular, honeycomb and kagome geometries, which are represented in Fig. 1.2. Most experiments with ultracold gases in optical lattices have been performed in primitive lattices (triangular, square and cubic), which have a single site per unit cell. Recently, the field has branched out to encompass honeycomb and superlattice geometries, with multiple sites per cell. Our kagome lattice was the first with three sites per cell. These multi-site per unit cell lattice geometries introduces a new, low-orbital degree of freedom that can be explored in optical lattices. It also expands on the number and type of condensed matter systems that can be emulated with ultracold gases.

The honeycomb lattice is the structure of graphene and its electronic band structure has linear dispersion at the edges of the first Brillouin zone. The effective mass of the charge carriers in a material is related to the curvature of the band, and the cusp in the band structure implies that the charge carriers are massless and can flow without friction through the material. For this reason, graphene a subject of immense theoretical and engineering interest.

In contrast, the kagome lattice has an energy band that is completely flat, so that there is no curvature and the charge carriers have infinite mass. This is no good for conduction, but represents frustration of a many-body system, where there are many available degenerate states that the gas can occupy (the density of states is very large and the energy of the quantum gas is low). This represents a manifestation of geometric frustration in the orbital degree of freedom, where no local order is established. Geometric frustration is a pressing topic of investigation in many-body physics, and material realizations of the kagome lattice have been elusive. Candidate materials such as SCGO, jarosites, herbertsmithite and volborthite have all been studied, but they are not ideal, defect-free realizations of the two-dimensional kagome geometry.

1.5   Simulating materials with ultracold atoms

In our lab we mitigate the decoherence challenge by storing atoms in a chamber from which we remove nearly all other particles. To remove them, we bake-out the steel vacuum chamber, raising it to about 150° C (300° F), while pumping any particles out with a vacuum pump.
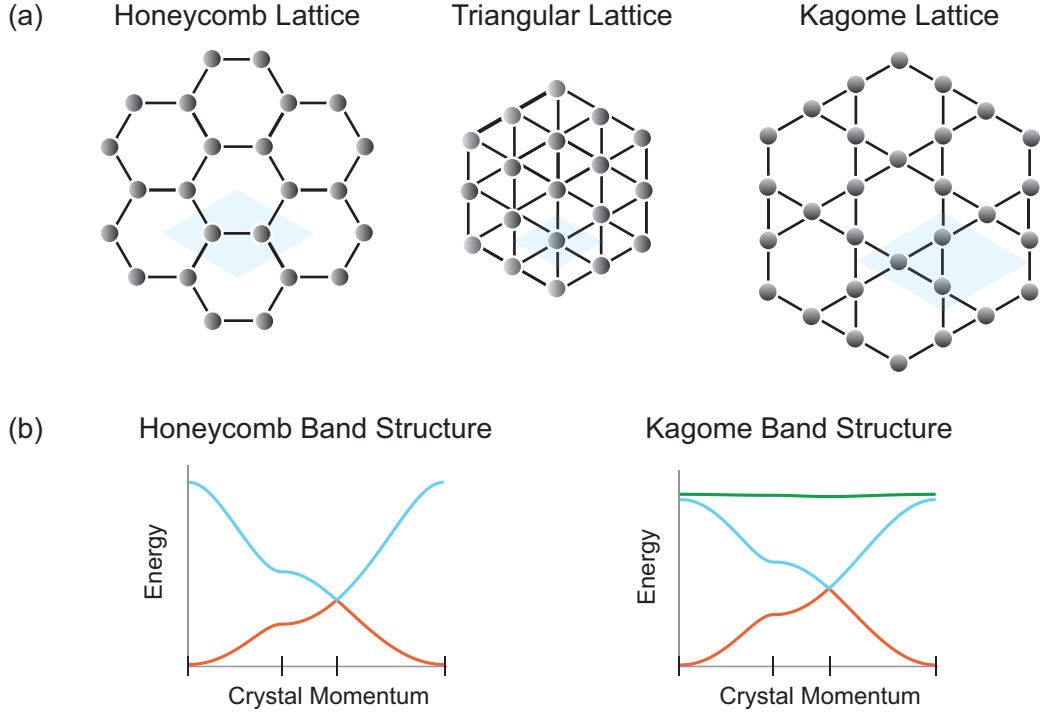
Figure 1.2: (a) Atoms are arranged in regular, periodic structures. The honeycomb, triangular and kagome lattice geometries are shown schematically, with unit cells indicated by blue parallelograms in each lattice. Every lattice is formed by repeating this unit cell, like tiles. The honeycomb has two sites in its unit cell, the triangular lattice has just one, and the kagome lattice has three. (b) The number of sites per unit cell determines the number of bands in the lattice band structure. Here we show the band structures of the honeycomb and kagome lattices, where energy is plotted against lattice momentum along a trajectory that traces through the lattice Brillouin zone. Tick marks indicate the high symmetry points in the lattice: Γ, M, K, Γ. The dashed line in the honeycomb band structure marks the K point, where the upper and lower bands meet and form an x. The linear way that the bands meet results in unique properties of graphene, a material in which carbon atoms are arranged in a honeycomb structure.

In the end, our vacuum chamber has roughly the same air pressure as the lunar atmosphere. This way, our atoms are unlikely to interact with anything outside of our control.

To simulate this situation in a controlled environment requires a delocalized wave function and a periodic potential. We create crystalline trapping potentials for neutral atoms by interfering laser beams. The resulting lattice spacings are about 1,000 times larger than those of a real material. To simulate a real material requires that the wavefunction subjected to this potential is about 1 micron across, which is huge for a quantum state.

In 2015, we celebrated the 20th anniversary of the creation of a quantum state of matter

with this large spatial wavefunction [8]. The Bose-Einstein condensate (BEC), when subjected to the periodic potential of an optical lattice, acquires the periodicity of the lattice and is described by the same physics as that which describes electronic wavefunctions of real materials.

By loading a BEC into an optical lattice, we can learn what sort of optical or electronic properties that a material with that lattice structure would have. Moreover, these materials can be dynamically manipulated, because the crystal lattice is created by laser beams that can be tuned and because the timescales of the atoms in the lattice are much slower than those of real materials. In the field of optical lattices, we have produced increasingly complicated crystal lattice structures, and the kagome lattice reported in this thesis represents one such step forward in the simulation of materials using ultracold atoms in optical lattices.

1.5.1 Lattices of laser light

Yes, light is both a wave and a particle. And also it is neither. Those are just classical analogies that help us understand. Sometimes one analogy is more helpful than the other, sometimes the other is more apt. They are both correct, and anything we understand in one way can also be understood in the other.

To introduce optical lattices, we consider beams of light as described by waves. Imagine standing at the bank of a lake, like the one shown on the left of Fig. 1.3. There is no wind, the water is completely still. Pick up a rock and toss it into the lake– the wave radiates outward. For your next experiment, use two rocks, and throw them some distance apart. Now there are two waves, radiating outward. Where the waves meet, their behavior seems peculiar. They interfere. Where the peaks of the waves meet, they add to a wave that is taller than either individually was, and where a peak meets a trough, they cancel and the water is the height of the rest of the lake. After the waves have moved through one another, when you look out, you will notice a moving checkerboard pattern, like an egg crate.

It is also possible, though admittedly a bit contrived, to make a standing wave on the water, where every point along the wave vibrates with constant amplitude so that the wave doesn't appear to be moving but the peaks become troughs and vise versa. In this case, if you examine the surface of the lake, you'll find some locations where the surface of the water undulates up and down. Here, the wave amplitude is large. Nearby, you'll find other locations where the surface of the water is, at least locally, still. The water there remains at a constant height, so that the wave amplitude is locally zero.

When we interfere laser beams, we can create standing waves of light that have stationary intensity maxima and minima, examples are shown on the right side of Fig. 1.3. Atoms exposed to a standing wave of light are trapped in either the maximum or minimum intensity points, depending on the details of the atom and the color of the light. This interference pattern acts like an egg crate for the atoms.

Interference
on the surface of a lake

Interference
of green laser beams
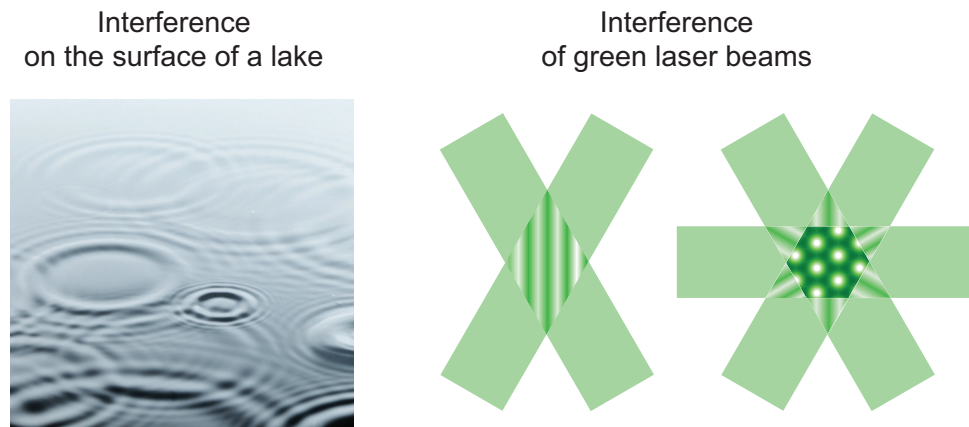
Figure 1.3: Waves on the surface of a calm lake expand outward, and interfere where they cross. Laser beams form an interference pattern where they cross. Two beams will form a stripe pattern, and three beams from equal angles form a triangular lattice geometry.

1.5.2 Atoms

In order to create a large quantum wavefunction, we cool a cloud of atoms until it forms a quantum state called a Bose-Einstein condensate. In our lab we create some of the coldest gases in the universe. We begin with a pure sample of ^{87}Rb. That we use rubidium doesn't particularly matter, the physics that we study is universal and many different atoms have been used in this sort of experiment, but in this lab we use rubidium. Rubidium is solid at room temperature (300 Kelvin), and we work with a gas, so first we heat the solid in an oven with a hole in it. The atoms fly out of the hole and we cool them over the course of a few seconds by strategically hitting them with lasers [9]. In the end, the atoms reach ~ 100 nanoKelvin. That is, one billion times colder than room temperature, and less than one millionth of a degree Fahrenheit above absolute zero.

Temperature is the measure of kinetic energy of the particles around us. At these extremely low temperatures, we have removed so much of the kinetic energy from the atoms that you might expect that the atoms would be completely still. But they cannot be completely still, because if something is completely still, we will be able to know exactly where it is, and that would violate the fundamental uncertainty of quantum mechanics. Kinetic energy of a particle is typically large, and it's energy scale dominates when considering the motion of a particle, but when it is nearly completely removed, the laws of quantum mechanics become increasingly relevant. The wavefunction that describes the atom, the probability distribution of finding the atom in a given location, is small at room temperature, but as the temperature decreases, the spatial extent of the wavefunction grows larger. At 100 nK, the 100,000 atoms that we started with have wavefunctions that completely overlap and fill the optical bowl that contains them. The atoms are indistinguishable, so that when the probabilities overlap, they become described by a single wavefunction.

In our work, we use a dilute gas of bosons, which undergoes a phase transition to a Bose-Einstein condensate at these low temperatures due to an effect of bosonic particle statistics. Upon crossing this phase transition, the coherence length of the particles becomes infinite. The condensate is a few microns across, large enough to see in a child's microscope. All of our experiments begin with a condensate. The atoms that make up the condensate can be approximated as non-interacting, just like a cloud of electrons in a material. We can impose a periodic potential on the gas, just like the ions in a material. However, because we create the condensate, we know exactly what it is made of, and because we impose the periodic potential, we can manipulate it at will. We thus simulate materials in a highly controlled environment, allowing controlled quantum simulation of materials physics.

1.5.3   Tools

Manipulation

In a real material, the crystalline structure emerges from the balance of forces within a strongly correlated electronic material. In an optical lattice, it is specified experimentally. The lattice is created at the interference of laser beams, and the interference pattern can be dynamically controlled by tuning properties of the lasers.

The depth of the lattice – the height of the barriers between sites – is controlled by changing the intensity of the lasers. This height will determine the probability that an atom will tunnel from one site to the next, as well as the interaction energy that it will experience when it shares a lattice site with another atom. The lattice depth can be changed slowly, so that the atoms respond adiabatically, or it can be shifted quickly, freezing the motion of the atoms. It can also be modulated to create momentum-conserving excitations in the lattice to upper bands [10].

In our work we create an optical superlattice at the overlap of two distinct lattices, which provides yet another degree of control. The two lattices that comprise the superlattice can be shifted relative to one another, which allows for the realization of various metastable states in upper bands of the superlattice [11].

All of these lattice manipulations can be performed on timescales that are either fast or slow compared to the tunneling time of atoms in the lattice. The most rapid tunneling events occur at a rate of about 100 tunneling events per second, where laser beam parameters can typically be tuned at least an order of magnitude more rapidly. This is a huge advantage of optical lattices relative to real materials, as electron dynamics are typically on the order of femtoseconds (10^{15} events per second) and thus very hard to observe with modern techniques. Given that coherence times of the $\sim 100,000$ identical particle condensate are typically about a second, this also means that we can have many tunneling events within a coherence time, which is an impressive feat when compared to other methods of quantum computing.

Finally, we can tune the entropy and temperature of the atomic gas before imposing the optical lattice, so that we can choose the thermal occupation of each energy band.

Detection in momentum space

Releasing atoms from optical confinement and allowing them to expand before imaging leads to a momentum-space representation of the gas. After they expand, atoms are imaged with a technique called absorption imaging. A laser beam passes through the atoms and onto a camera. The atoms absorb light from the lasers and cast a shadow onto the camera. The depth of the absorption indicates the number of atoms that absorbed light from the photons. An example of an absorption image after atoms are released from a triangular lattice is shown in Fig. 1.4.

In a bulk gas, without an optical lattice, atoms expand with a speed that is determined by their energy, as $E = \frac{1}{2}mv^2$, where E is the particle energy, m is its mass and v is the velocity with which it will expand. However, in an optical lattice, atoms are in a quantum superposition of states that move at several different velocities. The lattice imparts momentum to the atoms, because the atom wavefunction takes on the periodicity of the lattice (Bloch's theorem again). When atoms are released from optical confinement, they fly out with momentum imparted by the lattice. The exact distribution of the atomic state in momentum space is determined by the lattice geometry. Conversely, by examining this pattern, we can infer the lattice potential.

Equivalently, consider a superfluid in an optical lattice potential which remains phase coherent across the lattice. When the atoms are released, they expand from each node of the trapping potential. This expansion from an array of point sources leads to an interference of the matter-waves that results, in the far field, in an image of the atoms in the Fourier plane. This is similar to x-ray diffraction, in which coherent light is reflected from a material where the ions locations act as a point source for the reflected x-rays. In this case, it is the matter-wave that interferes. In this superfluid limit, an image of the atoms in the Fourier plane also corresponds to the Wannier state of the ground band of the lattice.
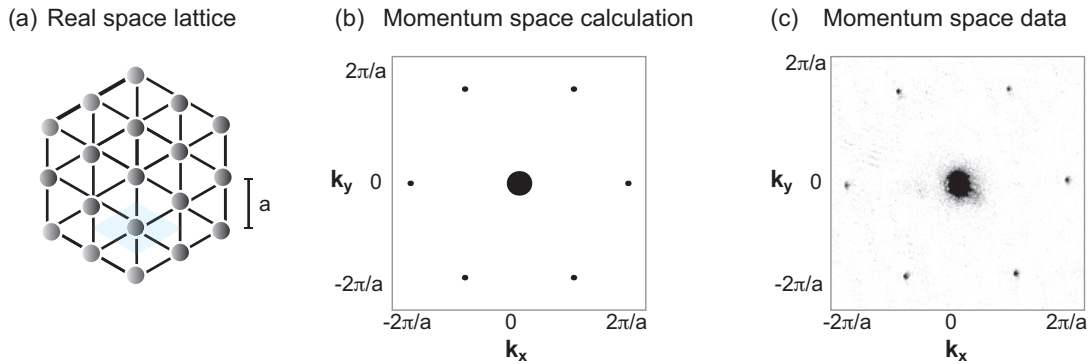
Figure 1.4: Image in momentum space of a stationary Bose-Einstein condensate in an optical lattice. This corresponds to the ground-state $k = 0$ Wannier function, and, more generally, to the correlation function of the atoms in the lattice.
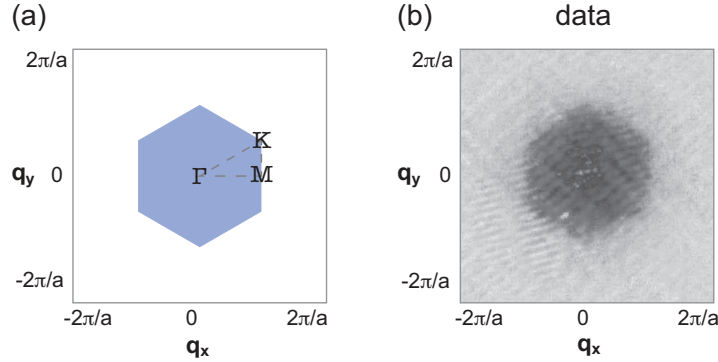
Figure 1.5: The first Brillouin zone of the triangular optical lattice. This image is taken by heating a cloud of atoms until it fills the first Brillouin zone, and then mapping lattice quasimomentum into real momentum before momentum-space imaging.

Another tool provided by optical lattices is called band mapping, an example for a thermal gas that fills the first energy band of the triangular lattice is shown in 1.5. The atoms in the lattice potential experience the band structure of that lattice, and by adiabatically ramping down the optical lattice, we map the band structure of the lattice into a free-particle band structure, thus mapping quasimomentum into real momentum. We then take a momentum-space picture, where now we observe the shape of the occupied Brillouin zone.

1.6 Comparing laser-based materials to real materials

There are many advantages of creating artificial materials rather than directly probing real materials. The first is that the composition of the artificial material is well-understood. We create artificial materials in an ultrahigh vacuum chamber using techniques of atomic physics that ensure that the only atoms involved in our simulations are the ones we put in the simulation. This means that our materials are without defects, which change the properties of many real materials (though sometimes in interesting ways). The artificial materials are made at the interference of laser light, so that all lattice sites are exactly spaced, and those sites are not mobile relative to one another (i.e. there are no phonon modes).

A second advantage is that the length scale of the artificial materials are magnified relative to a real material. Optical lattice spacings are hundreds of nanometers, which is thousands of times longer than the few angstrom spacings of a real material. This means that spatial features can be directly observed. This magnification has another subtle consequence. The length scale of the lattice sites determine the timescale of dynamics for particles moving on the lattice. Where in a real material particles move in a lattice on the femtosecond timescale, dynamics in an optical lattice occur in milliseconds.

A third advantage of these artificial materials is that the Bose-Einstein condensate and the crystal lattice structure are independent of one another. The experimentalist may introduce,

modify or extinguish the crystal lattice structure and measure the response of the condensate to these changes. The lattice-depth is tuned with the intensity of the laser beams and, in a bichromatic superlattice, the crystalline structure is tuned with the phase of the laser beams. Because the dynamics of lattice-trapped particles occur on millisecond timescales, the material properties may be changed either quickly or slowly relative to particle response. This means that the condensate can be used to probe the lattice geometry, as in the experiment of chapter 4, or it can be trapped in the lattice like electrons in a real material, as in the simulation reported in chapter 5.

1.7 This thesis

I joined the lattice experiment (E5, as it's called in the Stamper-Kurn group) in the fall of 2010, just as Dr. Jennie Guzman and Dr. Gyu-Boong Jo were working on elegant experiments concerning the formation of domains in a spinor Bose-Einstein condensate [12]. I was coming from a background in particle physics, and this made it especially exciting to join a lab with data to analyze. With Jennie's help I was able to dive right in to analysis. With the excellent and careful mentorship of Jennie and Gyu-Boong, I quickly learned both the experimental techniques and the theoretical underpinnings of atomic physics and quantum simulation. Jennie was an expert experimentalist, having built the entire apparatus. Gyu-Boong had joined recently ready to finish up work with spinors to push on the construction of a bichromatic optical kagome lattice. Together, the three of us constructed the first version of the optical lattice within just a few months, the publication reporting this achievement is included in appendix A. With this lattice we learned a lot about the construction and operation of a bichromatic optical lattice, discussed in chapter 2 and chapter 3. Jennie and Gyu-Boong left in the fall of 2012, just after we were joined by fellow graduate student Thomas (Tom) Barter.

Tom and I recovered the experiment after the long series of events that led up to the flood. We completely rebuilt the optical lattice and this new lattice is the subject of this dissertation. Among his many contributions, Tom took charge of recovering the BEC, constructed the 532-nm lattice, designed and implemented the phase stabilization system for the bichromatic lattice, and performed data analysis. We were joined by Vincent Klinkhamer for one year in 2013, who worked hard and had a positive attitude in the face of many big tasks. He designed, created and tested the coils that produce magnetic bias fields and make our work possible. Soon after, we were joined by fellow Berkeley grad student Tsz-Him (Zephy) Leung, who was an excellent addition to our group. Zephy tested and implemented all of the intensity stabilization circuits in the lab, and worked tirelessly every time we took data for our experiments. Soon after Zephy joined the lab, we finished construction of the 1064-nm honeycomb lattice and Tom, Zephy and I took diffraction data that showed a large momentum-space asymmetry and is discussed in chapter 4. At that time we were joined by another one-year master student, Severin Daiss, who contributed to our understanding of that asymmetric diffraction data. After Severin's departure, we began taking data for the

final work in this thesis, the superfluid to Mott insulator transition discussed in chapter 5. We were joined by a post-doc Dr. Masayuki Okano, who performed calculations concerning the ground state of lattice-trapped gases and who joined us in the many days of alignment and data taking required for the manuscript of appendix C. Finally, we were joined by another one-year student Luca Bayha, who had an excellent sense for the physics that we were studying and contributed to many of our discussions of the behavior of particles in lattices under increasing interactions.

This dissertation discusses the design, construction, testing and use of a quantum simulator of materials in the triangular, honeycomb and kagome crystal lattice structures. The general technique for creating a bichromatic optical lattice in the triangular, honeycomb and kagome geometries is described in chapter 2. Important calculations of the properties of lattice-trapped gases and the technique for their calibrations are also discussed. We constructed a lattice that is easy to align and exceptionally stable, and chapter 3 discusses many technical details concerning the construction, testing and use of the optical lattice.

The work in this dissertation led to two manuscripts, and in this dissertation we aim to supplement but not repeat the findings in those manuscripts. In the first, included in appendix B, we developed a sensitive matter-wave diffraction technique to measure precisely an optical lattice configuration, in analogy to x-ray diffraction from solids. Tuning the interaction time between light and atoms led to strong enhancement of the effects of slight potential asymmetries. This effect was explained theoretically through time-dependent perturbation treatment of matter-wave diffraction and also time-independent perturbative treatment of lattice band structure in the presence of small inversion-symmetry breaking term. The discussion in chapter 4 provides more detail into the nature of the asymmetric perturbation, and also describes in more detail the origin of the oscillatory asymmetry signal.

Finally, chapter 5 discusses details concerning a test of the mean-field treatment of the Bose-Hubbard model that is independent of the temperature and trapping frequency of the lattice-trapped gas. This test goes beyond previous experimental studies that attempt to identify critical points in a phase diagram, and tests instead the predictions along an entire line of the phase diagram. The test required the development of a new method of comparing optical lattice experiments, and relied on the tunable geometry of our bichromatic optical lattice. The manuscript is currently in review and is included in appendix C.

Chapter 2

Triangular, Honeycomb and Kagome Lattices

This chapter discusses the formation of optical lattices of the triangular, honeycomb and kagome geometries. The technique was first realized and reported in the following publication [13]:

- *G.-B. Jo, J. Guzman, C. K. Thomas, P. Hosur, A. Vishwanath, and D. M. Stamper-Kurn, "Ultracold Atoms in a Tunable Optical Kagome Lattice," Phys. Rev. Lett.* **108***, 045305 (2012). Included in appendix A.*

The work in this dissertation begins with the creation of artificial crystalline lattice structures for neutral atoms using coherent beams of light. The beams interfere with one another, giving rise to periodically varying patterns of beam intensity and polarization. Because neutral atoms experience an optical dipole force that depends on intensity and polarization, the periodically varying intensity structures act as a periodically varying potential energy landscape – a crystal lattice structure – with a periodicity that is determined by the wavevector of the beams. Neutral atoms may be prepared in quantum states where their centers of mass are delocalized over many sites of an optical lattice so that, together, the atoms and optical lattice emulate a solid-state material. Bloch's theorem is applied, as in solid-state, to determine energy eigenstates and band structure of atoms within such lattices.

This chapter describes the crystal lattices that we create in the lab. We make an optical superlattice, formed at the overlap of two optical lattices that are created by laser beams of different wavelength. The resulting pattern is complex – there are multiple sites per unit cell in the superlattice – and tunable – the lattice structure depends on the overlap of the two composite lattices. I start by describing the formation of the two lattices of intensity and then explain how they give rise to lattices of potential energy in which atoms may be trapped. Although the intensity lattices are patterns of both intensity and polarization, I neglect the effect of beam polarization in this chapter. This is valid in the potential lattices formed at intensity minima, but the subject is revisited in chapter 4 where we study a lattice formed at intensity maxima.
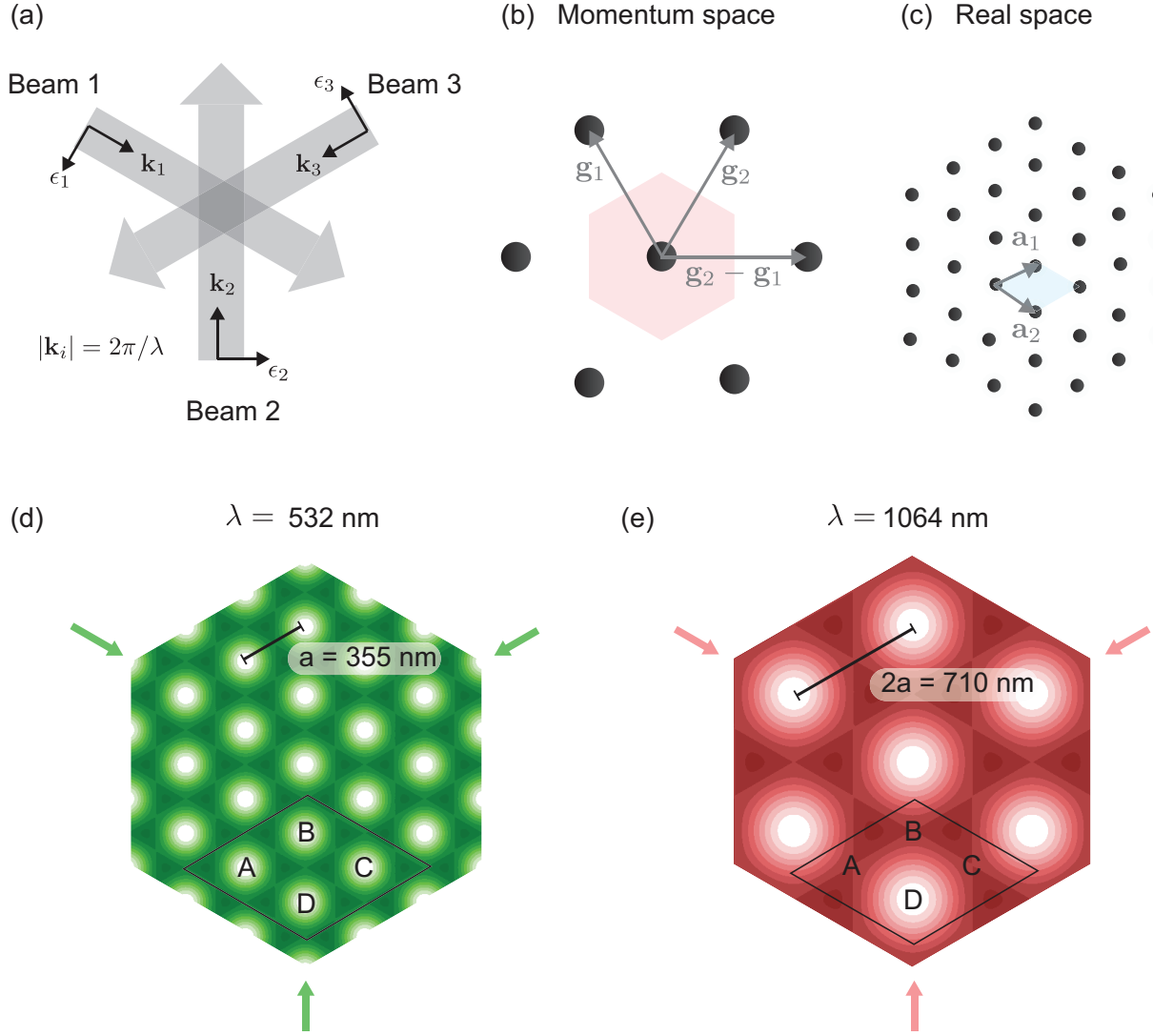
Figure 2.1: Method for creating triangular lattices of intensity minima. (a) Three coherent beams of wavelength λ and in-plane polarization are incident from equal angles at the location of the atoms. For each beam i, the momentum vectors, $\mathbf{k}_i$, and polarization vectors, ϵ_i, are indicated. (b) Atoms scattering from one beam into another result in momentum transfer to the reciprocal-space lattice vectors, $\mathbf{g}_i$, with $|\mathbf{g}_i| = \sqrt{3}|\mathbf{k}_i|$. The first Brillouin zone is indicated in pink. (c) The triangular real space lattice with basis vectors $\mathbf{a}_i$ is derived from these momentum-space vectors, where $|\mathbf{g}_i| = 2\pi/|\mathbf{a}_i|$. A unit cell indicated in blue. (d) The intensity lattice when $\lambda = 532$ nm has lattice spacing $a = 355$ nm. (e) A lattice created with light at twice the wavelength produces a lattice with twice the lattice spacing. A unit cell for the 1064-nm lattice is indicated and encompasses four sites of the 532-nm lattice unit cell.

2.1 Triangular and honeycomb optical lattices

2.1.1 Intensity lattices

The tunable optical superlattice used in this work is comprised of two triangular lattices of intensity minima that are formed using the same technique, illustrated in Fig. 2.1(a), with light of different wavelengths. Each lattice is derived from a single laser, split into three beams that propagate and have linear polarization in the horizontal plane. They pass through optics to control intensity and phase and finally intersect, incident from equal angles, at the location of the atoms. To calculate the resulting interference pattern, we write the momentum vectors, $\mathbf{k}_i$, and polarization vectors, ϵ_i, for each beam, which are shown in Fig. 2.1(a). We define the scalar $k = 2\pi/\lambda$:

$$
\begin{aligned}
\mathbf{k}_1 &= k \left(\tfrac{\sqrt{3}}{2}, -\tfrac{1}{2}, 0 \right) & \epsilon_1 &= \left(-\tfrac{1}{2}, -\tfrac{\sqrt{3}}{2}, 0 \right) \\
\mathbf{k}_2 &= k \left(0, 1, 0 \right) & \epsilon_2 &= (1, 0, 0) \\
\mathbf{k}_3 &= k \left(-\tfrac{\sqrt{3}}{2}, -\tfrac{1}{2}, 0 \right) & \epsilon_3 &= \left(-\tfrac{1}{2}, \tfrac{\sqrt{3}}{2}, 0 \right)
\end{aligned}
\tag{2.1}
$$

The intensity pattern is determined by the time-averaged amplitude squared of the sum of electric fields from each beam:

$$
\begin{aligned}
I(\mathbf{r}) &\propto \int_0^{\frac{2\pi}{\omega}} \frac{\omega}{2\pi} |\sum_\alpha E_\alpha(\mathbf{r})|^2 dt \\
&= \int_0^{\frac{2\pi}{\omega}} \frac{\omega}{2\pi} |E_0 \left(\epsilon_1 \cos \left[\mathbf{k_1} \cdot \mathbf{r} - \omega t \right] + \epsilon_2 \cos \left[\mathbf{k_2} \cdot \mathbf{r} - \omega t \right] + \epsilon_3 \cos \left[\mathbf{k_3} \cdot \mathbf{r} - \omega t \right] \right) |^2 dt \\
&= \frac{1}{2} E_0^2 \left(3 - \cos \left[\mathbf{g_1} \cdot \mathbf{r} \right] - \cos \left[\mathbf{g_2} \cdot \mathbf{r} \right] - \cos \left[(\mathbf{g_1} - \mathbf{g_2}) \cdot \mathbf{r} \right] \right)
\end{aligned}
$$

$$\tag{2.2}$$
$$\tag{2.3}$$

where E_0 is the electric field amplitude of a single beam and in the last line I have used the definition of the reciprocal lattice vectors, indicated in Fig. 2.1(b),

$$
\mathbf{g}_1 = \mathbf{k}_2 - \mathbf{k}_1 \tag{2.4}
$$

$$
\mathbf{g}_2 = \mathbf{k}_2 - \mathbf{k}_3, \tag{2.5}
$$

which correspond to the stimulated absorption and emission of a photon by an atom between lattice beams. The reciprocal space basis vectors $\mathbf{g}_i$ and corresponding real space basis vectors $\mathbf{a}_i$ are shown in Figs. 2.1(b) and 2.1(c). The length of the momentum-space vectors is given by $|\mathbf{g}_i| = \sqrt{3}|\mathbf{k}_i| = 2\pi/|\mathbf{a}_i|$, so that $\mathbf{g}_{i,532} = 2\mathbf{g}_{i,1064}$.

From the reciprocal lattice vectors we generate the first Brillouin zone, indicated in pink in Fig. 2.1(b), by bisecting each reciprocal lattice vector. The high symmetry points in the first Brillouin zone (not labeled) are at lattice quasimomenta $\mathbf{q} \in \{\Gamma, M, K\}$, which are defined

$$\Gamma = \begin{pmatrix} 0 \\ 0 \end{pmatrix} \qquad M = \frac{|\mathbf{g}|}{2} \begin{pmatrix} 1 \\ 0 \end{pmatrix} \qquad K = \frac{|\mathbf{g}|}{2} \begin{pmatrix} 1 \\ \tan(\pi/6) \end{pmatrix}$$

The intensity lattice of (2.3) is a triangular lattice of intensity minima with lattice spacing $a = |\mathbf{a}_i|$, given by Eq. (2.6). The peak-to-peak height of the interference pattern is proportional to $9/4|E_0|^2$. If one of the three beams is extinguished, the resulting pattern is a one-dimensional lattice with a peak-to-peak depth proportional to $|E_0|^2$. This assumes that all beams are equal intensity where the lattice is formed. By adding a third beam of equal intensity, the lattice depth increases by a factor of $9/4$. I highlight this comparison because experiments measuring the response of cold atoms to the imposition of three-beam and two-beam lattices were performed for the purpose of calibrating the lattice depth precisely.

$$a = \lambda/(2\sin^2(\pi/3)) \tag{2.6}$$

Figures 2.1(d) and 2.1(e) show the calculated intensity pattern for light at two commensurate wavelengths, $\lambda = 532$ nm and $\lambda = 1064$ nm, and identifies the lattice spacing between sites of intensity minima as $a = 355$ nm and $2a$, respectively. A unit cell of the 1064-nm lattice contains four sites of the 532-nm lattice, labeled A – D in the figure.

The calculations in Figs. 2.1(d) and 2.1(e) also show that the points of maximum intensity form a honeycomb lattice around each minimum intensity point. The height of these honeycomb-lattice peaks accounts for just $1/9$ of the total peak-to-peak height of the lattice, and the remaining $8/9$ of this height is accounted for by the triangular-lattice troughs.

2.1.2 Potential energy lattices

The potential landscape $V(\mathbf{r})$ of either lattice has the same structure as the intensity landscapes $I(\mathbf{r})$ in Eq. (2.3), but the pattern is normalized to V_0.

$$V(\mathbf{r}) = V_0 \left(\frac{2}{3} - \frac{2}{9} \left(\cos[\mathbf{g_1} \cdot \mathbf{r}] + \cos[\mathbf{g_2} \cdot \mathbf{r}] + \cos[(\mathbf{g_1} - \mathbf{g_2}) \cdot \mathbf{r}] \right) \right) \tag{2.7}$$

The sign of V_0 depends on the detuning of the light from atomic resonance. The principal atomic resonances of ^{87}Rb atoms are at wavelengths 780 and 795 nm, so that the 532-nm lattice is blue-detuned and the 1064-nm lattice is red-detuned from atomic resonance. The potentials are inverted for the wavelengths of light used in this work. The 532-nm lattice forms a lattice potential with wells in the triangular geometry and peaks in the honeycomb

geometry. The 1064-nm lattice forms a lattice potential with peaks in the triangular geometry and wells in the honeycomb geometry.

$$V_0 > 0 \quad when\ \lambda = 532\ nm \tag{2.8}$$
$$V_0 < 0 \quad when\ \lambda = 1064\ nm \tag{2.9}$$

In the lab, we refer to the lattice depth as $V_\lambda := |V_0|$, so that the depth of the 532-nm lattice is $V_{532} = V_0$ and of the 1064-nm lattice is $V_{1064} = -V_0$.

Recoil energies

It is useful to define the lattice recoil energy, $E_{r,lattice}$, to parameterize the depth of the potential energy lattice. I am going to be explicit about definitions of recoil energy, because our conventions are not always consistent. A recoil energy can refer to a single-photon recoil energy, or to the lattice recoil energy.

$$E_{r,light} = \frac{\hbar^2}{2m_{Rb}} \left(\frac{2\pi}{\lambda_{light}} \right)^2 \tag{2.10}$$

$$E_{r,lattice} = \frac{\hbar^2}{2m_{Rb}} \left(\frac{\pi}{a} \right)^2 \tag{2.11}$$

$$\tag{2.12}$$

where λ_{light} is the wavelength with which the lattice is created, a is the spacing of the lattice, m_{Rb} is the rubidium mass and $\hbar$ is the reduced Planck constant. These recoil energy terms are equal in lattices formed by retroreflected beams, but differ in the triangular lattices of our experiment. In our triangular lattice geometries, the relationship between spacing and wavelength is in Eq. (2.6), so that the recoil energies are related as $E_{r,lattice} = 9/16 \times E_{r,light}$.

Our notation in the lab can be confusing because we refer to the triangular lattices as the "532-nm lattice" and the "1064-nm lattice", in reference to the wavelength of light with which they are created, despite the fact that the lattice spacings a are given by $2a = \lambda_{light}/\sin^2(\pi/3)$. We use the notation $E_{r,532} := E_{r,lattice}$.

$$E_{r,532}/h = 4.5\ \text{kHz} \qquad \textit{the lattice recoil energy for the 532-nm triangular lattice} \tag{2.13}$$
$$E_{r,\lambda_{532}}/h = 8\ \text{kHz} \qquad \textit{the photon recoil energy for the 532-nm light} \tag{2.14}$$
$$E_{r,1064}/h = 1.1\ \text{kHz} \quad \textit{the lattice recoil energy for the 1064-nm honeycomb lattice} \tag{2.15}$$
$$E_{r,\lambda_{1064}}/h = 2\ \text{kHz} \qquad \textit{the photon recoil energy for the 1064-nm light} \tag{2.16}$$

where h is Planck's constant.

In the lab we also use light at $\lambda = 1064$ nm to form an additional lattice that is orthogonal to the plane of the triangular lattices. This vertical lattice is formed by retroreflecting the beam, so that $E_{r,\perp} = E_{r,\lambda_{1064}}$.

2.2   Band structure and Bloch states

We first consider the states of atoms in either triangular lattice of intensity minima. To solve for the band structure and states in each two-dimensional lattice, we discretize the Schrödinger equation in reciprocal space. In a periodic potential, we have

$$\left(\frac{\mathbf{p}^2}{2m} + V(\mathbf{r})\right)\psi_{\mathbf{q}}^{(N)}(\mathbf{r}) = E_{\mathbf{q}}^{(N)}\psi_{\mathbf{q}}^{(N)}(\mathbf{r}) \tag{2.17}$$

where $V(\mathbf{r}) = V(\mathbf{r} + \mathbf{a})$, the band index (N) labels the solutions, and the vector $\mathbf{q} = (q_x, q_y)$ is within the lattice Brillouin zone.

Bloch's theorem says that (2.17) is solved by wavefunctions that are the product of a plane wave and a periodic function with the same periodicity as the potential:

$$\psi_{\mathbf{q}}^{(N)}(\mathbf{r}) = e^{i\mathbf{q}\cdot\mathbf{r}/\hbar} \cdot u_{\mathbf{q}}^{(N)}(\mathbf{r}) \tag{2.18}$$

$$u_{\mathbf{q}}^{(N)}(\mathbf{r}) = u_{\mathbf{q}}^{(N)}(\mathbf{r} + \mathbf{a}) \tag{2.19}$$

where $u_{\mathbf{q}}^{(N)}(\mathbf{r})$ are the Bloch wavefunctions.

Inserting these solutions functions into the Schrodinger equation gives an equation for the Bloch functions,

$$\left(\frac{1}{2m}(\mathbf{p}+\mathbf{q})^2 + V(\mathbf{r})\right)u_{\mathbf{q}}^{(N)}(\mathbf{r}) = E_{\mathbf{q}}^{(N)}u_{\mathbf{q}}^{(N)}(\mathbf{r}) \tag{2.20}$$

Both the potential $V(\mathbf{r})$ and the functions $u(\mathbf{r})$ can be written as discrete Fourier sums:

$$V(\mathbf{r}) = \sum_{j,l} V_{j,l}e^{i(j\mathbf{g_1}+l\mathbf{g_2})\cdot\mathbf{r}} \tag{2.21}$$

$$u_{\mathbf{q}}^{(N)}(r) = \sum_{m,n} c_{\mathbf{q},m,n}^{(N)}e^{i(m\mathbf{g_1}+n\mathbf{g_2})\cdot\mathbf{r}} \tag{2.22}$$

Expanding cosine terms of Eq. (2.7) gives

$$V(\mathbf{r}) = V_0\left(\frac{2}{3} + \frac{1}{9}\sum_{(j,l)\in\mathcal{J}} e^{i(j\mathbf{g_1}+l\mathbf{g_2})\cdot\mathbf{r}}\right) \tag{2.23}$$

where V_0 depends on the lattice depth and beam detuning, as in Eq. (2.9), j and l are integers and we define the set $\mathcal{J} = \{(0,1),(0,-1),(1,0),(-1,0),(1,1),(-1,-1)\}$.

Note that another way to understand and derive the potential is to consider the potential that comes from the second order process where an atom absorbs light from one beam and

emits into the other beam. The terms of the expression (2.23) correspond to the absorption and emission involving each possible pair of lattice beams j and l. The first term, 2/3, comes from absorption from and re-emission back into each beam, i.e. where $j = l$, and the sum is over all pairs of beams. For example, absorbing a photon from beam 2 and emitting a photon into beam 1 results in a momentum transfer $\mathbf{g}_1 = \mathbf{k}_2 - \mathbf{k}_1$, this term corresponds to $j = 1, \ l = 0$.

We write the potential term of the Hamiltonian:

$$V(\mathbf{r})u_{\mathbf{q}}^{(N)}(\mathbf{r}) = \frac{2V_0}{3} - \frac{V_0}{9} \sum_{\{j,l\}\epsilon\mathcal{J}} e^{i(j\mathbf{g}_1+l\mathbf{g}_2)\cdot\mathbf{r}} \sum_{m,n} c_{\mathbf{q},m,n}^{(N)} e^{i(m\mathbf{g}_1+n\mathbf{g}_2)\cdot\mathbf{r}} \tag{2.24}$$

$$= \frac{2V_0}{3} - \frac{V_0}{9} \sum_{m,n,\{j,l\}\epsilon\mathcal{J}} c_{\mathbf{q},m,n}^{(N)} e^{i[(m+j)\mathbf{g}_1+(n+l)\mathbf{g}_2]\cdot\mathbf{r}}$$

The kinetic term of the Hamiltonian:

$$\frac{1}{2m}\left(\mathbf{p}+\mathbf{q}\right)\left(\mathbf{p}+\mathbf{q}\right)u_{\mathbf{q}}^{(N)}(r) = \frac{\hbar^2 k^2}{2m}\sum_{m,n}|(m\tilde{\mathbf{g}}_1+n\tilde{\mathbf{g}}_2)+\mathbf{q}|^2 c_{\mathbf{q},m,n}^{(N)} e^{i(m\mathbf{g}_1+n\mathbf{g}_2)\cdot\mathbf{r}} \tag{2.25}$$

where I define $\tilde{\mathbf{g}}_i = \mathbf{g}_i/k$, to pull out the scalar $k = 2\pi/\lambda_{light}$. The kinetic energy prefactor is thus the single-photon recoil energy, $E_{r,\lambda_{light}}$, defined in Eq. (2.10).

Now the Schrödinger equation is

$$\sum_{m'n'} E_{\mathbf{q}}^{(N)} c_{\mathbf{q},m',n'} e^{i(m'\mathbf{g}_1+n'\mathbf{g}_2)} = V_0 \left(\frac{2}{3} - \frac{1}{9}\sum_{m,n,\{j,l\}\in\mathcal{J}} c_{\mathbf{q},m,n}^{(N)} e^{i[(m+j)\mathbf{g}_1+(n+l)\mathbf{g}_2]\cdot\mathbf{r}}\right) \tag{2.26}$$

$$+ \frac{\hbar^2 k^2}{2m}\left(\sum_{m,n}|(m\tilde{\mathbf{g}}_1+n\tilde{\mathbf{g}}_2)+\mathbf{q}|^2 c_{\mathbf{q},m,n}^{(N)} e^{i(m\mathbf{g}_1+n\mathbf{g}_2)\cdot\mathbf{r}}\right) \tag{2.27}$$

$$\tag{2.28}$$

which has solutions

$$E_{\mathbf{q}}^{(N)} c_{\mathbf{q},m',n'}^{(N)} = \sum_{m',n'} \mathcal{H}_{(m,n),(m',n')} \cdot c_{\mathbf{q},m',n'}^{(N)} \tag{2.29}$$

where

$$\mathcal{H}_{(m,n),(m',n')} = \begin{cases} \frac{2V_0}{3} + \frac{\hbar^2 k^2}{2m}|(m\tilde{\mathbf{g}}_1+n\tilde{\mathbf{g}}_2)+\mathbf{q}|^2 & \text{for } m = m', \ n = n' \\ -\frac{V_0}{9} & \text{for } m' = m+j, \ n' = n+l, \text{ and } j,l \in \mathcal{J} \\ 0 & \text{otherwise} \end{cases}$$

For a given V_0, $\mathcal{H}$ is an infinite square matrix, where each entry represents a point on the reciprocal lattice, $\mathbf{k} \in m\mathbf{g}_1 + n\mathbf{g}_2$, and the vector $\mathbf{q}$ spans the first Brillouin zone. To diagonalize the matrix at a given point $\mathbf{q}$ within the Brillouin zone, we truncate the matrix between $(m, n) = (-M, -M)$ and $(m, n) = (M, M)$, and thus consider wavefunctions with momenta within this bound. By choosing sufficiently large (M, M), we find an accurate representation of low-energy states, with eigenenergy $E_\mathbf{q}^{(N)}$ and eigenvector $u_q^{(N)}$.

Consider the case where $M = 5$. Here, the number of points along each axis in discretized reciprocal space is 11, since an atom at $\mathbf{q} = (0, 0)$ may scatter out to $+5\mathbf{g}_1$ and $-5\mathbf{g}_1$). The truncated Hamiltonian is an $11^2 \times 11^2$ square matrix. We diagonalize it at $\mathbf{q} = \Gamma = (0, 0)$ and find 11^2 eigenenergies $E_\Gamma^{(N)}$. The ground state energy $E_\Gamma^{(1)}$ is the lowest of these energies, and the corresponding Bloch function $u_\Gamma^{(1)}$ is a normalized vector in reciprocal states with a complex number, $c_{m,n}$, at each of the 11^2 points $\mathbf{k} \in m\mathbf{g}_1 + n\mathbf{g}_2$. The amplitude of each of these complex numbers indicates the probability that atoms will be detected at that point in momentum space. In the case of low-energy states, the amplitude will be largest at low momenta. Higher energy states have larger amplitudes at larger momenta. Very high energy states show nonzero amplitude at momenta near the cutoff momenta $k = M\mathbf{g}_1 + M\mathbf{g}_2$, and their eigenenergies and Bloch functions will not be accurately calculated with this truncated matrix.

Up until now, our treatment applies to both the triangular lattice, formed by light at $\lambda = 532$ nm and the honeycomb lattice, formed by light at $\lambda = 1064$ nm. The honeycomb lattice has an enlarged unit cell and thus reduced Brillouin zone relative to the 532-nm triangular lattice ($2\mathbf{g}_{i,1064} = \mathbf{g}_{i,532}$).

Figure 2.2 shows the result of a calculation for the 532-nm triangular lattice using this $11^2 \times 11^2$ Hamiltonian. In Fig. 2.2(a) the band structure is calculated for a lattice of depth $V_{532} = h \times 4.5$ kHz $= 1E_{r,532}$. Here, we parameterize the lattice depth by the lattice recoil energy of Eq. (2.13). To plot this band structure, we diagonalize the matrix for each point $\mathbf{q}$ along a slice through points of high symmetry in the Brillouin zone – Γ, M, K, Γ – and plot the four lowest energy solutions, $E_\mathbf{q}^{(1)}$ through $E_\mathbf{q}^{(4)}$. At this shallow lattice depth, the band structure is the free-particle dispersion on the triangular lattice Brillouin zone, $E(\mathbf{q}) = \hbar^2 \mathbf{q}^2 / (2m)$.

The same calculation is repeated for a lattice that is 10 recoil energies deep, with $V_0 = V_{532} = h \times 45$ kHz $= 10E_{r,532}$, and the band structure is plotted in Fig. 2.2(b). In this deeper triangular lattice, the band structure deviates from the free-particle dispersion. The energy gap between the ground and first excited energy bands increases as the lattice depth increases.

Another interesting feature of Fig. 2.2(b) is that the ground band has less curvature compared to the ground band of the shallower lattice. If we relate the band structure in Fig. 2.2(b) to a free-particle dispersion, this reduction in curvature can be accounted for with an effective mass that is larger than the true particle mass, $m^* > m$.

(a) $V_{532}/h = 4.5$ kHz $= 1$ $E_{r,532}$ (b) $V_{532}/h = 45$ kHz $= 10$ $E_{r,532}$
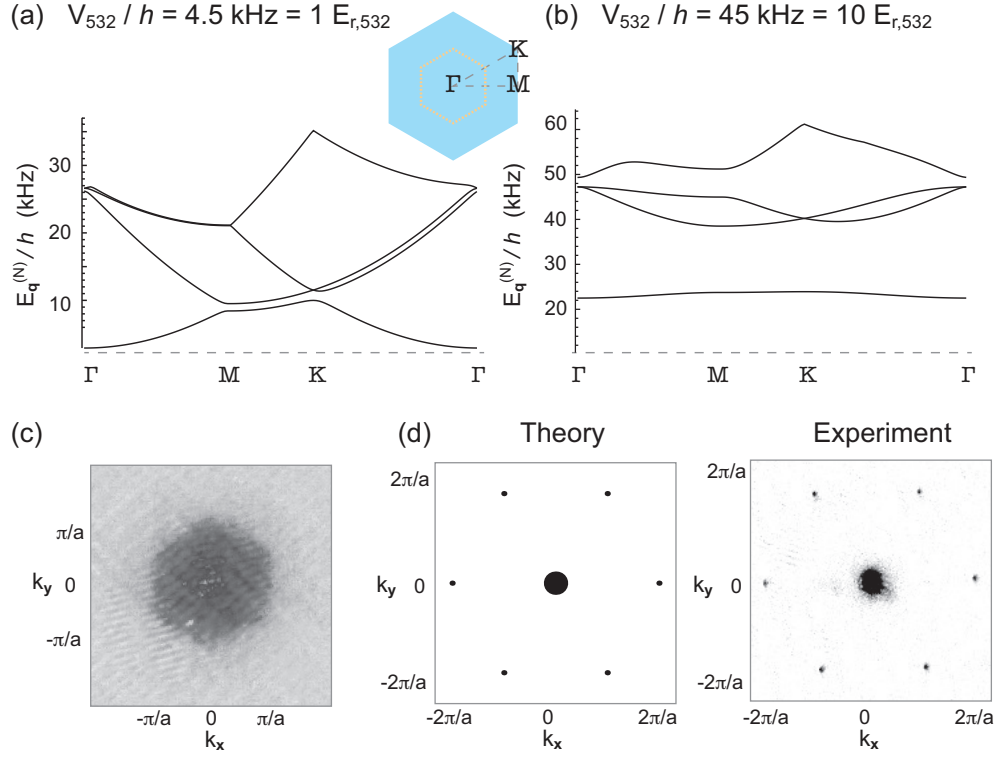
Figure 2.2: The band structure of the triangular lattice for lattice depths of 1 $E_{r,532}$ (a) and 10 $E_{r,532}$ (b). The inset shows the Brillouin zone as a blue solid hexagon, with a dashed line through the points of high symmetry. For reference, a yellow dashed line indicates the reduced Brillouin zone of the 1064-nm lattice. (c) A normal gas of atoms at $T \sim 1.4$ μK fill the lowest Brillouin zone of the triangular lattice shown in (b). A band-mapping procedure maps quasimomentum $\mathbf{q}$ to momentum $\mathbf{k}$, and an absorption image after time of flight shows a momentum-space representation of the gas filling the lowest band. (d) A stationary, lattice-trapped Bose-Einstein condensate at $T \sim 0.1$ μK occupies only the $\mathbf{q} = \Gamma$ point of the lowest energy band of the lattice. An absorption image after time of flight shows a momentum-space representation of the gas. The density distribution has peaks at points m, n with population determined by the total atom number and the probability $|c_{\Gamma,m,n}|^2$. The calculated Bloch function of a single atom is shown next to the image of the condensate loaded into the optical lattice, where spot size indicates the amplitude of the Bloch function $|c_{\Gamma,m,n}|$.

$$E(\mathbf{q}) = \hbar^2 \mathbf{q}^2 / (2m^*) \tag{2.30}$$

Because there is a large band gap in the deeper lattice, we can load a "hot" cloud of atoms, with thermal energy $k_B T / h \sim 30$ kHz, which corresponds to a temperature $T = 1.4 \mu$K. This

normal gas fills the first energy band. We then perform a band mapping measurement in which quasimomentum $\mathbf{q}$ is converted to real momentum $\mathbf{k}$ and use momentum-space imaging [14] to get a direct image of the first Brillouin zone of the triangular lattice, shown in Fig. 2.2(c).

Alternatively, we load the lattice with a stationary Bose-Einstein condensate, which occupies only the $\mathbf{q} = \Gamma$ point of the first band. Figure 2.2(d) shows the calculated Bloch wavefunction $u_\Gamma^{(1)}$, where the size of each point on the k-space grid $k \in m\mathbf{g}_1 + n\mathbf{g}_2$ represents the amplitude $|c_{\mathbf{q},m,n}|$. Also shown is the image in momentum-space of the condensate wavefunction after it is loaded into the optical lattice. The likeness of these two images confirms that loading atoms into the lattice primarily puts atoms in the state $u_\Gamma^{(1)}$.

Following the same procedure for the 1064-nm honeycomb lattice, with $-V_0 = V_{1064} = h \times 25$ kHz $\sim 23\, E_{r,1064}$, where we parameterize the lattice depth by the lattice recoil energy of Eq. (2.15). The band structure calculation results in the well-known band structure of the graphene lattice shown in Fig. 2.3(a), where again we slice through each of the symmetry points of the Brillouin zone. The first and second energy bands have a cusp at the K-point, which gives rise to the novel electronic properties of graphene, in which the charge carriers have zero effective mass.

To understand this effective mass, we generalize the concept presented by Eq. (2.30) and define the inertial effective mass tensor in in the two-dimensional Brillouin zone as

$$[M_{eff}^{-1}]_{i,j} = \frac{1}{\hbar^2} \frac{\partial^2 E}{\partial q_i \partial q_j}, \tag{2.31}$$

so that the effective mass of a particle at a point $\mathbf{q}$ within a band is related to the inverse of the curvature of the band at that point. At the $K-$point of the honeycomb lattice, the curvature of the lower band is infinite, so the effective mass of particles at the K-point is zero.

2.3 Bichromatic optical superlattice

This dissertation focuses on the more complex superlattices that result from combining the 532-nm and 1064-nm lattices, shown in Fig. 2.4. Because the triangular lattices of intensity minima are formed with commensurate wavelengths, their overlap results in a periodic superlattice of intensity with the same unit cell as that of the lattice formed by light with $\lambda = 1064$ nm. The geometry of the superlattice depends on the relative phase of the two patterns, which is controlled by introducing a phase shift along the reciprocal lattice basis vectors, $\mathbf{g}_1$ and $\mathbf{g}_2$.

The upper row of Fig. 2.4 shows the overlap of the two optical lattices in three configurations of the bichromatic lattice.

Recall that in either lattice of intensity, the peaks of the honeycomb geometry account for just 1/9 of the total lattice depth, and the remaining 8/9 of of the potential is accounted for
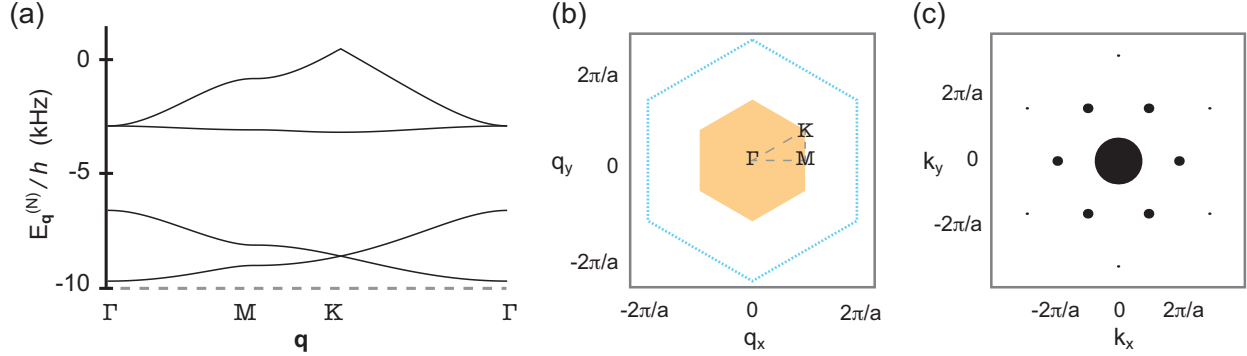
Figure 2.3: (a)The band structure of the honeycomb lattice with a lattice depth $V_{1064} = h \times 25$ kHz $= 23\ E_{r,1064}$, where the last term is parameterized in units of lattice recoil energy. (b) The Brillouin zone of the 1064-nm lattice is shown as a solid yellow hexagon, with symmetry points indicated. For reference, a blue dashed line indicates the larger Brillouin zone of the 532-nm lattice. (b) The calculated ground state of a condensate in this lattice at $\mathbf{q} = \Gamma$.

by the triangular-lattice wells. For this reason, it is possible to overlap the potential lattices using optical powers for which the prominent effect of each lattice is from its triangular lattice of intensity minima. The 532-nm lattice sites form a lattice of potential energy wells in the triangular pattern of Fig. 2.1(d), and the primary effect of the 1064-nm lattice is to lift the degeneracy of the four site unit cell, thereby introducing an energy offset $V_{A,B,C,D}$ at the points of intensity minima. The result is the exclusion of one or more of the sites within a unit cell, so that particles may tunnel to the low-lying sites but the high-energy sites are forbidden or disfavored. In the kagome configuration, the D-site is raised by energy $\Delta V = 8/9 V_{1064}$.

The superlattice potential is the sum of the potentials from each triangular lattice of intensity minima. The natural choice of basis vector for the superlattice is that of the enlarged unit cell of the 1064-nm lattice, since $k_{532} = 2k_{1064}$. (The requirement on the precision of this ratio is discussed in chapter 3). We define the vectors $\mathbf{G}_i := \mathbf{g}_i|_{\lambda=1064}$, where the capital indicates we have evaluated $\mathbf{g}_i$ for the 1064-nm light, and note that absorption and emission of a photon from the 1064-nm lattice beams will lead to momentum transfer $\mathbf{G}_i$, while absorption and emission from the 532-nm beams will lead to momentum transfer $2\mathbf{G}_i$.

We include a phase by which one of the lattices may be shifted relative to the other. In the lab, we shift the lattices along the reciprocal lattice $\mathbf{G}_1$ and $\mathbf{G}_2$. Although a phase could be included on either or both lattices, the relevant quantity is a relative phase shift between the two lattices, so we include phase shifts only on the 1064-nm lattice, with phase ϕ_{12} along $\mathbf{G}_1$ and ϕ_{23} along $\mathbf{G}_2$. The expression for the potential landscape of the bichromatic lattice is written in Eq. (2.32).
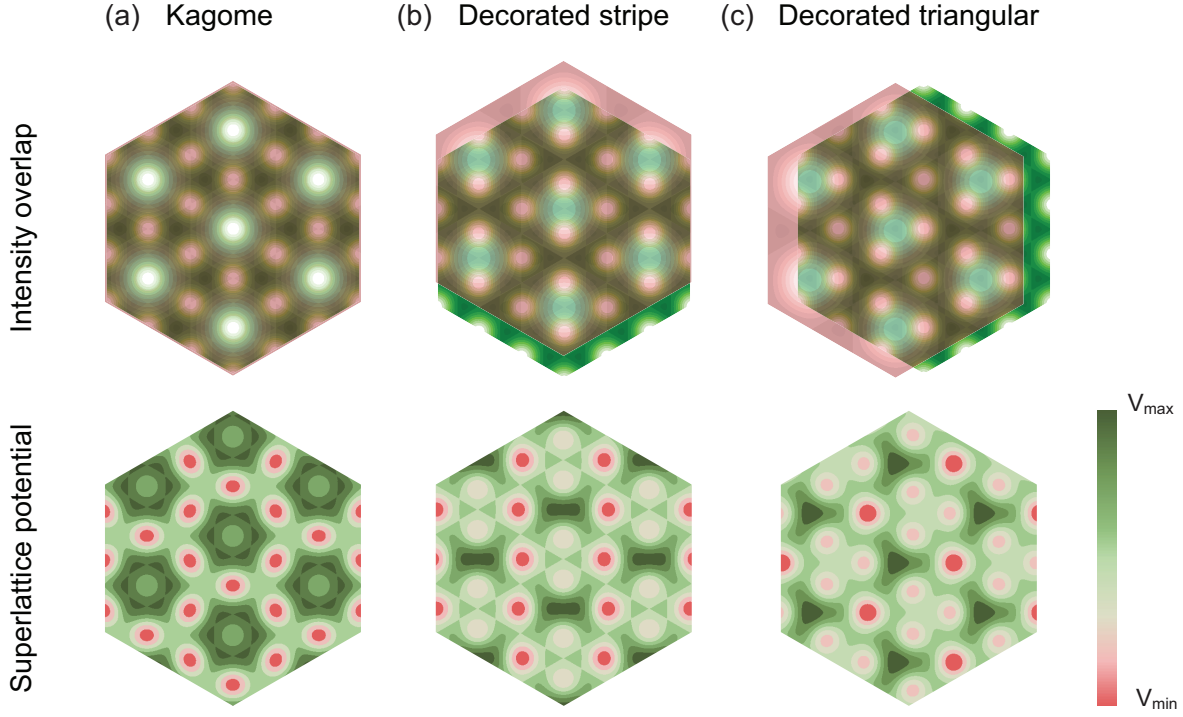
Figure 2.4: The optical superlattices are created by overlapping the lattices formed by light at wavelengths 532 nm and 1064 nm. Shifts of the relative phase between the two lattices produce different superlattice geometries: (a) Kagome lattice, (b) the decorated one-dimensional stripe lattice and (c) the decorated triangular lattice. The potential wells are at the sites of the 532-nm triangular lattice, and the 1064-nm lattice raises the energy somewhere in the unit cell by energy $\Delta V = 8/9 \times V_{1064}$. Lattices in (b) and (c) are called 'decorated' lattices because tunneling is mediated by sites that are raised in energy.

$$V(\mathbf{r}) = V_{532}\left(\frac{2}{3} - \frac{2}{9}\left(\cos\left[2\mathbf{G}_1 \cdot \mathbf{r}+\right] + \cos\left[2\mathbf{G}_2 \cdot \mathbf{r}\right] + \cos\left[(2\mathbf{G}_1 - 2\mathbf{G}_2) \cdot \mathbf{r}\right]\right)\right)$$
$$- V_{1064}\left(\frac{2}{3} - \frac{2}{9}\left(\cos\left[\mathbf{G}_1 \cdot \mathbf{r} + \phi_{12}\right] + \cos\left[\mathbf{G}_2 \cdot \mathbf{r} + \phi_{23}\right] + \cos\left[(\mathbf{G}_1 - \mathbf{G}_2) \cdot \mathbf{r} + \phi_{12} - \phi_{23}\right]\right)\right)$$

$$(2.32)$$

where the capitalized $\mathbf{G}_i$ represents the reciprocal lattice vector, $\mathbf{g}_i$, for the 1064-nm lattice, with $k_{1064} = 2\pi/\lambda_{1064}$, and V_{532} and V_{1064} are the depths of the potentials and we have used the relation $V_\lambda = |V_0, \lambda|$.

Note again that this potential could alternatively be derived by considering diffraction into various orders, with atoms picking up appropriate phases from beams 1 and 3 as they scatter with 1064-nm lattice beam photons (beam 2 acts as a reference, with no additional

phase). Here we have defined the phase of beam 1 relative to beam 2 as ϕ_{12} and the phase of beam 3 relative to beam 2 as ϕ_{23}.

2.3.1 Band structure of the kagome lattice

The numerical solution for band structure and eigenstates of the superlattice follows the same basic prescription as in section 2.2. Just as before, the potential of Eq. (2.32) is written in exponential form to solve for the band structure by expanding the cosine terms. The kinetic term of the kagome lattice Hamiltonian is unchanged from the honeycomb lattice case; it is parameterized by the 1064-nm photon recoil energy, $E_{r,\lambda_{1064}}/h = 2$ kHz (2.16).

Figure 2.5 shows the band structures for the bichromatic lattice in the kagome configuration, where $\phi_{12} = \phi_{23} = 0$ and the high-energy site of the 1064-nm lattice overlaps precisely with site D of the 532-nm lattice, so that the potential energy at site D is raised by $\Delta V = 8/9 \times V_{1064}$. The band structures are shown for $V_{532}/h = 45$ kHz and a range of increasing V_{1064}. When $V_{1064} = 0$, the lattice is the 532-nm triangular lattice, where the four bands shown represent the first band of the 532-nm triangular lattice (blue hexagon in the figure), folded into the reduced Brillouin zone of the 1064-nm lattice.

With increasing V_{1064}, the lattice changes from the 532-nm triangular lattice into the kagome lattice, with the fourth band lifted in energy as the unit cell becomes the three-site unit cell of the kagome lattice. The two lowest energy levels of the kagome lattice are similar to those of the honeycomb lattice. The curvature of these bands at the K-point is again very high (though it may not be infinite), so particles there will have a (nearly) zero effective mass (2.31) at the K point within the Brillouin zone.

The third energy level is flat across all momenta. Particles in this dispersionless band will have an infinite effective mass. This can be understood in the simple picture of effective mass of Eq. (2.30), where the curvature of the free-particle dispersion at $\mathbf{q} = \Gamma$ is reduced by introducing an increased effective mass. A more complete picture is evident in the effective mass tensor Eq. (2.31), which is zero for *all* points in the Brillouin zone.

2.3.2 Ground states of the bichromatic lattices

The superlattice geometries of high symmetry are illustrated in Fig. 2.4. The Hamiltonian is diagonalized for each of these geometries and the ground state Bloch functions at $\mathbf{q} = \Gamma$ are shown in Fig. 2.6.

When atoms are loaded into a bichromatic optical lattice, the relative phases of the two constituent lattices is random, and we analyze the time-of-flight patterns of a condensate loaded into the lattice to determine their relative phase. chapter 3 describes the process by which we tune and stabilize the relative phase of the lattices. We find that, once we create a bichromatic lattice with the desired phase, we are able to stabilize the phase actively and drift over a few hours is negligible.
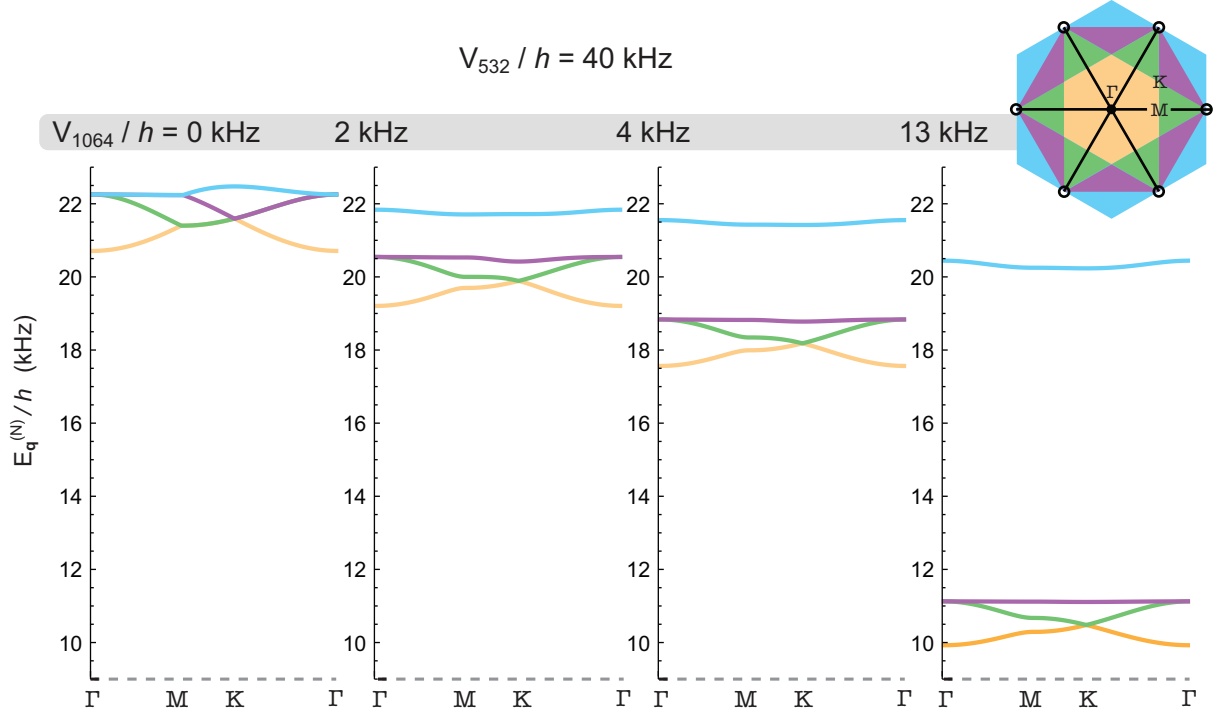
Figure 2.5: Band structure as the superlattice geometry is tuned from 532-nm triangular lattice to the kagome lattice. The lattice depth of the 532-nm light is held constant at $V_{532}/h = 40$ kHz as the depth of the 1064-nm lattice is increased. The first four bands of the kagome lattice are indicated in the Brillouin zone schematic. The largest Brillouin zone, indicated in blue, is that of the 532-nm triangular lattice. It is split into four subbands in the basis of the 1064-nm lattice, $\mathbf{G}_i$. The subbands are distinguished by color. When $V_{1064}/h = 0$ kHz, the lowest band of the 532-nm triangular lattice is folded into the reduced Brillouin zone of the four-site basis. As V_{1064} increases and the D-site of the kagome lattice is removed, the fourth energy band is separated from the lower three bands, which tend towards the tight-binding band structure of the kagome lattice, with a dispersionless third band.

2.4 Signatures of lattice geometry in k-space data

2.4.1 Signature of kagome lattice geometry

When we create the bichromatic lattice, we determine its geometry by examining the diffraction data of Fig. 2.6. The similarity between the kagome and decorated triangular lattices makes this challenging, but careful analysis of the relative weight of the zero- first- and second-order peaks shows a clear signature of the kagome lattice.

To understand the signature, consider a delocalized, coherent superfluid diffracting from a real-space lattice. Each lattice site can be treated as a point-source for an expanding

$V_{532}/h = 40$ kHz $V_{1064}/h = 13$ kHz

(a) Kagome lattice   (b) Decorated stripe lattice   (c) Decorated triangular lattice
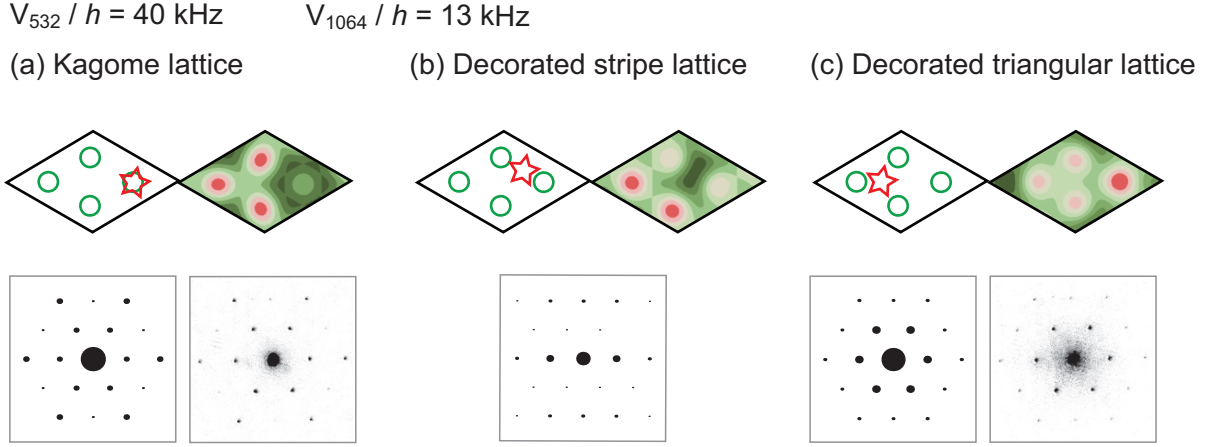
Figure 2.6: The bichromatic lattice geometries. For each, a unit cell of lattices of intensity (upper left) and potential (upper right) are shown, as are the calculated (lower left) and experimentally detected (lower right) ground-state wavefunctions at $\mathbf{q} = \Gamma$. The intensity lattice unit cell has open circles indicating the intensity minima of the 532-nm lattice and open stars indicating the intensity minima of the 1064-nm lattice. In the potential lattice unit cells, red represents potential minima and green represents potential maxima. The Bloch functions are plotted against against momentum k_x, and k_y. (a) The kagome lattice geometry is formed when the intensity minimum of the 1064-nm lattice coincides with one of the intensity minima of the 532-nm lattice. The resulting potential has three degenerate sites in the unit cell, and one lifted by an energy ΔV. (b) The decorated stripe lattice geometry is formed when the 1064-nm lattice intensity minimum is equidistant from just two of the sites in the unit cell. (c). The decorated triangular lattice is formed when the 1064-nm lattice intensity minimum is equidistant from three of the sites in the 532-nm unit cell. All three are lifted in energy, and tunneling between low energy sites is mediated by these high-energy sites.

matter-wave, and we will analyze the population of atoms that is diffracted to the zero- first- and second-order diffraction peaks. The concept is illustrated in Fig. 2.7.

Consider the diffraction of atoms from the kagome lattice to the first-order peak along the basis vector, $\mathbf{G}_2$, shown in Fig. 2.7(a). The vector $\mathbf{G}_2$ is orthogonal to the real-space vector connecting sites A and D. Sites A and D are equidistant from the point of first-order diffraction, so that matter-waves expanding from these real-space lattice sites to $\mathbf{G}_2$ will have the same phase at the location of first-order diffraction. The same is true for sites B and C. The only relative phase, then, for interference at $\mathbf{G}_2$ is given by $\mathbf{k} \cdot (\mathbf{r}_B - \mathbf{r}_A) = \mathbf{G}_2 \cdot \mathbf{a}_2/2 = \pi$. Similarly, the second order diffraction peak, at $2\mathbf{G}_2$ will have phase $2\mathbf{G}_2 \cdot \mathbf{a}_2 = 2\pi$. This argument holds for scattering along all six directions: $\pm\mathbf{G}_1, \pm\mathbf{G}_2$, and $\pm G_3$, where we have defined the vector $G_3 = \mathbf{G}_2 - \mathbf{G}_1$ for convenience.

Consider the real-space unit cell wavefunction, ψ. It is a sum of the Wannier functions
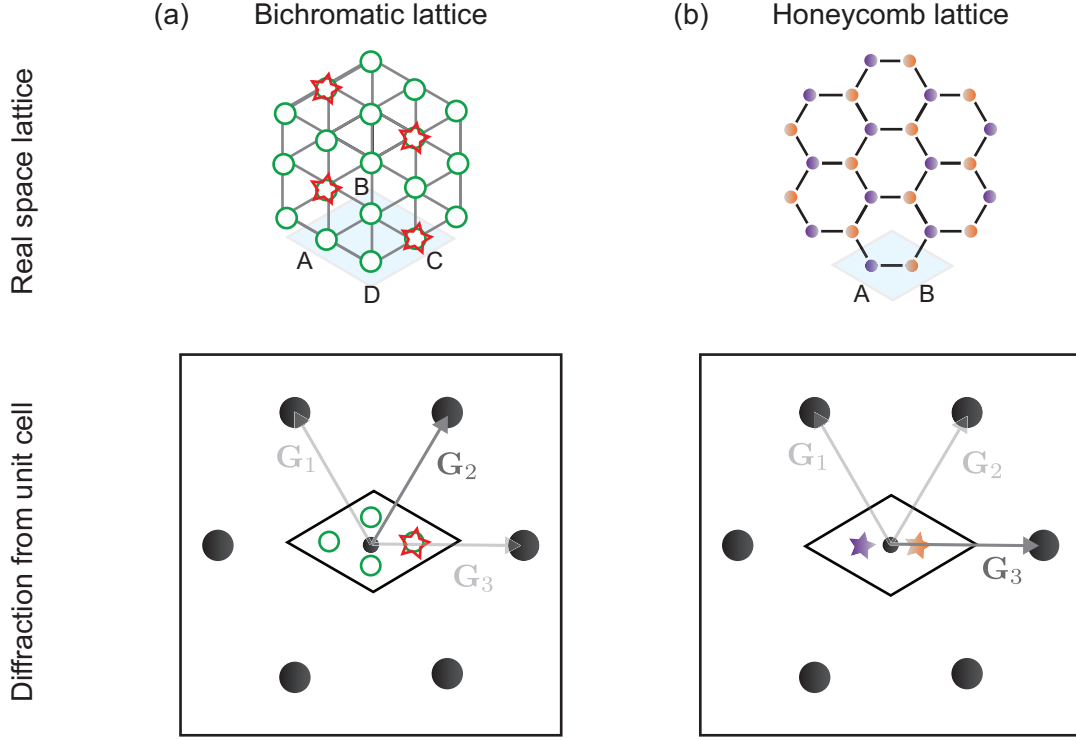
Figure 2.7: Determining unit cell population by superfluid diffraction images.

$w(\mathbf{r} - \mathbf{s}_\alpha)$ at each site within the unit cell $\alpha \in \{A, B, C, D\}$.

$$\psi = \sum_\alpha \psi_\alpha w_\alpha(\mathbf{r} - \mathbf{s}_\alpha) \tag{2.33}$$

where $|w_\alpha(\mathbf{r})|^2 = 1$ and $|\psi|^2 = 1$. If we assume a Gaussian Wannier state that is cylindrically symmetric, then $w_\alpha(\mathbf{r}) = w$, with Fourier components at momentum $\mathbf{k}$ of $\tilde{w}_\mathbf{k}$ and the population of atoms diffracted to momentum $\mathbf{k}$ is given by Eq. (2.35).

$$P_\mathbf{k} = |\tilde{w}_\mathbf{k}|^2 |\psi_A e^{i\mathbf{k}\cdot\mathbf{r}_A} + \psi_B e^{i\mathbf{k}\cdot\mathbf{r}_B} + \psi_C e^{i\mathbf{k}\cdot\mathbf{r}_C} + \psi_D e^{i\mathbf{k}\cdot\mathbf{r}_D}|^2 \tag{2.34}$$

$$\tag{2.35}$$

where $\tilde{w}_\mathbf{k}$ have the relation $\tilde{w}_\mathbf{k} = \tilde{w}_0 e^{-\mathbf{k}^2/\mathbf{k}_0^2}$, so that the first three peaks are

$$P_0 = |\tilde{w}_0|^2 |\psi_A + \psi_B + \psi_C + \psi_D|^2 \tag{2.36}$$
$$P_{\mathbf{G}_i} = |\tilde{w}_{\mathbf{G}_i}|^2 |\psi_A - \psi_B - \psi_C + \psi_D|^2 \tag{2.37}$$
$$P_{2\mathbf{G}_i} = |\tilde{w}_{2\mathbf{G}_i}|^2 |\psi_A + \psi_B + \psi_C + \psi_D|^2 \tag{2.38}$$

To identify the kagome lattice by its momentum-space signature, consider normalizing the ratio of populations in the first- and second- order peaks by their Wannier weights $\tilde{w}$.

$$
\begin{aligned}
\tilde{P}_i &= \frac{P_{\mathbf{G}_i} + P_{-\mathbf{G}_i}}{2P_0} \frac{|\tilde{w}_0|^2}{|\tilde{w}_{\mathbf{G}_i}|^2} \qquad\qquad = \frac{|\psi_A - \psi_B - \psi_C + \psi_D|^2}{\sum_\alpha |\psi_\alpha|^2} && (2.39)\\
&= \frac{P_{\mathbf{G}_i} + P_{-\mathbf{G}_i}}{2P_0} \left(\frac{|\tilde{w}_0|^2}{|\tilde{w}_{2\mathbf{G}_i}|^2} \right)^{1/4} && (2.40)\\
&= \frac{P_{\mathbf{G}_i} + P_{-\mathbf{G}_i}}{2P_0} \left(\frac{2P_0}{P_{2\mathbf{G}_i} + P_{-2\mathbf{G}_i}} \right)^{1/4} && (2.41)
\end{aligned}
$$

Equation (2.41) allows for identification of the real-space wavefunction by measurements of the momentum-space wavefunction. In it, we have removed the dependence on the Wannier weights $\tilde{w}$ by recognizing the relation between ratios of first- and second- order Wannier weights, $|\tilde{w}_0/\tilde{w}_{\mathbf{G}_1}|^2 = |\tilde{w}_0/\tilde{w}_{\mathbf{G}_2}|^{2 \times 1/4}$. The second-order Wannier weight ratio is equivalent to the ratio of populations in those peaks, which is a measurable quantity.

Consider the value of $\tilde{P}_i$ in the 532-nm triangular lattice, where we continue to use the four-site unit cell. Here, all ψ_α are equal and $\tilde{P} = 0$. This is what we expect, since $\mathbf{G}_i$ are the basis vectors of the reduced Brillouin zone, and the 532-nm triangular lattice will only have diffraction at even multiples of $\mathbf{G}_i$, with destructive interference at these intermediate peaks.

In the decorated 1D stripe lattice, a symmetry is broken and $\tilde{P}_i$ is either 0 or 1, depending on i. In the decorated triangular lattice, just one site is occupied and the second-order diffraction is suppressed by e^{-4k^2/k_0^2}, so that $\tilde{P}_i \sim 1$. In the kagome lattice,

$$
\begin{aligned}
\tilde{P}_i &= \frac{|\psi_A - \psi_B - \psi_C|^2}{|\psi_A + \psi_B + \psi_C|^2} = \frac{|1/3|^2}{|1|^2}\\
&= 1/9 && (2.42)
\end{aligned}
$$

Experimentally, it is straightforward to measure the populations in the zero- first- and second-order peaks and find $\tilde{P}_i$ as in Eq. (2.41). It increases to 1/9 and saturates when V_{1064} increases, assuming that V_{1064} is sufficiently small to consider cylindrically symmetric functions w. When V_{1064} becomes comparable to V_{532}, the assumption of a cylindrically-symmetric Wannier function breaks down. We can introduce the asymmetry parameter ϵ, where $\epsilon = 1$ for a symmetric wavefunction and $\epsilon < 1$ when it becomes asymmetric. Then $\tilde{P}_i$ is

$$
\tilde{P}_i = \frac{(2 - \epsilon)^2}{9} \left(\frac{9}{(2 + \epsilon^4)^2} \right)^{1/4} \tag{2.43}
$$

2.4.2 Signature of honeycomb lattice symmetry

We can define a similar term in the honeycomb lattice, which has two sites in a unit cell as shown in Fig. 2.7(b). Consider the diffraction in the direction along $\mathbf{G}_3$, the vector that connects the two sites A and B. In this case, $\mathbf{G}_i \cdot (\mathbf{r}_A - \mathbf{r}_B) = 2\pi/3$ and we have

$$P_0 = |w_0|^2 |\psi_A + \psi_B|^2 \tag{2.44}$$

$$P_{\mathbf{G}_i} = |w_{\mathbf{G}_i}|^2 |\psi_A + \psi_B e^{i2\pi/3}|^2 \tag{2.45}$$

$$P_{2\mathbf{G}_i} = |w_{2\mathbf{G}_i}|^2 |\psi_A + \psi_B e^{-i2\pi/3}|^2 \tag{2.46}$$

Here we will exploit the similarity between the diffraction at $\mathbf{G}_i$ and $2\mathbf{G}_i$ to define a term

$$\tilde{Q}_i = \frac{P_{\mathbf{G}_i} + P_{-\mathbf{G}_i}}{2P_0} \frac{|\tilde{w}_0|^2}{|\tilde{w}_{\mathbf{G}_i}|^2} = \frac{|\psi_A + \psi_B e^{2\pi i/3}|^2}{|\psi_A + \psi_B|^2} \tag{2.47}$$

$$= \frac{P_{\mathbf{G}_i} + P_{-\mathbf{G}_i}}{2P_0} \left(\frac{|\tilde{w}_{\mathbf{G}_i}|^2}{|\tilde{w}_{2\mathbf{G}_i}|^2} \right)^{1/3} \tag{2.48}$$

$$= \frac{P_{\mathbf{G}_i} + P_{-\mathbf{G}_i}}{2P_0} \left(\frac{P_{\mathbf{G}_i} + P_{-\mathbf{G}_i}}{P_{2\mathbf{G}_i} + P_{-2\mathbf{G}_i}} \right)^{1/3} \tag{2.49}$$

For a honeycomb lattice with equal population in sites A and B, $\tilde{Q}_i = 1/4$, and population imbalances will result in $\tilde{Q}_i$ that range between $1/4$ and 1.

Characterizing the symmetry of the sites A and B of the honeycomb lattice is important because the band structure has a cusp at the K-points only when the sites are identical. chapter 4 describes experiments performed out-of-equilibrium to characterize the symmetry of a honeycomb optical lattice. The result in Eq. (2.49) provides another signature, which may be useful when analyzing ground-state wavefunction data.

2.5 Calibration of lattice depths

The depth $|V_0|$ of an optical lattice depends on the power, waist and overlap of the lattice beams. The power of each beam is stabilized actively, and their waists are the same day-to-day, but the beam positions can drift throughout the day and certainly differ from one day to the next. To create the same optical lattice for every iteration of the experiment, we calibrate the ratio of beam power to lattice depth using lattice modulation spectroscopy [10]. We repeat this calibration regularly throughout the day.

The alignment and stability are discussed further in chapter 3. Our construction of the optical lattices is robust, and the lattice depths do not change substantially over the course of a single day. Here I will present the calculations for the calibrations, which depend on the numerics we have discussed in this chapter.

2.5.1 Lattice modulation spectroscopy

In lattice modulation spectroscopy, we load a stationary condensate into the ground state of an optical lattice, so that it occupies $\mathbf{q} = \Gamma$ point of the ground band. Sinusoidal modulation of the lattice beam power by a few percent with frequency ω promotes atoms to the $\mathbf{q} = \Gamma$ points of upper bands of the lattice. A band mapping procedure maps lattice quasimomentum $\mathbf{q}$ into real momentum $\mathbf{k}$. This is followed by a time-of-flight image. The atoms occupying upper bands are detected at the appropriate high-order momenta.

We use the lowest energy excitation, which maps to the first order peaks at $\pm\mathbf{g}_1, \pm\mathbf{g}_2$, and $\pm \mathbf{g}_3$, where $\mathbf{g}_3 = \mathbf{g}_2 - \mathbf{g}_1$. We measure the population of atoms $\sum_i P_{\mathbf{g}i}$ to measure the resonance frequency of the excitation. Assuming that the lattice is uniform and that the excited states are stable to decay, we consider the transition probability due to the perturbation from a low-amplitude modulation of lattice potential $V(\mathbf{r})$

$$P_{1\to n} = \frac{V_{1n}^2}{\hbar} \frac{\sin^2\left[(\omega_0 - \omega)t/2\right]}{(\omega_0 - \omega)^2} \tag{2.50}$$

where the resonant frequency ω_0 is given by the energy gap $E_{1n} = E_1 - E_n = h \times \omega_0$ and the matrix element $V_{1n} = \langle \psi_1 | V(\mathbf{r}) | \psi_n \rangle$ is nonzero only for states with the six-fold rotational symmetry of the optical lattice.

Figure 2.8 shows the wavefunctions of the 532-nm triangular lattice that correspond to the $\mathbf{q} = \Gamma$ states of the first 10 energy bands, where the area of a point on the momentum-space grid, $k \in m\mathbf{g}_1 + n\mathbf{g}_2$, represents the population of atoms at that momentum, i.e. $|c_{m,n}|^2$. The color of the points represents the complex phase of the coefficient $c_{m,n}$. The phases indicate the expected symmetries of the $\mathbf{q} = \Gamma$ wavefunctions of a two-dimensional C_6 symmetric lattice: the s-band ($|\psi_1\rangle$), two p-bands ($|\psi_2\rangle$ and $|\psi_3\rangle$), and the first d-band ($|\psi_4\rangle$).

The states with nonzero matrix element V_{1n} are states $|\psi_4\rangle$ and $|\psi_8\rangle$, which have the six-fold rotational symmetry of the ground-state and symmetry-preserving optical lattice potential perturbation.

After modulation, atoms are at the $\mathbf{q} = \Gamma$ point of the upper bands, and we perform a band mapping measurement to determine which band has been populated. The $\mathbf{q} = \Gamma$ point in any band maps to a point on the reciprocal lattice ($\mathbf{k} \in m\mathbf{g}_1 + n\mathbf{g}_2$). Each point on the grid represents the $\mathbf{q} = \Gamma$ point of six different bands. This technique does not distinguish, then, among the six bands that touch at each reciprocal lattice vector. However, in a sufficiently deep lattice, there is only one symmetry-allowed transition to each point. To experimentally distinguish the bands that touch at the $\mathbf{q} = \Gamma$ points, one could perform this experiment with a normal gas or a non-stationary condensate, as the bands touch only at the Γ point, and sampling any nonzero quasimomentum will distinguish among these bands.
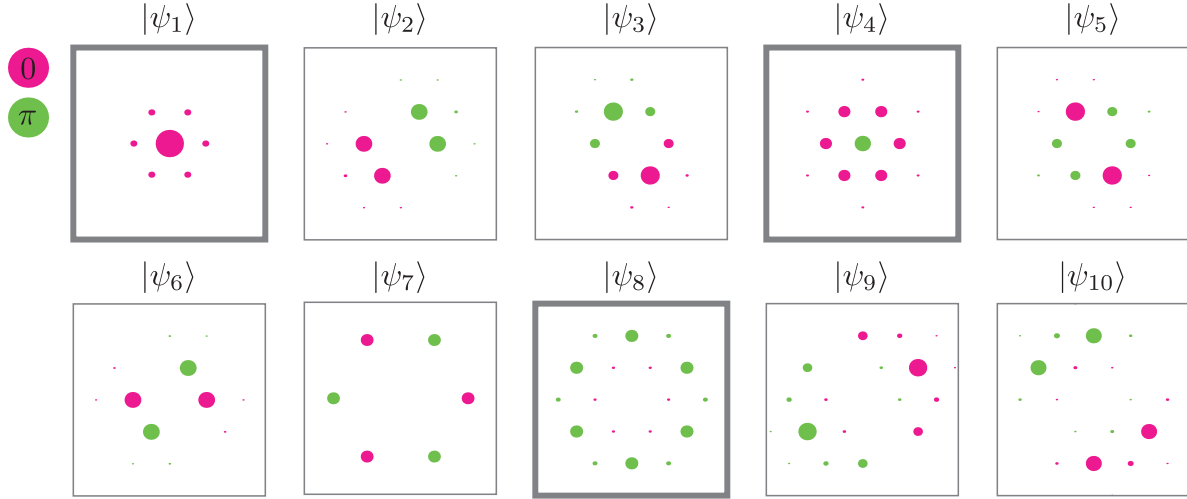
Figure 2.8: The $\mathbf{q} = \Gamma$ wavefunctions of the low-energy bands of the triangular lattice of 532-nm light. The center of each figure represents $\mathbf{k} = 0$, and every point in the figure is on the grid $\mathbf{k} \in m\mathbf{g}_1 + n\mathbf{g}_2$, where m and n are integers. The point size represents amplitude of the wavefunction at that momentum, and the color represents phase. The wavefunctions $|\psi_1\rangle$, $|\psi_4\rangle$ and $|\psi_8\rangle$ have the same symmetry as the lattice, and transitions among these states are allowed by the parity-symmetric perturbation of intensity modulation of the optical lattice.

Energy gaps and lattice depth

Consider a shallow lattice, with depth comparable to the lattice recoil energy (2.13), the free-particle dispersion on its Brillouin zone will have an energy gap between states $|\psi_1\rangle$ and $|\psi_4\rangle$ of $E_{14}/h = 24$ kHz. Here, $|\mathbf{g}_i| = \sqrt{3}|\mathbf{k}_i|$, and $\mathbf{k}_i$ is the photon-momentum of beam i. The smallest possible energy gap between the first state and the next manifold is $3\hbar^2 k^2/(2m) = 3E_{r,\lambda_{532}}/h = 24$ kHz (2.14). The excitation to $|\psi_8\rangle$ is at the energy $E_{18}/h = 72$ kHz. The gaps E_{14} and E_{18} increase with increasing lattice depth as shown in Fig. 2.9(a).

2.5.2   Experimental calibrations

Experimentally, we first align the lattice beams following a procedure detailed in chapter 3. After the beam pointing is aligned as well as possible for each beam, the relative beam powers are modified to ensure that the diffraction of a BEC from the ground state of the lattice is 6-fold symmetric. Beam 2, is used as a reference, and the other beam powers are derived from that power to result in a symmetric lattice.

Method: 3-beam triangular lattice modulation without vertical lattice

Figure 2.9(b) shows preliminary lattice modulation taken on 23 March, 2016, from lattice modulation spectroscopy. The absorption images after lattice modulation and band mapping
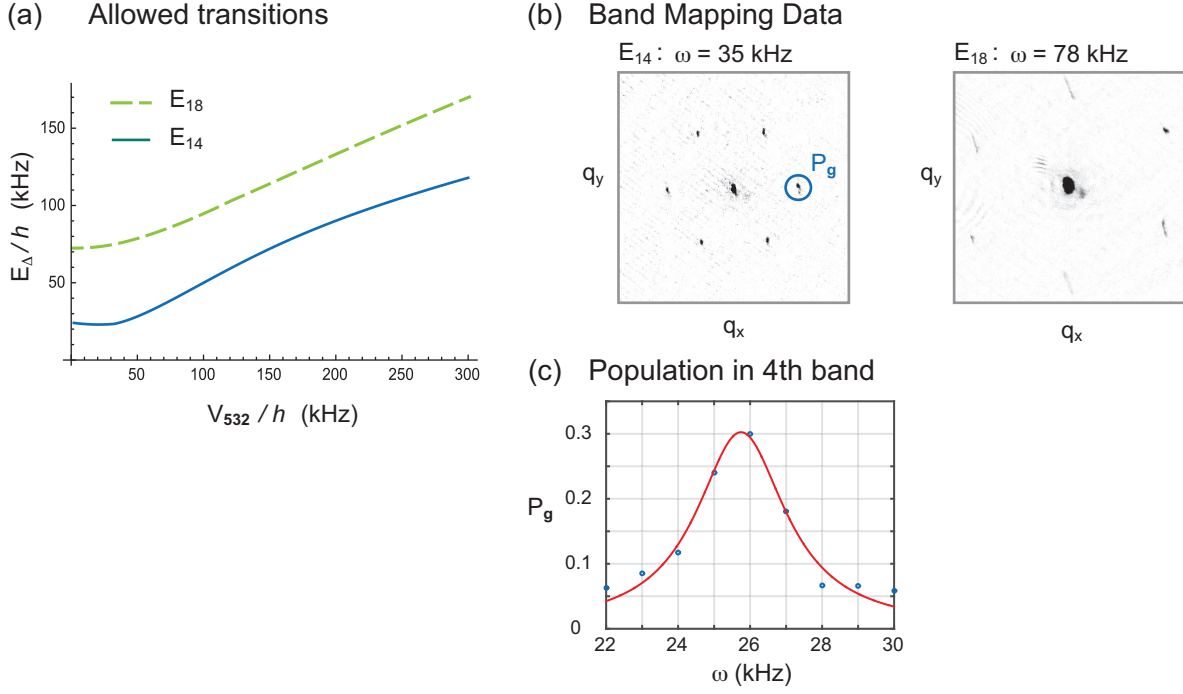
Figure 2.9: Lattice calibration by modulation spectroscopy. (a) The energy gap between ground and excited bands at $\mathbf{q} = \Gamma$ for allowed transitions by the lattice modulation perturbation. (b) Lattice modulation excites atoms to the Γ points of upper bands, which band map to distinct momenta. Atoms promoted to the fourth band are mapped to the vectors $\mathbf{g}_i$. Preliminary images taken without a vertical lattice in a triangular lattice of depth near $V_{532}/h = 60$ kHz show resonances at their modulation frequency to the fourth band near $\omega \sim 35$ kHz and to the eighth band near $\omega \sim 78$ kHz. (c) The final calibration data represent the sum of population of atoms that map to the first order peaks, $\sum_i P_{\mathbf{g}}$. These atoms occupy the fourth band before the band mapping procedure. In this data there is an additional deep vertical lattice has been included, so the lattice calibration is performed at lower lattice depths than are shown in (b).

show that atoms have been promoted from the $\mathbf{q} = \Gamma$ point of the first band, to the $\mathbf{q} = \Gamma$ point of the fourth and eighth energy bands, with energies $E_\Gamma^{(4)}$ and $E_\Gamma^{(8)}$, respectively. The images shown are for a modulation frequency of $\omega = 35$ and $\omega = 78$ kHz , respectively. These resonances both indicate a that the lattice depth is $V_{532}/h \sim 60$ kHz deep.

To check whether this is roughly what we expect, we consider the beam powers and waists that form the lattice. More details about the experimental setup are given in chapter 3. Briefly, there are 200 mW of power in beam 2, which has a Gaussian waist of $w_{0,b2} = 100\mu m$, and a $\sim 6\%$ modulation of lattice beam power for 6 ms. The power in other beams is determined relative to the beam 2 power. The maximum possible depth with three perfectly overlapped beams with $w_0 = 100$ μm is 356 kHz/Watt, so that 200 mW would correspond

to a 71 kHz deep lattice.

Our measurement of a 60 kHz deep lattice is consistent with this calculation of lattice depth given perfect overlap of beams at the measured powers and beam waists.

Method: 2-beam stripe lattice modulation without vertical lattice

For another consistency check, we perform lattice modulation spectroscopy measurements on the one-dimensional stripe lattices formed with each pair of lattice beams. This is not a reliable measurement of the full, three-beam, triangular lattice depth, but it is an important consistency check of our system. A one-dimensional lattice formed at the intersection of two of the 532-nm lattice beams has a lattice spacing $a = \lambda/\sin(\pi/3)$, and thus a lattice recoil energy of $E_{r,532stripe}/h = 6$ kHz, by Eq. (2.11). To do this calibration, we use the same powers in each beam as in the three-beam case, but block one beam.

There are three such one-dimensional stripe lattices, formed by blocking each of the three beams. By convention we label each 1D stripe lattice by the pair of beams that form it, so the '1 & 2 stripe' has the reciprocal lattice vector $\mathbf{g}_1$, the '2 & 3 stripe', has the reciprocal lattice vector $\mathbf{g}_2$ and the '3 & 1 stripe' has the reciprocal lattice vector $\mathbf{g}_2 - \mathbf{g}_1$.

In data from calibration of the three pairs of one-dimensional lattices, we measured resonance frequencies $\omega \sim 26$ kHz for both the 1 & 2 stripe and 2 & 3 stripe lattices, and $\omega \sim 30$ kHz for the 3 & 1 stripe lattice. In this lattice one-dimensional strip lattice geometry of 532-nm beams, the allowed excitation is between bands 1 and 3, and a gap of $E_{13}/h = 26$ kHz corresponds to a lattice depth $V_{532,1D}/h = 26$ kHz, which, with all three 1D lattices perfectly aligned, would lead to a 3-beam lattice depth of $V_{532,1D}/h \times 9/4 = 58$ kHz. These 2-beam calibrations are thus also consistent with our measured 3-beam lattice depth.

Note that one-dimensional measurements are not used for final data calibrations.
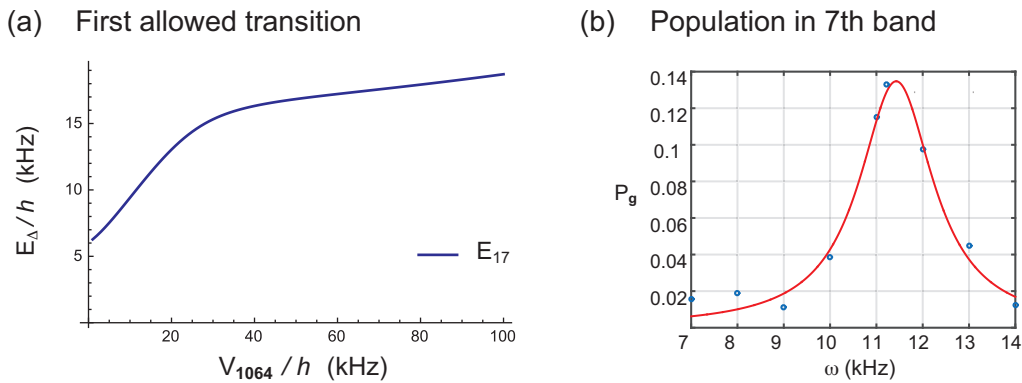
Figure 2.10: (a) The energy gap of the allowed transition by intensity modulation, between states $|\psi_1\rangle$ and $|\psi_7\rangle$, of the honeycomb lattice. (b) The measured population of atoms in the upper band as a function of modulation frequency ω.

Method: 3-beam lattice modulation with vertical lattice

In the final method of calibrating the optical lattices, we perform modulation spectroscopy in each three beam in-plane lattice and count the atoms in the upper band. In these data, we also include the optical confinement of the BEC and a deep one-dimensional lattice orthogonal to the triangular lattice plane (the vertical lattice), both at the settings they will have when data is being taken. The vertical lattice is independently calibrated with the same lattice modulation spectroscopy method.

In this chapter, we have considered very generally the calculations for ideal optical lattices formed by plane waves. In reality, there are additional confining potentials in the experimental system that must be taken into consideration. These concerns are discussed at length in chapter 3. Here we simply note that the optical dipole trap and the vertical lattice are both formed by light at the wavelength 1064 nm, so they add additional confinement to the system. They may physically move the atomic cloud, which has a radius of $\sim 10\ \mu$m, to a particular position in the blue-detuned 532-nm lattice, which extends for a radius of $\sim 100\ \mu$m. The 532-nm lattice beams have curvature, and do not form interference patterns of uniform depth throughout the entire extent of the interference pattern. Note that the depth is approximately uniform over the extent of the 10μm cloud, so that our plane-wave treatment is valid for lattice-trapped atoms.

Still, we found that a small misalignment can result in a shift in position of the atoms within the 532-nm lattice that depends on the power in the optical dipole trap and the vertical lattice (this effect is not as much of a concern with the in-plane 1064-nm lattice because of the low powers used and because of the in-plane interference). As a result, we use high powers of optical trapping beams to pin the atoms to one position in the lattice for calibrations as well as for all experiments.

The deep vertical lattice changes the transport properties of atoms trapped in the in-plane lattices, reducing the coherence of the atoms at higher lattice depth. Our calibration technique depends on having strong, coherent signal at the first-order diffraction vectors $\mathbf{G}_i$, so that including the vertical lattice means that calibrations must be performed at lower overall lattice depth. We typically find resonances like the one from August 2016 that is shown in Fig. 2.9(c) near $\omega = 26$ kHz, which corresponds to a lattice depth $V_{532}/h \sim 40$ kHz, just above the frequency where the dependence of energy gap on lattice depth begins to increase.

To calibrate the 1064-nm lattice, we load a two-dimensional honeycomb lattice and perform lattice modulation spectroscopy. The transition that preserves the symmetry of the optical lattice potential is $|\psi_1\rangle \rightarrow |\psi_7\rangle$. Figure 2.10(a) shows the energy gap as it varies by the full optical lattice potential depth V_{1064}. This curve displays a strong dependence at low-lattice depth that saturates at higher depth, so that calibrations should always be performed in lattices with energy gaps lower than $E_{17}/h \sim 15$ kHz to maximize sensitivity to lattice depth. In Fig. 2.10(b) shows a typical calibration curve from August, 2016.

Throughout data taking in the summer of 2016, calibrations were performed roughly every hour between experimental repetitions. The construction and stability of our optical

lattice setup is discussed in chapter 3. In a full day of datataking, the 532-nm lattice depth was stable to within 1% rms of the overall measured depth.

2.6 Calculating U and J

To calculate the tunneling energy and on-site energy of lattice-trapped atoms requires determination of the Wannier functions, $w_i(\mathbf{r})$ of atoms on each lattice site, i.

In a three-dimensional lattice, these terms are derived from the Wannier functions as

$$J_{i,j} = -\int d^3\mathbf{r} \ w_i(\mathbf{r}) \left(\frac{-\hbar^2}{2m} \nabla^2 + V(\mathbf{r}) \right) w_j(\mathbf{r}) \tag{2.51}$$

$$U_i = g_{3D} \int d^3\mathbf{r} |w_i(\mathbf{r})|^4 \tag{2.52}$$

where i and j label sites. The term $g_{3D} = 4\pi\hbar^2 a_{Rb}/m_{Rb}$, and a_{Rb} is the s-wave scattering length of rubidium, given by $a_{Rb} \sim 100 a_0$, where the Bohr radius is $a_0 = 0.053$ nm [15]. Translational invariance of the lattice allows us to drop the subscript on the terms U, which will be the same for all sites i. We define J as the nearest-neighbor tunneling energy, which will be the same for all nearest neighbors i and j, so those subscripts are also dropped.

2.6.1 Harmonic well approximation

In a very deep lattice, a well is approximately parabolic, with a trapping frequency that depends on the particle mass m, lattice spacing a, and the lattice depth $sE_{r,lattice}$, where s is the lattice depth in lattice recoil energies, as defined in (2.11)

$$\omega_{lattice} = \sqrt{\frac{sE_{r,lattice}/m}{2a^2}} \tag{2.53}$$

where s is

In our lattice, the overall trapping frequency $\bar{\omega}$ is the quantity

$$\bar{\omega} = (\omega_{plane} \times \omega_{plane} \times \omega_{\text{VL}})^{1/3} \tag{2.54}$$

where ω_{plane} represents the in-plane lattice trapping frequencies, determined by the in-plane lattice depth, and ω_{VL} is the trap frequency of a site of the vertical lattice. And we can write the harmonic oscillator length for a lattice site as

$$\bar{a}_{ho} = \sqrt{\hbar/m\bar{\omega}} \tag{2.55}$$

Within this approximation, we may write a Wannier function as a Gaussian distribution centered a lattice site i:

$$w_i(\mathbf{r}) = \left(\frac{1}{\pi \bar{a}_{ho}^2}\right)^{3/4} e^{-(\mathbf{r}-\mathbf{r}_i)^2/(2\bar{a}_{ho}^2)} \tag{2.56}$$

and the on-site interaction energy U is given by

$$U = \frac{\hbar a_{Rb}}{\sqrt{\pi/2}} \frac{\bar{\omega}}{\bar{a}_{ho}} \tag{2.57}$$

2.6.2   Numerical treatments

We calculate the Wannier functions of atoms in our lattices following two approaches. In the first, we take a very simple numerical approach. We solve for the single particle band structure of a lattice as in section 2.2. We compute the Wannier functions at each site by assuming they are real when taking the Fourier transforms of the Bloch states, $u_{\mathbf{q}}^{(N)}(\mathbf{r})$, defined in Eq. (2.19). These Wannier functions are used to find the tunneling energy, J and the on-site interaction energy U of atoms in the optical lattices.

In a second approach, we use a steepest-descent minimization algorithm to generate maximally localized generalized Wannier states [16]. The calculation finds the Wannier basis with the global minimum of the spatial spread of the Wannier function, and outputs the tunneling energy J and on-site interaction energy U. This code was created to calculate Wannier states in two-dimensional lattices. To apply it to our system correctly, we must integrate out the dependence of U on the vertical lattice to determine g_{2D}.

$$g_{2D} = g_{3D} \int dz \, |w(x,y,z)|^4 \tag{2.58}$$

$$= g_{3D}/(\sqrt{2\pi}a_{ho,z}) \tag{2.59}$$

where $a_{ho,z}$ is the harmonic oscillator length of the vertical lattice and the term g_{2D} is used to compute the on-site energy of the in-plane lattices as a function of their lattice depth, by integrating over x and y as in Eq. (2.52).

We find that the computed on-site interaction and tunneling energies within and between the low-energy sites obtained from these two approaches agree. The first method is computationally very simple, as it doesn't require a minimization algorithm.

We apply this treatment to both the triangular and kagome optical lattices for varying depth V_{532} and a vertical lattice depth $V_\perp/h = 41$ kHz to find U and J as shown in Fig. 2.11(a). In these calculations, the kagome lattice is formed at the overlap of the 532-nm triangular lattice with a 1064-nm lattice of depth $V_{1064}/h = 15$ kHz. The results for U and J are indistinguishable in the triangular and kagome lattice cases, despite the addition of the

1064-nm potential in the kagome configuration. This confirms our understanding that the low powers used in creating the kagome geometry do not significantly change the curvature at the bottom of the potential wells formed by the remaining 532-nm lattice sites. Equation (2.60) is the result of fitting the ratio U/J, with V measured in kHz.

$$U/J \sim 0.0311 \ e^{0.732V^{0.521}} \tag{2.60}$$
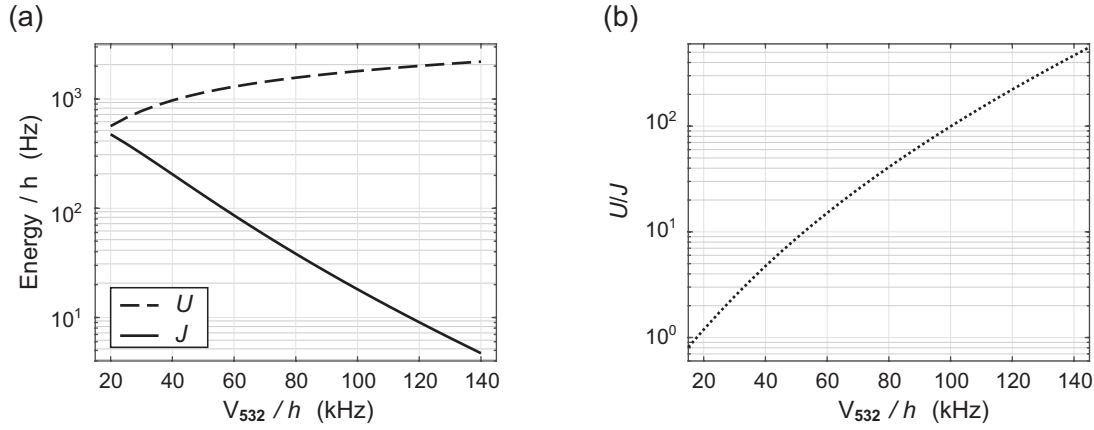
Figure 2.11: (a) Calculated on-site repulsion energy, U, and tunneling energy, J, for atoms trapped in this system for various 532-nm lattice depths, V_{532}. These quantities are equal for the triangular and kagome lattices, because the addition of the 1064-nm lattice in the kagome configuration does not distort the bottom of the 532-nm lattice wells, where atoms reside. In these calculations, the vertical lattice depth is $V_{\perp}/h = 41$ kHz and the 1064-nm lattice depth is $V_{1064}/h = 15$ kHz. (b) The ratio U/J in the lattices.

Chapter 3

Creating a bichromatic optical superlattice
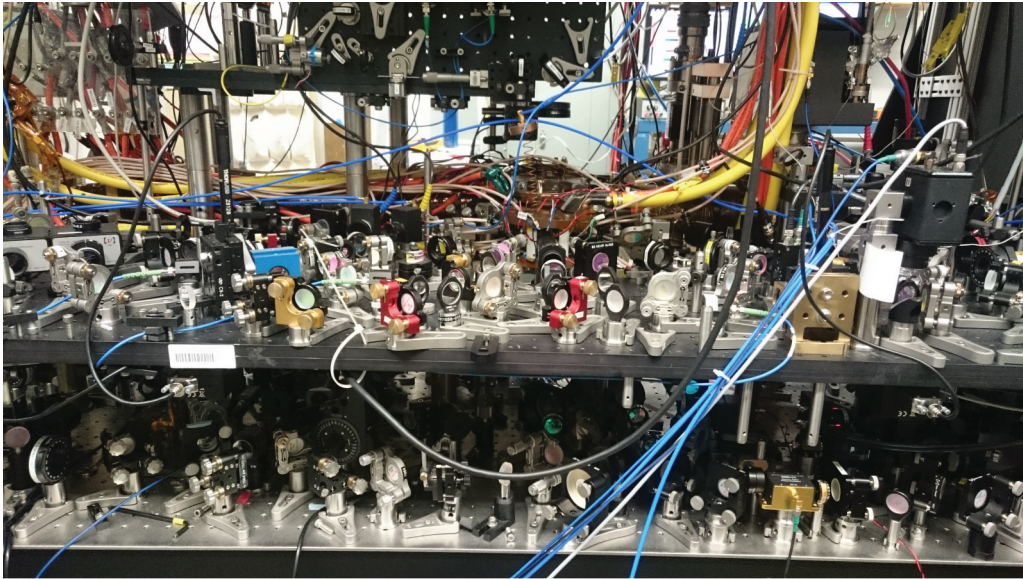
Figure 3.1: The optical lattice experiment.

We perform quantum simulations with artificial materials to gain insight into the physics of materials. The artificial materials are formed at the overlap of a Bose-Einstein condensate and an optical lattice. The schemes for building the triangular, honeycomb and kagome lattices were explained in chapter 2.

In section 1.6 we outlined a few advantages that artificial materials have over solid state materials. Artificial materials created at the interference of coherent light are without defects, their lattice spacings are immutable, their length scales are magnified and their time dynamics are slowed. The lattice and quantum gas that propagates within it are indepen-

dent of one another, and can thus be independently controlled. All of these advantages amount to experimental control over the lattice parameters that determine the behavior of the lattice-trapped atoms. The sensitivity of the material to experimental controls is also the central challenge of building this quantum simulator. Any change in the intensity of the laser light or the structure of the superlattice changes the parameters of the artificial material, and therefore these changes must be well-controlled.

A single simulation requires creation of a condensate, loading it into a lattice, and extinguishing the lattice to measure the properties of the gas. This is a destructive process, and the simulation is repeated many times. The experimental parameters must be well-controlled within each simulation, as well as stable over the course of many simulations. We use these features to set the goals for our quantum simulator.

3.1 Desired specs of the quantum simulator

In this thesis, the primary goal of the simulator is to quantitatively test a theory about the ground-state of lattice-trapped bosons in various lattice geometries in the limits $U/J \sim 1$ and $U/J \sim 100$, as described in chapter 5. To reach these interaction strengths requires stability in lattice beam power over three orders of magnitude, from about 100 microwatts per beam, to about 300 milliwatts per beam. This test also requires that the lattice have a low number of atoms per lattice site, ideally $n \sim 1$.

1. Pure Bose-Einstein condensates produced in under 20 seconds

2. Loose optical confinement, $\bar{\omega} < 30$ Hz to achieve $n \sim 1$ atom per site

3. Lattice beam intensities actively stabilized over three orders of magnitude in beam power

4. Alignment procedure should take less than 1 hour

5. Alignment should last for more than 1 hour; or a full day with minor adjustments

6. Bichromatic lattice beams are commensurate over the spatial extent of the gas

7. Relative phase of the two lattices is stable to within 10 nm and controlled in software

3.2 Early experiments

The machinery necessary to create a Bose-Einstein condensate of rubidium was built by students and postdocs before my time here and is described in the thesis of Dr. Jennie Guzman. Figure 3.2 provides photographs and a brief review of some important stages of our sequence. Further detail can be found in Jennie's thesis and will be updated in the forthcoming thesis of Thomas Barter. The main chamber of our vacuum system is at a pressure below 10^{-10} Torr and the final BEC, which has $50,000 < N < 300,000$ atoms at temperature $50 < T < 100$ nK, has a lifetime of $\tau \sim 20$ seconds.

In my early years of grad school, we performed experiments in this apparatus, studying the formation of magnetic domains with a spinor rubidium condensate [12], and built the first version of a bichromatic triangular superlattice described in chapter 2. The successful realization of the kagome lattice is of interest to the condensed matter physics community, and the work was published in PRL and is included in appendix A [13].

Unfortunately, though the creation of the kagome lattice geometry was novel, the lattice described in the publication of appendix A did not meet several of the specifications outlined in section 3.1. First, the alignment procedure took roughly 6-8 hours. Second, the lattice beams drifted substantially during data taking, and the lattice geometry was stable for no more than 30 minutes. Third, the trap geometry was not ideal to reach low lattice filling; it was tight along one direction and the resulting lattice filling was $n \sim 4$. Fourth, upon
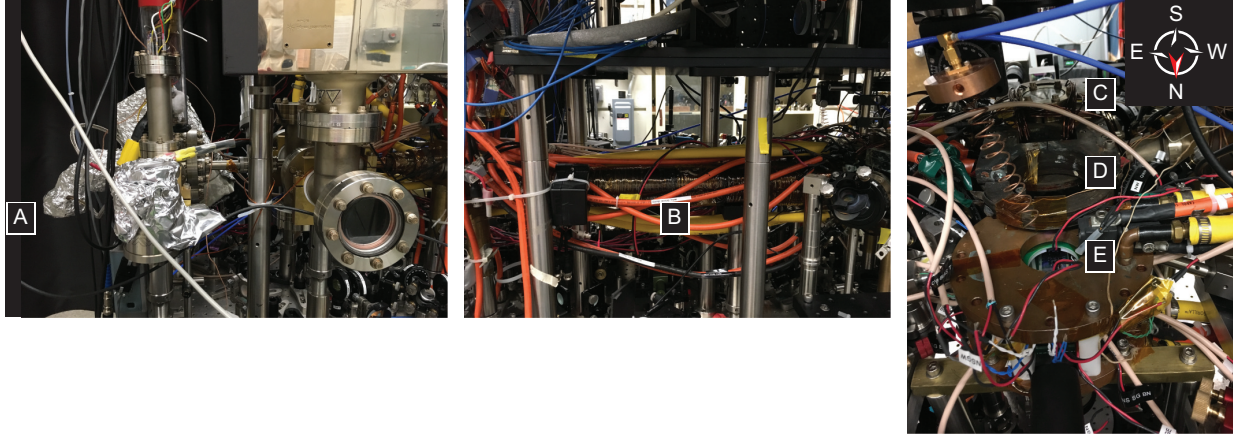
Figure 3.2: The vacuum chamber in which the Bose-Einstein condensate (BEC) is created and probed. [A] Atoms are heated in an oven, which is wrapped in aluminum foil. They exit the oven at high velocity through a collimating nozzle. The oven chamber has a pressure of 10^{-8} Torr. [B] The atoms are laser cooled as they travel through the Zeeman slower, which provides differential pumping of the chamber and produces a magnetic field that increases in strength as the atoms are slowed, so that they are resonant with a counter-propagating cooling beam. The main chamber has a pressure of $< 10^{-10}$ Torr. [C] Atoms are caught in a magneto-optical trap (MOT), which employs optical cooling from all directions as well as magnetic trapping by a quadrupole field generated by a pair of coils in an anti-Helmholtz configuration. After a compressed MOT stage (CMOT), atoms are magnetically transported via displaced pairs of coils in the anti-Helmholtz configuration [D] into the glass cell [E]. Roughly 10^8 atoms are magnetically trapped in the glass cell at a temperature of 300 μK. These atoms are cooled by magnetic and optical evaporation to create a Bose-Einstein condensate.

introduction of a vertical lattice in conjunction with the in-plane lattices reported, the atoms in the lattice experienced substantial heating due to instabilities in beam intensity and lattice phase.

Many of these shortcomings stemmed from the same source – the height of the vacuum chamber. The chamber was mounted just 5 inches above the optical table. In order for laser beams to propagate horizontally to the location of the atoms, a large breadboard was mounted four inches above the table. This upper breadboard was nearly touching any table-mounted optics. The optics table, which hosted elements for the beam shaping of the optical dipole trap and very little else, was inaccessible. This had two effects. First, it limited the space for the optics necessary to create the optical lattice. To build the lattice, optics were mounted on breadboards that were mounted on top of breadboards. This tiered breadboard system increased sensitivity to drifts in temperature or building vibrations.

Second, the shape of the optical dipole trap was difficult to change. The existing surfboard-shaped optical trap was ideal for work with a spinor condensate, but the ideal

trap geometry for a low-filling lattice is a diffuse ball. Since the optics that determined the shape of the ODT could not be accessed, the lattice was built with the surfboard shaped trap and had high filling, near $n \sim 4$.

We planned to address these challenges incrementally. There was no straightforward way to re-design the lattice optics so that they could occupy only the table and a single breadboard. Our plan was to reduce sensitivity of the system on physical drifts of the upper breadboards, as well as try to make space on the upper breadboard to reshape the ODT. Still, there were space constraints that stemmed from the height of the vacuum chamber and the inaccessibility of the entire lower level.

3.3 A failed gate valve

In April of 2013, two weeks before my qualifying exam and roughly halfway through my graduate school career, we ran out of rubidium in the oven. The protocol for loading rubidium into an oven is in appendix D. As discussed in Fig. 3.2, the vacuum system is separated into two regions: the oven chamber at 10^{-8} Torr and the main chamber at $< 10^{-10}$ Torr. A gate valve separates the oven chamber from the Zeeman slower and the rest of the main chamber. The gate valve can be closed to form a vacuum seal between the two chambers and allow opening the oven chamber without contaminating the main chamber.

When we opened the oven chamber to replace the rubidium ampule, we discovered that the gate valve that is supposed to seal the oven chamber from the main chamber was damaged. We suspect that it failed because it used a viton seal, as opposed to an all-metal one. Viton is a polymer that is possibly not robust against being struck with a few grams of (pyrophoric) rubidium over the course of a few years. We recommend using all-metal gate valves for experiments with rubidium.

3.3.1 Oven change

Appendix appendix D contains information and the procedure for changing an oven ampule in our experiments. In brief, one must first connect the oven chamber to an additional set of clean vacuum components that contains a turbo pump and a residual gas analyzer (RGA). To do this, these components are attached to the oven chamber at a right-angle valve (RAV), and they are pumped down with a turbo pump. Then the RAV that separates these components from the oven chamber is opened. The turbo pump is then used to fill the entire oven chamber with nitrogen. The nitrogen flows from a cylinder, through a regulator, through a vat of liquid nitrogen, which condenses any water vapor that might be mixed with the gas (so that it is clean and can be put into the vacuum chamber), and finally through the turbo pump inlet, This slight, positive pressure in the vacuum chamber allows us to open the oven chamber. When a window or a flange is removed from the chamber, there is a flow of nitrogen out of the oven, minimizing the amount of atmospheric air that enters the chamber. This helps to keep the oven clean, and also prevents any trace amounts of

rubidium from catching fire (rubidium is pyrophoric, meaning that it catches fire on contact with air or water).

In the oven chamber, there is an oven that contains rubiduim, and a nozzle through which the rubidium passes when heated. The next element is called a cold catcher. The cold catcher is a piece of cold copper with a hole in it, and any rubidum that doesn't make it through the hole sticks to the cold metal. Once the oven chamber is open and the oven itself is removed, the next step is to clean the rubidium off of the cold catcher. To do this, we remove the flange below the cold catcher (the oven shutter, in the case of this experiment), and spray small amounts of methanol onto it. After the cold catcher is clean, we place a new ampule of rubidium into the oven. An ampule contains 5 grams of rubidium and is under vacuum (and must stay that way at all times). In addition to the ampule, we place a small magnetic ball in the oven, which will be used to break the ampule in the very last step of this process, i.e. *after* the oven chamber reaches the desired pressure.

After the chamber is re-assembled, it's temperature is raised to 150° C while a turbo pump pulls out the residual air and water in the chamber in a process called a bake-out. To bake-out a vacuum chamber, we put thermocouples on various regions of the chamber to monitor temperature, bearing in mind that some vacuum components (like a gate valve) are not robust to large temperature differentials, and other elements (like the RGA) have limits to the temperature that they can withstand. Next, we wrap the entire chamber in one layer of aluminum foil. This is then wrapped in heat tapes, which are long fiberglass-filled belts that are plugged in to high voltage sources to heat the chamber to $\sim 150°$ C. The temperature is increased slowly throughout a day, until the chamber is hot. The RGA monitors the amount of air and water that are in the chamber as it is baked. After roughly two days of baking out the chamber, it reaches the desired pressure. At this point, we unwrap the tape and foil from the chamber and close the RAV so that the turbo and RGA can be safely removed. Finally, we break the rubidium ampule using a strong magnet against the outside of the oven chamber to move the magnetic ball inside the oven until it crushes the glass of the ampule.

3.3.2 Failed gate valve

During the oven change of 2013, we discovered that the gate valve that separates the two chambers did not form a vacuum seal. In our procedure, we flushed the turbo and RGA nitrogen and then tried to slowly open the RAV connecting them to the oven chamber. In retrospect, we should have opened the RAV first, and then slowly introduced nitrogen to the chamber, because it is difficult to open a RAV slowly. Due to the damaged gate value, pressure of nitrogen in the main chamber spiked to $\sim 10^{-3}$ Torr when the RAV was opened, which could have broken the main chamber ion gauge and ion pump. We turned them off quickly enough and were fortunate that neither broke.

We then used the RGA and found that there was water in the chamber. This was likely because we had not baked out the additional vacuum components connecting the RGA and turbo pump to the oven chamber. If the gate valve had formed a seal, only a bake out of the

Figure 3.3: These pictures are from the oven change of 2013. On the left, Thomas Barter and I prepare to open the right angle valve that separates the RGA and turbo pump from the oven chamber. While flowing gaseous nitrogen through the chamber, we remove the oven from the chamber. The copper cold catcher is visible through the opening. It is covered in rubidium so that it appears white. We clean the rubidium off of the cold catcher before replacing the rubidium ampule.

oven chamber would have been necessary to removed the water contamination. However, the contamination of the main chamber necessitated that we bake out the entire vacuum system. To prepare the main chamber, we replaced the gate valve with an all-metal one, and also replaced some filaments in the titanium sublimation pump, which are used for pumping at very low pressures.

Rather than try to work around the stacks of lattice optics that were very near the chamber, we decided to remove them. All optics that were on the main table (those used for trapping and cooling the atoms) were left alone and covered with a thin sheet so as to prevent them from being covered in fiberglass fragments.

3.3.3 Lifting the chamber

A main chamber bake out necessitated removing all of the tiered breadboards so that we could access the chamber. This provided an opportunity to consider some changes to the optics and setup in our lab. We decided to lift the chamber an additional four inches to allow for improved access to the optical table, addressing many of our previous challenges in studying physics in a bichromatic lattice described in chapter 2. We also separated the magnetic trapping coils around the glass cell to increase optical access to the atoms.

Many of our challenges in studying physics in the bichromatic lattice stemmed from the height of the chamber. After removing the breadboards, we removed all of the clamps that held the chamber in place and lifted it manually by four inches. The entire Stamper-Kurn group stood around our optics table, everyone lifting a piece of the chamber and trying to hold it level and steady, so as not to torque any one part of it. The flange that connects
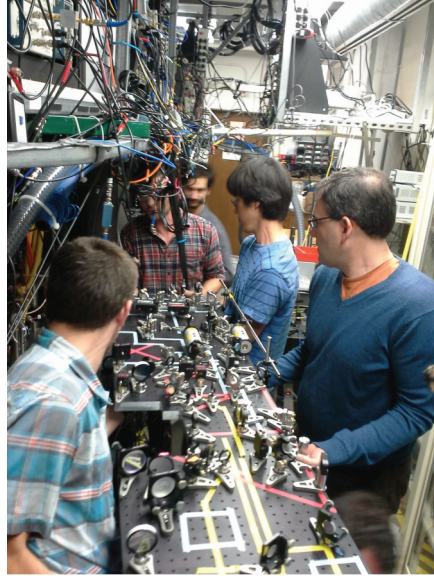
Figure 3.4: Before baking out the main chamber, we removed all breadboards and lifted the chamber by four inches. Group members held the chamber up while posts were slipped into place to mount the chamber. This photo shows the group replacing one of the raised breadboards.

the main and oven chambers is 1/4" in diameter, and it somehow survived this brute-force method of lifting the chamber. I ran around, slipping between my labmates, adding four inches of post on every mount before instructing everyone to set it down slowly.

The main chamber bake out followed the same procedure as the bake out described previously. We baked at 150° C to remove water from the chamber. The process took about one week in total, but was interrupted by the flood I described in section 1.1.

3.4   Scheme

We create a quantum simulator of the triangular, honeycomb and kagome crystal lattice structures. The band structures of these lattices and the general method for creating them with lasers were described in chapter 2. In this section I will explain the experimental details of building this quantum simulator.

3.4.1   Overview

Each simulation starts with creating a pure Bose-Einstein condensate of $\sim 100,000$ rubidium atoms in the $|F = 1, m_F = -1\rangle$ state in a hybrid magnetic and optical trap. The BEC is then transferred into a crossed-dipole trap. The optical beams for trapping have a wavelength of

1064 nm, which is red-detuned from the rubidium atomic resonances, so that the atoms are attracted to the points of maximum intensity.

The condensate is then loaded into the optical lattices. This includes the bichromatic in-plane lattice that is composed of two triangular lattices of intensity minima formed with light at the commensurate wavelengths 532 nm and 1064 nm, as well as a retro-reflected, one-dimensional vertical lattice that is orthogonal to the plane.

Finally, the atoms are measured by absorption imaging. In-situ images can be taken if the lattice and trapping potential is kept on; or time of flight images can be taken, where atoms are allowed to expand in free space or weak magnetic confinement beforehand. Our system is equipped with multiple imaging axes: along each trapping beam as well as out of the lattice plane.

3.4.2   Bichromatic lattice concerns

Here I outline a few major experimental concerns in creating a bichromatic superlattice following the scheme described in chapter 2.

Frequency

We do not need to stabilize the ratio of the frequencies of the 532-nm laser and the 1064-nm lasers in order for the lattices to be commensurate over the extent of the cloud. The requirement that they are commensurate – that the wavelength of the 1064-nm light is twice that of the 532-nm light – is necessary for the overlap of the lattices to produce a periodic bichromatic lattice with the same unit cell as that of the 1064-nm lattice.

The gas is about 10 μm across. Commensurate beams have $k_{532} = 2k_{1064}$, but if our lasers deviate from this then there is some offset Δk. A wavelength difference of 1 nm results in a drift over the extent of the cloud

$$\phi = l \, \Delta k \tag{3.1}$$

$$= 6 \times 10^{-4} \tag{3.2}$$

where in the last line I have used a wavelength difference of 1 nm. This means that if the lattices have wavelengths that differ from $\lambda_{1064} = 2\lambda_{532}$ by a nanometer, the nodes of the two lattices that overlap at one end of the gas will be displaced at the other end by 0.05 nm. This is too small an offset to affect our measurements. We monitor the frequency of both beams and they are commensurate to within 1 nm.

Frequency noise on the two lasers will differ, because they are not locked relative to one another. However, our scheme involves independently stabilizing the phase of each constituent lattice. The resulting superlattice is stable.

Phase

All three beams of each color have the same path length from the laser source to the atoms, so that the system is passively phase stable. This is a huge advantage of our system relative to others that require retro-reflection, where there is inherently a large path length difference.

We estimate that the path length differences among the lattice beams is on the order of 2 cm. Such path lengths would introduce phase noise on a 1064-nm laser beam with a MHz linewidth of

$$\Delta\phi = \Delta f \Delta l / c$$
$$= 10^{-5}$$

which corresponds to a difference of 0.01 nm at the atoms. By keeping path lengths similar, we ensure passive stability of the optical lattices. Without active stabilization, the lifetimes of the in-plane lattices are about $\tau = 1$ second.

Each three-beam lattice is actively stabilized using two Mach-Zehnder interferometers. For each lattice, the phase of one of the beams is taken as a reference, and the phases of the other two beams are locked to it using the interferometric error signals. In this way, we build two triangular lattices of intensity minima that are stationary in space.

The relative position of the two lattices is experimentally specified using a tunable thickness of glass in one path of each interferometer. Laser light passing through a glass wedge is phase-shifted by $\phi = n_\lambda k_\lambda t$, where t is the thickness of the glass. Light at the wavelengths 532 nm and 1064 nm have a different index of refraction in glass (BK7), with

$$n_{532} = 1.51947 \tag{3.3}$$
$$n_{1064} = 1.50663 \tag{3.4}$$

Because of the difference index of refraction, changing the thickness of the glass traversed along one path of the interferometer changes the relative phase between the two lattices along the axis defined by those two beams. The interferometer uses a Thorlabs BK7 wedged window on a translation stage to tune the thickness of glass through which the beams pass. A second wedged window is included to correct for angular deflection of the beams. The system is shown schematically in Fig. 3.5(a). The displacement of a lattice in response to actuating the wedge by some distance x is given by

$$\phi(x) = n_\lambda k x \ \sin\left(3°\right)$$
$$d(x) = \frac{\phi\left(x\right)\lambda}{2\pi}$$

where n_λ is the index of refraction at wavelength λ and k is the wavevector of the light. The difference in this displacement for 532-nm light and 1064-nm light is plotted in Fig. 3.5(b). The length of a unit cell translation vector is 710 nm, so moving the wedge by a distance $x = 1$ mm will translate the relative lattice position through an entire unit cell.
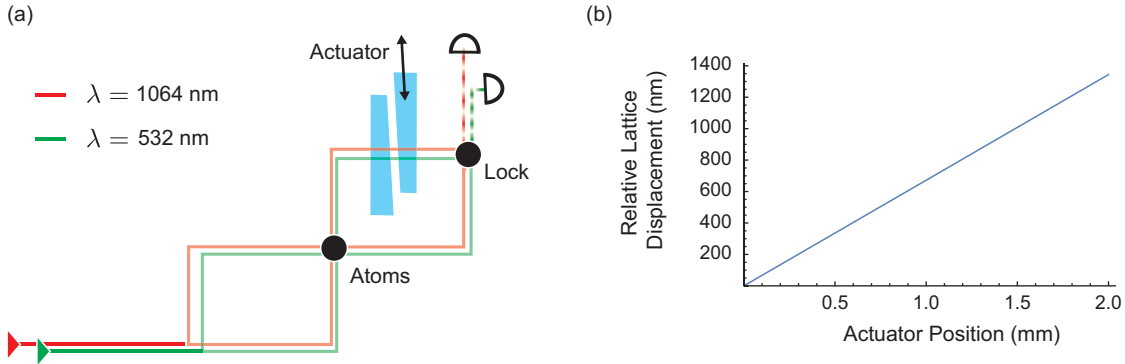
Figure 3.5: A pair of wedged windows in one path of the interferometer provide lattice geometry control. (a) This schematic shows the principle behind our in-loop phase shift scheme, but is not an exact representation of our experiment. Two points at which beams interfere are indicated by black dots. The first is the location of the atoms, and the second is labeled lock and is the point at which the phases are stabilized. The Mach-Zehnder interferometer has a wedge window on a translation stage in one path, after the atoms and before the phase is locked. The wedge is actuated along the 3° face of the window so that beams are not differentially deflected as the actuator is shifted. The second window corrects for differential angular displacement of the two beams after they pass through the wedge. (b) Plot of relative displacement of lattices in nm as a function of the position of the wedge. The length of the basis vector of the bichromatic lattice is 710 nm, so a 1 mm shift in wedge position corresponds to a translation through the entire unit cell.

3.5 Design: the BEC

3.5.1 Magnetic quadrupole trap

Each experiment begins by creating a BEC of rubidium atoms in the $|F = 1, m_F = -1\rangle$ state. The early stages of cooling produce 10^8 atoms at 300 μK at the location of the glass cell. They are confined in a quadrupole field created by the so-called "Feshbach coils" that are above and below the glass cell in an approximate anti-Helmholtz configuration.

To calibrate the field strength, we measure the point at which the current in the coils produces a magnetic field that counteracts gravity so that the atoms levitate.

$$gm_{Rb} = \frac{1}{2} \, \mu_{Bohr} B' \tag{3.5}$$

$$B' = 30.5 \text{ Gauss/cm}$$

where g is the acceleration due to gravity and μ_B is the Bohr magneton. To measure this value, we optically confine atoms and then release them into a weak magnetic potential and measure the vertical center of the atomic gas as a function of time after release. If they expand but do not fall, then gravity is being compensated by the magnetic trap. In our system, gravity is compensated when there are 18.64 amps running through the Feschbach coils, where the set point voltage is 1.56 V. Thus we measure that in this system, at the location of the optically trapped atoms, we have a field gradient of

$$B'_{Feschbach} = 1.64 \text{ G/cm/Amp} \tag{3.6}$$

in the z direction.

At the center of the trap, we approximate the field as a quadrupole field, with a linear slope of 1.64 G/cm/Amp axially, the trapping potential is then

$$U \sim \frac{1}{2} \, \mu_{\text{Bohr}} \, 10^{-4} I \sqrt{\frac{x^2}{4} + \frac{y^2}{4} + z^2} \times 1.64 \text{G/cm/Amp} \tag{3.7}$$

The effect of gravity is to modify the slope in the z direction by $m_{Rb}gz$. An important feature of the magnetic trap is the cusp at the origin. Atoms near the cusp may flip from the trapped $m_F = -1$ state to the other magnetic sublevels that are not trapped in the quadrupole field. This mechanism is called Majorana loss and its rate increases as the temperature of the magnetically-confined gas decreases.

3.5.2 Bias fields

Bias fields are generated by three pairs of Helmholtz coils around the glass cell, oriented along the cardinal directions indicated in Fig. 3.2. Vincent Klinkhamer designed coils on printed circuit boards, pictured in Fig. 3.6. The circular boards are mounted above and below the glass cell, providing the 'Up/Down' bias field. The long rectangular coils are positioned along the glass cell and create the 'East/West' bias field. The square coils are used to create the 'North/South' bias field. The design of the coils is so that they can be very close to the glass cell, but minimally block optical access to the atoms. The three bias coils create bias fields of 7.6 G/A (East/West), 2.8 G/A (North/South) and 3.4 G/A (Up/Down), respectively, and each has a maximum current of 2 Amps. There is an additional set of bias coils wrapped inside the large mount that holds the gradient coils. When we separated the Feshbach mounts to increase the optical access, we also changed these coils so that they form

a true Helmholtz configuration. They create another Up/Down bias field of roughly 1.6 G/A and have a maximum current of 10 Amps.

The three bias coils create bias fields of 7.6 G/A (East/West), 2.8G/A (North/South) and 3.4G/A (Up/Down) respectively.
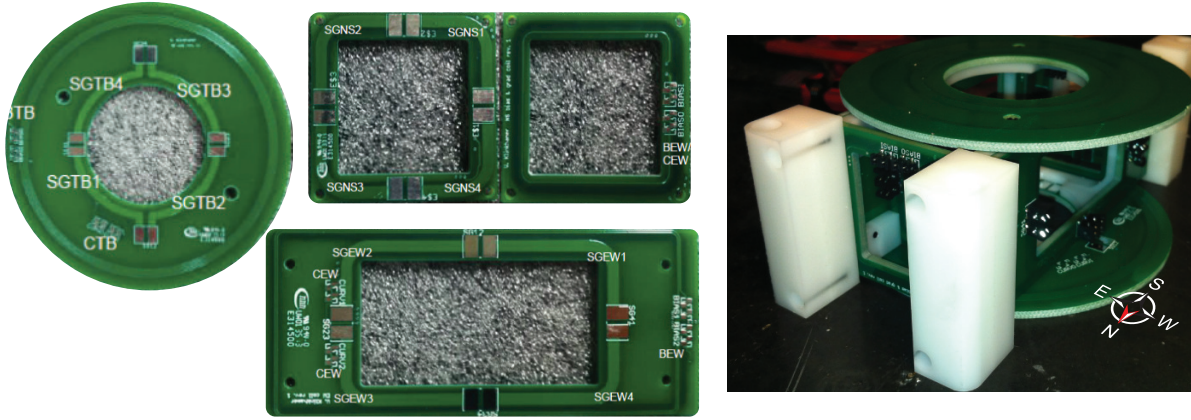
Figure 3.6: The coils surrounding the glass cell are printed on circuit boards. They were designed and tested by Vincent Klinkhamer. The bias field coils create a uniform field at the atoms of 7.6 G/A, 2.8 G/A and 4.4 G/A in the East/West, North/South, and Up/Down directions, respectively. All have a maximum current of 2 Amps. The boards also contain gradient and curvature coils, which generate magnetic fields of 0.03 G/cm/A and 0.69 G/A at the atoms, respectively.

3.5.3   BEC in a hybrid magnetic and optical trap

We make a BEC in a hybrid magnetic/optical trap. We create the condensate in a hybrid trap because we want to exploit the steep slope in entropy per particle (and thus in phase space density per particle) from decompressing a magnetic trap into an optical trap. We follow the prescription in Ref. [9].

We create a magnetic trap with a field gradient at the optical trap of 184.5 G/cm by running 112.5 amps through the Feshbach coils. We expose the atoms to an optical potential created by a 6 Watt beam of light with wavelength $\lambda = 1064$ nm, focused to 50 micron beam waist, that is aligned to roughly one beam waist below the field zero of the magnetic trap. This beam is called 'ODTa' in our lab. Without a magnetic potential, this beam forms a tight trap along two directions, say $\hat{e}_j$ and $\hat{e}_k$, and is loosely confining along the direction of propagation, $\hat{e}_i$, so that its trapping frequencies are $(\omega_i, \omega_j, \omega_k) \sim 2\pi(4, 920, 920)$ Hz.

This hybrid trap combines the advantages of each type of trap. Displacing the ODTa beam along the vertical direction creates a trap that avoids the cusp of the magnetic trap. The magnetic trap provides confinement along the direction of propagation of the beam, so that the trap frequencies are $(\omega_i, \omega_j, \omega_k) \sim 2\pi(83, 920, 920)$ Hz.

We make a condensate by first decompressing the magnetic trap by decreasing the magnetic field strength to the lowest value that compensates gravity (3.6), and then evaporatively cooling the atoms in the hybrid trap. Throughout this sequence, the trap center of the magnetic confinement must be stationary. We achieve this by tuning the Up/Down bias field as described in Fig. 3.8.
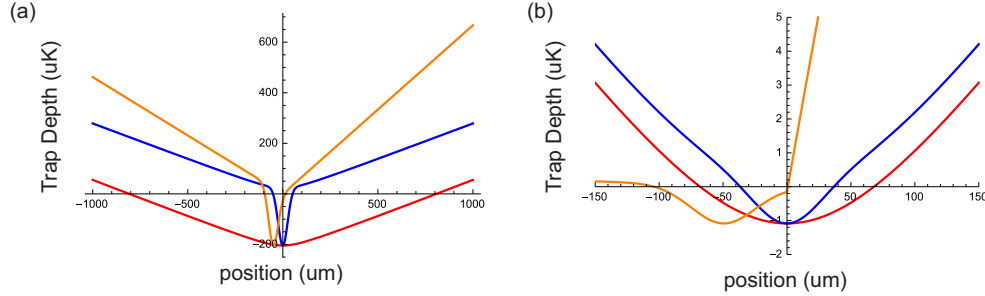
Figure 3.7: Hybrid trap parameters. (a) The hybrid trap shape where we overlay cardinal axes x (red) y (blue) and z (orange) and plot trap depth in temperature. $(\omega_i, \omega_j, \omega_k) = 2\pi(83, 920, 920)$ Hz (b) Hybrid Trap after evaporation to Bose condensation. The settings are such that the magnetic field strength just compensates gravity (apparent by the flatness in the of the orange curve). The trap frequencies are $(\omega_i, \omega_j, \omega_k) \sim 2\pi(35, 70, 70)$ Hz.

3.6   Design: optics table

3.6.1   Overview

To create the trapping and lattice potentials, we use just two high-power lasers, one at 1064 nm and the other at 532 nm. The 1064-nm beam is split into six paths: two for the optical dipole traps, one for a vertical lattice, and three for the in-plane triangular lattice of intensity minima. The 532-nm beam is split into the three lattice beam paths. We minimize drift and vibrational noise by building the entire setup on the optics table and a single mounted breadboard.

To facilitate alignment, we co-propagate as many beams as possible when they enter the glass cell. The lattice beams are combined using dichroic mirrors. The out-of-plane polarized ODT beams co-propagate with two of the in-plane polarized lattice beams. The difference in polarization ensures that the ODT beams do not interfere with the lattice beams.

3.6.2   Optics

Figure 3.9 shows a simplified schematic of the optical table (a) and the upper breadboard (b) that is at the height of the glass cell. Some advice regarding design of optical tables: leave
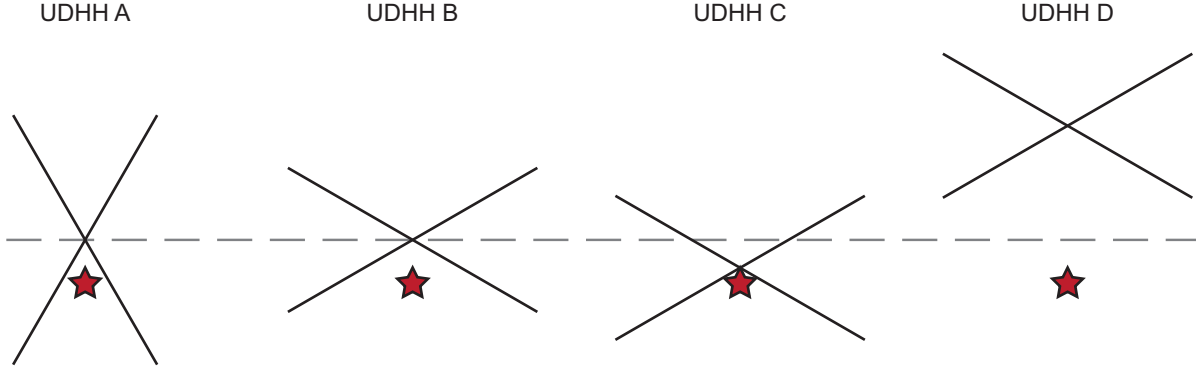
Figure 3.8: The settings of the Up/Down bias field throughout the sequence. The position of the optical trap is represented by the red star, and the black lines represent the magnetic quadrupole field. Initially, there is some bias field (UDHHA) that optimizes transport from the MOT chamber into the glass cell. The ODT is aligned to about one beam waist $w_0 \sim 50\mu$m below the magnetic field zero, which is the optimal position for transfer of atoms into the optical trap. When the trap is decompressed, the bias field must change in order to maintain constant distance between the optical trap and the magnetic field zero, this is the job of UDHHB. In order to create a BEC in the hybrid trap, we use UDHHC to bring the field zero closer to the optical trap, to increase confinement along the direction of beam propagation. After creating the BEC and transferring into an all-optical trap, we use UDHHD to push the field far away, so that it provides gravity compensation but provides very little radial confinement. This is used for momentum focused imaging, where atoms are released into this very weakly confining trap and allowed to evolve for a quarter of a cycle in this trap (~ 80 ms) before imaging.

room in the paths to insert power meters, don't use pellicle beam splitters for applications requiring phase stability, use pedestals rather than posts to mount optics, and use a washer when bolting forks down to the optics table. Using a washer allows you to remove a fork without significantly moving the optic it's holding. If you bolt down a fork without a washer, or with forks with built-in washers and bolts, like Thorlabs part number CF125C, then you will move the optic when you unscrew the bolt.

For our 1064 nm laser, we use a homemade ECDL with a Thorlabs diode M9-A64-0300. We fiber couple about 100 mW of power into a Nufern amplifier, part numbers SUB-1151-62 or NUA-1064-PD-0015-C0. We always have two Nufern amplifiers, so that when one breaks we don't have to wait for the repair, we just switch to the 'spare'. In the past five years, approximately four Nufern amplifiers have failed and the group is now switching to a new high power 1064-nm laser source.

The output beam from the Nufern has roughly 12 watts of power (this is below the specified output power by a few watts). The beam is split into six paths: two for the optical dipole traps, one for a vertical lattice, and three for the in-plane triangular lattice of intensity
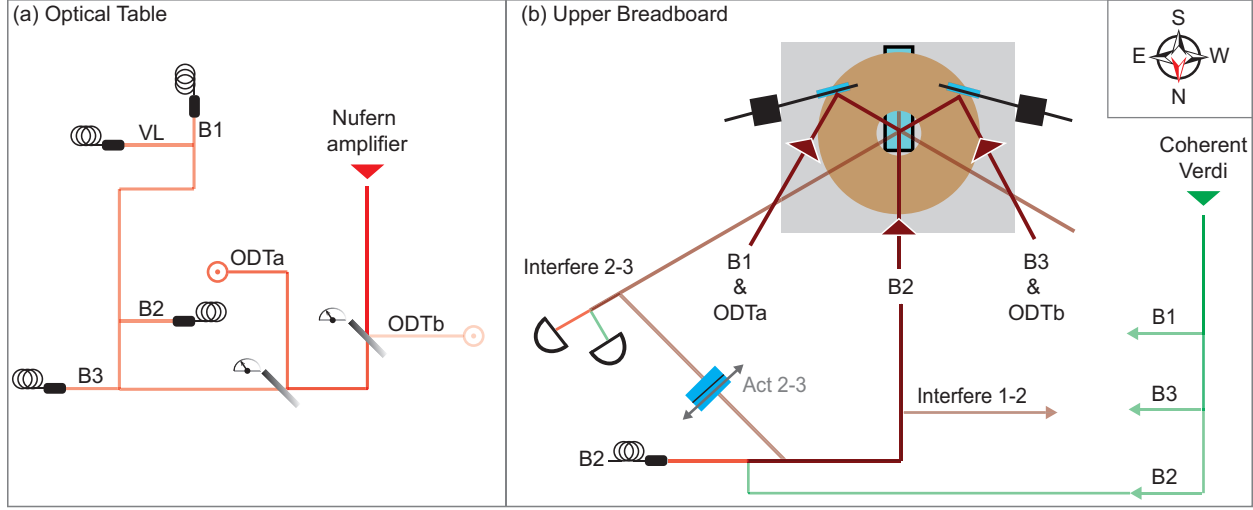
Figure 3.9: Lattice optics. (a) The 1064-nm laser outputs roughly 15 watts of power and is split into six beam paths: the first two are for the optical dipole traps, the four lattice beams split off after that. All beams are picked off using $\lambda/2$ waveplates and polarization beam splitting plates. The first two waveplates are controlled by software, so that power can be shifted among ODTa, ODTb and the lattices, but the power division among the lattices are fixed (and optimized so that each in-plane lattice beam has equal power). The lattice beams are fiber coupled, and the ODTs propagate in free space to the upper breadboard. The vertical lattice and the top-down imaging paths are not shown. (b) The upper breadboard contains optics for the 532-nm light from the Coherent Verdi source. The beams are separated by waveplates and polarization beam splitting plates. They are combined with the 1064-nm lattice beams with dichroic mirrors before being focused onto the atoms. The ODT beams are also combined at the location of a high power PBS just before the focusing optics. Not shown are the paths of imaging beams that also co-propagate with ODTa and ODTb. One of the two interferometer paths is shown: interferometer 2-3. The combined 1064-nm and 532-nm lattice light is picked off from beam 2 before the atoms, and beam 3 after the atoms. The beam 2 path travels through actuated wedged windows, labeled Act 2-3, to allow for bichromatic geometry control. The two beams are combined with a 50-50 beam splitter. After the splitter, the colors are separated and the beat signal for each color is measured on a photodiode.

minima. When we account for loss throughout the setup, we have roughly 10 watts of optical power to work with.

Transferring atoms from a magnetic trap to an optical trap requires a deep trap and thus high optical power. Our experiment uses about 6 watts in one of the trapping beams, dubbed 'ODTa,' which has gaussian beam waists at the atoms of roughly $w_0 \sim 50~\mu m$. The rest of the power is split among the second ODT beam, 'ODTb,' with waists $w_0 \sim 55~\mu m$, the three in-plane beams, with waists $w_0 \sim 100~\mu m$ and the vertical lattice beam waists

$w_0 \sim 200 \ \mu m$.

Each path is split from the main path using a waveplate and a high power polarization beam splitting (PBS) plate from CVI. We can move power between ODTa, ODTb and the in-plane lattices during the experiment by rotating two waveplates that are controlled by Labview, which communicates with our sequence generator via RS232.

The power in each beam is controlled by passing the beam through an acousto-optic modulator (AOM) and using a first-order diffracted peak. Figure 3.10 shows the frequency shifts for each 1064-nm beam.
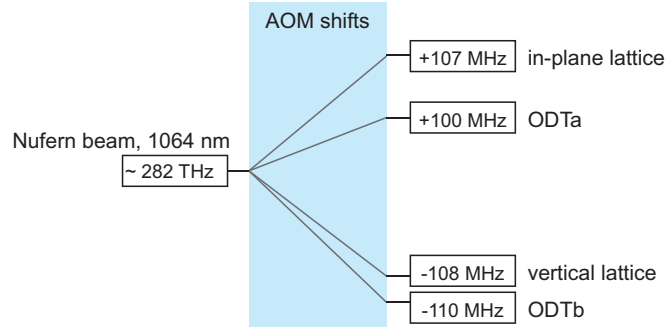
Figure 3.10: Frequency shifts for the 1064 nm beams. All optical intensities are controlled by acousto-optic modulators that impart a small frequency shift on the beams. This scheme ensures that the ODTs do not interfere with one another. We use AOMs from Crystal Technologies, part number 3110-197, with a maximum drive power of 2.5 watts.

The ODT beams propagate in free-space from the optical table, to the upper breadboard, and finally intersect at the location of the atoms. The three 1064-nm in-plane lattice beams travel in fibers from the table to the upper breadboard. We use 1 m PM fibers, Thorlabs part number P3-1064-PM-FC-1, and output couplers from Schafter Kirchoff to produce beams with 2.15 mm waists on the upper breadboard. The fibers have a damage threshold of 500 mW. We use output couplers at both the input and output of the optical fibers and find that we get $> 80\%$ fiber coupling efficiency using two mirrors, and occasionally a lens on a translation stage, before a fiber. The many degrees of freedom provided by, for example, Thorlabs input coupler PAFA-X-4-C are unnecessary and difficult to work with, though some of them remain in the system. Alignment of the polarization of the input beam along the fast axis of the fibers can be challenging and is important to minimize phase noise in the lattice. The last optic before each fiber is a PBS on a rotation mount, which is used in conjunction with a waveplate to fine-tune the alignment.

After each fiber, a beam passes through a dichroic that combines it with the 532-nm light, and then the combined beams are reflected from two mirrors, pass through a PBS cube and are focused to the atoms by a lens with $f = 250$ mm. The cubes are high-power, broadband PBS cubes from Advanced Thin Films, model number PBS1005-SBB. The original table was designed using CVI beam splitters, part number PBSH-450-1300, but those cubes grossly distorted the beam profiles.

The ODT beams are polarized out of the plane, and the lattice beams are polarized in the plane, and the two are combined on the high power PBS cubes from Advanced Thin Films. At the atoms, the gaussian beam waists of the ODT beams are $w_0 \sim 50~\mu m$ and of the lattice beams are $\sim 100~\mu m$. Because there are so few optical elements between the fibers and the atoms, the beams do not drift and require alignment only every few days. The intensities of all 1064-nm beams are measured after the atoms (and thus after the fiber and the PBS), and stabilized via feedback to drive power of the AOMs.

For convenience, the lattice beams are numbered 1 through 3 as indicated in Fig. 3.9. Beam 2 is normally incident on the glass cell and passes through the entire chamber, emerging near the MOT optics. The other two beams pass through the cell at 60° angles and the output beams are used for stabilization.

By keeping all in-plane lattice beam paths from the laser source to the atoms the same length to within a few cm, we achieve passive stability of the lattice – without active feedback, we have a lifetime in the lattices of $\tau \sim 1$ second – though the lattice phase slowly drifts, resulting in displacement of the lattice by about a 300 nm in 10 minutes, depending on whether the laser curtain is open or closed.

The three-beam lattice is stabilized in space using two Mach-Zehnder interferometers. Beam 2 is the reference beam and is modulated with a modulation depth of $\sim 1\%$ using an electro-optic modulator (EOM). Coated BK7 windows are used to pickoff $\sim 1\%$ of the light in two places along the beam 2 path before it is focused onto the atoms. The other two beams have pickoffs after they pass through the atoms, each of which is aligned to interfere with a pickoff from beam 2 onto a photodiode. The beat signal is demodulated and sent to a homebuilt lock box with a proportional and an integral gain stage. The signal is then sent to the modulation ports on the function generators (Agient 33600A series) that drive the AOMs. The phase stabilization is achieved by frequency modulation of the output of these function generators to correct the phase of beams 1 and 3, so that they each match the phase of beam 2. In this way, we build a triangular lattice of intensity minima using 1064-nm light that is stationary in space.

The 532-nm laser is an 18 Watt Verdi from Coherent, the Diode-Pumped Solid-State Lasers, High-Power CW Output at 532 nm, which has a quoted linewidth of 5 MHz.

The output of the Verdi is split into four paths using $\lambda/2$ waveplates and plate polarization beam splitters. The first goes into a power dump, and the remaining three interfere at the atoms to form the in-plane triangular lattice. Each beam intensity is stabilized using deflection from a high power AOM from IntraAction, part number AOM-402AF1.

The beams are combined with the 1064 lattice beams before the PBS and focusing lens. Though the goal was for all beams to have gaussian waists of 100 μm, there is thermal lensing in the AOMs that changes the beam divergence. The measured gaussian beam waists are 70, 100 and 60 μm for beams 1, 2 and 3, respectively. Currently, the experiment is being upgraded with better AOMs that have less thermal lensing.

The phases of the 532-nm light are stabilized with the same Mach-Zehnder interferometer paths as was used in the 1064-nm lattice. Figure 3.9 illustrates one of the two paths. The entire path of the interferometer, from the intensity pickoffs to the 50:50 cube, is common

to both the 1064 nm light and the 532 nm light. Any phase noise from motion of the breadboard or optics elements will be on both the 1064 nm light and the 532 nm light. The in-loop actuated wedge window scheme that was described in Fig. 3.5 is used to shift the relative phase of the two lattices along the 2-3 interferometer is labeled in Fig. 3.9 as Act 2-3.

All beams are equidistant to the atoms, but not equidistant to the interferometer. Beams 1 and 3 pass through the atoms before being picked off and sent to an interferometer with the pickoff from beam 2. The interferometer pickoffs for beam 2 are before the atoms, because beam 2 continues to travel back through the MOT chamber after passing through the atoms.

We elected to use the light of beams 1 and 3 after passing through the atoms, because the final optic before the atoms is a mirror on a long lever-like mirror post, shown near the glass cell in Fig. 3.9. These mirror posts are likely to vibrate and add phase noise to the system and so they should be included in the interferometer loop.

A shortcoming of this design is that, though the distance between the source and the atoms is the same, the distance between the source and the photodiodes are not. The early pickoff of beam 2 results in a path length difference to each interferometer of ≤ 20 cm relative to both other beams. This may be the reason that the phase stabilization does not improve the lifetime of atoms in the lattice, although it is effective at maintaining a stable bichromatic lattice geometry. In a future upgrade, lengthening the beam 2 paths to the interferometers would likely improve the stability of the system.

3.6.3   Power, beam waists and lattice depths

The ODT beams have gaussian beam waists at the atoms of roughly $w_0 \sim 50$ μm, and all six in-plane beams, have waists $w_0 \sim 100$ μm. The vertical lattice beam has waists $\sim 200 \mu m$.

Because of our wide variety of lattice geometries and spacings, we always quote our lattice depths in kHz, rather than the commonly used parameterization of recoil energies. A recoil energy can refer to a single-photon recoil energy, or to the lattice recoil energy. This was discussed in chapter 2 and results are shown in the Table below.

$$E_{r,light} = \frac{\hbar^2}{2m_{Rb}} \left(\frac{2\pi}{\lambda_{light}} \right)^2$$

$$E_{r,lattice} = \frac{\hbar^2}{2m_{Rb}} \left(\frac{\pi}{a} \right)^2$$

3.7   Design: active stability

3.7.1   Intensity stabilization

When working with a Bose-Einstein condensate, it is important to minimize fluctuations in the intensity of the lasers that are used for optical trapping. Laser intensity fluctuations

	532 nm Triangular	1064 nm Honeycomb	1064 nm Vertical
V_λ/h	356 kHz/Watt	907 kHz/Watt	806 kHz/Watt

Table 3.1: Calculated (ideal) relationship between beam power and peak-to-peak lattice depth, V_λ, for the lattices in our system, assuming beam waists $w_0 = 100$ microns. Depths assume beams of equal power and full interference depth. These numbers are used to get a sense of the power needed for each lattice, true lattice depths are calibrated using modulation spectroscopy of atoms in lattices. The triangular and honeycomb lattices have a depth $V_\lambda = 9/2 \times V_0$, the potential depth of a single beam. To find the depth of the one-dimensional lattice formed at the interference of just two of the three beams, we would multiply the depth listed by 4/9.

promote atoms into excited states, which leads to heating of the ensemble. When an optical lattice is imposed, the number of low-energy excited states to which atoms may be promoted increases, giving more opportunity for unwanted heating of the atomic ensemble. Ideally, in an optical lattice, the beam powers would be absolutely stable throughout the full range of beam power that are used in a quantum simulation, in our case up to 1 watt per beam. We specify and stabilize beam powers actively, which entails setting a voltage on a computer that is sent to a feedback loop that controls the beam power.

Creating and holding a Bose-Einstein condensate in an optical dipole trap requires some minimum beam power, on the order of milliwatts in our experiment, below which the atoms are no longer trapped (so fluctuations in power have no effect). While high beam powers are used in the experimental sequence, their stability is not typically relevant for the experiments performed on the final condensate. To create the lowest entropy condensates, with entropy per particle of $S/N \sim 0.001 k_B$, feedback parameters are optimized for the beam power of the final trap [17].

In our optical lattice, however, the atoms are trapped in an optical dipole trap regardless of the lattice beam power, so even the lowest beam powers can be a source of heating. Our goal is to stabilize beam power over three orders of magnitude, between 1 mW and 1 W per beam, a significantly larger dynamic range than necessary in typical experiments on Bose-Einstein condensates.

The feedback loop

The scheme for intensity stabilization is shown in Fig. 3.11. The feedback loop involves both optical and electronic elements. A set point voltage is sent from a computer and controls the amplitude of a high frequency (~ 100 MHz) RF source. The amplitude-controlled RF is sent into an acousto-optic modulator (AOM), and the power of the RF signal determines the optical power that is deflected into the stabilized beam. The beam travels to the atoms, but a small fraction ($\sim 0.1\%$) of the beam power is picked off of the main beam and directed into a photodiode. The photodiode voltage is sent to an electronic feedback circuit that compares
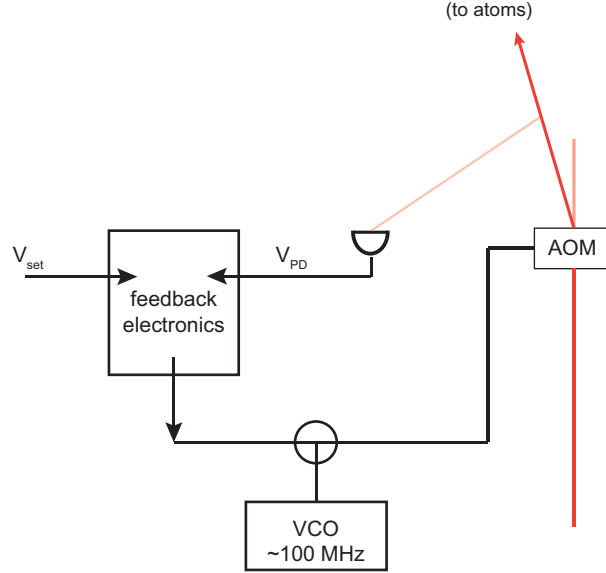
Figure 3.11: Schematic of generic intensity stabilization scheme. The feedback electronics compare a set point voltage, V_{set}, to the voltage measured on a photodiode, V_{PD}. The output controls the power of a radio frequency signal generated by a voltage controlled oscillator (VCO) that drives an acousto-optic modulator (AOM). The power of the RF signal controlling the AOM determines the amount of optical power in the deflected beam that is sent to the atoms. The closed loop system controls the power in the deflected beam.

the set point voltage with the detected voltage and corrects differences by changing the voltage that controls the amplitude of the RF signal.

To design and optimize the feedback circuit requires a measurement of the open-loop response function of the system without feedback. The open-loop response is measured by sending a voltage into the system and measuring its output, in this case that entails varying the setpoint and measuring the voltage on the photodiode. Figure 3.12(a) shows the DC response of a system, where we measure the optical power as a function of input voltage. Figure 3.12(b) shows the open-loop response a function of frequency in a Bode plot of the transfer function of the open-loop system. Here we plot both gain $|G|$ and phase ϕ of the output signal relative to the input signal. When the phase offset is $-\pi/2$, the output is completely out of phase with the input.

The feedback circuit corrects differences between the input set point voltage and the output voltage of the system. It has its own transfer function, and the multiplicative effect of the two transfer functions should have maximum gain at DC and unity gain once the signals are $\pi/2$ out of phase, because any feedback at higher frequencies would drive the system away from the desired set point.

Analog feedback systems are linear systems, meaning that they have the same transfer function regardless of the input voltage. This means that stabilizing a system that responds

linearly in voltage is possible for all input voltages. However, if the response of the system isn't linear, then optimal feedback is only achieved in a limited range of set voltages, limiting the dynamic range of the system. The feedback circuit uses integral feedback, and the circuit design and PCB are included in appendix E. An integrator loop is maximum at DC and drops by 10 dB per decade in power, and 20 dB per decade in voltage.

Open loop system

In the feedback loop I have described, the beam passes through an acousto-optic modulator (AOM), which does not respond linearly in voltage. The deflected intensity is

$$I/I_0 = \sin^2\left(\pi/2\sqrt{P/P_0}\right) \tag{3.8}$$

$$\sim \pi^2 P/(2P_0) - ... \tag{3.9}$$

where I is the deflected intensity, I_0 is the incident intensity, P is the RF drive power and P_0 is a parameter that depends on the wavelength of light and properties of the crystal. The efficiency is roughly linear in drive power, and thus quadratic in voltage.

The open-loop system can be built using a mixer from Minicircuits to combine the input signal with the RF signal that drives the AOM. The intensity is then measured on a photodiode, which produces a current that is linear in optical power, so that the measured voltage scales linearly with the optical intensity. The transfer function of this system is shown in Fig. 3.12(a) and 3.12(b). Every element in the system responds linearly in input voltage except the AOM, so the result is a DC response that is quadratic in input voltage. The feedback system can't be optimized at both 1 mW beam power and 1 W beam power.

This is always a problem when using an AOM to control beam intensity, for both ODTs and lattice beams. The typical solution for an ODT is to optimize feedback at the final trapping beam power, at the cost of beam power fluctuations throughout optical evaporation used to create the condensate. While this is a reasonable method to create a high number, low temperature condensate, it is not ideal for our experiment.

We elected to linearize the signal in analog for two reasons. The first is that our lab has expertise in analog feedback systems, and we were concerned about adding electronic noise to the system with an arbitrary VGA. The second is that we were bolstered by successes in another experiment in our group, E4, where they created a condensate with a record low entropy per particle shortly before we started working on this project [17]. Their success required only a Hamamatsu IR-enhanced Si PIN photodiode (S11499-01) and a strong signal of atoms with which they could determine the optimal feedback parameters at the very low powers used to hold their BEC. They compromised feedback parameters at higher power, and swept through particularly noisy regions of intensity rapidly enough to reduce atom loss.

Our detector is designed with the same enhanced silicon photodiode, but connected it to a logarithmic amplifier (Analog Devices AD8304), so that the voltage out of the photodiode is proportional to $\log V^2 = 2\log V$. The error signal is then proportional to the log of the
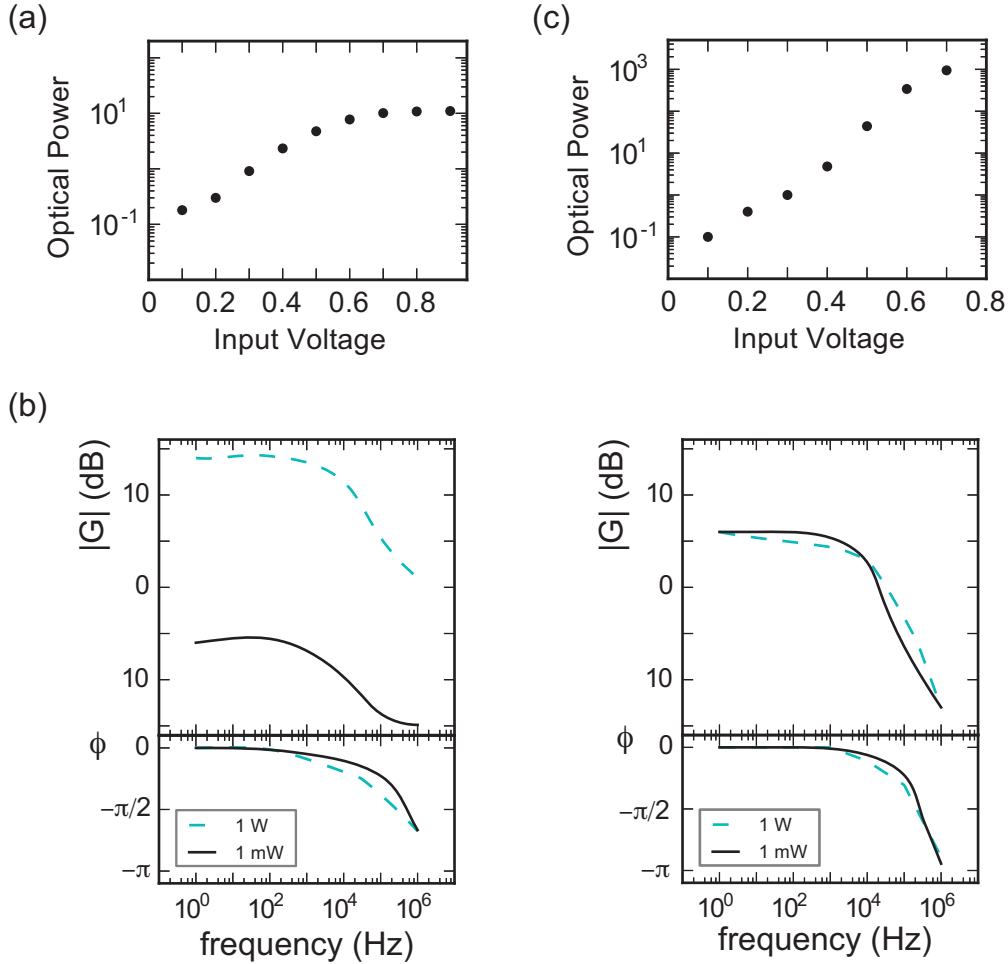
Figure 3.12: Open loop response functions of the feedback systems. (a) The DC response of an open-loop system that uses a mixer, an AOM and a linear photodiode. (b) Because the optical power is not linear in set point voltage, the transfer function differs at high and low optical powers. This means that a feedback circuit can only be optimized in one of these two limits. (c) The DC response of an open-loop system that uses an exponential amplifier, AOM and logarithmic photodiode. The open-loop response is linear across a broad range of optical powers. (d) The optimal feedback parameters are the same at high and low optical powers.

power in the beam. It is combined, not with a mixer, but with an exponential amplifier (Analog Devices ADL 5330) with the RF signal from the VCO, so that the signal going into the AO is proportional to V. The result is plotted in Fig. 3.12(c), where the optical power is linear-in-log over approximately three orders of magnitude in beam power. This means that the open-loop gain and phase of the system is the same at high or low optical power, as shown in Fig. 3.12(d).
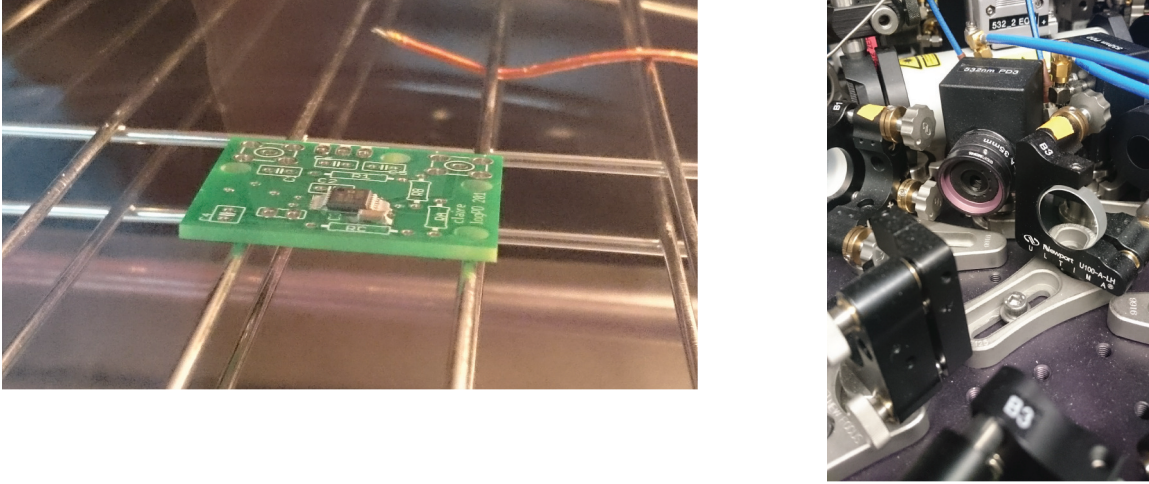
Figure 3.13: Images of logarithmic photodiode during and after construction. Left: The logarithmic amplifier is surface mounted to a PCB in a toaster oven. The circuit design is detailed in appendix E. Right: The photodiode in use after construction.

The photodiode circuit required surface mounting the AD8304, which we did in a toaster oven in the lab. The left image of Fig. 3.13 shows the circuit as it toasts, just before the solder is wicked, and the image on the right shows the constructed photodiode used in our system.

Finally, we calibrate the photodiodes by measuring beam power as a function of set point. This must be repeated regularly, after alignment, because the prefactor changes based on the amount of light that is picked off or going into the photodiode. The exponential slope for a given photodiode is given by its construction. Calibrations for the 532-nm lattice beams are shown in Fig. 3.14.

Closed-loop system

The requirements for the new photodiode and amplifier system necessitated modification of our analog feedback boards. Circuit diagrams and technical details for the photodiode and feedback boards are included in appendix E.

To test the closed-loop feedback system, we monitored the closed-loop system and looked at amplitude noise suppression while driving it with 'artificial noise' across a broad band of frequencies with the spectrum analyzer. We measured 10 dB suppression up to 30 kHz. Next, we setup a "spy photodiode" to monitor noise on the closed-loop system. This test is sensitive to any electronic noise added to the system by the new photodiode. The laser we used had very low intensity noise, except for at low frequencies, where we measured 20 dB
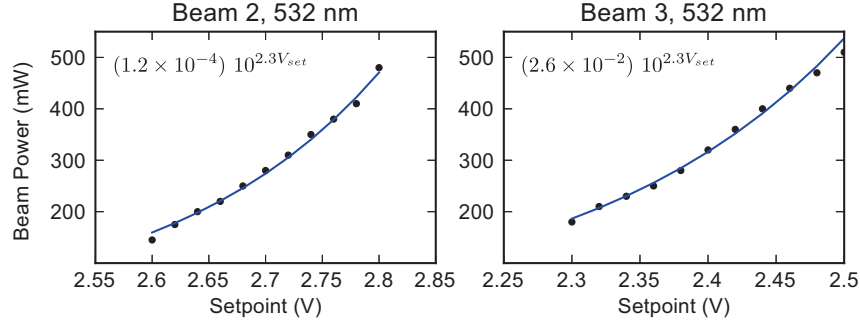
Figure 3.14: Calibrating the photodiodes. Each photodiode is calibrated by disabling intensity stabilization, sending a control voltage directly into the exponential amplifier, and measuring the voltage on the photodiode. This is compared to a measurement of the optical power in the lattice *beam* (not the pickoff), P_{opt}. The signal is fit to the curve $P_{opt} = P_z 10^{V_{out}/V_y}$ to determine the slope V_y and intercept P_z of each photodiode. The value of P_z depends on the pickoff percentage and the alignment into the photodiode. The design value for V_y is 400 mV/decade. Once calibrated, the slope of the circuit will not change, but the intercept is alignment-dependent and should be checked regularly to ensure precise knowledge of the correspondence between beam power and photodiode voltage.

suppression on the spy photodiode.

This system works effectively over at least three orders of magnitude in beam power, and this dynamic range can be extended by modifying the circuitry as explained in appendix E. The bandwidth of the system can be high, up to 100s of kHz, but the slew rate is fairly slow. The AD8304 has a slew rate of 15 V/μs, so that it takes 100 ns to respond to a ramp over three orders of magnitude in optical power. This is comparable to the AO response time, given by the speed of sound through the crystal and the size of the beam. Feedback for small fluctuations in voltage is limited by the bandwidth, where large changes in voltages are limited by the slew rate. As such, we cannot change the lattice beam power from minimum to maximum in less than a few hundred nanoseconds.

3.7.2 Phase

For all four interferometers, beam 2 is the reference beam and is modulated at high frequency with a modulation depth of $\sim 1\%$ using an electro-optic modulator (EOM). The beat signal measured on each of the four photodiodes is demodulated at the modulation frequency to measure the phase difference between bean 2 and the other beam. The error signal is fed back into the AOM modulation frequency to correct the phase of beams 1 and 3, so that they each match the phase of beam 2 and each of the lattices is stationary in space. The phase of each lattice is determined by the interferometer. The wedge window in the path of the interferometer provides a differential phase shift for the 532nm light relative to the 1064nm light, so that the relative phase of the lattices is tunable.

The feedback scheme is similar to that described in section 2.2.2 of the thesis of Daniel Greif from ETH Zurich, and the specifics of our setup will be explained in more detail in the forthcoming thesis of Thomas Barter.

3.8 Using the quantum simulator

The steps to align the system are outlined in this section and are performed daily.

3.8.1 Bose-Einstein condensate

The early stages of cooling produce 10^8 rubidium atoms in the $|1, -1\rangle$ state at a temperature of $300 \, \mu$ K at the location of the glass cell that are confined by a magnetic quadrupole trap generated by the Feschbach coils. When we align our system, we start by creating the 'ODTa condensate' in the hybrid trap shown in Fig. 3.7(b).

The procedure for aligning the trap is as follows. We first take an image of the gas from the top, in 'top-down imaging', to ensure that ODTa crosses through the magnetic trap center after the atoms are transported into the glass cell. During decompression the magnetic trap center will move slightly. We tune the bias field in all directions in order to maintain a constant relative position between the beam and the magnetic trap. We have found that if everything is well aligned, the gas does not move substantially in the North-South direction.

We align the optical trap to optimize the number of atoms in the final BEC. We generally find that this optimal location is below the magnetic field zero by roughly one to two beam waists, where $w_0 = 50 \, \mu$m.

We then decompress the magnetic trap, lowering it until it just compensates gravity. We use forced RF evaporation to cool the atoms until they experience the optical trap. To reach Bose condensation, we tighten the confinement along the direction of beam propagation by tuning the Up/Down bias field, bringing the quadrupole zero closer to the optical trap.

3.8.2 Transfer into crossed dipole trap

The next step is to transfer the BEC into a crossed dipole trap.

We take an in-trap image of the ODTa condensate and mark its position. We align ODTb so that it crosses that point. To fine tune the ODTb alignment, we transfer atoms from ODTa to ODTb, by reducing the ODTa power while increasing the power in ODTb. We measure and optimize the number of atoms transferred into ODTb.

After alignment is complete, the BEC can be transferred into the crossed dipole trap formed at the intersection of ODTa and ODTb beams. If the Up/Down bias field is not properly handled during transfer into the crossed dipole trap, it is possible to have a competition between the hybrid trap and the crossed dipole trap, which makes for confusing trap frequencies and data in two nearly-overlapping traps.

A complete description of the up-down Helmholtz coils is shown in Fig. 3.8.

Optical dipole trap parameters

Ultracold atoms at the bottom of an optical dipole trap are modeled as a harmonic oscillator. To measure the trap frequencies, we pull the atoms away from the center and release them, then measure their position as a function of time. We move them using a sudden change in the magnetic bias field, which moves the zero of the quadrupole field. Figure 3.15 shows measurements of the trapping frequency for different settings of the optical trap. In Fig. 3.15(a), we measured the trap frequency in the x direction $\omega_x = 18$ Hz at the lowest power of our ODTs. In Figs. 3.15(b) and 3.15(c) we simultaneously measure both in-plane trap frequencies for the gas with and without the vertical lattice. To measure both trap frequencies, we move and measure the position at an angle relative to the $\hat{x}$ and $\hat{y}$ directions. These data show the trap frequencies when the ODT power is increased to a power near the one used in our experiments. They also show the increase of the in-plane trap frequencies when the vertical lattice is imposed.

To measure the trapping frequency in $\hat{z}$, we reduce the magnetic field gradient for a short time, thereby releasing the atoms from the trap. We measure the oscillation in the $\hat{z}$ direction by imaging from the side. We repeat this procedure for many different values of the Setpoint of the ODTs, and the results of these measurements are datapoints shown in Fig. 3.16(a). The curves represent the expected scaling of trapping frequency given the calibration of the ODT photodiodes.

These trapping frequencies correspond to a central filling in the lattice potential that is shown in 3.16(b) as a function of total atom number. Our experiments of Mott insulator physics that are described in chapter 5 were performed with atom number $\sim 10^5$, and an ODT setpoint of 2.2V, so that our central filling was ~ 1.5, which is the tip of the $n = 2$ Mott lobe.

3.8.3 Align the vertical lattice

After the ODTs are aligned, we align the vertical lattice. The vertical lattice is a one-dimensional lattice formed by a retro-reflected beam of 1064-nm light propagating along $\hat{z}$. The beam passes through and EOM, an AOM, an optical fiber, and a telescope before it is focused onto the atoms. There are mirrors in the path of the telescope that should not be used for alignment. There are mirrors before and after the telescope that should be used to align the beam to the atoms.

To align the vertical lattice, we first use the recorded in-situ position of the crossed dipole trap that was taken with top-down imaging. We block the retroreflecting mirror to align the first pass of the beam through the atoms. We create a diffuse cloud of atoms and shine the vertical lattice beam onto the cloud. The focus of the beam acts as a weak optical-dipole trap, and an increased density of atoms is detected at the location of the beam. This is aligned to the recorded in-situ position of the crossed dipole trap. The beam then travels through the glass cell, and onto an upper breadboard, where it is retro-reflected and refocused onto
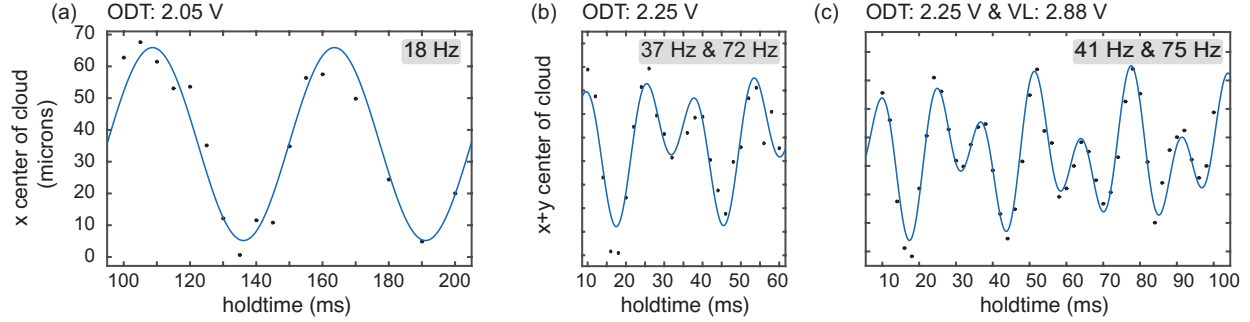
Figure 3.15: Trap Frequencies are measured by moving the atoms away from the trap center by moving the magnetic quadrupole trap center using bias fields. After the displacement the gas is held in the trap for a variable amount of time, during which it oscillates in space. Atoms are released from the trap before imaging with absorption imaging. The displacement is measured as a function of time. (a) Trap frequency measurement data along $\hat{x}$ for the BEC in a crossed optical dipole trap with magnetic compensation against gravity. The trapping frequency in $\hat{x}$ of $\omega_x = 18$ kHz. In the future, this trap can be used to create a low-density optical lattice. (b) Trap frequency measurements after moving the field in both the $\hat{x}$ and $\hat{y}$ directions, and measuring the position at an angle to the cardinal axes of the trap provides a measurement of both ω_x and ω_y in one measurement. These data show the trap frequencies when the ODT power is increased to a power near the one used in our experiments. They also show the increase of the in-plane trap frequencies when the vertical lattice is imposed.

the atoms. This second pass interferes at the atoms with the first pass, forming a vertical lattice that can be aligned using Kapitza-Dirac diffraction.

To align the second pass of the vertical lattice, we switch imaging systems and image the cloud from the side. We expose the Bose-Einstein condensate to the retro-reflected lattice for a short time τ, which leads to Kapitza-Dirac diffraction of the atoms. During this pulse, atoms exchange momentum with the lattice photons. Atoms are then released from the trap and they expand with the momentum they have acquired before they are imaged with absorption imaging. We detect the atoms that have exchanged momentum with lattice photons. The Kapitza-Dirac effect is discussed further in chapter 4. For a short pulse, a deeper lattice results in higher population of diffracted atoms. To align the lattice, we tune the retro-reflecting mirror to maximize the number of atoms diffracted by the Kapitza-Dirac pulse. Finally, we return to top-down imaging to ensure that the vertical lattice has not distorted the optical trap, which would indicate a problem with alignment that likely stems a misalignment of the first pass of the vertical lattice.

After the vertical lattice is aligned, we return to side-imaging to calibrate the lattice as described in chapter 2. In brief, we load atoms into the vertical lattice and modulate the intensity of the beams to promote atoms to a higher energy level. We then ramp the lattice down in a few ms, which maps the quasimomentum of the atoms to real momentum, and take an absorption image in momentum space. By varying the frequency of modulation and
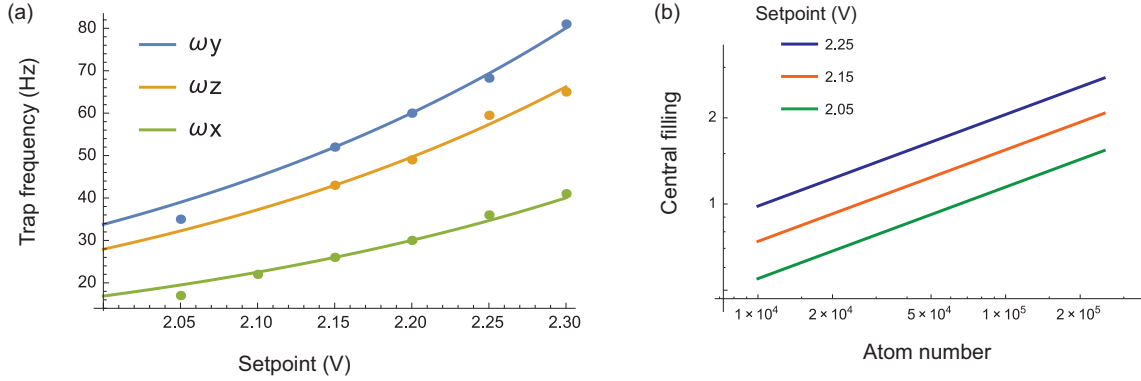
Figure 3.16: Measured trapping frequencies (circles) for different ODT setpoints, and their expected scaling (curves), with an exponential slope of 2.5. (b) Expected central filling in the lattice as a function of trapping frequency as a function of total atom number.

finding a resonance, we determine the level-spacing of the lattice. This spacing is lattice depth dependent, so that we can determine the correspondence between laser beam power and lattice depth.

In our two-dimensional lattice experiments, we work with a vertical lattice depth $V_\perp/h = 41$ kHz, which typically corresponds to a setpoint of 2.88 V. The gas is thus divided into two-dimensional planes with a single-atom tunneling rate of 5 Hz.

3.8.4 Align in-plane lattices

Next, we align the triangular lattices.

1064 nm lattice

The 1064-nm lattice is easy to align because the ODTs, which are already aligned, co-propagate with two of the lattice beams. We overlap lattice beam 1 with ODTa at the location of the focusing lens, and at the location of the atoms (using the side-imaging camera). We repeat this process for beam 3 and ODTb. Beam 2 propagates through the vacuum chamber, and its position is recorded on a camera. The 1064-nm beams rarely require alignment because they are fiber coupled and have few elements between the fiber output and the atoms.

After they are aligned, we load atoms into the honeycomb lattice with roughly the same optical power in each beam and release them from the trapping potentials in time-of-flight imaging. To load the lattice, we ramp on all three lattice beams with a base-ten exponential increase in beam power by increasing the set point voltage to the logarithmic photodiode by about 0.6 V at a rate of 5 mV/ms, so that the total load time is roughly 100 ms. We measure the symmetry of the diffraction pattern, comparing the number of atoms diffracted to each of
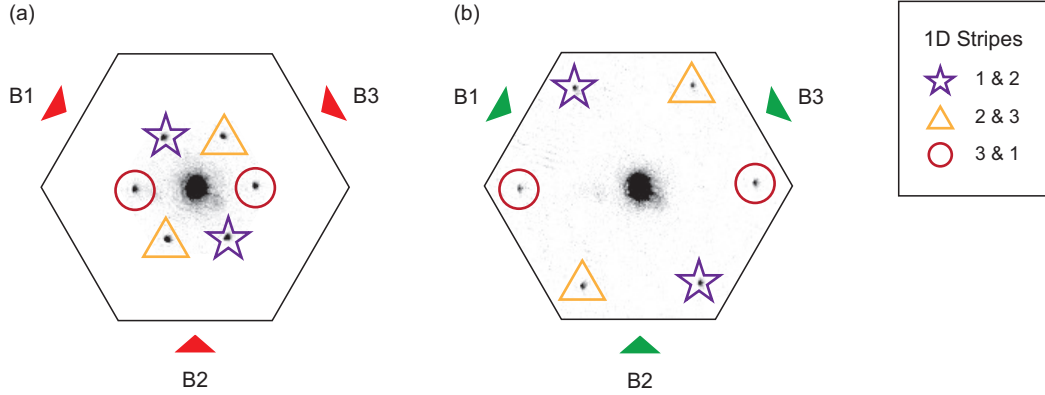
Figure 3.17: The number of atoms diffracted along each lattice vector is determined by the lattice depth along that axis. The three beams of each constituent lattice are indicated by red (1064 nm light) and green (532-nm light) arrows. Any two beams alone form a one-dimensional stripe lattice along the vector sum of the lattice beams. For example, beams 1 and 2 alone will create peaks indicated by purple stars. Well-aligned lattice beams create a diffraction pattern that is nearly six-fold symmetric. Small misalignments or differences in beam profiles are adjusted by tuning the power in each beam so that the number of atoms diffracted in each of the three directions is equal. The process is the same in the honeycomb lattice formed by light at the wavelength 1064 nm (a), and in the triangular lattice formed by light at wavelength 532 nm (b). The percentage of first-order diffracted atoms along each one-dimensional stripe direction is measured. In either lattice, after following this procedure and averaging data for ten images, $33\% \pm 0.03\%$ of the number of atoms in the first-order peaks are diffracted along each of the three stripe directions, where the error quoted is the standard error in the mean.

the six diffraction peaks. To balance the diffraction of atoms to each of the momentum space basis vectors, and thus balance the tunneling rates along each real-space lattice vector, we follow a procedure described in Fig. 3.17(a). Each pair of beams is responsible for diffraction along one of the basis vectors. If there is an imbalance in population of atoms diffracted along one axis, it is due to an imbalance in lattice depth along two real-space lattice vectors. The difference may be due to a slight misalignment of the beams, or due to a small difference in beam-waists and thus lattice depths. The imbalance is adjusted by changing the relative powers in each of the beams. For example, if diffraction along the direction formed by the interference of beams 1&2 is weak relative to the other two directions, then the power in beam 3 can be reduced so that the population of atoms diffracted in all directions is equal. We typically achieve symmetry of $33\pm0.03\%$ over 10 datasets, where the error is the standard error in the mean.

Finally, we load atoms into the honeycomb lattice formed by the 1064-nm light and calibrate the depth by modulating the intensity of the beams to promote atoms to upper bands. This procedure is detailed in chapter 2.

532 nm lattice

Though they follow the same paths, the 532-nm lattice beams don't exactly co-propagate with the 1064-nm beams because as they experience differential dispersion when they travel through optical elements (namely the glass cell). Beams 1 and 3 enter the glass cell at 60° angles, so the 532-nm beam is displaced from the 1064-nm beams. Beam 2 enters the cell at a normal angle of incidence, so it can be aligned to co-propagate with the 1064-nm beam 2 for preliminary alignment.

We have cameras and have recorded the displacements between the 1064-nm beams and the 532-nm beams. Aligning the 1064-nm lattice first and then aligning the 532-nm lattice to these displacements has had limited success.

Rubidium atoms are repelled from the focus of a 532-nm laser beam. To align the lattice, we align each beam to the location of the crossed-dipole trap (i.e. the in-trap BEC). We take an in-trap image of a cloud of atoms filling one of the two ODT beams, shown in Fig. 3.18. Then we impose a single beam of 532-nm light, which repels atoms from one point of the trap. A deficit of atoms in an in-trap image indicates the location of the intersection of the 532-nm beam with the ODT. The 532-nm beam is then aligned to the in-plane position of the in-trap BEC, and the out-of-plane (up/down) position of the beams are aligned by maximizing the contrast of the cuts.

After aligning each 532-nm lattice beam to the correct position, we load atoms into the 532-nm triangular lattice and check the balance of the beams as shown schematically in Fig. 3.17(b). We achieve the same symmetry of the triangular lattice as we did for the honeycomb lattice, where $33 \pm 0.03\%$ of atoms are diffracted along each of the three k-vectors. Finally, we calibrate the depth of the 532-nm lattice as described in chapter 2.

Bichromatic lattice

Finally, with both constituent lattices aligned and calibrated, we load the bichromatic lattice by ramping on the vertical lattice and both in-plane lattices simultaneously. The displacement of the two in-plane lattices is determined by the thickness of the glass wedge that is in the path of the interferometers. We scan along either path until we create the desired bichromatic lattice structure.

The glass wedges allow us to scan along the one-dimensional lattices formed by beams 1 and 2 and beams 3 and 2. In each interferometer, beam 2 passes through a pair of wedged windows. One wedge is mounted on a translation stage, and the actuator is controlled in software. The actuators determine the thickness of glass traversed by the beams, which determines the relative phase shift of the two lattices, as described in Fig. 3.5.

Actuator 1-2 changes the balance of number of atoms diffracted to the one-dimensional stripes that involve beam 1: the 1-2 stripe and the 1-3 stripe. This data shows a scan along actuator 1-2 as the bichromatic lattice is tuned between a 1&3 stripe lattice and a 1&2 stripe lattice. Actuator 1-3 interchanges the number of atoms diffracted to beams involving beam
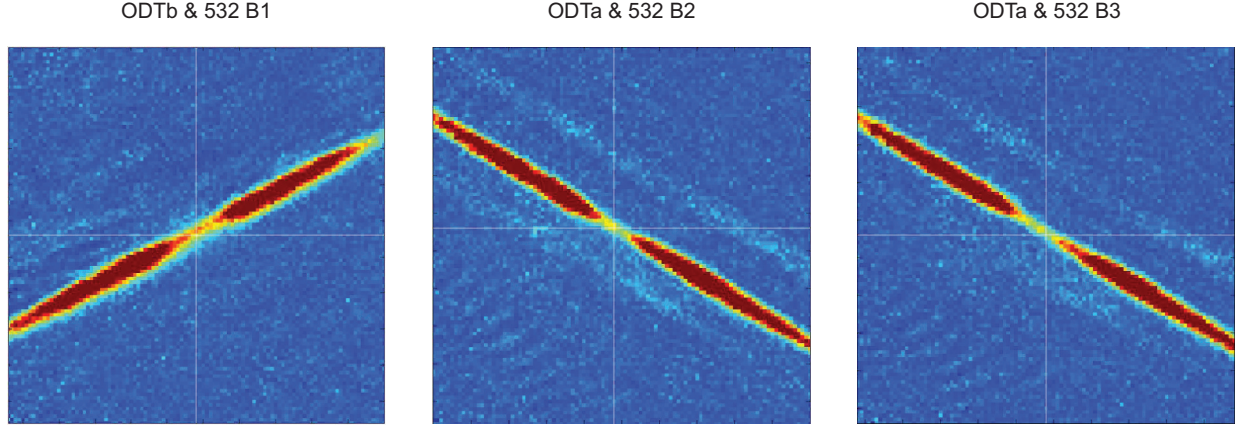
Figure 3.18: Aligning the 532-nm lattice. Atoms are loaded so that they fill an optical dipole trap, and one beam of the 532-nm lattice is imposed before an in-trap absorption image. Atoms are repelled from the focus of the 532-nm beam, and the cut in the cloud indicates the overlap of the 532-nm beam and the ODT. The in-trap position of the crossed-dipole trap is recorded, and is indicated by the crosshairs in these images. The 532-nm beam is aligned to cut the cloud at the position of the cross of ODTa and ODTb. Beam 1 (left image) travels along the same direction as ODTa, so atoms must first be transferred into ODTb in order to cut the cloud. Similarly, beam 3 (right image) is used to cut ODTb. Beam 2 (center image) can be used with either trap.

3: the 1-3 stripe and the 2-3 stripe. To create the kagome geometry, we balance populations along all three directions to create a six-fold symmetric lattice.

The procedure is as follows. We first scan Actuator 1-2 until we create a lattice that is balanced in the direction of the lattice formed by beams 2 and 3. From that point, we scan Actuator 2-3 until we form the kagome lattice. From the kagome lattice, we can scan either interferometer to shift between the kagome lattice and the decorated stripes, as in [13].

Note that the diffraction pattern of the kagome lattice has the same symmetry as that of the decorated triangular lattice. After we find the kagome lattice, we check the ratio of zero-, first- and second-order diffraction (see chapter 2 and appendix A) to ensure that $\tilde{P}_i \sim 1/9$ and the diffraction is from the kagome lattice configuration, rather than the decorated triangular configuration.

3.9 Stability

3.9.1 Hourly stability after warmup

Currently the biggest challenge in the setup is a drift of beams over the course of the first few hours of the day. The timescales indicate that the problem relates to the temperature in the room, which increases in the first four hours after turning on the oven and lasers. If a
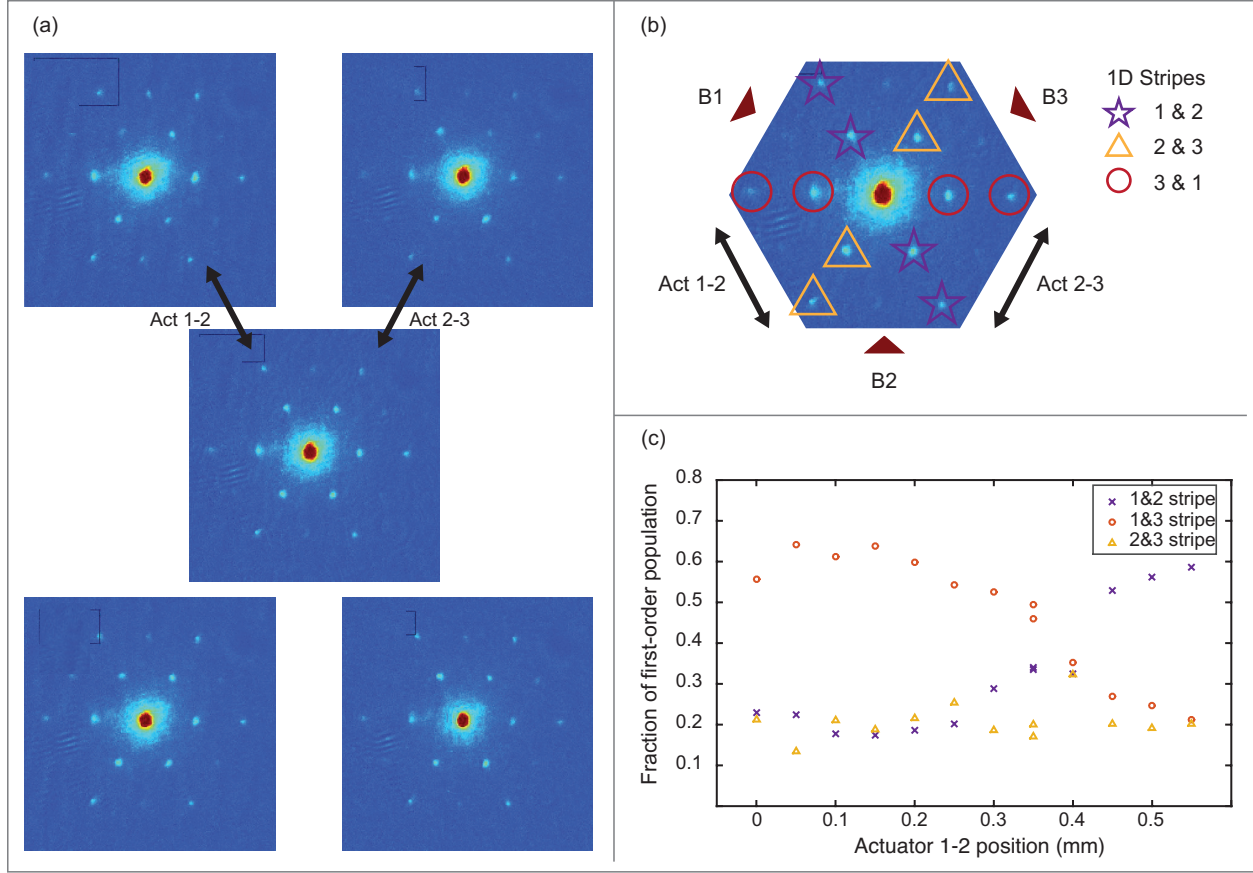
Figure 3.19: Scanning the bichromatic lattice. (a) Images of the bichromatic lattice when the relative position of the underlying lattices is slightly offset from the kagome configuration can be helpful when the lattice is nearly aligned. (b) Three lattice beams, indicated by deep red arrows, intersect at equal angles to form the bichromatic lattice. Any two of the three beams will form a one-dimensional stripe lattice, along the vector sum of the lattice beams. To shift the relative position of the lattices along the axis of the one-dimensional stripe formed by beams 1 and 2 (purple stars), we actuate a wedge window that is the beam 2 path of the Mach-Zehnder interferometer with beam 1. Actuator 2-3 controls the phase along the yellow triangles. These two actuators span the full lattice space. (c) Data represent the fraction of atoms along each lattice axis, normalized to the total population of first-order peaks, and are plotted as a function of the setting of actuator 1-2, measured in mm. The data show that translating the wedge by 0.5 mm shifts the diffraction asymmetry from being dominant along the beams 1&3 stripe axis and the beams 1&2 stripe axis. The observed half-period oscillation represents a translation through half of the unit cell, which is consistent with the calculation of wedge displacement in Fig. 3.5.

beam of one of the in-plane lattices drifts after the alignment procedure, the shift will affect

the lattice depth along the two lattice directions relevant to that beam. The result is an imbalance in lattice depths, and thus an imbalance in the diffraction peak populations. This can be corrected either by realigning the beam, or by re-balancing the power in each beam to compensate for slight misalignments.

The problem is that, after we balance the diffracted population of each individual lattice using beam powers, we balance the bichromatic lattice using the wedge windows. If a constituent lattice is not balanced in power, there is no setting of the wedge windows that will result in a diffraction pattern with the proper symmetry. We have wasted hours trying to create a symmetric kagome lattice diffraction pattern only to realize that the underlying lattices are not properly balanced because of this slow morning drift of the beams. After the beams have settled, we must re-balance and re-calibrate each lattice.

Because it happens in both lattices, and the 1064-nm lattice pointing is very stable, we suspect that the ODTs are drifting. ODTb has been fiber coupled very recently. ODTa has very high power and cannot be fiber coupled. ODTa should be aligned to the 1064-nm beam 1, rather than the other way around.

This drift manifests as a shift in lattice geometry. If we are looking at the bichromatic lattice signal, we have often suspected a relative drift in the two color lattices as responsible for the apparent shift in geometry. This leads to a lot of time wasted trying to balance the lattice by shifting the lattices relative to one another, when really there is an imbalance in one or both of the constituent lattices.

We find that this drift stabilizes after the first two hours of working with the lattice. Every hour throughout datataking we check the symmetry of the diffraction pattern of each constituent lattice as well as the bichromatic lattice. We find that they do not require re-balancing or re-alignment for 5-6 hours of data taking.

We measure the balance of diffraction into the three directions with a method similar to that described in Fig 3.19(b) for both the kagome lattice and the triangular lattice, but here we use the outer peaks to measure the balance. After the lattices are aligned and balanced, we measure the fraction of atoms diffracted into each of the three directions. Superfluid images from throughout the night are analyzed, and the RMS deviation from 33% population in each direction is 2.6% in *both* the kagome and the triangular lattices. This indicates that, not only are the lattice beams stable in pointing, but also the phase offset between the two lattices is stable enough that a population imbalance due to their offset is below the resolution of this measurement. If we ascribe the full 2.6% deviation to a drift in geometry, it would mean that the nodes are overlapped to within 18 nm.

We re-calibrated the lattice depths every hour and found that they were stable to within 0.7% over the course of data taking.

3.9.2   Heating and lifetime of trapped atoms

We achieve a BEC lifetime of ~ 20 seconds with our intensity stabilization system. The lifetime in the vertical lattice is 4.5 seconds. The lifetime in the in-plane lattices is 1 second with or without active phase stabilization.
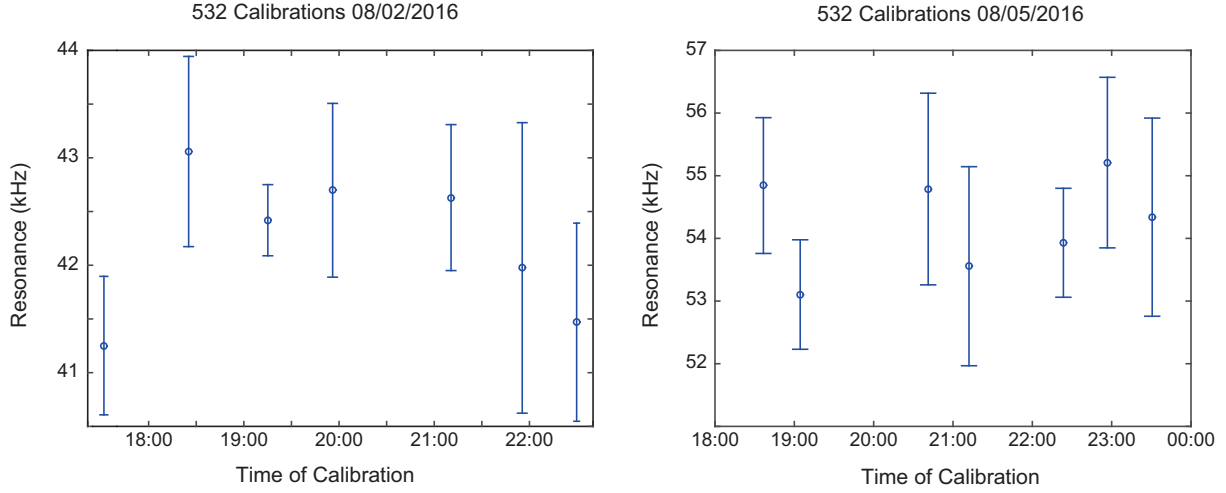
Figure 3.20: Calibrations throughout an evening of taking data. The lattice depth is stable over the course of hours. Data indicate the measured resonance frequency, and error bars indicate width of the resonance. Data from 08/02 are particularly stable, the spread in the resonance frequencies is consistent with the width of the measured resonances. The calibrations that night have a standard error of just 0.7 %. The measured resonances on 08/05 were broader and less stable.

We measure heating of atoms in the two-dimensional lattices by loading a Bose-Einstein condensate into a lattice, holding them there for 30 ms, and then reducing the in-plane lattice potentials to measure the reduction in condensate fraction due to heating in the lattice. When loaded into a shallow optical lattice, the condensate returns to the initial condensate fraction. When we load into the deepest optical lattices used for our experiments, where $V_{532} = 100$ kHz, we find that atoms that were held in the kagome lattice return to 90%±6% of the initial condensate fraction, where atoms in the triangular lattice return to 92%±8%. The likeness of these heating measurements indicates that our phase feedback system effectively stabilizes the two lattices relative to one another, and the bichromatic lattice does not experience significantly more heating than the monochromatic 532-nm lattice.

3.10 Revisiting the specs

1. Pure Bose-Einstein condensates produced in under 20 seconds

   a) The hybrid trap enables rapid (for our system) condensate production

   b) Tilt evaporation gives fine control over final atom number

2. Loose optical confinement, $\bar{\omega} < 30$ Hz to achieve $n \sim 1$ atom per site

    a) Our measured trapping frequencies and atom numbers allow for filling in the lattice of either $n = 1$ or $n = 2$.

    b) We performed experiments with $n \sim 1.5$

    c) The challenge in performing experiments with $n = 1$ related to thermal lensing in the AOMs used for 532-nm light. Moving to lower fillings will be straightforward now that the AOMs have been exchanged for others with less thermal lensing, but careful calibrations of trapping frequencies will be required to ensure that the trap frequency is constant at all lattice depths.

3. Lattice beam intensities actively stabilized over three orders of magnitude in beam power.

    a) This is achieved using logarithmic photodiodes and exponential amplifiers in the intensity stabilization of all beams.

4. Alignment procedure should take less than 1 hour

    a) By co-propagating the ODT beams, fiber coupling the 1064-nm lattice beams, and having cameras to monitor the beam positions, alignment of the 1064-nm lattice system takes fewer than 20 minutes

    b) The 532-nm lattice alignment can take more than 1 hour. We had inconsistent success in using cameras for this alignment, and had to fall back on using the atoms. This will be easier with larger 532-nm lattice beams.

5. Alignment should last for more than 1 hour; or a full day with minor adjustments

    a) At the beginning of the day, the ODT beams, which propagate in free space, drift, leading to an imbalance in the lattice diffraction.

    b) That drift requires minor adjustment after a few hours of running.

    c) After this drift, the system is stable for more than 5 hours of data taking.

6. Bichromatic lattice beams are commensurate over the spatial extent of the gas

    a) This is easily achieved without frequency referencing the lattices relative to one another.

7. Relative phase of the two lattices is stable and controlled in software

    a) The lattices are passively stable because of the optics design. Without phase stabilization the lifetime of atoms trapped in the in-plane lattices is $\tau \sim 1$ second. The vertical lattice reduces this lifetime.

    b) The relative phase is controlled with two Mach-Zehnder interferometers where one lattice beam acts as a reference for the other two.

c) The relative phase of the two lattices is controlled by passing the beams through a variable thickness of glass, where they acquire a differential phase shift. The thickness of wedge traversed is controlled in software.

3.10.1 Summary of recommended machine improvements

There were a few major drawbacks of the system as of the last experiment described in this thesis. The first is the drift of the laser beams that occurs in the first few hours of use. It took us a long time to realize that it is the ODT that drifts. Before we realized that, we would recommence the alignment procedure, aligning everything to the atoms (ie. to the new ODT position), rather than aligning the ODT beams to the already overlapping positions of all of the other 9 beams. We know that it is the ODT that drifts because the 1064-nm lattice beams are fiber coupled, and we see the same imbalance in either lattice after the drift.

The second drawback is the thermal lensing in the AOMs used for the 532-nm lattice beams. The beam waists were much tighter than planned at the location of the atoms. Originally, we planned to have 532-nm beams with gaussian waists that were twice the waists of the ODT beams. This would enable work with low trapping frequencies for the full range of lattice depths. We could compensate the change in trap curvature from the 532-nm beams by increasing the power in the red-detuned ODT beams. To mitigate the problems posed by tight 532-nm lattice beams, we tightened the trapping potential from the ODT. Effectively, the ODT beams pin the atoms at a given position and are tight enough to dominate the curvature of the trap for all powers of the 532-nm lattice beams. This meant that we didn't need to worry about the delicate balance of powers in compensating trapping frequencies, but also resulted in a higher than originally desired central filling.

Third, the in-plane lattices are passively stable because of the care that was taken to equalize the beam path lengths between the laser source and the atoms. However, the path lengths to the interferometer detection differs because the pickoff that sends beam 2 to the interferometers is before the atoms. The beam 2 path is ~ 20 cm shorter than the other paths. I think this is why our phase feedback does not lengthen the lifetime of atoms in the lattice. We find that phase stabilization with high gain heats the atoms, and this is likely because we are mapping phase noise detected at the photodiode onto the atoms. Currently we use very low gain to stabilize the lattices relative to one another, but it does not provide added stability and longer lifetime of atoms in the lattices.

Fourth, the vertical lattice doesn't have a robust phase stabilization system, so that the lifetime of atoms in the lattice is sometimes limited by the vertical lattice lifetime.

Finally, the Nufern amplifier used for the 1064-nm light regularly died and needed to be replaced with a spare. We are very good at replacing the Nufern, and are now able to recover the lattice within 2 days of replacing the Nufern. As impressive as it is, this is not a skill I want to have.

Several of these issues have already been addressed in the lab. The lower power, ODTb beam, has been fiber coupled, so that the only beam that can drift is ODTa. ODTa will

henceforth be aligned to the lattice beam position. The AOMs for the 532-nm light have been replaced with new ones that have substantially less thermal lensing. The 532-nm beams are also likely to be fiber coupled. Finally, after the most recent death of a Nufern, it will very soon be replaced with a Mephisto source.

Chapter 4

Characterizing an optical honeycomb lattice

This chapter supplements the publication included in Appendix appendix B in which we developed a sensitive matter-wave diffraction technique to characterize a honeycomb optical lattice with a small offset in energy among the two sites in a unit cell. The technique is analogous to x-ray diffraction from solids, except we may tune the interaction time between the matter-wave and the lattice. We find that tuning this time leads to strong enhancement of the effects of a slight lattice asymmetry, which we explain theoretically using two different perturbative treatments:

- *C. K. Thomas, T. H. Barter, T.-H. Leung, S. Daiss and D. M. Stamper-Kurn, "Signatures of spatial inversion asymmetry of an optical lattice observed in matter-wave diffraction," Phys. Rev. A **93**, 063613 (2016).*

The first lattice that we built was the 1064-nm triangular lattice of intensity minima. As discussed in chapter 3, we aligned the lattice first co-propagating lattice beams 1 and 3 to the appropriate trapping beams that form the crossed dipole trap that holds the atomic cloud, ODTa and ODTb, respectively. Beam 2 was then positioned so that it passed through the center of the glass cell and out of the center of the window on the other side of the vacuum chamber. To check whether we had effectively aligned the optical lattice, we created a Bose-Einstein condensate in the $|F = 1, m_F = -1\rangle$ state of rubidium and exposed it to honeycomb lattice with depth $V_{1064}/h = 87$ kHz ~ 80 $E_{r,lattice}$ for a short pulse-time $\tau = 70$ μs.

During a pulse of the optical lattice, the atoms undergo stimulated absorption and emission of photons into each of the optical lattice beams. This process results in momentum transfer from the lattice beams to the atoms by the vector sums and differences of integer multiples of the reciprocal lattice vectors $\mathbf{G}_i$, where we use capital letters to indicate the reciprocal lattice vectors of the 1064-nm lattice light. By measuring atoms in momentum-space imaging, we separate atoms based on the momentum they have acquired during the interaction time τ.
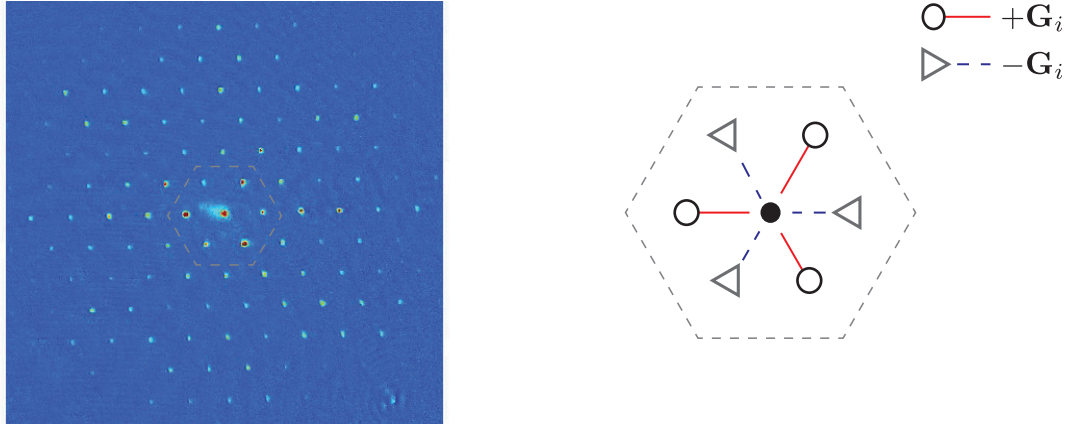
Figure 4.1: A matter-wave exposed briefly to an optical lattice potential and then released from optical confinement before absorption imaging produces a diffraction image (left). The matter-wave plays the role of x-rays in characterizing the crystal lattice potential. In this image, the underlying honeycomb lattice has a small inversion asymmetry ($\sim 2\%$ of the lattice depth), but the settings for the experiment reveal a large inversion asymmetry in the population of atoms diffracted to $\mathbf{G}_i$ and $-\mathbf{G}_i$, indicated in diagram on right.

We perform this experiment after alignment to test two aspects of the optical lattice. First, trigonal symmetry of the diffraction pattern indicates that the intensities of all the lattice beams are equal at the location of the atoms. Second, high order diffraction indicates a deep optical lattice. In a well-aligned lattice, each lattice beam will have its maximum intensity at the location of the atoms, and in a well-balanced lattice, each of those intensities is equal.

The first time-of-flight image that we took after preliminary alignment is shown in Fig. 4.1. It shows diffraction out to many orders, indicating that our alignment technique that takes just $\sim$10 minutes is very effective, where alignment of previous lattices in our lab had required use of the atoms and had taken hours. It also shows trigonal (C_3) symmetry – the image is unchanged under rotation by $2\pi/3$. However, we were puzzled by the apparent inversion asymmetry in the diffraction image. The first-order diffraction peaks show a clear asymmetry in the number of atoms diffracted to $\mathbf{G}_i$ and $-\mathbf{G}_i$, indicated in Fig. 4.1. [1]

The visiting master's student, Severen Daiss, suggested that this asymmetry may be due to the spin-dependence of the lattice for atoms in the $|F = 1, m_F = -1\rangle$ state of rubidium. The honeycomb lattice constructed using our technique (Fig. 2.1), with in-plane polarized beams, has opposite circular polarization at the location of each of the two sites in a unit cell, which we label A and B. Atoms in the $|F = 1, m_F = -1\rangle$ state of rubidium are sensitive to this difference in polarization via the ac Stark effect, but the resulting offset in energy at each site is very small, $< 2.3\%$ of the total lattice depth V_{1064}. Because the asymmetry is so small, we initially rejected the explanation that such a small asymmetry could give rise

---

[1]This chapter changes labeling of basis vectors relative to other chapters.

to such a large asymmetric signal, and we searched for other problems in our experimental setup to try to explain the apparent breaking of C_6 symmetry, i.e. rotations by $\pi/3$.

We quantified the first-order asymmetry with the parameter $\mathcal{A}$ of Eq. (4.1), and experimented with changing the interaction time τ. Our observations, plotted in Fig. 4.2, were even more puzzling. The asymmetry of the data is oscillatory, and described by multiple frequencies. We now understand this oscillation of asymmetry in momentum-space as arising from the interference of the Bloch states of an inversion-symmetric honeycomb lattice with a small inversion-asymmetric perturbation. The theory curve, with no fit parameters and only the lattice depth as an input parameter, is plotted in blue. For some pulse times in these data, the slight real-space inversion-asymmetry produces an enhanced signal in momentum-space.

$$\mathcal{A} = \frac{\sum_i p(\mathbf{G}_i) - p(-\mathbf{G}_i)}{\sum_i p(\mathbf{G}_i) + (-\mathbf{G}_i)} \tag{4.1}$$

and report a theoretical description of non-interacting particles diffracted by the pulse of the optical lattice, where the matter-wave acts as a sensitive probe of the optical lattice. We observe an oscillatory signal in the asymmetry $\mathcal{A}$ as we vary the pulse time τ. The data and the result of our theoretical treatments are plotted in Fig. 4.2, where the solid, blue theory curve has no free parameters and takes only the lattice depth as an input parameter, which was calibrated by other means.

Highlighted in grey are regions of our data where the theoretical treatment does not capture the signal and Fig. 4.2(b) shows the source of the discrepancy. The discrepancy is an artifact of the definition of the parameter $\mathcal{A}$ that we use to quantify our observations, which is normalized to the total first-order peak population. Our measurement $\mathcal{A}$ is thus least sensitive at points where the wavefunction has minimal population in the first order, and these are the points of maximum discrepancy between our theoretical treatment and experimental observations. This experiment represents a sensitive probe of the precise geometry and depth of the optical lattice to which the atoms are exposed.

We also believe that our theoretical description explains data published in other works in which a momentum-space asymmetry was observed in a Bose-Einstein condensate of two spin states of ^{87}Rb in the ground state of a honeycomb lattice potential formed by this same method. The data was interpreted as evidence of a "twisted superfluid" ground state of the optical lattice [18, 19], but we suggest that it was an artifact of the detection technique in which, effectively, the atoms were exposed to a pulse of an inversion-asymmetric lattice with an asymmetry and pulse time comparable to the parameters that result in the maximum observed momentum-space asymmetry in our data. This pulse was the result of the transient honeycomb lattice that repulsion from one atomic spin state creates for the second spin state just after the condensate is released from trapping potentials to expand in time-of-flight imaging.

This chapter describes how we came to understand the process by which a large asymmetry in the momentum-space signal emerges from a small asymmetry in the real-space lattice.

This work is published and is included in appendix B, and here the aim is to supplement the publication rather than repeat its findings.
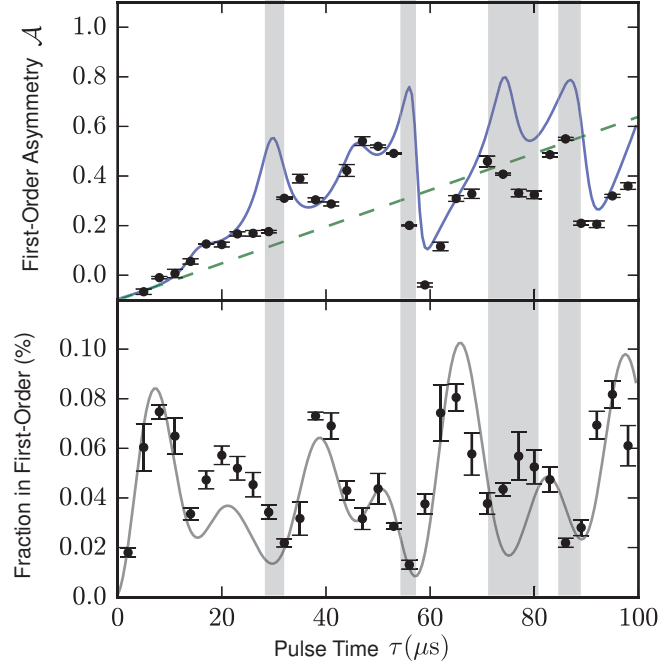
Figure 4.2: The asymmetry in momentum-space data is measured as a function of pulse time τ and the result of a calculation with no free parameters is shown in blue. The result of a simpler treatment, that does not take into account any kinetic energy of the particles during the pulse, is shown (green, dashed) and also agrees quantitatively with the short time behavior where this approximation is valid. The points of largest discrepancy between theory and experimental data occur near 30, 58 and 70-85 μs, where the total population of atoms in the first order peaks (the denomenator of $\mathcal{A}$) is at its minima. The lower plot shows total population in the first-order peaks as a percent of the total number of atoms in an image, and the theory curve is from the same calculation that predicts the oscillations of $\mathcal{A}$.

4.1   Circular polarization and Zeeman splitting

First, let us discuss the origin of the real-space asymmetry in the honeycomb optical lattice. The in-plane polarization of 1064 nm beams that interfere to create the honeycomb lattice can be decomposed into left- and right- circularly polarized light (σ^+ and σ^-, respectively) relative to the vertical axis. The intensity pattern of each circular polarization of light is a triangular pattern of identical form, except that the intensity pattern of one circular

polarization is offset spatially from that of the other circular polarization. We write the two intensity patterns $I_{\pm}(\mathbf{r})$ in Eq. (4.2), where $\mathbf{G}_i$ are shown in Fig. 4.2. $I_{+}(\mathbf{r})$ ($I_{-}(\mathbf{r})$) correspond to the intensity pattern and lattice potential created by $\sigma^+(\sigma^-)$ light, and the sum $I_{+}(\mathbf{r}) + I_{-}(\mathbf{r})$ is the balanced honeycomb intensity lattice of Eq. (2.3) and Fig. 2.1(e).

$$I_{\pm}(\mathbf{r}) = \frac{3}{2} + \cos\left[\mathbf{G}_1 \cdot \mathbf{r} \pm 4\pi/3\right] + \cos\left[\mathbf{G}_2 \cdot \mathbf{r} \mp 2\pi/3\right] \tag{4.2}$$
$$+ \cos\left[\mathbf{G}_3 \cdot \mathbf{r} \pm 2\pi/3\right]$$

In the ac Stark effect, circular polarization lifts the degeneracy of the magnetic sublevels of the trapped atom, which in our system is equivalent to imposing a spatially-varying 'fictitious magnetic field' on the atoms [20]. We also impose a dominant external magnetic field $\mathbf{B}_0$, oriented at an angle θ from the vertical axis, which is orthogonal to the lattice plane. In the magnetic field, the atoms experience a linear Zeeman shift that is proportional to $|\mathbf{B}_0 + \mathbf{B}(\mathbf{r})| = B_0\sqrt{1 + \frac{\mathbf{B}(\mathbf{r})}{\mathbf{B}_0}}\cos\theta \sim B_0 + \frac{1}{2}B(\mathbf{r})\cos\theta$.

This effective field leads to a potential for atoms in the $|F = 1, m_F\rangle$ state that depends on the polarization of the lattice [21], with

$$V_{\pm}(\mathbf{r}) = \frac{\hbar}{8}\frac{\Gamma^2}{\Delta}\frac{I_{\pm}(\mathbf{r})}{I_{sat}}\left(1 \pm \frac{1}{3 \cdot 2}\frac{\Delta_{fs}}{\Delta}g_F m_F \cos\theta\right) \tag{4.3}$$

where Γ is the spontaneous decay rate, Δ_{fs} is the fine structure splitting, Δ is the detuning of our 1064 nm lattice beams from the D-line doublet of Rubidium at 780 and 795 nm and $|\Delta| \gg \Delta_{fs}$.

The full honeycomb lattice potential is $V_{1064}(\mathbf{r}) = V_{+}(\mathbf{r}) + V_{-}(\mathbf{r})$, which can also be expressed as a sum of scalar and vector components of the ac Stark shift.

$$V_{1064}(\mathbf{r}) = V_{+}(\mathbf{r}) + V_{-}(\mathbf{r}) \tag{4.4}$$
$$= \frac{\hbar}{8}\frac{\Gamma^2}{\Delta I_{sat}}\left[(I_{+}(\mathbf{r}) + I_{-}(\mathbf{r})) - \frac{1}{6}\frac{\Delta_{fs}}{\Delta}(I_{+}(\mathbf{r}) - I_{-}(\mathbf{r}))g_F m_F \cos\theta\right]$$
$$= V_s(\mathbf{r}) + V_a(\mathbf{r}) \tag{4.5}$$

Consider the inversion operation, which takes $\mathbf{r} \to -\mathbf{r}$ and thus interchanges the two lattices $V_{+}(\mathbf{r})$ and $V_{-}(\mathbf{r})$. The first term $V_s(\mathbf{r})$ is symmetric, $V_s(-\mathbf{r}) = V_s(\mathbf{r})$, and the second term $V_a(\mathbf{r})$ is antisymmetric, $V_a(-\mathbf{r}) = -V_a(\mathbf{r})$, under inversion.

For alkali atoms, $V_a(\mathbf{r})$ is suppressed with respect to $V_s(\mathbf{r})$ owing to the large optical detuning from the atomic resonance. For the wavelength of light used in our lattice, the ratio $2|V_a(\mathbf{r})/V_s(\mathbf{r})|$ is at most 2.3%, so that $V_a(\mathbf{r})$ adds only a small inversion-symmetry-breaking potential atop a graphene-like, inversion-symmetric honeycomb lattice.

4.1.1   Inversion symmetry

The honeycomb lattice has two sites in its unit cell, A and B, shown as different colors in Fig. 4.3. In the lattice, sites A form a triangular lattice, as do sites B. The potentials $V_+(\mathbf{r})$ and $V_-(\mathbf{r})$ correspond to the triangular lattices of A sites and B sites, respectively. If the two lattice sites are equivalent, then it has twelve plane symmetries, and if they are inequivalent, then it has six plane symmetries. The twelve symmetry operations are illustrated in Fig. 4.3.

(a) Between-site mirror   (b) Through-site mirror   (c) π/3 rotation   (d) 2π/3 rotation
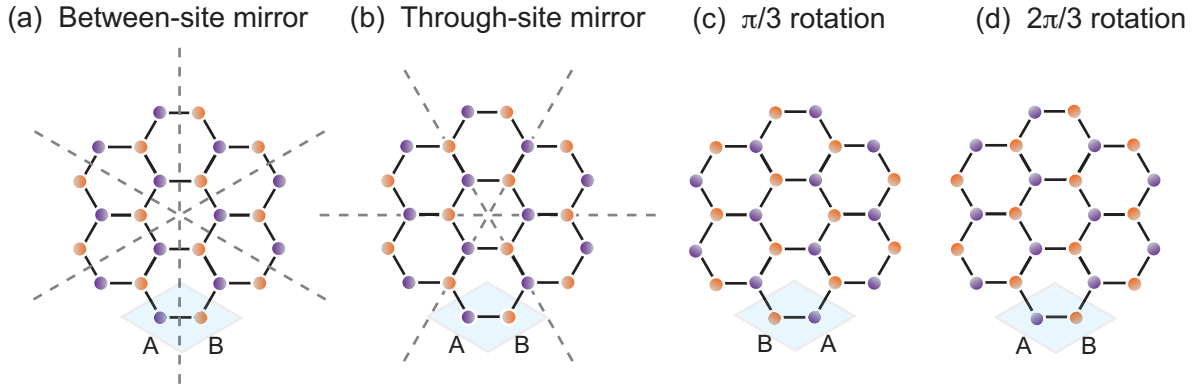
Figure 4.3: To assess the symmetry group of the two-dimensional honeycomb lattice, we consider twelve symmetry operations: (a) Three mirror symmetries along the through-site planes, indicated by grey dashed lines. These mirror operations exchange sites A and B and any honeycomb lattice in which sites A and B differ will be antisymmetric under these operations. (b) The three mirror operations along the between-site planes map A sites to A sites, and any honeycomb geometry is symmetric under these operation. (c) Three rotations by $\pi/3$ exchange sites A and B. (d) Three rotations by $2\pi/3$ map the lattice back onto itself and any honeycomb lattice is symmetric under this operation. A lattice is in the C_6 symmetry group if it is symmetric under all six of these rotations, and in the C_3 symmetry group if it symmetric under only the three rotations by $2\pi/3$.

The potential $V_s(\mathbf{r})$ is symmetric under all twelve operations in Fig. 4.3, because sites A and B are equivalent. The potential $V_a(\mathbf{r})$ lifts the degeneracy between sites A and B, thereby breaking half of the lattice symmetries. The honeycomb lattice with an offset in energy between the sites is left with only the three through-site mirror symmetries and three rotational symmetries (it is in the C_3 symmetry group). The broken symmetries all involve operations that exchange sites A and B. We can identify these operations by defining the parity operator, which exchanges sites A and B.

$$\hat{P} := \begin{matrix} \mathbf{r} \to -\mathbf{r} \\ \mathbf{k} \to -\mathbf{k} \end{matrix} \qquad\qquad \hat{P}^2 = 1 \qquad\qquad (4.6)$$

4.2 Raman-Nath regime

We first treat the problem in the Raman-Nath regime, where the optical lattice is analogous to a phase grating for the Bose-Einstein condensate, a coherent matter-wave, and we neglect the motion of the atoms during the pulse, and thus the kinetic energy term in the Hamiltonians. The atoms in the condensate are exposed to the lattice potential $V_{1046}(\mathbf{r})$ for time τ, during which they acquire a phase that is potential-dependent, and thus spatially-dependent. When the atoms are subsequently released in time of flight, the spatially varying phase results in an interference pattern with peaks at integer multiples of the reciprocal lattice vectors $\mathbf{G}_i$. In the Raman Nath regime, we can consider the pulse time τ to be a small parameter, so that $\psi(\tau) \sim (1 - iV(\mathbf{r})\tau - \frac{1}{2}V(\mathbf{r})^2\tau^2)\psi(0)$.

We consider only the effect of atoms scattering in the symmetric and antisymmetric potentials and find that an asymmetry in the first-order diffraction peaks at $p(\mathbf{G}_i)$ and $p(-\mathbf{G}_i)$ should arise even in this simplistic treatment. We consider scattering in k-space, where both the scalar and vector Stark shift optical lattice potentials, $V_s(\mathbf{r})$ and $V_a(\mathbf{r})$ are characterized in momentum space by their Fourier components $\beta_{s,a}(\pm\mathbf{G}_i)$ at the wavevectors $\pm\mathbf{G}_i$. Because both potentials are real, we know that $\beta_{s,a}(\mathbf{G}_i) = \beta_{s,a}^*(-\mathbf{G}_i)$. C_3 rotational symmetry requires that all i are equivalent. The dominant term V_s is inversion-symmetric, so that and the Fourier components $V_s(\pm\mathbf{G}_i) = \beta_s$ are real. The symmetry breaking term V_a will have Fourier components of equal magnitude and opposite sign, so that they must be pure imaginary and $V_a(\pm\mathbf{G}_i) = \pm i\beta_a$ where β_s and β_a are both real.

We now consider the probability amplitudes $p(\pm\mathbf{G}_i)$ for atoms diffracting from their initial zero momentum to a final wavevector $\pm\mathbf{G}_i$ within a time τ. As discussed in the paper, such diffraction can be achieved by one first-order process, with amplitude $-i(\beta_s \pm i\beta_a)\tau/hbar$, and by two second-order processes, which sum to an amplitude $(-i)^2(\beta_s \mp \beta_a)^2\tau^2/\hbar^2$. Summing the first- and second-order amplitudes, we observe the probabilities for diffraction into opposite wavevectors differ from one another.

Let $B_{s,a} = \beta_{s,a}\tau/\hbar$ to calculate the asymmetry parameter $\mathcal{A}$ at short times at for small lattice asymmetry ($|\beta_a| \ll |\beta_s|$), neglecting terms of order $\mathcal{O}(\tau^4)$.

$$
\begin{aligned}
P(\pm\mathbf{G}_i) &= |\frac{-i(\beta_s \mp i\beta_a)\tau}{\hbar} - \frac{\tau^2(\beta_s \pm i\beta_a)^2}{\hbar^2}|^2 \quad\quad (4.7)\\
&= |\mp B_a - (B_s^2 - B_a^2)^2 + i(-B_s \mp 2B_sB_a)|^2 \\
&= \pm 2B_a(B_s^2 - B_a^2) + B_s \pm 4B_s^2B_a \quad\quad (4.8)
\end{aligned}
$$

$$\mathcal{A} = \frac{\sum_i p(\mathbf{G}_i) - p(-\mathbf{G}_i)}{\sum_i p(\mathbf{G}_i) + p(-\mathbf{G}_i)} \tag{4.9}$$

$$= \frac{12 B_a B_s - 4 B_a^3}{2 B_s} \tag{4.10}$$

$$\approx \frac{12 B_a B_s}{2 B_s} = 6 \beta_a \tau / \hbar \tag{4.11}$$

This shows that even in the Raman-Nath regime, exposing a spin-polarized gas to an inversion-asymmetric lattice, even when the antisymmetric component is very small compared to the symmetric term, will give rise to an inversion asymmetry in the momentum-space picture. This describes only an initial rise of $\mathcal{A}$, which is still small within the Raman-Nath regime.

4.3 Hamiltonians and symmetries

A more sophisticated understanding of the experiment is that rapidly introducing the lattice potential projects the initial state into the eigenbasis of the lattice Hamiltonian. The stationary Bose-Einstein condensate has momentum $\mathbf{k} = (0,0)$, so when it is exposed to the lattice it is projected into the $\mathbf{q} = \Gamma$ Bloch states, $|\psi_n\rangle = \sum_l b_{n,l} \ e^{i l \mathbf{g}_l \cdot \mathbf{r}}$, that have nonzero populations $|b_0|^2$. The Bloch states were defined in Eq. (2.19), and here the subscript n is the band index and l represents a point in momentum-space. [2] During the pulse time τ each eigenstate evolves as in Eq. (4.13). After the pulse we measure the state $|\Phi(\tau)\rangle$, with

$$\mathcal{H} |\psi_n\rangle = E_n |\psi_n\rangle \tag{4.12}$$

$$|\Phi(\tau)\rangle = \sum_n |\psi_n\rangle \, e^{-i E_n \tau / \hbar} \tag{4.13}$$

where $|\psi_n\rangle$ are the Bloch states with energy E_n, the subscript n identifies the energy band, with indexing so that $n = 1$ is the ground state, and we drop the label $\mathbf{q}$, which is zero for the states of interest.

Note that the effect of inversion on the unperturbed Hamiltonian, and the perturbation:

$$[\hat{P}, \mathcal{H}_0] = 0 \qquad\qquad \hat{P} \mathcal{H}_0 \hat{P} = \mathcal{H}_0$$

$$\{\hat{P}, \mathcal{H}_a\} = 0 \qquad\qquad \hat{P} \mathcal{H}_a \hat{P} = -\mathcal{H}_a$$

The parity operator indicates the inversion-symmetry of the lattice. The Hamiltonian $\mathcal{H}_0$ is inversion-symmetric, and the perturbation $\mathcal{H}_a$ is inversion-antisymmetric.

---

[2] In this notation, l corresponds to each pair of integers m, n on the momentum-space grid defined by $k \in m \mathbf{G}_1 + n \mathbf{G}_2$, with $l = 0$ corresponding to $m = n = 0$.
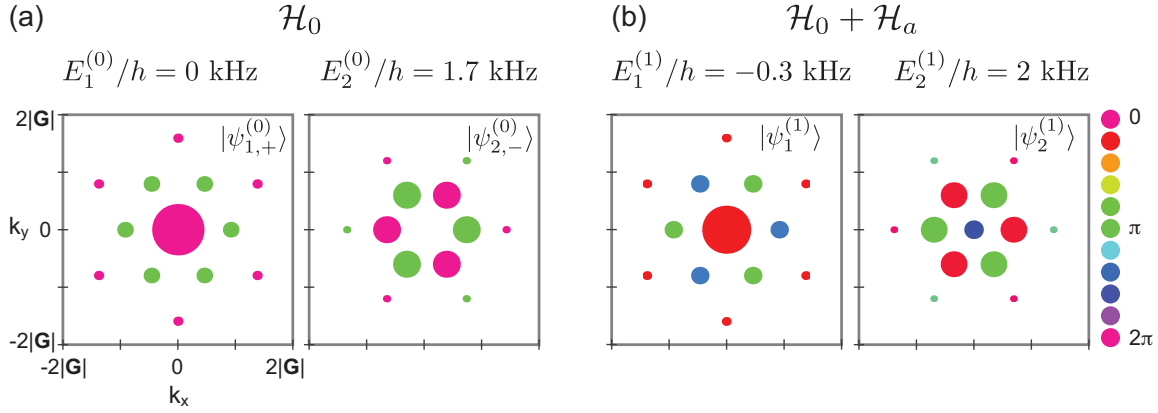
Figure 4.4: The ground state and first excited state of the Hamiltonians in the Bloch basis. The area of each spot represents the complex coefficient $|b_{n,l}|^2$ and color represents phase. Axis labels on the far left image apply to all images. (a) The ground state (left) and first excited state (right) of the unperturbed Hamiltonian $\mathcal{H}_0$, where all coefficients have phases 0 or π. (b) The ground state (left) and first excited state (right) of the perturbed Hamiltonian $\mathcal{H}_0 + \mathcal{H}_a$. The perturbation shifts the eigenenergies and hybridizes the eigenstates, so that both states are asymmetric under inversion and have some population at $\mathbf{k} = (0,0)$.

4.3.1 Bloch states and energy spectrum at $\mathbf{q} = \Gamma$

To find the Bloch states and energies of the $\mathbf{q} = \Gamma = (0,0)$, we follow the prescription detailed in section 2.2 for both the symmetric Hamiltonian, $\mathcal{H}_0$, and the asymmetric Hamiltonian, $\mathcal{H}_0 + \mathcal{H}_a$, using the potentials defined in Eq. (4.4). Note that solutions for the unperturbed Hamiltonian, $\mathcal{H}_0$, were presented in section 2.2.

We solve the Schrödinger equation for $\mathcal{H}_0$ and find eigenenergies, $E_n^{(0)}$, and the Bloch states, $|\psi_n^{(0)}\rangle$, where the superscript indicates the order of the perturbation. The ground state and first excited state are shown in Fig. 4.4(a), where the area of each spot represents the amplitude squared of each coefficient, $|b_{n,l}|^2$, and color represents its complex phase. The probability that the condensate at $\mathbf{k} = (0,0)$ is projected into an eigenstate is proportional to $|b_{n,0}|^2$, so in these states it is clear that the BEC will be projected into into ground state but not the first excited state. Note that there are other excited states, $|\psi_n\rangle$, that have nonzero coefficients $b_{n,0}$. Because of the symmetry of the Hamiltonian, the complex phases of the coefficients $b_{n,l}$ only take on the values 0 and π. The coefficients of the ground state have six-fold rotational symmetry, but those of the first-excited state have only three-fold rotational symmetry. We can identify the symmetry of the eigenstates of the unperturbed Hamiltonian using the parity operator. Examining the eigenstates in Fig. 4.4(a), we see that

$$\langle \psi_1^{(0)} | \hat{P} | \psi_1^{(0)} \rangle = +1 \tag{4.14}$$

$$\langle \psi_2^{(0)} | \hat{P} | \psi_2^{(0)} \rangle = -1 \tag{4.15}$$

We label the eigenstates of $\mathcal{H}_0$ by their parity expectation value, with inversion-symmetric states labeled $|\psi_{i,+}^{(0)}\rangle$ and inversion-antisymmetric states labeled $|\psi_{j,-}^{(0)}\rangle$, where i and j indicate the band index.

We also diagonalize the asymmetric Hamiltonian $\mathcal{H}_0 + \mathcal{H}_a$ at $\mathbf{q} = \Gamma$ to find the eigenstates, $|\psi_n^{(1)}\rangle$, and eigenenergies $E_n^{(1)}$, and plot them in 4.4(b). The ground and first-excited states are shown in the right panel of Fig. 4.4. Here we see that the effect of the perturbation is to hybridize these two states, so that the eigenstates both have nonzero coefficients b_0, and the complex phases of both states have only three-fold rotational symmetry. These states are inversion-asymmetric, with expectation values of $\hat{P}$ that can be between -1 and $+1$.

4.3.2 Inversion asymmetry and time evolution

The asymmetry signal can be predicted by examining the states of the unperturbed Hamiltonian, $\mathcal{H}_0$. During the pulse, the wavefunction evolves in each eigenstate at a frequency determined by its eigenenergy. When the momentum-space wavefunction is measured, the populated asymmetric states – those with nonzero $|b_{n,l}|^2$ – interfere with one another and with the rest of the symmetric states in the system, leading to the oscillatory signal of $\mathcal{A}(\tau)$.

The initial state is a zero-momentum condensate that can be written in the basis of inversion-even eigenstates as $|\Phi(0)\rangle = \sum_i c_i |\psi_{i,+}^{(0)}\rangle$, where the coefficient c_i is the $k = 0$ coefficient of the Bloch function for the ith band, i.e. $c_i = b_{i,0}$. Considering the asymmetric perturbation out to second order in perturbation theory (see appendix B for details), this initial state evolves in time during the pulse time as

$$|\Phi(t)\rangle = \sum_i c_i e^{-i\omega_{i,+}t} \left(|\psi_{i,+}^{(0)}\rangle + \sum_j \alpha_{j,i} |\psi_{j,-}^{(0)}\rangle \right) + \sum_{j,k} -\alpha_{j,k} c_k e^{-i\omega_{j,-}t} |\psi_{j,-}^{(0)}\rangle \tag{4.16}$$

where $\omega_{i,+} = E_{i,+}/\hbar$ and $\omega_{j,-} = E_{j,-}/\hbar$ and $\alpha_{j,i} = \frac{\langle \psi_{j,-}^{(0)} | \mathcal{H}_a | \psi_{i,+}^{(0)} \rangle}{E_{j,-}^{(0)} - E_{i,+}^{(0)}}$.

In Eq. (4.16), the sum on i represents the incorporation of inversion antisymmetry into the even eigenstates $|\psi_{i,+}^{(0)}\rangle$ of the unperturbed Hamiltonian. The last term of Eq. (4.16) represents fully antisymmetric states $|\psi_{j,-}^{(0)}\rangle$ for which the perturbation introduces population at zero momentum.

To calculate the expected inversion asymmetry of $|\Phi(t)\rangle$ using the eigenstates of $\mathcal{H}_0$, we define a 6×6 diagonal matrix, where each entry along the diagonal represents a wavevector corresponding to a first-order diffraction peak. The matrix, $\hat{M}$, has matrix element ± 1 for the wave vectors $\pm \mathbf{G}_i$, and 0 at all other momenta. The expectation value $\langle \Phi | \hat{M} | \Phi \rangle = $

$\sum_i P(\mathbf{G}_i) - P(-\mathbf{G}_i)$ is is the numerator of the asymmetry metric $\mathcal{A}$. By definition, $\hat{M}$ is an inversion-antisymmetric operator. The expectation value of any antisymmetric operator is nonzero only for states of opposite inversion symmetry:

$$\langle \psi_{i,+}^{(0)} | \hat{M} | \psi_{k,+}^{(0)} \rangle = \langle \psi_{i,+}^{(0)} | \hat{P}(\hat{P}\hat{M}\hat{P})\hat{P} | \psi_{k,+}^{(0)} \rangle \tag{4.17}$$

$$= \langle \psi_{i,+}^{(0)} | (-\hat{M}) | \psi_{k,+}^{(0)} \rangle \tag{4.18}$$

$$= 0$$

$$\langle \psi_{i,+}^{(0)} | \hat{M} | \psi_{j,-}^{(0)} \rangle = \langle \psi_{i,+}^{(0)} | \hat{P}(\hat{P}\hat{M}\hat{P})\hat{P} | \psi_{j,-}^{(0)} \rangle \tag{4.19}$$

$$= \langle \psi_{i,+}^{(0)} | \hat{M} | \psi_{j,-}^{(0)} \rangle \tag{4.20}$$

We thus consider only terms of opposite inversion symmetry in Eq. (4.16) to write down $M = \langle \Phi(t) | \hat{M} | \Phi(t) \rangle$, which we split into two terms

$$M = M_1(t) + M_2(t) \tag{4.21}$$

$$M_1(t) = \sum_i c_i^* e^{i\omega_{i,+}t} \left(\langle \psi_{i,+}^{(0)} | + \sum_j \alpha_{j,i}^* \langle \psi_{j,-}^{(0)} | \right) \hat{M} \sum_k c_k e^{-i\omega_{k,+}t} \left(| \psi_{k,+}^{(0)} \rangle + \sum_l \alpha_{l,k} | \psi_{l,-}^{(0)} \rangle \right)$$

$$= \sum_{i,k,l} c_i^* c_k \alpha_{l,k} e^{-i(\omega_{k,+}-\omega_{i,+})t} \langle \psi_{i,+}^{(0)} | M | \psi_{l,-}^{(0)} \rangle + \sum_{i,k,j} c_i^* c_k \alpha_{j,i}^* e^{-i(\omega_{k,+}-\omega_{i,+})t} \langle \psi_{j,-}^{(0)} | M | \psi_{k,+}^{(0)} \rangle$$

$$= \sum_{i,k,l} \left(c_i^* c_k e^{-i(\omega_{k,+}-\omega_{i,+})t} \alpha_{j,i}^* M_{j,k} + \text{c.c.} \right) \tag{4.22}$$

$$M_2(t) = \sum_{i,j,k} \left(c_k^* c_i e^{-i(\omega_{j,-}-\omega_{k,+})t} (-\alpha_{j,i}) M_{j,k}^* + \text{c.c.} \right) \tag{4.23}$$

where i, j, and k identify band indices and we have consistently used notation where i and k label inversion symmetric states $| \psi_+^{(0)} \rangle$ and j and l label inversion antisymmetric states $| \psi_-^{(0)} \rangle$.

Consider $M(t)$ in the case that two states of $\mathcal{H}_0$ of opposite inversion-symmetry, $| \psi_{i,+}^{(0)} \rangle$ and $| \psi_{j,-}^{(0)} \rangle$, are close in energy so that $\alpha_{j,i}$ is large and the states are strongly mixed. The newly asymmetric states interfere with all remaining symmetric states $| \psi_{i,+}^{(0)} \rangle$, as described by both $M_1(t)$ and $M_2(t)$, and these oscillations will have equal amplitude. They also interfere with one another, as described by $M_2(t)$ when $k = i$.

These equations show that, simply by analyzing the eigenstates of the unperturbed Hamiltonian, we can identify the relevant states in developing an asymmetry, and predict the oscillation of $\mathcal{A}(\tau)$.

4.3.3 Identifying relevant eigenstates

In our publication we identified the criteria that states of the unperturbed Hamiltonian $\mathcal{H}_0$ must meet to significantly contribute to the signal of $\mathcal{A}$ after the perturbation. Beyond the requirement that they are non-degenerate, the criteria can be clearly read off of Eqs. (4.21) – the coefficients c, α and M must be large. Otherwise stated, the overlap of the symmetric states with the initial condensate, c_i and c_k, must be large, the symmetric $|\psi_{i,+}\rangle$ and antisymmetric $|\psi_{j,-}\rangle$ states must be close in energy so that $\alpha_{i,j}$ is large, and the symmetric $|\psi_{k,+}\rangle$ and antisymmetric $|\psi_{j,-}\rangle$ states must have large amplitude in the first order peaks, so that $M_{j,k}$ is large. Note that these can be met for either $i = k$ or $i \neq k$.

Eigenstates of our system that satisfy the criteria are plotted in Fig. 4.6. In our lattice there is just one pair of states whose hybridization dominates the asymmetry signal. The ground state ($i = 1$) and first excited state ($j = 2$) are close in energy, separated by just 2 kHz, so that α_{ji} is large and they are strongly mixed by the perturbation. Being low-energy states, they have high population at the first-order momenta $\pm\mathbf{G}_i$, and the ground state has a large population at $\mathbf{k} = (0,0)$, so that c_i is large and they satisfy all of our criteria. Their oscillation with one another at 2 kHz is the strongest contributor to the asymmetric signal, with amplitude $|c_1|^2 M_{1,2}$, followed by their oscillation with other high energy states, $|\psi_{k,+}^{(0)}\rangle$ with amplitude $c_1 c_k M_{2,k}$. The most relevant states $|\psi_{k,+}\rangle$ are the non-degenerate states of $\mathcal{H}_0$ that have highest population at $\mathbf{k} = 0$ and $\mathbf{k} = \pm\mathbf{G}_i$, so that c_k and $M_{2,k}$ are large. The states $|\psi_{k,+}\rangle$ are nearly unaffected by the perturbation, and contribute to the oscillation in $\mathcal{A}$ just through their oscillation with the lowest energy states.

The lower panel of Fig. 4.6 shows the eigenstates of the perturbed Hamiltonian $\mathcal{H}_0 + \mathcal{H}_a$. We do not include $\pm$ subscripts to indicate symmetry under inversion, because the perturbed states are neither symmetric nor antisymmetric, but asymmetric as indicated by color in the low-energy states in the grey box of Fig. 4.6. The eigenenergies E_n/h are indicated by horizontal lines, the thickness of which indicate the value of $c_i c_k M_{2,k}$ and thus the amplitude of oscillation with states $|\psi_1\rangle$ and $|\psi_2\rangle$.

Our paper demonstrated that we could account for the experimentally observed asymmetry signal $\mathcal{A}(\tau)$ with the calculation of $M(t)$ by considering the complete eigenbasis of the Hamiltonian $\mathcal{H}_0$ and calculating the time evolution during the pulse as in Eq. (4.21). The results of this calculation are plotted as a grey line in Fig. 4.5.

We also showed that the dominant oscillation in $\mathcal{A}(\tau)$ was accounted for by considering oscillation among just three states, $|\psi_{1,+}^{(0)}\rangle$, $|\psi_{2,-}^{(0)}\rangle$, and $|\psi_{31,+}^{(0)}\rangle$. The results of this three-state calculation are plotted in the red dotted line of Fig. 4.5.

Figure 4.5 also shows that by considering just a few more states, the remaining states shown in Fig. 4.6, we account for the entire oscillation signal. We plot the calculated signal that results from including the next states that satisfy our criteria and are plotted in Fig. 4.6. By including states $|\psi_{25,+}^{(0)}\rangle$ and $|\psi_{14,+}^{(0)}\rangle$ in addition to the three states already considered, we produce the blue dot-dashed curve, which closely approximates the full calculation. By including the remaining states of Fig. 4.6, we produce the black dashed curve. This calculation considers only eight states of the symmetric Hamiltonian $\mathcal{H}_0$ and nearly perfectly

overlaps with the calculation that considers all states in the eigenbasis.
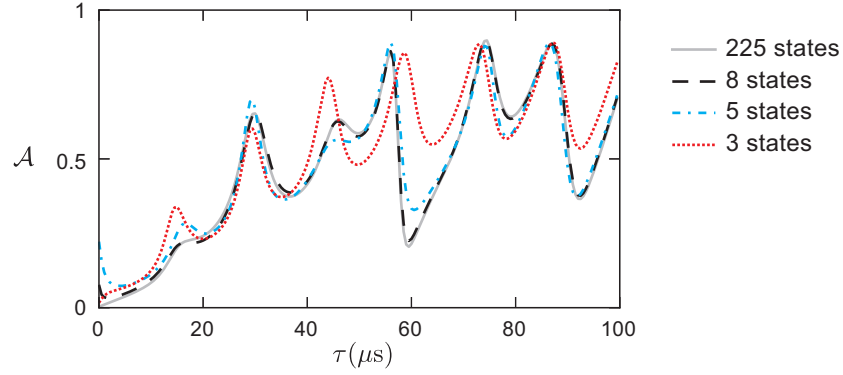
Figure 4.5: Considering just eight of the 225 eigenstates calculated very closely represents the complete treatment. The result of the asymmetry calculation considering only three, five or all eight states of Fig. 4.6. All calculations involve states $|\psi_{1,+}^{(0)}\rangle$ and $|\psi_{2,-}^{(0)}\rangle$ and the third state $|\psi_{31,+}^{(0)}\rangle$; the five-state calculation includes states $|\psi_{25,+}^{(0)}\rangle$ and $|\psi_{14,+}^{(0)}\rangle$, and the eight-state calculation involves all states shown in the figure.
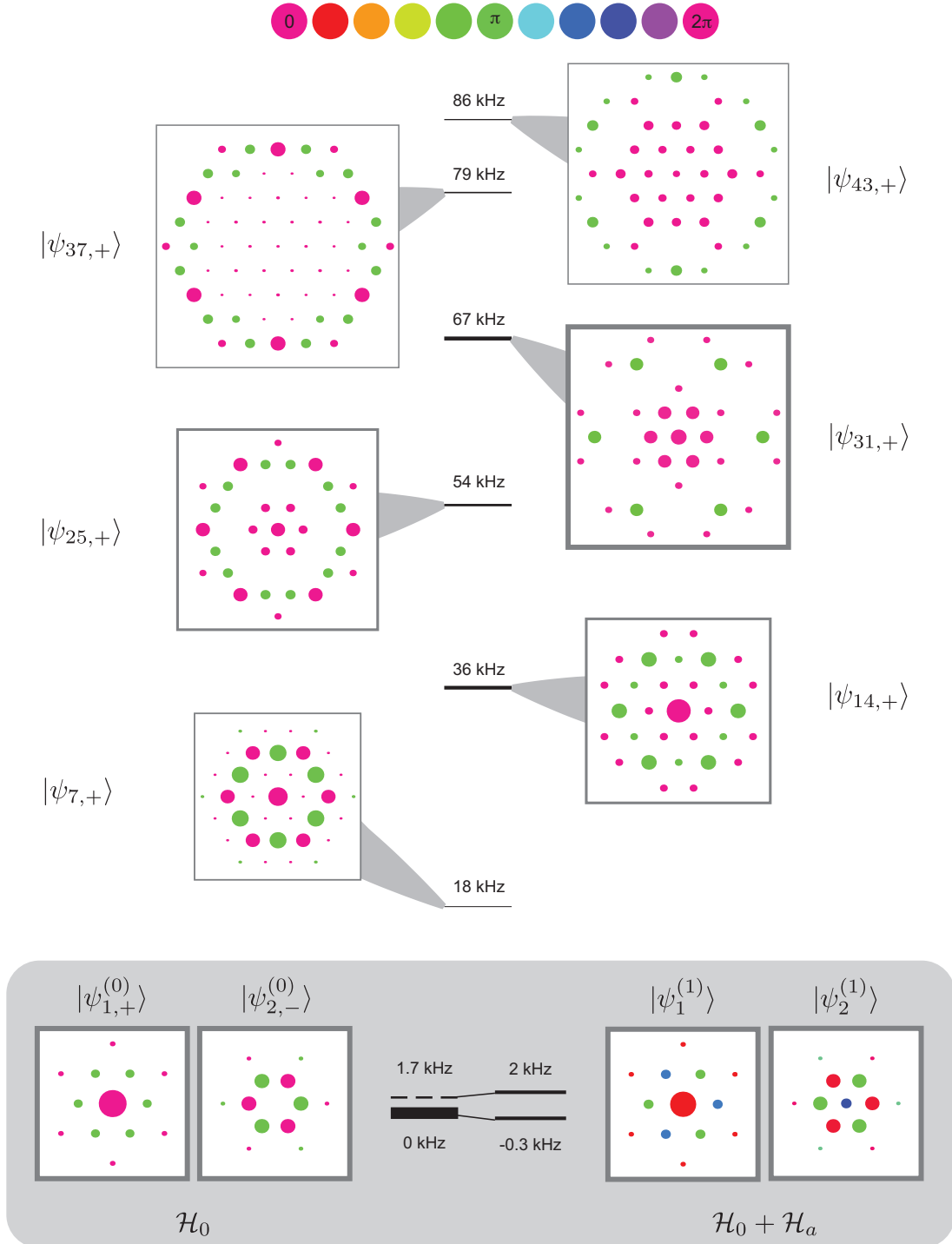
Figure 4.6: Eigenstates and energies of the perturbed and unperturbed Hamiltonians, where the primary source of asymmetry at the vectors $\mathbf{G}_i$ is from the hybridization of the lower two states $|\psi_{1,+}^{(0)}\rangle$ and $|\psi_{2,-}^{(0)}\rangle$. They oscillate with upper states $|\psi_{k,+}\rangle$ that are unaffected by the asymmetric perturbation. Eigenenergies of each state are indicated along the center of the figure, with line thickness indicating the amplitude of oscillation.

Chapter 5

Increasing Interactions

This chapter discusses the phase transition between the superfluid and Mott insulating phases of a lattice-trapped gas under strengthening particle-particle interactions in two configurations of the bichromatic lattice. The transition is studied under the same conditions in the triangular and kagome lattices, and the effect of geometry on the phase transition is examined. This work was reported in the following manuscript that is currently in review and included in appendix C.

- *C. K. Thomas, T. H. Barter, T.-H. Leung, M. Okano, G. B. Jo, J. Guzman, I. Kimchi, A. Vishwanath and D. M. Stamper-Kurn, "Mean-field scaling of the superfluid to Mott insulator transition in a 2D optical superlattice," arXiv: 1702.04433 (2017).*

5.1   Summary of the experiment and results

We take advantage of the tunability and repeatability of our optical superlattice to perform a quantum simulation of the Bose-Hubbard model that is insensitive to many of the experimental parameters that often plague optical lattice simulations [3, 4, 22]. The Bose-Hubbard Hamiltonian that describes bosonic quantum gases trapped in periodic lattices is written (5.1) by indexing each lattice site and considering the behavior and associated energy scales of atoms on the lattice: atoms can tunnel among neighboring sites, with energy J, or they can share a single site, in which case they repel one another with energy U.

$$\mathcal{H}_{BH} = -J \sum_{\langle i,j \rangle} \hat{a}_i^\dagger \hat{a}_j + \sum_i \frac{U}{2} \hat{n}_i(\hat{n}_i - 1) \tag{5.1}$$

where $\langle i, j \rangle$ indicates a sum over all nearest neighbor lattice sites. The bosonic creation and annihilation operators on site i are $\hat{a}_i^\dagger$ and $\hat{a}_i$, respectively, so that the number of particles on site i is given by the number operator $\hat{n}_i = \hat{a}_i^\dagger \hat{a}_i$.

In Eq. (5.1), the energies J and U are of opposite sign, so that there is a competition between them in determining the lowest energy state of the Hamiltonian. When the ratio

U/J is small, the ground state of the lattice is delocalized and phase coherent – a superfluid. In the limit of large U/J, the ground state is the number-squeezed Mott insulating state, wherein each lattice site hosts exactly the same integer number of particles.

A lattice-trapped gas at zero temperature undergoes a phase transition between the superfluid and Mott insulating states that is driven by long-range quantum fluctuations. As inter-particle interactions grow stronger, U/J increases and long-range fluctuations allow the system to sample the full extent of the lattice to find the state that minimizes the free energy of the Hamiltonian. Mapping out the phase diagram of Eq. (5.1) necessitates treatment of strong interactions and long-range quantum fluctuations, which can be complicated to describe theoretically, but fairly straightforward to realize experimentally with a low-temperature gas.

In an optical lattice, the ratio U/J increases with lattice depth, which is determined by laser beam intensity and is thus straightforward to control. The values of U and J for a particular calibrated lattice depth are determined from the ground-state Wannier functions as described in section 2.6. Roughly speaking, increased lattice depth leads to narrower Wannier functions, which decreases the tunneling rate and increases the on-site repulsion.

In this work, we propose and implement a quantitative test of the phase diagram of the Bose-Hubbard Hamiltonian that is valid at non-zero temperature and in the presence of the inhomogeneity introduced by the trapping potential. We focus on a mean-field treatment of Eq. (5.1), which predicts that all system properties are determined by the characteristic system energies once they are scaled by the product of the lattice coordination number, z, and the tunneling energy, J, irrespective of the specific geometry of the lattice in which the bosons propagate. We perform a direct test of the mean-field scaling prediction using our optical superlattice, with which we can engineer two identical experiments that differ only in lattice coordination number. We compare the loss in coherence along the entire trajectory of the transition between the superfluid and Mott insulating phases in the kagome and triangular lattices, with $z = 4$ and $z = 6$, respectively. This is a test of mean-field predictions that does not depend on comparing the phase transition point to a theoretical model that must take into account all experimental parameters. Our test allows for systematic experimental or measurement errors that are common to both experiments.

In our Gutzweiller mean-field treatment of Eq. (5.1), we show that even when distinct quantum simulation experiments differ in any particular parameter – atom number, external trapping frequency, lattice spacing, unit cell volume or number of cites per unit cell – these differences are accounted for if a generalized characteristic density N/K is held constant. The argument is related to one presented in Rigol et. al. [22] that is discussed in section 5.5 and shows that any experiments performed with an optical square-lattice can be described by a characteristic density, $\tilde{\rho}$, which determines the system properties and the critical point of the superfluid-Mott insulating phase transition. This has far-reaching consequences in using ultracold atomic systems as quantum simulators, because it means that simulations with different experimental parameters can be compared with one another and their results extrapolated to the systems they aim to emulate.

We find that scaling the ratio U/J of the kagome lattice dataset by $\zeta = 1.6 \pm 0.1$ results

in optimal collapse of the phase transition data with the triangular lattice dataset, where the quoted error is a Monte Carlo statistical estimate. The analysis of scaling behavior shown in Fig. 5.1 was carried out by Thomas Barter. We compare our scaling measurement to the mean-field prediction of $\zeta_{mf} = z_{tri}/z_{kag} = 1.5$. While this scaling is consistent with mean-field predictions, it does not necessarily rule out the more sophisticated treatments of the transition. For example, a quantum Monte Carlo treatment of a gas with thermal energy $k_B T = \tau = 0$ in a homogenous lattice predicts critical points for the triangular and kagome lattices of $(U/J_{tri})^* = 50$ and $(U/J_{kag})^* = 29$, which have a ratio of 1.7. This ratio of critical points indicates that a deviation from mean-field scaling may be small in the $\tau = 0$, homogenous lattice treatment. However, it cannot be directly compared to our measurement, which tests scaling throughout the transition.

This experiment is a quantum simulation of condensed matter systems that differ in their lattice geometry under otherwise identical experimental parameters, and the ability to engineer such a scenario is unique to quantum simulation with ultracold atoms. Moreover, by comparing phase transition data in these systems, we circumvent many challenges that arise when trying to use ultracold atoms in optical lattices to perform quantitative tests of theoretical treatments of Hamiltonians relevant to condensed matter problems.
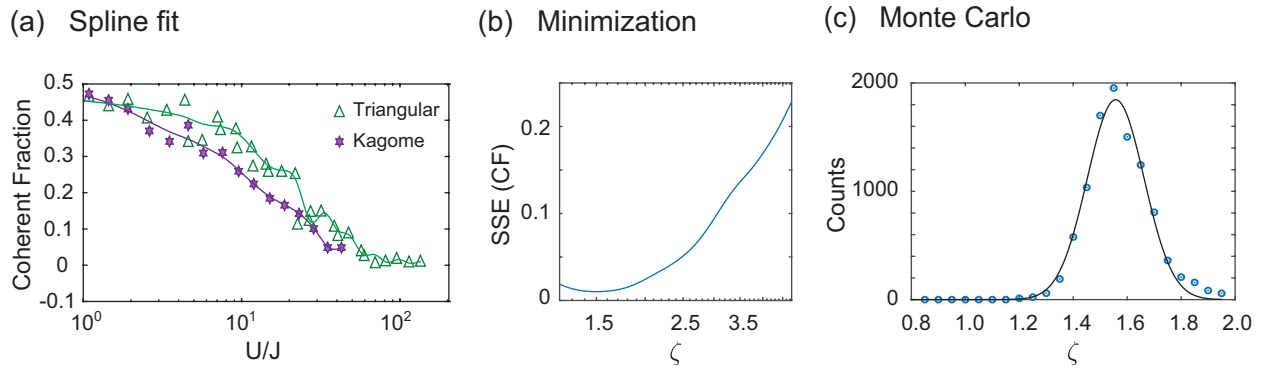
Figure 5.1: (a) The data are interpolated with a smoothing spline fit, which enables a comparison of the two datasets. (b) The x-axis of one smoothed curve is scaled by a scaling parameter ζ, and the sum of squared errors between the two curves is minimized. (c) This minimization is repeated many times for datasets generated from the statistical fluctuations in the coherent fraction data. The scaling analysis was carried out by Thomas Barter.

This chapter presents a mean-field treatment of an ultracold gas with finite temperature in an optical lattice with external harmonic confinement and the mean-field scaling prediction that results in section 5.2. In section 5.3, we describe the experimental techniques and the method of measuring the coherent fraction of atoms in a lattice. More sophisticated theoretical treatments of the Bose-Hubbard Hamiltonian are discussed in section 5.5. Finally, section 5.6 discusses experiments in which we drive the phase transition by changing the lattice geometry. In these experiments, we study the state of the lattice after tuning from

the triangular lattice, with $z = 6$, to the kagome lattice, with $z = 4$, and also to the decorated triangular lattice configuration of the superlattice, where again $z = 6$ but all tunneling events are second-order and mediated by sites that are raised in energy by Δ, so that the tunneling energy is given by $J' = J^2/\Delta$.

5.2 Mean-field theory with finite temperature gas and harmonic confinement

A mean-field treatment of the Bose-Hubbard model predicts that thermodynamic quantities like number, superfluid number, and entropy per lattice site are functions only of the scaled interaction strength, U/zJ, temperature, τ/zJ, and chemical potential, μ/zJ, where z is the lattice coordination number and $\tau = k_B T$. Aside from the inclusion of z, the mean-field theory is insensitive to the geometric structure of the lattice [23].

A mean-field treatment of the Bose-Hubbard model neglects non-local correlations, so that the ground state solution to Eq. (5.1) is separable and can be written as a product state of identical states on each lattice site [23–25]. For a sample with $\tau = 0$, each site i hosts an identical wavefunction $|\phi\rangle_i$, whereas when $\tau > 0$, each site hosts the density matrix ρ_i. The translationally invariant states $|\Psi\rangle$, for $\tau = 0$, and P, for $\tau > 0$, are written as

$$\tau = 0 \qquad\qquad |\Psi\rangle = \prod_i |\phi\rangle_i \tag{5.2}$$

$$\tau > 0 \qquad\qquad P = \prod_i \rho_i \tag{5.3}$$

We want to use the assumptions of mean-field theory to write the Bose-Hubbard Hamiltonian on the lattice system as a Hamiltonian on a single site i. Consider the $\tau = 0$ expectation value of the Hamiltonian,

$$E_{mf} = \langle\Psi| \mathcal{H}_{BH} |\Psi\rangle \tag{5.4}$$

$$= \langle\Psi| \sum_i \left(-J/2 \sum_{j=1}^{z} \left(\hat{a}_i^\dagger \hat{a}_j + \hat{a}_j^\dagger \hat{a}_i \right) + \frac{U}{2} \hat{n}_i(\hat{n}_i - 1) \right) |\Psi\rangle \tag{5.5}$$

Here, we have written the Hamiltonian as a sum over terms on site i, each of which will be identical, so that the sum results in an overall multiplicative term N, the total number of particles. The sum on j is a sum over all of the nearest neighbors of site i, up to the lattice coordination number, z. Again, translational invariance implies that the term being summed will be the same for all bonds, so that

$$E_{mf} = \langle \Psi | N \left(-zJ/2 \left(\hat{a}_i^\dagger \hat{a}_j + \hat{a}_j^\dagger \hat{a}_i \right) + \frac{U}{2} \hat{n}_i (\hat{n}_i - 1) \right) | \Psi \rangle \tag{5.6}$$

In a Gutzwiller approach to solving this Hamiltonian, we treat the kinetic term perturbatively to write a mean-field Hamiltonian on a single site i. We approximate the tunneling operator

$$\hat{a}_j^\dagger \hat{a}_i \simeq \langle \phi_j | \hat{a}_j^\dagger | \phi_j \rangle \hat{a}_i + \langle \phi_j | \hat{a}_j | \phi_j \rangle \hat{a}_i^\dagger - \langle \phi_j | \hat{a}_j^\dagger | \phi_j \rangle \langle \phi_i | \hat{a}_i | \phi_i \rangle \tag{5.7}$$
$$= \psi^* \hat{a}_i + \psi \hat{a}_i^\dagger - \psi^* \psi \tag{5.8}$$

where we have defined a complex number $\psi = \langle \phi_j | \hat{a}_j | \phi_j \rangle$ that represents the superfluid amplitude on site j. Translational invariance implies that ψ is the same on every lattice site. We can now write a mean-field Hamiltonian on a single site i.

$$E_{mf}/N = \langle \phi_i | \left(-zJ \left(\psi^* \hat{a}_i + \psi \hat{a}_i^\dagger - |\psi|^2 \right) + \frac{U}{2} \hat{n}_i (\hat{n}_i - 1) \right) | \phi_i \rangle \tag{5.9}$$
$$= \langle \phi_i | \mathcal{H}_{mf} | \phi_i \rangle \tag{5.10}$$

To find the ground-state of this Hamiltonian, we minimize the free energy with respect to superfluid amplitude ψ and on-site wavefunction $|\phi_i\rangle$ subject to the constraint that particle number is conserved.

$$\mathcal{H}_{mf}^{(c)} = -zJ(\psi^* \hat{a}_i + \psi \hat{a}_i^\dagger) + zJ\psi^* \psi + \frac{U}{2} \hat{n}_i (\hat{n}_i - 1) - \mu \hat{n}_i \tag{5.11}$$

where the superscript (c) indicates that the Hamiltonian is constrained.

The mean-field solution for $|\Psi\rangle$ is now determined by minimizing the constrained, single-site Hamiltonian $\mathcal{H}_{mf}^{(c)}$ with respect to the wavefunction, $|\phi\rangle$, and the superfluid amplitude, ψ. In practice, we perform this minimization by first minimizing $\mathcal{H}_{mf}^{(c)}$ with respect to $|\phi\rangle$ for many different chosen values of superfluid amplitude ψ, and then finding the minimum of all such solutions. To map out the phase diagram, we repeat this procedure at each value of μ and J.

When $\tau > 0$, we must consider the full eigenspectrum of the Hamiltonian and write the thermal density matrix on a site as

$$\mathcal{H}_{mf}^{(c)} | \phi_\gamma \rangle = E_\gamma | \phi_\gamma \rangle \tag{5.12}$$

with level-occupancy that depends on temperature $\beta = 1/\tau$.

$$Z = \sum_\gamma e^{-\beta E_\gamma} \tag{5.13}$$

$$\rho_i = \frac{1}{Z} e^{-\beta \mathcal{H}_{mf}^{(c)}} \tag{5.14}$$

In this case, the superfluid amplitude is simply $\psi = \text{Tr}[\hat{a}\rho_i]$, and again we minimize the energy with respect to ψ and ρ.

5.2.1   Scaling

If we scale all energy terms by the product zJ, the states and density matrix are unchanged.

$$\rho_i = \frac{1}{Z} e^{-(\beta z J)(\mathcal{H}_{mf}^{(c)}/zJ)} \tag{5.15}$$

$$= \frac{1}{Z} e^{-\beta \mathcal{H}_{mf}^{(c)}} \tag{5.16}$$

Therefore, the equation of state for atoms in the lattice must also be invariant to this scaling, so that per-site system properties such as particle number, n, superfluid number, n_{sf}, and entropy, s, must also be invariant to the scaling of system energies by the product zJ. We write

$$f\left(\frac{\mu}{zJ}, \frac{U}{zJ}, \frac{\tau}{zJ}\right) = f\left(\tilde{\mu}, \tilde{U}, \tilde{\tau}\right) \tag{5.17}$$

with $f \in \{n, n_{sf}, s\}$.

In the local density approximation, we account for the harmonic confining potential of the atoms with a local shift in the chemical potential, $\mu(\mathbf{r})$. The bulk properties of the harmonically-confined, lattice-trapped gas are calculated by integrating over the spatial extent of the system,

$$F\left(\tilde{\mu}, \tilde{U}, \tilde{\tau}\right) = \int_0^\infty d^3\mathbf{r} \ f\left(\tilde{\mu}(\mathbf{r}), \tilde{U}, \tilde{\tau}\right)\left(\frac{\alpha}{v}\right) \tag{5.18}$$

where F is a property of the bulk gas, such as atom number, superfluid number or entropy, and where harmonic confinement leads to a spatial dependence of the chemical potential, α is the number of sites in a unit cell of the lattice and v is the volume of that cell. This approximation ignores correlations across the trap.

We can remove the $\mathbf{r}$-dependence of the equation by a change of variable, using the relation $\mu(\mathbf{r}) = \mu_0 - 1/2m\bar{\omega}^2\mathbf{r}^2$, where m is the atomic mass, $\bar{\omega}$ is the harmonic trapping frequency, and μ_0 is the chemical potential at the center of the trap.

$$\mu = \mu_0 - 1/2m\bar{\omega}^2\mathbf{r}^2 \qquad\qquad \mathbf{r} = \sqrt{\frac{2\left(\mu_0 - \mu\right)}{m\bar{\omega}^2}}$$

$$d\mu = -m\bar{\omega}^2\mathbf{r}d\mathbf{r}$$

$$d^3\mathbf{r} = 4\pi\mathbf{r}^2d\mathbf{r}$$

$$= 4\pi\sqrt{\frac{2\left(\mu_0 - \mu\right)}{m\bar{\omega}^2}}\left(-\frac{d\mu}{m\bar{\omega}^2}\right)$$

$$= \frac{-4\sqrt{2}\pi}{(m\bar{\omega}^2)^{3/2}}\ \sqrt{(\mu_0 - \mu)}\ d\mu$$

so that Eq. (5.18) becomes

$$F\left(\tilde{\mu}_0, \tilde{U}, \tilde{\tau}\right) = \frac{4\sqrt{2}\pi}{(m\bar{\omega}^2)^{3/2}}\left(\frac{\alpha}{v}\right)\int_{-\infty}^{\tilde{\mu}_0}d\tilde{\mu}\ \sqrt{(\tilde{\mu}_0 - \tilde{\mu})}\ f\left(\tilde{\mu}, \tilde{U}, \tilde{\tau}\right) \qquad (5.19)$$

$$= K\int_{-\infty}^{\tilde{\mu}}d\tilde{\mu}'\, f(\tilde{\mu}', \tilde{U}, \tilde{\tau}). \qquad (5.20)$$

Where $F \in \{N, N_{\mathrm{sf}}, S\}$, $f \in \{n, n_{\mathrm{sf}}, s\}$ and the tilde indicates an energy scaled by zJ. The effective number of occupied lattice sites is given by

$$K = \frac{\pi\alpha}{v}\left(\frac{2zJ}{m\bar{\omega}^2}\right)^{3/2} \qquad (5.21)$$

where α is the number of equivalent sites in the unit cell, v is the unit cell volume, m is the atomic mass, and $\bar{\omega}$ is the geometric mean trapping frequency. The quantity N/K generalizes the "characteristic density," as defined by Rigol *et al.* [22], to non-square lattices.

This is to say that, though optical lattice experiments may differ in any particular parameter – N, α, v, $\bar{\omega}$ – any such differences are accounted for if the generalized characteristic density N/K is held constant. This has been discussed in the specific case of a single-site unit cell, where the characteristic density $\tilde{\rho} = Na^d(V/J)^{d/2}$, where V is the trap volume and d the dimensionality, determines system properties, and the superfluid-Mott insulator critical point has been measured for a variety of system parameters and also of $\tilde{\rho}$, confirming that system properties depend only on $\tilde{\rho}$ [6].

Specific to our experiment, Eq. (5.21) means that we can account for a change in α with a corresponding change in the overall trapping frequency of the harmonic confinement ω.

Example: a superfluid at $\tau = 0$

Eq. (5.19) applies everywhere within the Bose-Hubbard phase diagram, which means that we do not have to know the chemical potential or the temperature of the gas in order to perform a valid test of the mean-field scaling prediction.

We know only a zero-temperature approximation to the chemical potential, and only have an analytic expression in the superfluid limit. In this limit, where $\tau = 0$ and in the deep superfluid regime, we can explicitly write down the number density n to find the total number N according to Eq. (5.19).

$$n\left(\mu\left(\mathbf{r}\right),U,0\right) \; = \; \frac{1}{U}\left(\mu_0 - \frac{1}{2}m\omega^2 r^2\right) \; = \; \frac{zJ\tilde{\mu}}{U} \tag{5.22}$$

So that

$$N = \frac{\alpha}{\omega^3}\frac{4\sqrt{2}\pi}{m^{3/2}v}\left(zJ\right)^{3/2}\frac{zJ}{U}\int\limits_{-\infty}^{\tilde{\mu}_0} d\tilde{\mu}\,\tilde{\mu}\sqrt{(\tilde{\mu}_0 - \tilde{\mu})} \tag{5.23}$$

$$= \frac{\alpha}{\omega^3}\frac{4\sqrt{2}\pi}{m^{3/2}v}\frac{(zJ)^{5/2}}{U}\tilde{\mu}_0^{5/2} \tag{5.24}$$

and

$$\tilde{\mu}_0 = \left(\frac{15}{16}\frac{vm^{3/2}\omega^3 UN}{\sqrt{2}\pi\alpha}\right)^{2/5}\frac{1}{zJ} \tag{5.25}$$

$$\mu_0 = zJ\tilde{\mu}_0 \tag{5.26}$$

$$= \mu'\left(\frac{U_0}{U}\frac{v}{\alpha}\right)^{2/5} \tag{5.27}$$

where in the last line we relate this quantity to the chemical potential, μ', of a harmonically confined gas without an optical lattice. In Eq. (5.27) the dependence on zJ has dropped out, and the chemical potentials will be the same in any lattice if $\alpha U/\omega^3$ is held constant.

This example assumes a specific form of $n(\mu, U, \tau)$, which is valid in the $\tau = 0$ and deep-superfluid limit. However Eq. (5.19) applies everywhere within the Bose-Hubbard phase diagram.

5.2.2   Numerics

We follow the minimization procedure to calculate the expected superfluid fraction as a function of the ratio U/zJ, and plot it in 5.2 for two different values of system entropy. In this calculation we assume adiabatic increase of the lattice depth, so that τ/J is constant. As the lattice depth increases, J decreases so that the temperature τ also decreases [26]. An important note is that our blue-detuned lattice does not lead to the compression temperature runaway that is of concern in other lattice works.

In the low entropy case shown, $S/N = 0.4\ k_B$, the temperature of the gas starts lower than the Mott melting temperature $\tau^* \sim 0.2\ U/k_B$, and decreases to near $\tau \sim 0.04\ U$ [27]. In the high entropy case, $S/N = 1k_B$, the initial temperature is $\tau \sim 0.3\ U$. This is consistent

with our calculations of per site particle number as a function of radius, where, in the low entropy case, there is a Mott insulating shell with $n = 1$, but in the high entropy case exhibits no such plateau.
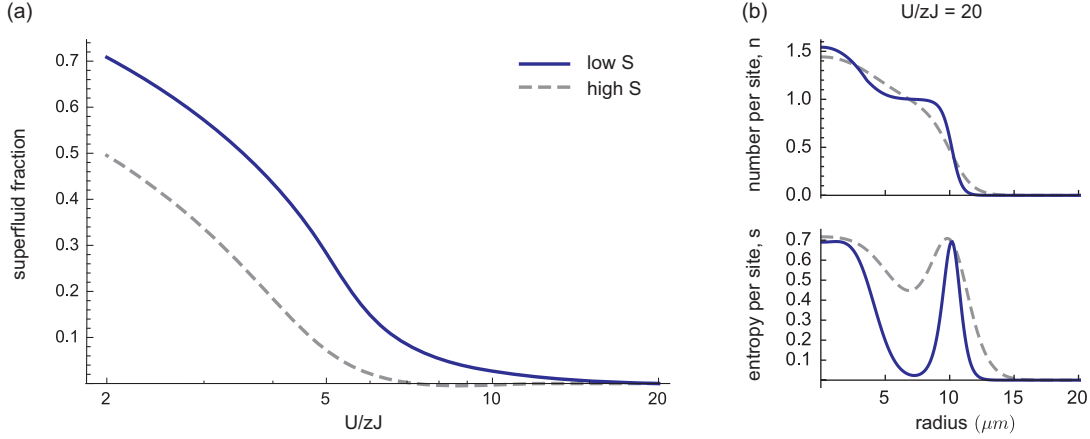
Figure 5.2: The predicted superfluid fraction as a function of U/zJ by finite temperature mean-field theory. We show calculations when considering two values of total entropy. The low-entropy case (dark blue, solid line) results in a local Mott insulator, as indicated by the plateau at $n = 1$, where $s = 0$. The high-entropy case undergoes the transition between the superfluid and normal phases. Our data of coherent fraction are consistent with the low-entropy calculation of superfluid fraction here, the difference in these metrics is discussed in section 5.4.

5.3 Experimental test of the mean-field hypothesis

5.3.1 Experimental sequence and parameters

We start every iteration of the experiment with a Bose-Einstein condensate of $N \sim 100,000 \pm 10\%$ atoms with no discernible thermal population. We find that using tilt evaporation results in a stable number and temperature, so that N and S are the same in every iteration. All experiments are randomized, so that there is no systematic bias between the two geometries or among lattice depths. We then increase the harmonic confinement of the trapping beams while loading the atoms into a vertical lattice of depth $V_\perp/h = 41$ kHz. The trapping frequencies from all red-detuned beams are $(\omega_x, \omega_y, \omega_z) = 2\pi\,(34, 64, 49)$ Hz, so that $\bar{\omega} = 2\pi \times 47$ Hz.

Finally, we ramp the in-plane lattice beams, in either the triangular or kagome lattice geometry, with a base-10 exponential increase of beam intensity. Using a base-10 increase rather than base-e further slows the initial ramp of beam intensity and improves the likeli-

hood of an adiabatic ramp, which may mitigate the challenges identified in adiabaticity of loading an optical lattice [28].

In the final lattices, for a given depth of the green lattice V_{532}, U and J are the same to within 1%, regardless of the lattice geometry. This is because the power in the 1064-lattice beams is low enough that it does not affect the curvature of the wells in which atoms reside, so that the Wannier functions are the same in either lattice.

In our experiment, for technical reasons, we did not change $\bar{\omega}$ to account for the difference in α, so that K of Eq. (5.21) was not held constant.

$$\eta = K^{tri}/K^{kag} \sim 1.43 \tag{5.28}$$

This means that in the kagome lattice, the total entropy and particle number are scaled by a factor of $\eta = 1.43$ relative to the triangular configuration. Figure 5.3 shows that the deviation in the mean-field treatment between the datasets due to this scaling is minimal. We do not expect this to be a large contribution error in the scaling measurement.

We consider the effect that this would have in mean-field treatment we have already described. Here we consider two lattices and plot superfluid fraction against the scaled parameter U/zJ for two lattices. The first that we consider, shown as green triangles in Fig. 5.3, represents a lattice with a constant number and entropy, consistent with the data in our experiment. For the second lattice, we scale the number and entropy by $\eta = 1.43$, and plot as purple six-pointed stars to represent the kagome lattice. The effect of this scaling in the mean-field treatment is shown in Fig. 5.3 and is smaller than the error bars in our experiment.
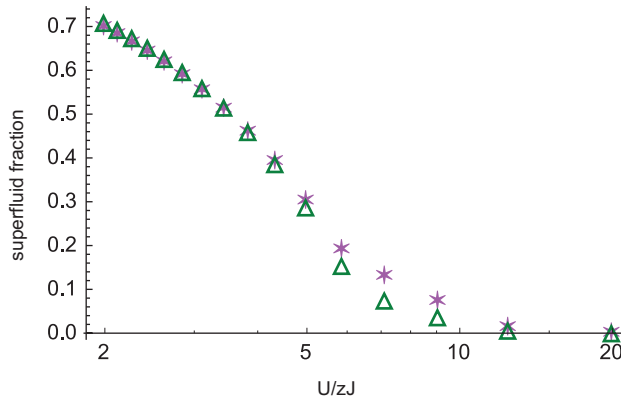
Figure 5.3: A mean-field treatment of a 2-dimensional lattice that includes external harmonic confinement and nonzero temperature, for experiments in which the total number, N, and entropy, S, differ by a factor of $\eta = 1.43$. This represents the difference in the experimental parameters for our kagome (filled purple stars) and triangular (open green triangles) lattices, and shows that though we have a deviation in lattice parameters, we do not expect it to have a strong influence on our scaling result.

5.4 Analysis

In this work we chose to measure the coherent fraction of atoms diffracted from the lattice. This amounts to a correlation function of lattice-trapped gas. It is representative of the superfluid fraction of atoms in the lattice, though the two parameters differ.

5.4.1 Superfluid fraction vs. measured coherent fraction

Coherent fraction offers a representation of the theoretically predicted superfluid fraction, but the two parameters differ throughout the phase transition. Here we highlight two major reasons for the difference. The first is quantum depletion, which causes part of the superfluid to turn up in the tail of the momentum distribution, leading to under-estimation of superfluid number. The second is related to the method of extracting data from the lattice-trapped gas. Atoms are released from the lattice and imaged in the far field, but during the expansion from the lattice they may collide with one another. In chapter 4 we showed that such collisions can lead to misinterpretation of data. In this experiment, collisions among superfluid atoms will result in their appearance at points in k-space other than the superfluid peaks, leading to under-estimation of superfluid number [29].

As interactions grow stronger, the width of the condensate grows and atoms are effectively pushed out of the condensate and into the higher quasimomentum states. These atoms, which are part of the superfluid fraction of the gas, will show up in the higher momentum tails of the distribution, so that they are counted as thermal population in our analysis. This picture of quantum depletion is simplistic. It turns out that there is a regime in which nonzero temperature and interactions can lead to a coherent fraction that is *larger* than the superfluid population [30].

5.4.2 Quantifying the coherent fraction

The measurement procedure is shown in Fig. 5.4 in the case of a superfluid in the kagome lattice, to fully illustrate the procedure. This same procedure, with the same analysis regions, is used for both the kagome and triangular lattice configurations.

After releasing the atoms from optical trapping, we allow them to expand for a quarter cycle in a weakly confining magnetic trap [31]. This procedure, known as "momentum focusing", allows for nearly 100 ms of expansion and thus ensures that the image is taken in the far-field and represents the ground-state of the initial lattice. It also produces a sharp image in momentum-space, so that the peaks that represent coherence are sharp.

After acquiring an image, as shown in the first image in Fig. 5.4, we block out all sharp peaks to fit the thermal distribution in the center of the cloud (at $k = 0$), and subtract that fit to produce the second image. The number of atoms remaining at $k = 0$ are the coherent contribution, and are summed. In the superfluid regime, this procedure yields the same coherent number as performing a parabolic fit to the coherent peak, but such fits don't

make sense in the Mott insulating regime, and our goal was to have an analysis procedure that is exactly the same for all data.

The next step is to count the coherent atoms in the satellite peaks. In theory, each satellite peak is a smaller copy of the zeroth order peak, so that the thermal background on each satellite peak should be the same, only scaled, relative to the zeroth order peak. However, the signal at the satellite peaks is small, so that the thermal regions are difficult to fit reliably. In order to quantify the superfluid in the satellite peaks, we consider two regions around each peak. First, the background region, shown in the third image of Fig. 5.4. These rings represent a region around each peak that contains thermal atoms associated with each peak. They are near the coherent peaks, and the thermal fit at the zeroth order in this data is broad enough that the signal in these rings represents the peak of the thermal distribution. We then sum the data within each satellite peak, shown in the final image of Fig. 5.4. This sum represents both the number of coherent atoms within the regions, on top of the thermal background. The thermal background is then subtracted, using the data from the background rings.

We found this metric to be robust to changes in the size of the analysis regions, so long as the regions encompass only one satellite peak.
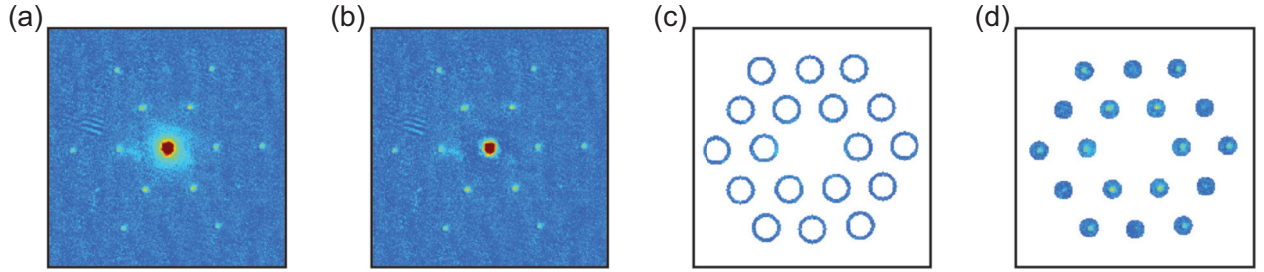
Figure 5.4: Analysis procedure. An absorption image is taken after releasing the atoms into a weakly confining magnetic trap and allowing them to evolve for a quarter-cycle, resulting in a momentum-focused image in the far-field. The second image shows the result after we fit the central thermal cloud and subtract it from the image. This 2 dimensional fit is performed by blocking out the central condensate peak as well as the satellite peaks. The number of condensed atoms in the central peak is counted after the subtraction. The third and fourth images indicate measurements of the satellite condensate number. The satellite peaks don't have enough signal for full bimodal fits. We measure the coherent number by summing population at each coherent peak and subtracting the thermal background measured in the rings. We sampled many different ring sizes to ensure that this was a consistent representation of the thermal background.

State determination by other means

Our measurement of the coherent fraction is performed with a single image. Another more sensitive approach is to take two images, one in which the peak is saturated, so that the non-condensed atomic population is emphasized, and another that is not saturated so that the coherent population can be counted or fit [28, 32]. The method is otherwise comparable to our work. Coherent fraction is also sometimes measured with bimodal fits to the satellite peaks [6].

The most commonly used metric for the state of a lattice-trapped gas is the visibility $\mathcal{V}$ [33]. We think of the measurement in momentum-space as a measurement of the correlation function of lattice-trapped atoms. They scatter from the lattice, resulting in a diffraction pattern on the camera, where the atomic density is spatially varying as $n(\mathbf{r}) \sim |\tilde{w}(\mathbf{k})|^2 \mathcal{S}(\mathbf{k})$, where

$$\mathcal{S}(\mathbf{k}) = \sum_{i,j} e^{i\mathbf{k}\cdot(\mathbf{r}_i - \mathbf{r}_j)} \langle \hat{a}_i^\dagger \hat{a}_j \rangle \tag{5.29}$$

where $\mathbf{r}_i$ labels the position of site i, $\tilde{w}$ is the Fourier transform of the Wannier function $w(\mathbf{r}_i)$. The correlation function $\langle \hat{a}_i^\dagger \hat{a}_j \rangle$ determines the sharpness of the interference peaks. The visibility, defined as

$$\mathcal{V} = \frac{n_{max} - n_{min}}{n_{max} + n_{min}} = \frac{\mathcal{S}_{max} - \mathcal{S}_{min}}{\mathcal{S}_{max} + \mathcal{S}_{min}} \tag{5.30}$$

is then used to quantify the extent of correlations in the lattice-trapped gas. The claim in the second equality is that because the Wannier envelope is the same for n_{min} and n_{max}, it cancels and results in a direct measurement of the contrast in structure factor $\mathcal{S}$. The claim is that this measurement is not sensitive to saturation of the image or mean-field broadening of the individual peaks.

In a square lattice, it is fairly straightforward to define regions of the image to use for the maximum and minimum interference peaks, as illustrated in Fig. 5.5(a). Generally, the maximum density is measured at the location of first-order diffraction, and the minimum density is measured at a point that is equidistant from the zeroth order peak and maximally distant from neighboring first-order peaks. This minimum is at the center of the second Brillouin zone.

The main challenge in applying this metric to our work is that to test the mean-field scaling hypothesis requires an analysis technique that is identical for the triangular and kagome lattices. In both lattices, the location of n_{max} is the same, at the location of the first-order diffraction of the triangular lattice (and second order of the kagome lattice). However, the number of atoms diffracted to that position differs, even when the superfluid fraction in each lattice is identical. The visibility metric generally emphasizes signal of coherence, but is not a very quantitative measurement of the state of a lattice-trapped gas.
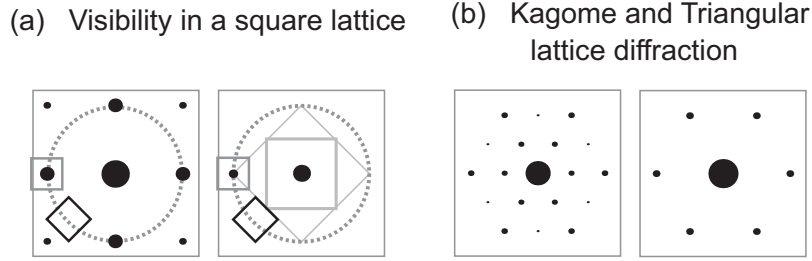
Figure 5.5: (a) The visibility measurement, defined in a square lattice, is hard to define in a lattice with multiple sites in a unit cell and impossible to define consistently for the triangular and kagome lattices in a way that does not systematically change the visibility between the lattices. (b) By definition the visibility will differ in a triangular and kagome lattice that have the same coherent fraction, as indicated by spot-sizes in these calculations deep in the superfluid regime of both lattices.

The central peak width is often cited in conjunction with the visibility $\mathcal{V}$ [34]. Experiments that can resolve independently each site of the optical lattice in real-space have been used to identify the transition by measuring, for example, the string-order parameter that arises due to correlated particle-hole pairs at the transition point [35], or the closing of the Higgs-mode energy gap [7]. A more direct metric for the state of a lattice-trapped gas would be to directly measure its compressibility as the system undergoes the phase transition.

5.5   Sophisticated theoretical treatments

Quantum Monte Carlo data [22, 36] has shown in general that mean-field calculations, which do not include any quantum fluctuations, typically predict a more robust superfluid and thus overestimate the value of U/J at which the superfluid phase will become Mott insulating. A variety of analytical approaches have been developed and compared to the quantum Monte Carlo simulations for simple lattices, and these analytical approaches can be more easily applied than full quantum Monte Carlo simulations when considering complex lattices like the ones reported in this work.

In the mean-field treatments like the Gutzwiller treatment, a lattice system is assumed to be described by a product of density matrices at each lattice site [23–25]. Thermodynamic quantities such as the total density, the superfluid density, and the entropy per particle are then functions only of the scaled interaction strength U/zJ, temperature τ/zJ and chemical potential μ/zJ where z is the lattice coordination number. These treatments thus predict mean-field scaling as well as critical value U/J_c at which a phase transition will occur. In the Gutzwiller calculation presented in this chapter, we treated the tunneling term as a small parameter in Eq. (5.8) to write a separable Hamiltonian.

Many different forms of high-order perturbation theory also depend on a strong-coupling assumption, which is valid because the phase transitions take place at a relatively low values

of J/U [25, 37–39]. We will discuss some results from various perturbative treatments that have been performed for our lattice geometries in the limit of a $\tau = 0$ gas in an infinite and homogenous optical lattice. We then show results from a quantum Monte Carlo treatment in a homogenous lattice for the triangular and kagome geometries, in the case of finite temperature and with a per-site filling of $n = 3$ (in contrast to our experiments, which were performed in a harmonically confining trap with a central filling of $n = 2$). This calculation was performed by Itamar Kimchi during his time here at Berkeley but is unpublished. The results indicate that in a homogenous lattice, when $\tau \sim .03\ U$, the kagome and triangular lattices do not deviate significantly from the mean-field scaling prediction, but their deviation from scaling increases with rising temperature.

Finally, we discuss quantum Monte Carlo calculations for a sample with realistic experimental parameters for an ultracold optical lattice experiment [22]. This data shows that the external harmonic confinement reduces the sensitivity of the phase transition to the temperature of the gas, while leading to an increase in critical point at nearly all characteristic densities $\tilde{\rho}$ relative to a homogenous treatment. This prediction is confirmed in experiments performed in a 2-dimensional square lattice [6], but has not been performed for our optical lattice geometries. Many experimental studies find transition points that are in accord with homogenous quantum Monte Carlo treatments, which is curious given their experimental parameters indicate that they should be sensitive to the effects of external confinement and nonzero temperature [7, 35].

5.5.1 Zero temperature gases in homogenous lattices

First we discuss perturbative treatments of the Bose-Hubbard Hamiltonian in the strong-coupling limit that have been applied to lattice geometries relevant to this work. Treating the Hamiltonian in this limit of small J/U is valid because the transition while J/U remains relatively small, and this is the same limit in which we solved the mean-field Hamiltonian above.

Both methods employ an effective potential method, which modifies the Hamiltonian by adding on-site source and drain terms η and η^*, so that the tunneling term that is treated perturbatively is no longer simply $\sum_{\langle i,j \rangle} \hat{a}_j^\dagger \hat{a}_i$ as in (5.8), but is now

$$\sum_{\langle i,j \rangle} \hat{a}_j^\dagger \hat{a}_i + \sum_i \left(\eta^* \hat{a}_i + \eta \hat{a}_i^\dagger \right) \tag{5.31}$$

This treatment results in a Kato formula for the energy correction due to the perturbation that is solved diagrammatically.

Process chain approach: triangular, cubic and honeycomb

The process-chain approach to solving the equations from the effective potential treatment yields high-precision computations of phase boundaries that are in strong agreement with

full quantum Monte Carlo calculations [40, 41]. This approach has been applied to the three-dimensional cubic lattice ($z = 6$), as well as to the two-dimensional lattices of square ($z = 4$), triangular ($z = 6$), and honeycomb ($z = 3$) geometries. Table 5.5.1 compares the calculated critical points with those from other methods.

The published results from this method enable comparisons of critical points $(U/J)^*$ among various lattice geometries, which will give a sense for the scale of any expected deviations from mean-field scaling, but this ratio is not equivalent to the mean-field scaling ratio ζ that is measured in our manuscript. The mean-field scaling prediction applies to all thermodynamic quantities of lattice-trapped gases, at all interaction strengths, whereas here we are able only to compare the critical points $(U/J)^*$.

In this method, the ratio of determined critical points for two-dimensional triangular to honeycomb lattice is $(U/J)^*_{tri}/(U/J)^*_{honey} \sim 2.3$, which is comparable to the mean-field scaling prediction of $\zeta = z_{tri}/z_{honey} = 2$. However, a treatment of the triangular and cubic lattices, which have the same coordination number ($z = 6$) but differ in dimensionality, predicts critical points that differ by about 10%, with the cubic lattice exhibiting a phase transition at a smaller value of U/J. Such a large deviation from the mean-field scaling prediction would be evident in our experiment.

This result suggests that it would be interesting to use our superlattice to compare the transition in the two-dimensional triangular lattice with a three-dimensional kagome lattice, where we introduce tunneling along the vertical axis thereby increasing the number of nearest neighbors at a site by two. These lattices would have the same coordination number, $z = 6$, and differ in dimensionality, so that they might show the same deviation of critical point (and thus deviation from mean-field scaling).

Another significant finding of this work is that, though the critical point for the first Mott lobe differs from the mean-field prediction for a two-dimensional lattice, the relationship between it and the critical points of higher Mott lobes is well-captured by a mean-field treatment.

Line-dot diagrams: triangular and kagome

Lin et. al. [37] use the same effective potential method, this time solving with a line-dot diagram representation to find critical points $(U/J)^*$. This method overestimates the critical point when compared to the more accurate treatments (Table 5.5.1), but has been applied to two-dimensional lattices of both triangular and kagome geometry.

This treatment predicts a critical point for the transition between the superfluid phase and Mott insulating phase with filling $n = 2$ of a $\tau = 0$ gas in a homogenous, two-dimensional lattice of the triangular ($z = 6$) and kagome ($z = 4$) geometries of $(U/J)^*_{tri,n=2} = 50$ and $(U/J)^*_{kag,n=2} = 29.4$. These values are comparable to the points in our data at which coherent fraction goes to zero (see Fig. 2 of appendix C, though our data are more consistent with the higher predictions of mean-field theory. As we will discuss, including external harmonic confinement in a quantum Monte Carlo treatment increases the prediction of U/J^* relative to the homogenous case.

These are the only published results of predictions in the kagome lattice, for which $z = 4$, and they are similar to predictions by other means of a two-dimensional square lattice, which also has $z = 4$. Again, we can compare the ratios of critical points $(U/J)^*$, which will give a sense for the scale of any expected deviations from mean-field scaling, but this ratio is not equivalent to the mean-field scaling ratio ζ that is measured in our manuscript. Though this treatment does not depend on mean-field scaling arguments, the critical points exhibit only a small modification to a mean-field scaling prediction. In this treatment, the ratio $(U/J)^*_{tri}/(U/J)^*_{kag} \sim 1.7$, which we compare to the mean field scaling ratio $\zeta = z_{tri}/z_{kag} = 1.5$. This ratio is within error of our scaling measurement of $\zeta = 1.6 \pm 0.1$, though we emphasize that the scaling measurement is performed along the entire trajectory of loss in coherence, so it cannot be directly compared with the ratio above.

Summary of calculated critical points

A summary of predictions from a few theoretical treatments for a zero temperature gas in an infinite lattice without external harmonic confinement. We show a variety of lattice geometries and treatments to give a sense of how the predicted critical points compare amongst themselves.

	Lattice structure	QMC [36]		Strong-coupling, $U/J \gg 1$		
				Mean-field	Effective potential	
	square ($z = 4$)	17		23	17	
n = 1	cubic ($z = 6$)	29		35	29	
	triangular ($z = 6$)			35	27	29
	square ($z = 4$)			40	28	
n = 2	cubic ($z = 6$)			60	50	
	triangular ($z = 6$)			60	45	50

Process-chain [40, 41]   Line-dot [37]

Table 5.1: Predicted Critical Values $(U/J)^*$ for a Homogenous Lattice with $\tau = 0$. Generally, the mean-field treatment overestimates the critical point relative to quantum Monte Carlo calculations, whereas high-order perturbation theory treatments using the effective potential method give more accurate estimates. Where they can be compared, the process-chain method of solving the effective potential Hamiltonian perturbatively yields critical points that agree with those from qMC data. The predictions from a line-dot approach deviate from those of the process-chain method, suggesting that they may be less reliable, but they have been performed for the triangular and kagome lattices and are thus relevant to our work in these lattices, where we have a central filling of $n = 2$. Not shown are the results of the line-dot approach for the kagome lattice, which predicts an $n = 1$ transition at $(U/J)^* \sim 18$ and $n = 2$ at $(U/J)^* \sim 30$ [37], and the results of the process-chain approach for a honeycomb lattice ($z = 3$), which finds, for example, a transition in the $n = 1$ case of $(U/J)^* \sim 12$. The high-order perturbation treatment results can be compared among lattices with different z to give a sense for deviations of critical points from mean-field scaling. However, mean-field scaling is a prediction of thermodynamic properties for *all* values of U/J, and here we can compare only the critical points. This table shows that critical points in two-dimensional lattices tend to have a ratio near that predicted in mean field scaling parameter $\zeta = z/z$, but there is a discrepancy in lattices of the same coordination number and different dimensionality.

5.5.2   Nonzero temperature gases in homogenous lattices: kagome and triangular

Itamar Kimchi performed quantum Monte Carlo calculations for the homogenous kagome and triangular lattices considering nonzero temperatures and a filling of $n = 3$ atoms per site. This is not directly applicable to our experiments, which are performed with a central filling of $n = 2$, but can give qualitative data of the expected deviations from mean-field scaling in the system that is treated.

These calculations show that in the low temperature limit, where $\tau < 0.03\ U$, homogenous qMC does not predict a large deviation from the mean-field scaling prediction. As temperature increases to near the melting temperature of the Mott insulator, $\tau = 0.3\ U$, the

deviation from mean-field scaling grows and in the high temperature limit, where the loss in coherence is due to a transition between the superfluid and normal phases, there is a large difference between the coherent fraction in the kagome and triangular lattices after scaling the interaction energy U by the mean-field scaling parameter zJ.
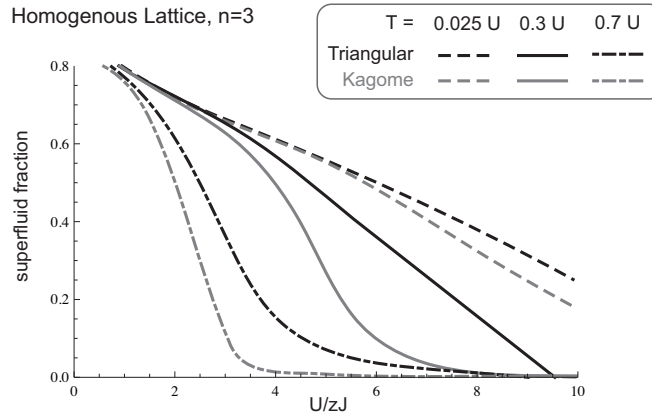
Figure 5.6: Quantum Monte Carlo simulation for a homogenous gas with nonzero temperature in the kagome and triangular lattices. At very low temperature, where our experiments are performed, there is very little deviation from the mean-field scaling prediction in the two lattices. As temperature increases, the separation between superfluid fraction in the two lattices increases, note that these transitions correspond to a transition between the superfluid and normal gas.

5.5.3 Nonzero temperature gases in harmonically confined lattices

Finally, we highlight the results of a quantum Monte Carlo calculation that considers a finite temperature gas in a harmonically confined trap that has been performed for the square lattice and discuss its implications to our work [22]. When the lattice-trapped gas draws near the critical point where Mott insulating domains are formed, the particle-particle correlations diverge and the local density approximation fails. In this region, finite-size effects should play an important role that is neglected by all previously discussed homogenous lattice treatments.

In this quantum Monte Carlo treatment it was shown that experimental details like particle number and harmonic confinement are accounted for by just one parameter, the characteristic density $\tilde{\rho} = Na^d(V/J)^{d/2}$ of the lattice-trapped gas. A trapping potential leads to a higher critical value than for the homogenous system, for nearly all values of $\tilde{\rho}$, especially in the case where $n = 1$. This is a powerful statement for two reasons. First, it means that the critical point of a phase transition will vary based on the trapping frquency, lattice spacing, number of atoms, and dimensionality of the optical lattice system. This

seems to indicate that any quantum simulation will only give information that is specific to the apparatus. However, the identification of the parameter $\tilde{\rho}$ means that all such systems may be compared to one another on a single phase diagram, and that their findings can be generalized to the material systems that they aim to emulate. The superfluid-Mott insulator critical point has been measured for a variety of system parameters and also of $\tilde{\rho}$, confirming that system properties depend only on $\tilde{\rho}$ [6]. Intriguingly, this seems to hold true even in cases where the local density approximation is not valid [22]. In our work, we generalized this concept to non-square lattices, which may have multiple sites per unit cell. The generalized characteristic density N/K, where K is defined in (5.21), also allows for the comparison of critical points in lattices of different geometry.

This work also finds that in two dimensions, the effect of nonzero temperature is mitigated by the harmonic confinement, for $\tau \leq J/2$ the critical value at which Mott insulating regions form is changed only by a few percent. This likely impacts the nonzero temperature predictions of deviations between the kagome and triangular lattice that are apparent in Fig. 5.6.

5.6 Geometry-tuned phase transitions

As a quantum simulator, our experiment explores the effect of lattice geometry on the superfluid to Mott insulator transition of a lattice-trapped Bose gas. In several solid-state materials, the analogous phase transition in fermionic matter, between metal and Mott insulating phases, is observed coincidently with structural transitions of the crystalline lattice [42]. Distinguishing cause from effect in such simultaneous transitions is complicated by the strong mutual influence between the electronic and lattice structures [43, 44], and by the limited quality and tunability of crystalline samples [45, 46]. In our work, because the optical lattice is imposed externally and independent of the state of the trapped atoms, we may explore cleanly the causal influence of structural crystalline changes on transport properties. In the publication we showed the transition from Mott insulator to superfluid driven by change in geometry from kagome to triangular.

5.6.1 Transient dynamics

In the experiments reported in our manuscript, we showed that a rapid quench from the Mott insulating state of the kagome lattice to the superfluid regime of the triangular lattice resulted in rapid heating of the gas. This introduction of empty sites is an analog to "hole-doping" in condensed matter physics.

We explored quenching between the lattices in both directions, in the superfluid and Mott insulating regimes of both lattices. The timescales that we observed for a rapid early increase in $\tilde{P}_i$ were similar (50-150 μs) for a variety of different lattice depths, all of which are much faster than the characteristic timescales h/zJ.
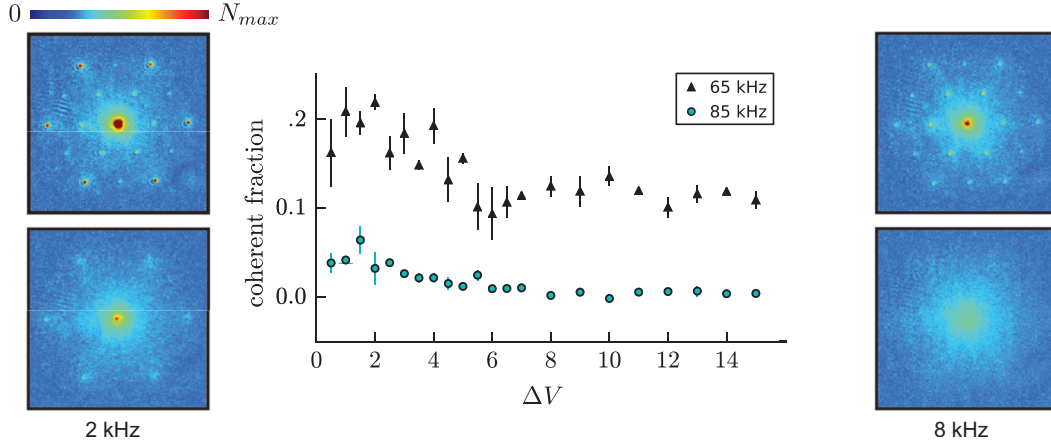
Figure 5.7: Geometry-induced superfluid to Mott insulator transition for constant U and J. Images revealing the momentum distribution of the atoms in the lattice. We show distributions after atoms are released from the triangular (left) and decorated triangular (right) geometries for $V_{532} = 65$ and 85 kHz. The central plot shows coherent fraction, which decreases as atoms are expelled from three of every four sites, causing a phase transition between the superfluid triangular lattice and the Mott insulator in the decorated triangular lattice.

Such timescales within the ground band of the lattice represents dynamics of strongly-interacting superfluid. However, projection of superfluid atoms into higher bands would lead to single-particle oscillations at high frequency, similar to that reported in chapter 4.

To distinguish these two possibilities, we immediately followed the quench with bandmapping measurements to find which bands were occupied after the quench. We found that when we "hole-dope" the triangular lattice by introducing vacant sites, the increase in population at the 1064-nm peaks appears in the ground-band of the triangular lattice, and there is no discernible population of atoms in upper bands. This means that the rapid motion of atoms in momentum-space images represent ground-band physics of a strongly interacting superfluid rapidly redistributing within the unit cell of the lattice. At all lattice depths in bandmapping measurements we observed the same increase in population at the 1064-nm peaks within the triangular ground band, and no occupation in higher bands.

5.6.2   Scanning ΔV in the decorated triangular lattice

This data has not been published and shows a transition between the Mott insulator of the decorated triangular lattice (with spacing $2a$) to the superfluid of the triangular lattice (with

spacing a).

The procedure for these experiments is the same as the one described in the manuscript in appendix C, except that here we work in the decorated triangular lattice configuration of our bichromatic superlattice. We prepare a nearly pure ^{87}Rb Bose-Einstein condensates of between 0.5 and 3×10^5 atoms in the $|F = 1, m_F = -1\rangle$ hyperfine state with a negligible thermal fraction in a red-detuned crossed optical dipole trap, characterized by trap frequencies of $(\omega_x, \omega_y, \omega_z) = 2\pi \times (34, 64, 49)$ Hz. We then impose a one-dimensional lattice with $V_{pp} = \hbar \times 41$ kHz formed by a retroreflected 1064-nm-wavelength beam propagating vertically. The gas is thus divided among approximately 17 two-dimensional planes with a tunneling rate of 5 Hz, so that they are effectively decoupled over the timescale of our experiments. Finally, we adiabatically load the atoms into the bichromatic lattice with a simultaneous exponential increase of the six lattice beam intensities to the final trap depths shown in Fig. 5.7.

After allowing 30 ms for the lattice-trapped gas to equilibrate, the atoms are released from the lattice, allowed to expand, and then probed by absorption imaging. The vertical lattice is ramped off about 150 μs prior to the turn-off of the superlattice and optical traps, as this was observed to reduce the s-wave scattering out of the vertical lattice in the momentum-space measurements, resulting in more accurate measurements of condensate fraction.

In Fig. 5.7, we characterize the superfluid to Mott insulator transition with the coherent fraction of atoms in an image, which we calculate as the coherent population N_c, obtained by summing the coherent signal in all peaks of the momentum distribution, divided by the total atom number N_{tot}, determined by summing over the entire image. Data shown in Fig. 5.7 are averages over 3 - 5 experimental repetitions, and error bars are statistical.

In Fig. 5.7 (a), we compare the time-of-flight images obtained for atoms expanding from the bichromatic lattice at two different values of V_{532} (and thus U/J). The coherent peaks in the upper panels show the change in lattice geometry from triangular to decorated triangular.

The reduction of coherent fraction with the increase of ΔV is indicative of a change in the transport properties of itinerant particles due to a structural change of the lattice potential in which they propagate. To ensure that the loss in superfluidity is due to the change in lattice geometry and not heating from the increased intensity of the 1064-nm lattice we performed round trips between the two lattices, wherein we tune ΔV to its final value, hold, and then return to the initial value of 0.5 kHz and observe minimal heating.

We have observed a geometrically-tuned transition from the superfluid triangular lattice to the Mott insulating decorated triangular lattice, while holding the tunneling and on-site interaction energies constant. The chemical potential μ increases with ΔV by 12%, which slightly increases the central filling of the trapped gas. We performed these experiments at a variety of triangular lattice depths, and observe increase in Mott insulating signal (loss in coherence) for triangular lattices near the transition point. At the deepest triangular lattice we observe the complete phase transition into the decorated triangular Mott insulating phase.

Chapter 6

Conclusion

6.1 Overview

This thesis describes the construction and testing of a quantum simulator using ultracold atoms in a bichromatic optical superlattice of tunable geometry. Optical lattices take a bottom-up approach to studying the physics of crystalline materials. In an optical lattice experiment, the crystal structure is specified experimentally and it is distinct from the itinerant particles that propagate within. Individual properties of either the lattice or the quantum gas may be adjusted without modification of other physical properties of the material. These artificial crystals allow for ideal realizations of Hamiltonians and thus have the potential to test the many condensed matter theories that attempt to describe properties of real materials [47, 48].

However, interpreting data from optical lattice experiments to make quantitative statements about condensed matter theories is challenging. In this thesis, we developed a variety of experimental and theoretical techniques to make straightforward, quantitative statements using optical lattices. This conclusion discusses the implications of our work to the fields of both atomic and condensed matter physics, as well as future directions in our lab.

6.2 Theoretical motivations for this work

The work in this thesis is motivated by two central challenges in condensed matter theory. First, we built a lattice that may take on the two-dimensional kagome lattice geometry, paving the way for exploration of geometric frustration in a well-controlled optical lattice simulation. Second, we studied a phase transition that is driven by strong inter-particle interactions, which often make exact numerical solutions challenging

6.2.1 Geometric frustration in the kagome lattice

A central motivation for creating the bichromatic optical lattice was realization of the two-dimensional kagome lattice. The structure of the kagome lattice gives rise to a high degree of geometrical frustration [49, 50]. This frustration is apparent when there is antiferromagnetic ordering on the lattice. The ground state of the kagome antiferromagnet may be a quantum spin liquid or valence bond solid, but its nature remains uncertain despite decades of work [51–58].

The geometrical frustration is also apparent in the band structure of the kagome lattice. The three sites in the unit cell generate three connected *s*-orbital bands. The frustration besetting antiferromagnetic interactions implies that one of these bands be non-dispersing. Such flat bands accentuate the role of interparticle interactions, leading possibly to crystalline ordering [59] and supersolidity [60] for scalar bosons, and ferromagnetism of itinerant fermions [61].

The kagome lattice is an ideal system to simulate using ultracold atoms in optical lattices, because studying the geometrical frustration of the kagome magnet in real materials is complicated by their significant magnetic disorder [62, 63]. Our experimental apparatus is well-suited to study physics in the flat band of the kagome lattice. The flat band is the second excited band, and in this conclusion I will describe techniques by which we plan to populate the flat band band with a degenerate Bose gas of rubidium. Flat-band physics has also been recently studied in an optical Leib lattice [64, 65].

6.2.2 Interaction-driven phase transition

A lattice-trapped gas undergoes a phase transition between superfluid and Mott insulating states under increasing particle-particle interactions. Mapping out the phase diagram necessitates treatment of strong interactions and long-range quantum fluctuations, which can be complicated to describe theoretically. Quantum Monte Carlo calculations may be applied to specific lattice structures, but they are computationally difficult and require precise inputs of experimental parameters [22, 36]. A variety of approximate analytical treatments have also been developed citeDosSantos2009, Lin2012, Wei2016, Freericks1996.

Each of these treatments predicts a different trajectory of the change in coherence of the lattice-trapped gas as interparticle interactions increase. The theoretical treatments may be compared to quantum Monte Carlo treatments in systems for which quantum Monte Carlo calculations have been performed, but these are limited. To distinguish them experimentally remains an outstanding challenge, because of the assumptions they make about temperature and external confinement, and because those parameters change the critical point in a quantum Monte Carlo treatment.

In chapter 5, we increased the strength of interactions in two distinct lattice geometries – triangular and kagome – and measured the correlation function of lattice-trapped atoms as they underwent the interaction-driven phase transition between the superfluid and Mott insulating phases. By examining the relative behavior of identical gases trapped in lattices

that were identical but for their geometry, we were able to make a quantitative measurement concerning the phase transition that was insensitive to many experimental parameters.

6.3 New tools

To address these challenges required both technical and theoretical advances.

6.3.1 Engineering developments

Construction of a triangular superlattice

The design, construction and operation of our experiment are detailed in chapter 2 and chapter 3. Our experiment was the first non-square optical superlattice and is the first realization of the kagome lattice, which has also been realized in a photonic system [66].

The design of our optical lattice hinged on the recognition that the kagome lattice is a triangular lattice with one out of every four sites omitted. In our design, triangular lattices of intensity minima are formed with light at commensurate wavelengths, one of which is blue-detuned ($\lambda = 532$ nm) from the rubidium atomic resonances, and the other of which is red-detuned ($\lambda = 1064$ nm). This enabled us to create a kagome lattice simply by overlaying two lattices of intensity minima, as the atoms are attracted to the minima of the lattice formed by the blue-detuned light and repelled from the minima of the lattice formed by red-detuned light. The scheme also depends on the fact that triangular intensity lattices formed at the intersection of three beams incident from equal angles and with in-plane polarization will form a lattice in which the influence of the triangular pattern is stronger than that of the honeycomb pattern. This enabled us to form an optical kagome lattice and neglect the influence of the honeycomb lattice sites of the 1064-nm lattice. The three sites in the kagome lattice unit cell are nearly identical to the four sites in the triangular lattice unit cell. This enabled us to compare the properties of itinerant particles on the two lattices.

Geometry and stability

In creating a lattice with independent beam paths, rather than using retroreflected lattice beams, we were able to significantly relax the constraints on the stabilization of the two triangular lattices relative to one another. We recognized that by maintaining equal path lengths between the laser source and the atomic sample, we could create a passively stable lattice. Our data show that lifetimes of atoms in our lattices are roughly 1 second without active stabilization.

The scheme for stabilizing the lattices involves stabilizing each lattice independently, and tuning their position using a piece of glass in one path of each interferometer. This results in two lattices that are absolutely stable in space, with a phase determined by the amount of glass through which the beams pass. The lattices may be repositioned with respect to each other over essentially arbitrary trajectories, and under closed feedback control. This will be interesting for realizing artificial gauge fields in the optical lattices, because the lattice can

be tuned through arbitrary trajectories and even non-periodic paths under feedback control. It also makes possible experiments on topological effects such as a Thouless pump [67], or interferometry experiments that measure band curvature [68–70]. These experiments will be interesting to pursue in the future.

We also recognized that the constraint that the two lasers the form the bichromatic optical lattice are commensurate is not a very stringent one. The extent of the Bose-Einstein condensate is small, and the requirement that one laser have a wavelength that is twice that of the other over the extent of the quantum gas is not a strong constraining on the frequency of the laser sources. Any frequency noise in either laser is irrelevant to the other, because of the technique by which we stabilize the lattices in real space.

Layout

This system requires that many optical beams overlap at the location of the ~ 10 μm spot size of the atomic sample. We achieve ease of alignment by co-propagating as many optical beam paths as possible. Moreover, most of our alignment is achieved without use of atoms for diagnostics, which considerably expedites the alignment process.

Calibration

The optical lattice in this work has many components, which must all be stable and regularly calibrated. We used the most precise calibration technique – lattice modulation spectroscopy – regularly throughout each day while taking data for our experiment in which we made a quantitative test concerning the ground-state of a bosonic gas in an optical lattice. We found that the lattice is stable over the course of five hours. This implies that our alignment techniques are effective and our lattice design is stable.

6.3.2 Experimental and theoretical developments

Characterization of optical lattices

Precise quantum simulations require precise lattice characterization. We developed a new technique for characterizing optical lattices, discussed in chapter 4 and included in appendix B. Matter-wave diffraction was developed to measure precisely an optical lattice configuration, in analogy to x-ray diffraction from solids. Tuning the interaction time between light and atoms led to strong enhancement of the effects of slight potential asymmetries.

We developed a perturbation theory to explain the enhanced signal of momentum-space asymmetry from an inversion-asymmetric honeycomb lattice potential using a single-particle band structure of the unperturbed, symmetric honeycomb lattice. In this work, we identified criteria by which one can identify the states of the unperturbed Hamiltonian that will contribute to the momentum-space asymmetry when an asymmetric perturbation is introduced. This work provides an explanation for previously poorly-understood observations in

time-of-flight data in another experiment [18]. Together, these works have implications in how time-of-flight data from optical lattices must be interpreted.

In section 2.4, we developed an analysis of momentum-space data to determine the real-space superfluid population in each site within a unit cell. This was originally developed to distinguish the two C_6 symmetric superlattices in our bichromatic lattice system, the kagome lattice and the decorated triangular lattice. In this thesis it is also discussed as another test of the inversion symmetry of the honeycomb optical lattice.

Calculating Wannier functions

Another advance presented in this thesis was the calculation of tunneling and on-site interaction energies in an optical lattice using Wannier functions calculated simply as the Fourier transform of the single-particle Bloch states with the correct choice of phase so that the Wannier functions are real, as outlined in section 2.6. This effort was spearheaded by Prof. Dan Stamper-Kurn and Dr. Masayuki Okano, who calculated and compared this simple treatment to that of a full-scale minimization technique and found that there was no difference between the two calculations for the low-energy states.

Quantitative tests with an optical lattice

In our work, we take a new approach to using ultracold gases in optical lattices to test a condensed matter theory. Although the Bose-Hubbard model has been realized in many laboratories with ultracold bosons in optical lattices, using these systems to make quantitative statements about the model has remained a major challenge in the field. This is because there are many experimental parameters that shift the critical point of the phase transition between superfluid and Mott insulating ground states of the optical lattice, so that every optical lattice experiment *should* measure a different critical point [6, 22, 28]. Identifying the critical point of the phase transition in an optical lattice system in an attempt to distinguish various theoretical treatments of the Bose-Hubbard model is an extremely challenging task.

We developed a method to compare lattices of different geometry, with different trapping frequencies and with gases at nonzero temperature, which is distilled in Eq. (5.21). We use the tunable bichromatic lattice and the characteristic density to compare the phase transition in two lattices. Rather than test the theories at a single critical point, we test a prediction of the mean-field treatment of the Bose-Hubbard model that holds for the entire trajectory of loss in coherence as the atoms undergo the phase transition between superfluid and Mott insulating states. This is a straightforward quantitative test of a condensed matter treatment of the Bose-Hubbard model.

Extending this test to other theories

We developed a technique of using the characteristic density and multiple similar optical lattices to circumvent the many experimental challenges in testing particular condensed matter theories. This technique may be applied to increasingly complex theories.

Imagine two numerical methods that make different predictions of properties of lattice-trapped gases. Direct comparisons of these methods may require precise measurements of system properties that are beyond the capacity of a given optical lattice experiment. However, we might consider applying both methods to two distinct lattices. Each numerical method will predict a difference in the properties of the lattice trapped gas for the two lattice geometries. This difference is straightforward to detect in an experiment, and in this way the two numerical methods may be distinguished. This type of relative experimental test allows for more quantitative tests of theory.

6.4 Future directions in this apparatus

6.4.1 Probing the flat band

The study of geometric frustration in the kagome lattice requires populating the flat band with atoms. Loading a bosonic condensate into the flat band of the kagome lattice is a prominent goal in this lab. The flat band is an excited state of the kagome lattice, and the condensate occupies the ground state of the lattice. Loading atoms into the flat band will be achieved either by promoting the atoms to the flat band or by inverting the band structure.

In either case, loading atoms into the flat-band states results in substantial direct interactions between atoms in neighboring lattice sites [60]. At low fillings of the lattice, below $n = 1/3$ per unit cell, this long-range repulsive interaction can be accommodated by Wigner crystallization, with each boson in an isolated, single-particle Wannier state. At higher fillings, interactions must come into play. Huber and Altman predict the existence of a supersolid at intermediate filling (superfluid atop the Wigner crystal) giving way to a uniform superfluid at higher filling.

Here we introduce the methods by which we may load a condensed gas into the flat band of the kagome lattice.

Inverting the band structure

The first method is to shake the phase of the lattice to invert the tunneling parameter and thus invert the entire kagome band structure. This has been discussed extensively in experiments on imposing artificial gauge fields with optical lattices [47]. In our geometry it will also be interesting to consider the imaginary second-order tunneling that arises from shaking non-square optical lattices [71]. However, heating is often a problem in such shaking experiments and in the case of the flat band the signal might be hard to separate from heating.

Promoting atoms to the flat band state

Promoting atoms to the flat band will result in a metastable state, but the lifetime in this state may be quite long. By energy conservation, collisional relaxation into one of the lower

s-bands requires an atom be excited by an energy on the order of J. However, the spectrum of single particle states above the flat band is gapped by several recoil energies, precluding such relaxation. The lifetime of these flat band atoms may be sufficient to allow for the study of interaction-driven correlations.

Intensity modulation

Likely the technically simplest method of populating the flat band will be by intensity modulation at the frequency of the energy gap between the first and third s-bands. We expect that an overall modulation of the lattice strength cannot drive excitations at quasi-momentum $q = 0$ from the ground-state to the touching point of the second and third bands of the kagome lattice: at $q = 0$, the three-fold rotational symmetry of the kagome lattice is reflected in the energy eigenstates, which are eigenstates of the C_3 rotation operator; a modulation respecting that symmetry (like intensity modulation) preserves the eigenvalues, which differ for the ground and the next two excited states.

This has two significant implications. The first is that the transition probability to the third band at $q = 0$ is strongly dependent on lattice geometry. By tuning the geometry while modulating at the $q = 0$ band gap, we should observe a dip in transition probability that indicates the frustration of the flat band of the lattice. The second is that, when in the kagome geometry, even a small displacement of the initial condensate will enable excitation into the flat band. We can fully map out the band structure of the lattice, either by displacing the condensate before modulation, or by using a thermal gas that occupies many momenta. The response of the gas may be monitored by Bloch-state analysis of time-of-flight measurements, band-mapping measurements, or quantifying the energy absorbed by the gas via the atom loss or temperature increase.

Non-adiabatic changes in lattice geometry

The additional degrees of freedom available in a superlattice have been used to create artificial gauge fields and p-band band superfluids [11, 47, 72]. Non-adiabatic shifts of the two constituent lattices relative to one another can lead to population in arbitrary bands of the lattice, by the technique shown schematically in Fig. 6.1.

The procedure involves first loading atoms into one site of the four-site unit cell of the bichromatic lattice. This configuration is the decorated triangular lattice in which one site is deeper than the other three, and in the figure the D sites are the occupied sites. After the atoms are loaded into the D-site, the lattice is rapidly deformed by moving the intensity minimum of the 1064-nm lattice within the unit cell. Note that in our lattice this can be done by shifting the phases in-loop, so that the phases remain stable throughout the experiment. In Fig. 6.1(b), the D-site becomes the third-deepest well, with two deeper sites, sites A and B in the figure, and one shallower, site C in the figure. The occupied site now corresponds to the third band of a lattice. To illustrate the point, we show band mapping data from this lattice, which shows that atoms are occupying the third band. From here, the task will be to adiabatically deform the lattice to the kagome configuration by bringing the occupied atoms of site D into resonance with the two low-energy sites, A and B. This effectively flattens the

occupied band until it becomes that of the kagome lattice. The atoms in this upper state are metastable, so the lattice must be deformed slowly with respect to band gaps, but quickly compared to collisions that would cause relaxation into the lower bands.
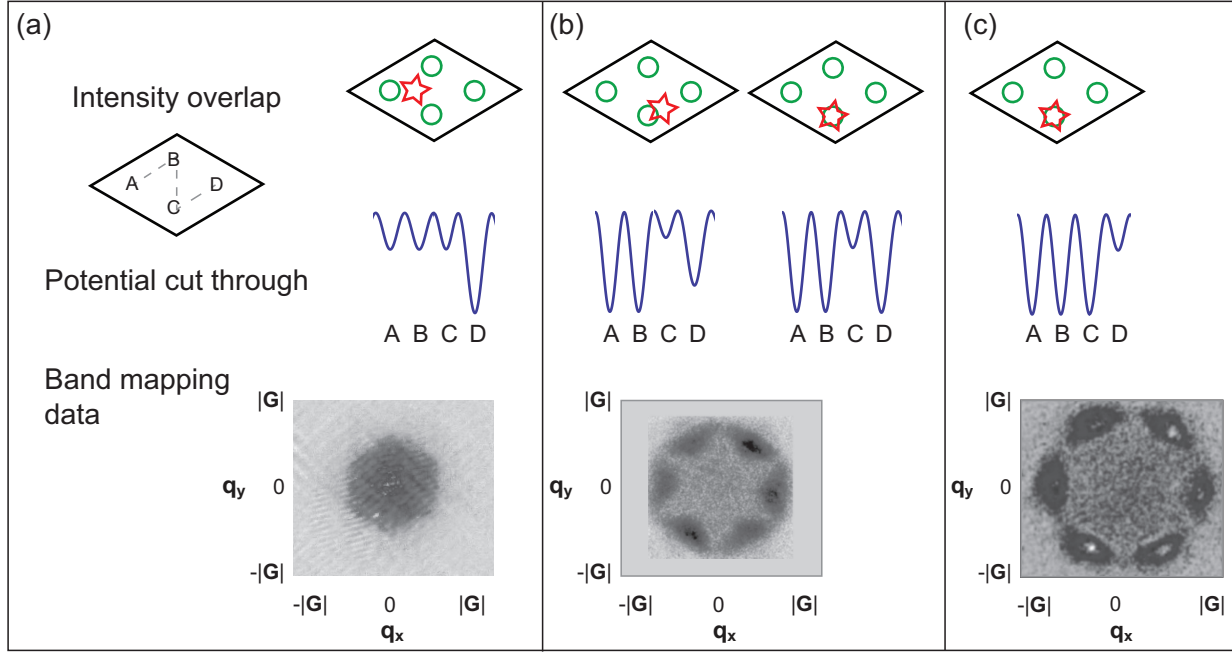
Figure 6.1: Loading atoms into upper bands of a bichromatic lattice. (a) Schematic of the bichromatic unit cell and illustration of a slice through the sites. Loading atoms into the decorated triangular lattice in which site D is lower in energy than any other sites. Ground state atoms occupy only site D. Band mapping of a thermal cloud in this lattice is shown in the lower panel. (b) Rapidly deforming the lattice so that site D corresponds to the third band of a bichromatic lattice (left). Band mapping image shows that the third band of a lattice is populated. This is not the kagome lattice, and the band has curvature, but adiabatically moving to the kagome lattice shown schematically on the right would flatten the third band where the atoms reside. (c) Alternatively, after loading atoms into site D, one can rapidly deform the lattice, exchanging all upper and lower sites. The result is an inverted triangular lattice, in which tunneling among D sites is mediated by the lower energy bands. This metastable state relies on second-order tunneling, which is negative.

6.4.2 Chiral state in an upper band triangular lattice

An alternative lattice deformation is shown in Fig. 6.1(c). Here, we would load atoms into the D-site as in Fig. 6.1(a) and then completely invert the lattice structure. This changes the lattice geometry the D-site decorated triangular lattice to the kagome lattice in which the D-site is raised in energy. The result is a metastable state occupying an upper-band

D-site decorated triangular lattice. Tunneling in this metastable lattice is mediated by the neighboring low energy sites, so that it is second order and negative, $J' \sim -J/\Delta$, where J is the tunneling parameter of the kagome lattice and J' represents the second order tunneling in this metastable triangular lattice configuration.

The upper band decorated triangular lattice formed by the method in Fig. 6.1(c) may host a chiral Mott insulating state. The phase diagram is calculated in Ref. [73]. While a conventional Mott insulator has a wavefunction that is a product of uncorrelated Fock states on each lattice site, a chiral Mott insulator maintains quantum correlations among neighboring sites despite the small value of U/J.

Procedure

To make the chiral superfluid we load atoms into the D-site triangular lattice and quickly shift the phases along both interferometers to reach the kagome lattice. In this way, atoms are prepared in the upper band of the kagome lattice, and can be described as a LW triangular lattice with negative, second-order tunneling.

The ground state of the low-depth, negative tunneling triangular lattice is the chiral superfluid, with flow in either clockwise or counter-clockwise direction, which spontaneously breaks the $K - K'$ symmetry of the bands. Superfluid peaks should appear at one or the other of those points. After establishing a chiral superfluid in a lattice of tubes, we will load the vertical lattice, so that every pancake has the same chirality and the signal will be unambiguous.

Appendix A

Ultracold Atoms in a Tunable Optical Kagome Lattice

This appendix includes the following paper [13], discussed in Chapter 2:

- G.-B. Jo, J. Guzman, C. K. Thomas, P. Hosur, A. Vishwanath, and D. M. Stamper-Kurn, "Ultracold Atoms in a Tunable Optical Kagome Lattice," Phys. Rev. Lett. **108**, 045305 (2012).

Ultracold Atoms in a Tunable Optical Kagome Lattice

Gyu-Boong Jo,[1] Jennie Guzman,[1] Claire K. Thomas,[1] Pavan Hosur,[1] Ashvin Vishwanath,[1,2] and Dan M. Stamper-Kurn[1,2]

[1]*Department of Physics, University of California, Berkeley California 94720, USA*
[2]*Materials Sciences Division, Lawrence Berkeley National Laboratory, Berkeley, California 94720, USA*
(Received 23 September 2011; published 25 January 2012)

We realize a two-dimensional kagome lattice for ultracold atoms by overlaying two commensurate triangular optical lattices generated by light at the wavelengths of 532 and 1064 nm. Stabilizing and tuning the relative position of the two lattices, we explore different lattice geometries including a kagome, a one-dimensional stripe, and a decorated triangular lattice. We characterize these geometries using Kapitza-Dirac diffraction and by analyzing the Bloch-state composition of a superfluid released suddenly from the lattice. The Bloch-state analysis also allows us to determine the ground-state distribution within the superlattice unit cell. The lattices implemented in this work offer a near-ideal realization of a paradigmatic model of many-body quantum physics, which can serve as a platform for future studies of geometric frustration.

Geometrically frustrated systems with a large degeneracy of low-energy states are of central interest in condensed-matter physics [1,2]. The kagome net—a pattern of corner-sharing triangular plaquettes—presents a particularly high degree of frustration. Such frustration impacts the kagome quantum antiferromagnet, for which the ground state, proposed to be a quantum spin liquid or valence bond solid [3–10], remains uncertain despite decades of work. Resolving such uncertainty by experiments on solid-state kagome magnets [11,12] is complicated by the significant magnetic disorder or anisotropy of such materials. For this reason, more faithful realizations of quantum many-body physics in the kagome lattice are needed.

Ultracold atoms trapped within optical lattices offer clean realizations of exotic phases of matter in condensed-matter physics [13]. Recently, nonprimitive optical lattices with multiple lattice sites per unit cell have been realized in the honeycomb [14] and checkerboard [15] geometries, and double-well superlattices [16,17], revealing nontrivial ordering and dynamics arising from a low-energy orbital degree of freedom [18]. The kagome lattice with ultracold atoms has attracted significant interest in this context as well [19,20], but it has not been experimentally demonstrated to our knowledge.

In this Letter, we present the realization of the kagome geometry in a two-dimensional optical superlattice for ultracold ^{87}Rb atoms. The kagome lattice is obtained by eliminating every fourth site from a triangular lattice of spacing $a/2$, with the eliminated sites forming a triangular lattice of spacing a. The remaining sites generate three connected s-orbital bands within a bandwidth on the order of the intersite tunneling energy. Intriguingly, the frustration besetting antiferromagnetic interactions also implies that one of these bands be nondispersing. Such flat bands, distinguishing the kagome configuration from other nonprimitive lattices [14–17], accentuate the role of interparticle interactions, leading possibly to crystalline ordering

[21] and supersolidity [22] for scalar bosons, and ferromagnetism of itinerant fermions [23]. Furthermore, geometric frustration of the kagome lattice shows macroscopic degeneracy of lowest-energy classical states with XY-type antiferromagnetic interactions in contrast to the triangular lattice [24]. Our work therefore opens the door to investigations of how geometric frustration affects both orbital and magnetic properties of materials.

Our kagome lattice is formed by overlaying short-wavelength (SW) and long-wavelength (LW) triangular lattices, formed with light at the commensurate wavelengths of 532 and 1064 nm, respectively [25]. In a single-wavelength lattice, formed by three plane waves of light of equal intensity I and wave vectors (and linear polarizations) lying in a plane and intersecting at equal angles, one obtains a triangular lattice of points with zero intensity, and a honeycomb lattice of points with maximum intensity $\frac{9}{2}I$ separated by a triangular lattice of intensity saddle points with intensity $4I$. Our SW-lattice light is blue detuned from the principal atomic resonances of rubidium, so that atoms are attracted to the triangular lattice of zero-intensity sites with a lattice spacing of $a/2 = (2/3) \times 532$ nm $= 355$ nm. The LW lattice is red-detuned, so that its zero-intensity points are potential-energy maxima for rubidium atoms. A unit cell of the LW lattice contains four sites of the SW triangular lattice, labeled A, B, C and D in Fig. 1. Aligning the positions of the LW potential maxima to coincide with sites D lowers the potential energies $V_{A,B,C}$ at the other sites by equal amounts $\Delta V = V_D - V_{A,B,C} = \frac{8}{9}V_{LW}$, where V_{LW} is the maximum scalar potential depth of the LW lattice (we ignore the $\sim 1\%$ vector shift in this lattice [26]). As ΔV is increased, atoms are excluded from sites D, while the remaining sites form the kagome optical lattice. The kagome geometry persists until $V_{LW} > 9V_{SW}$, at which point atoms become preferentially confined in the LW honeycomb lattice.
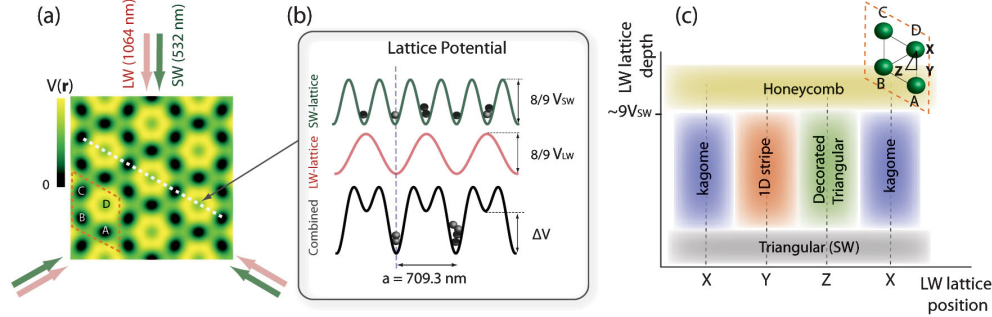
FIG. 1 (color).   Three bichromatic light beams intersecting at 120° form a kagome optical lattice for ultracold ^{87}Rb atoms, with the two-dimensional potential $V(\mathbf{r})$ shown in (a). Profiles of the potential of the SW, LW, and combined lattices are shown in (b). Sites D of the SW lattice are emptied as ΔV exceeds the chemical potential, so that the remaining sites A, B and C form the kagome geometry. (c) Different lattice geometries are created for intermediate LW-lattice depths ($V_{\mathrm{LW}} < 9V_{\mathrm{SW}}$) by displacing the potential maxima of the SW lattice to the high-symmetry points X, Y or Z within the unit cell. For higher LW-lattice depths, a honeycomb geometry prevails.

Compared with previous proposals [19,20], our simpler approach to creating a kagome lattice allows one to tune the lattice geometry, thereby controlling its degree of frustration. Aligning the LW potential maxima with the SW-lattice saddle points disfavors population in two sites of the four-site unit cell (e.g., $V_{B,C} < V_{A,D}$) producing a one-dimensional (1D) stripe lattice [Fig. 1(c) or Fig. 3(a)]. Aligning the LW potential maxima with the SW potential maxima disfavors population in three sites of the unit cell (e.g., $V_{A,B,D} > V_C$), producing a decorated triangular lattice with lowest-energy sites forming a triangular lattice while the remaining sites form a kagome lattice of local potential minima.

Experiments were conducted with scalar Bose-Einstein condensates of $\sim 3 \times 10^5$ ^{87}Rb atoms produced at temperatures of 80 nK in a red-detuned crossed optical dipole trap with trap frequencies of $(\omega_x, \omega_y, \omega_z) = 2\pi \times$ (60, 30, 350) Hz, with ω_z applying vertically. The large ~ 100 μm beam-waist diameters of the lattice beams ensured that the lattice potential modified the trapping frequencies by less than 10%. Laser alignments and relative intensities were tuned to produce sixfold symmetric diffraction patterns of condensates released from LW- and SW-only lattices. The relative displacement of the LW and SW lattices was measured using two two-color Mach-Zehnder interferometers, one for beams 1 and 2 and the other for beams 1 and 3, and stabilized using piezo-actuated mirrors in the optical paths [27]. A tilted glass plate within each interferometer introduced a relative shift between the two lattice colors that, following stabilization, was imparted onto the optical lattice.

We employed atom optics to characterize the lattice as it is tuned between various geometries. The atom-optical tools presented in this work may be useful for the characterization of other superlattices and for superlattice-based atom interferometry. The first of these tools is Kapitza-Dirac diffraction [28,29], for which the lattice potential is suddenly pulsed on for a duration τ, after which the con-

densate is imaged after a time of flight. Neglecting kinetic energy during the brief pulse, the condensate wavefunction acquires an imprinted phase $-V(\mathbf{r})\tau/\hbar$ proportional to the potential $V(\mathbf{r})$.

The corresponding momentum-space distribution is sensitive to the relative displacement of the LW and SW lattices. To exhibit this sensitivity we blocked one of the incident bichromatic lattice beams and examined the resulting one-dimensional superlattice, with potential energy given as $V(x) = V_{\mathrm{LW}} \sin^2[q(x + \delta x)/2] - V_{\mathrm{SW}} \sin^2(qx)$ where $2\pi/q = 614$ nm is the 1D LW-lattice spacing, and δx is the distance between the LW and SW intensity minima. The atomic populations at wave vectors $\pm q$ are given as

$$P_{\pm q} \propto |\pm iJ^{\mathrm{LW}}_{\pm 1}J^{\mathrm{SW}}_0 + J^{\mathrm{LW}}_{\mp 1}J^{\mathrm{SW}}_{\pm 1}e^{\mp i2q\delta x}|^2, \qquad (1)$$

where J_n is the nth-order Bessel function evaluated at $\phi_{\mathrm{LW,SW}} = V_{\mathrm{LW,SW}}\tau/2\hbar$, and where we consider terms up to second order in $\phi_{\mathrm{LW,SW}}$. The lack of inversion symmetry of the lattice produced by an incommensurate value of δx appears as a left/right momentum asymmetry in the diffracted matter wave (Fig. 2).

A second method to characterize the optical superlattice is the momentum-space analysis of a superfluid occupying the ground state of the lattice potential. Here, the optical lattice potential depth was ramped up from zero over 90 ms, held constant for 100 ms, and then suddenly switched off to allow for time-of-flight expansion of the trapped gas. For the momentum-space analysis, the maximum SW potential depth was kept constant at $V_{\mathrm{SW}}/h = 40$ kHz($= 8.8E_R$), where E_R is the recoil energy of the SW triangular lattice. We observed no significant decay of the diffraction peak holding up to 150 ms in the optical superlattices.

Varying the relative position of the two lattices we identify the three high-symmetry lattice configurations [Fig. 3(a)]. Given that the scalar condensate occupies the ground state of the lattice potential, its wave function can be taken as real and positive; thus, its momentum
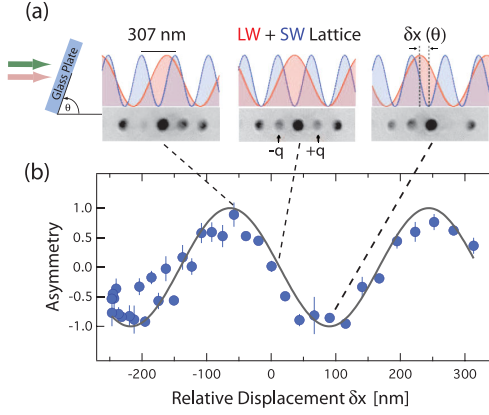
FIG. 2 (color).   Atom diffraction patterns, formed by a $\tau = 8$ μs pulse of the lattice potential (with $V_{SW}/h \sim 80$ kHz and $V_{LW}/h \sim 50$ kHz) followed by 26 ms time of flight, exhibit left/right momentum asymmetry [defined as $(P_{+q} - P_{-q})/(P_{+q} + P_{-q})$] that varies with the displacement δx between the LW- and SW-lattice intensity minima, in close agreement with the predicted behavior (solid line).

distribution is symmetric under inversion. Expansion from both the kagome and the decorated triangular lattices shows the threefold rotational symmetry of the optical superlattice. In the 1D stripe geometry, one expects equally weak occupation of two sites (e.g., A and D), and equally strong occupation of the other two sites (B and C) of the superlattice unit cell. Such a distribution is (nearly) invariant under displacements of $a/2$ along the A-D axis, and condensate diffraction along that axis should reflect the shorter periodicity of the SW lattice. The momentum distribution should also be symmetric under reflection about the A-D axis. Both traits are observed experimentally.

The Bloch-state momentum distributions allow one to quantify the ground-state wave function within a unit cell of the superlattice, which we express as $\psi(\mathbf{r}) = \sum_\alpha \psi_\alpha w_\alpha(\mathbf{r} - \mathbf{s}_\alpha)$, where $w_\alpha(\mathbf{r})$ is the normalized Wannier state wave function, $\mathbf{s}_\alpha$ the position, and $|\psi_\alpha|^2$ the fractional atomic population of site $\alpha \in \{A, B, C, D\}$ of the unit cell. At low V_{LW}/V_{SW}, we approximate $w_\alpha = w$ as cylindrically symmetric, Gaussian, and identical for all α. From the momentum-space populations $P_{\mathbf{G}_i}$ ($i \in \{1, 2, 3\}$) in the three first-order diffraction peaks of the LW lattice [30]—corresponding to the inner hexagon of peaks in time-of-flight images—and that at zero wave vector P_0, one determines the distinct quantities

$$\tilde{P}_i = \frac{P_{\mathbf{G}_i} + P_{-\mathbf{G}_i}}{2P_0} \frac{|\tilde{w}(0)|^2}{|\tilde{w}(\mathbf{G}_i)|^2} = \frac{|\psi_\beta + \psi_\gamma - \psi_\delta - \psi_\epsilon|^2}{|\sum_\alpha \psi_\alpha|^2},$$
(2)

where $\tilde{w}(0)$ and $\tilde{w}(\mathbf{G}_i)$ are now Fourier components of the Wannier function, and β, γ, δ and ϵ label the four sites
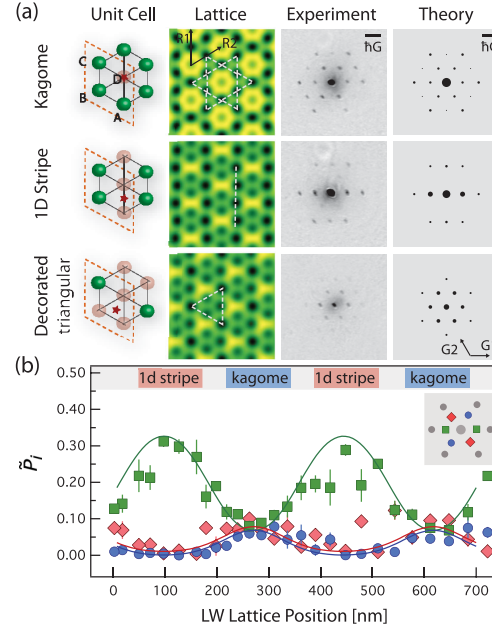

FIG. 3 (color).   The real- and momentum-space composition of a superfluid for various lattices. (a) The kagome and decorated triangular lattices maintain threefold rotational symmetry in configuration and momentum space, while the symmetry of the 1D stripe lattice is reduced to a parity symmetry (left-right in the images). For each setting, a schematic distinguishes between sites of high (green) and low (red) atomic population. The expected momentum distribution for measured values of $V_{SW}/h = 40$ kHz and $\Delta V/h = 14$ kHz is shown with the area of the black dot reflecting the fractional population. (b) Translating the LW-lattice potential maxima (marked as a star in the schematic) along the A-D axis tunes the lattice between kagome and 1D stripe geometries, as revealed by the population ratios $\tilde{P}_i$ identified according to the inset. The data (averages of 4–5 measurements) agree with calculations of the single-particle ground state (solid lines) with the lattice depth used in the experiment. Interaction effects are neglected since ΔV was higher than the chemical potential $\mu \sim h \times 3.5$ kHz of the condensate in the SW-only lattice.

so that $\mathbf{G}_i \cdot (\mathbf{s}_\beta - \mathbf{s}_\gamma) = 0$. The Wannier state Fourier components in Eq. (2) are determined from the second-order diffraction populations as $|\tilde{w}(0)|^2/|\tilde{w}(\mathbf{G}_i)|^2 = [2P_0/(P_{2\mathbf{G}_i} + P_{-2\mathbf{G}_i})]^{1/4}$. Together with the normalization $\sum_\alpha |\psi_\alpha|^2 = 1$ these quantities determine the atomic distribution in the unit cell [31].

We measured the population ratios $\tilde{P}_i$ as the superlattice geometry was gradually tuned. Translating the relative position of the two lattices [Fig. 3(b)], one advances from the kagome geometry, with equal population in the three ratios, to the 1D stripe geometry, with two identically small ratios, and then to another kagome-geometry lattice. Our data agree with a calculation of the single-particle ground-state for the known lattice depths.
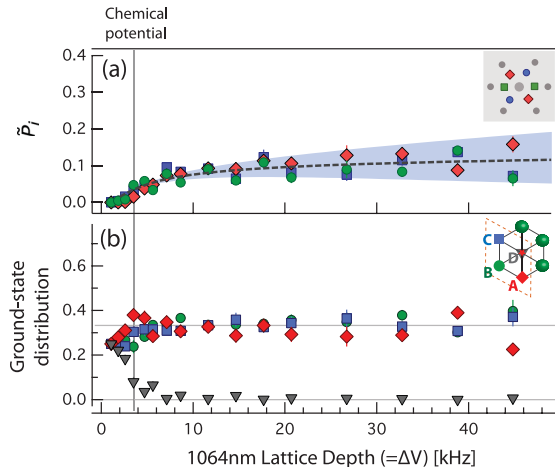
FIG. 4 (color). The superlattice was converted from a SW triangular to a kagome lattice by increasing V_{LW}. As ΔV exceeds the condensate chemical potential ($\mu/h \simeq 3.5$ kHz), (a) the momentum population ratios reach the asymptotic value of $1/9$ expected for a kagome lattice, and (b) the D-site population is extinguished. Data points represent averages of 7–10 measurements. In (a), the dashed curve indicates the predicted $\tilde{P}_i$ while the shaded region indicates the expected variation in $\tilde{P}_i$ given a shot-to-shot instability of $\sim$20 nm in the relative position of the LW and SW lattices.

We focus finally on the kagome-geometry lattice alignment, and examine the transition between the triangular and kagome geometries (Fig. 4). At zero V_{LW}, the atoms are confined in a SW triangular lattice, and the first-order LW-lattice diffraction orders are absent, indicating a unit-cell population of $(A, B, C, D) = (\frac{1}{4}, \frac{1}{4}, \frac{1}{4}, \frac{1}{4})$. As the LW-lattice depth is increased, the population ratios $\tilde{P}_i$ increase and the kagome geometry is achieved by gradually expelling atoms from one site of the unit cell. The population ratios tend toward a limiting value of $1/9$ that is a hallmark of diffraction from a kagome lattice wherein the atoms are distributed as $(A, B, C, D) = (\frac{1}{3}, \frac{1}{3}, \frac{1}{3}, 0)$.

Here, the ground state of the kagome lattice does not suffer from frustration. In the future, effects of frustration may be explored by transferring bosons into the excited s-orbital flat band, or by changing the sign of the hopping energy [32] so that the flat band becomes the lowest in energy. The present choice of wavelengths also yields kagome lattices for the fermionic isotopes ^{6}Li and ^{40}K. Introducing fermions into the lattice at the appropriate fillings would place the Fermi energy within the flat band, allowing for studies of flat-band ferromagnetism due to repulsive interactions [23] or enhanced Cooper pairing for attractive interactions [33]. Also, the demonstrated tunability of the superlattice opens new possibilities to emulate both ideal and deliberately distorted kagome lattices, potentially stabilizing the various candidate ground states of the kagome quantum antiferromagnet.

[1] A. P. Ramirez, Annu. Rev. Mater. Sci. **24**, 453 (1994).
[2] L. Balents, Nature (London) **464**, 199 (2010).
[3] V. Elser, Phys. Rev. Lett. **62**, 2405 (1989).
[4] J. B. Marston and C. Zeng, J. Appl. Phys. **69**, 5962 (1991).
[5] S. Sachdev, Phys. Rev. B **45**, 12 377 (1992).
[6] P. Nikolic and T. Senthil, Phys. Rev. B **68**, 214415 (2003).
[7] F. Wang and A. Vishwanath, Phys. Rev. B **74**, 174423 (2006).
[8] Y. Ran et al., Phys. Rev. Lett. **98**, 117205 (2007).
[9] R. R. P. Singh and D. A. Huse, Phys. Rev. B **76**, 180407 (2007).
[10] S. Yan, D. A. Huse, and S. R. White, Science **332**, 1173 (2011).
[11] M. P. Shores et al., J. Am. Chem. Soc. **127**, 13462 (2005).
[12] Z. Hiroi et al., J. Phys. Soc. Jpn. **70**, 3377 (2001).
[13] I. Bloch, J. Dalibard, and W. Zwerger, Rev. Mod. Phys. **80**, 885 (2008).
[14] P. Soltan-Panahi et al., Nature Phys. **7**, 434 (2011).
[15] G. Wirth, M. Olschlager, and A. Hemmerich, Nature Phys. **7**, 147 (2010).
[16] J. Sebby-Strabley et al., Phys. Rev. A **73**, 033605 (2006).
[17] S. Folling et al., Nature (London) **448**, 1029 (2007).
[18] P. Soltan-Panahi, D.-S. Luhmann, J. Struck, P. Windpassinger, and K. Sengstock, Nature Phys. **8**, 71 (2011).
[19] L. Santos et al., Phys. Rev. Lett. **93**, 030601 (2004).
[20] J. Ruostekoski, Phys. Rev. Lett. **103**, 080406 (2009).
[21] C. J. Wu et al., Phys. Rev. Lett. **99**, 070401 (2007).
[22] S. D. Huber and E. Altman, Phys. Rev. B **82**, 184502 (2010).
[23] H. Tasaki, Phys. Rev. Lett. **69**, 1608 (1992).
[24] J. Struck, C. lschlger, R. Le Targat, P. Soltan-Panahi, A. Eckardt, M. Lewenstein, P. Windpassinger, and K. Sengstock, Science **333**, 996 (2011).
[25] While the SW and LW wavelengths of 532.15 nm and 1063.96 nm are not perfectly commensurate, the relative displacement of the SW and LW lattices varies by only (18,9) nm over the $(d_x, d_y) = (28, 14)$ μm transverse diameter of the condensate.
[26] J. Dalibard and C. Cohen-Tannoudji, J. Opt. Soc. Am. B **6**, 2023 (1989).
[27] For Kaptiza-Dirac diffraction, stabilization was engaged with the lattice at negligible intensity before the brief high-intensity pulse. For Bloch-state analysis, stabilization was engaged upon the ramp-on of the lattice beams.
[28] P. L. Gould, G. A. Ruff, and D. E. Pritchard, Phys. Rev. Lett. **56**, 827 (1986).

[29] Y. B. Ovchinnikov *et al.*, Phys. Rev. Lett. **83**, 284 (1999).

[30] Momentum populations of condensed atoms are measured by integrating under the narrow time-of-flight atomic distributions. The contribution from the thermal atoms is subtracted, thereby accounting for finite-size, finite-temperature, and interaction effects during the expansion of the gas.

[31] We assume that all atoms lie in the ground band of the lattice potential with constant phase. Inverting Eqs. (2) gives a discrete degeneracy of solutions that is resolved by knowledge of the approximate populations.

[32] H. Lignier *et al.*, Phys. Rev. Lett. **99**, 220403 (2007).

[33] M. Imada and M. Kohno, Phys. Rev. Lett. **84**, 143 (2000).

Appendix B

Signatures of spatial inversion asymmetry of an optical lattice observed in matter-wave diffraction

This appendix includes the following paper [74], discussed in Chapter 4:

- *C. K. Thomas, T. H. Barter, T.-H. Leung, S. Daiss and D. M. Stamper-Kurn, "Signatures of spatial inversion asymmetry of an optical lattice observed in matter-wave diffraction," Phys. Rev. A* **93***, 063613 (2016).*

Signatures of spatial inversion asymmetry of an optical lattice observed in matter-wave diffraction

C. K. Thomas,[1] T. H. Barter,[1] T.-H. Leung,[1] S. Daiss,[2] and D. M. Stamper-Kurn[1,3,*]

[1]*Department of Physics, University of California, Berkeley, California 94720, USA*
[2]*Max-Planck-Institut für Quantenoptik, Hans-Kopfermann-Strasse 1, 85748 Garching, Germany*
[3]*Materials Sciences Division, Lawrence Berkeley National Laboratory, Berkeley, California 94720, USA*

The structure of a two-dimensional honeycomb optical lattice potential with small inversion asymmetry is characterized using coherent diffraction of ^{87}Rb atoms. We demonstrate that even a small potential asymmetry, with peak-to-peak amplitude of $\leqslant 2.3\%$ of the overall lattice potential, can lead to pronounced inversion asymmetry in the momentum-space diffraction pattern. The observed asymmetry is explained quantitatively by considering both Kapitza-Dirac scattering in the Raman-Nath regime and also either perturbative or full-numerical treatment of the band structure of a periodic potential with a weak inversion-symmetry-breaking term. Our results have relevance for both the experimental development of coherent atom optics and the proper interpretation of time-of-flight assays of atomic materials in optical lattices.

In x-ray crystallography, the diffraction of light is analyzed to determine the exact crystalline structure of a material. Similarly, with the availability of ultracold sources of coherent matter waves of atoms, one can use atomic diffraction to characterize potentials experienced by the atoms. Of particular interest are the optical lattice potentials produced by periodic patterns of light intensity and polarization, formed by the intersection of several coherent plane waves of light or by direct imaging. Lattice potentials of various geometries and dimensionalities, some incorporating atomic-spin dependence and gauge fields, have been produced or proposed for the purpose of creating synthetic atomic materials by placing quantum-degenerate atoms within them [1–3]. Just as in condensed matter, the characteristics of such synthetic atomic materials derive from the nature of the optical crystal upon which they are based. Matter-wave crystallography therefore becomes a vital tool in the study of such synthetic quantum matter [4].

A key first step in determining the structure of a lattice is the assignment of its point-group and space-group symmetries. The violation of a symmetry is identified in x-ray crystallography by a difference in the intensities of diffraction spots [5]. Following such work, here we detect the inversion asymmetry of an optical lattice by observing significant asymmetries in the diffraction of a coherent matter wave from the potential. For this, we produce a spin-polarized ^{87}Rb Bose-Einstein condensate at rest, and then impose for a variable pulse duration the two-dimensional honeycomb optical lattice potential produced by three light beams intersecting at equal angles [6]. The resulting Kapitza-Dirac diffraction is quantified by imaging the gas after it is allowed to expand freely. By tuning the pulse time and working with a deep optical lattice, we produce highly visible (over 50% contrast) inversion asymmetry in the populations of the first-order diffraction peaks even while the inversion-asymmetric part of the potential is $\leqslant 2.3\%$ of the overall lattice potential. This observation highlights

the extreme sensitivity of coherent matter-wave scattering in revealing features of a potential landscape under investigation.

Aside from demonstrating sensitive optical-lattice crystallography, our observation also has implications for the development of atom optics. Matter-wave interferometers for several applications have employed brief pulses of light to split and recombine atomic beams coherently [7,8]. Kapitza-Dirac diffraction, i.e., the diffraction of atoms from standing-wave rather than traveling-wave optical potentials, has the advantage that it is technically simple to implement, requiring only light waves at a single optical frequency [9,10]. However, as compared with Bragg or Raman diffraction, it has the disadvantage of being less efficient and less selective [11]. The technical simplicity has inspired modifications of Kapitza-Dirac diffraction employing several pulses of light so as to diffract atoms to selected diffraction orders with high efficiency [12], although the diffraction remained inversion symmetric, with as many atoms diffracted to the wave vector $+\mathbf{G}$ as to the wave vector $-\mathbf{G}$. We show that this last constraint can be lifted to produce inversion-asymmetric Kapitza-Dirac diffraction of matter waves in two dimensions. Similar to the previous demonstration in one dimension [13], we explain how this asymmetry arises from the interference between different diffraction pathways to the same final momentum state.

We begin by describing the optical lattice potential characterized in this work. As in Ref. [6] and illustrated in Fig. 1(a), we form a two-dimensional honeycomb lattice using three beams of light at the wavelength $\lambda = 1064$ nm, with equal intensity, propagating horizontally and intersecting at equal angles, with each beam linearly polarized in the lattice plane. We define a quantization axis orthogonal to the lattice plane and show in Fig. 1(b) that the beams produce a periodic pattern of varying intensity and optical polarization.

Rubidium atoms exposed to this optical lattice experience an ac-Stark shift that can be divided into scalar, vector, and tensor terms acting on the atomic hyperfine spin [14]. The tensor light shift is negligible in our experiment owing to the large detuning of the lattice light from the atomic transitions. Figure 1(d) shows the lattice potentials that result from the scalar and vector parts of the ac-Stark shift. The
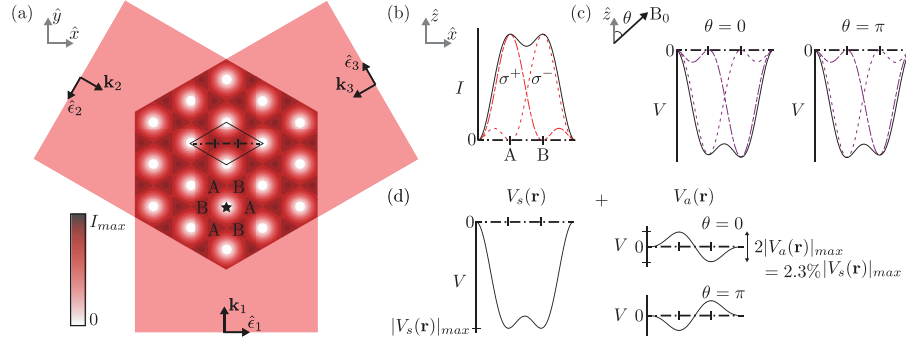
*dmsk@berkeley.edu

FIG. 1. Three 1064-nm beams interfere at $120°$ with in-plane polarization to create a honeycomb lattice of intensity maxima. We identify the unit cell of the lattice potential (solid line). A dashed line within the unit cell runs through the two potential minima, which are marked with ticks and labeled A and B. One-dimensional profiles of the light intensity (b) and optical potentials (c) and (d) along this line are shown. The star symbol, located at a minimum-intensity location, serves as a center for the spatial inversion operation that exchanges the A and B sites of the lattice. (b) We define a quantization axis orthogonal to the lattice plane and show that the light is predominantly σ^+ at site A and σ^- at site B. (c) The atoms are polarized by a uniform magnetic field B_0 at an angle θ from the quantization axis. We show the lattice potential for extreme values of $\cos\theta$, where the potential depth at sites A and B maximally differ. (d) The lattice potential is the sum of an inversion-symmetric potential $V_s(\mathbf{r})$ that arises from the scalar Stark shift and an inversion-antisymmetric potential $V_a(\mathbf{r})$ that comes from the vector Stark shift.

scalar light shift is proportional to light intensity and produces a honeycomb lattice potential $V_s(\mathbf{r})$ with two sites of equal depth per unit cell, labeled A and B in the figure. The vector light shift in the presence of a dominant external magnetic field produces a potential $V_a(\mathbf{r})$ that is approximately diagonal in the Zeeman basis defined by the field direction. $V_a(\mathbf{r})$ is proportional to both intensity and the dot product of helicity and atomic spin [14]. The helicity in the lattice is staggered so that $V_a(\mathbf{r})$ is of opposite sign at each of the two sites in the unit cell.

The scalar and vector light shift potentials differ in their inversion symmetry, with $V_s(\mathbf{r})$ being symmetric and $V_a(\mathbf{r})$ being antisymmetric under spatial inversion. Figure 1(a) shows one of the zero-intensity locations within the optical lattice as an example of the center of the inversion operation. The result of this operation is to switch sites A and B.

For alkali atoms, $V_a(\mathbf{r})$ is suppressed with respect to $V_s(\mathbf{r})$ owing to the large optical detuning from the atomic resonance. For the wavelength of light used in our lattice, the ratio $2|V_a(\mathbf{r})/V_s(\mathbf{r})|$ is at most 2.3%, so that $V_a(\mathbf{r})$ adds only a small inversion-symmetry-breaking potential atop a graphenelike, inversion-symmetric honeycomb lattice. Within this limit, we control the magnitude and sign of $V_a(\mathbf{r})$ by tilting the dominant external magnetic field $\mathbf{B}_0$ by an angle θ with respect to the (vertical) axis defined by the optical helicity. For atoms spin polarized along $\mathbf{B}_0$, the asymmetric potential is then $V_a(\mathbf{r}) \propto \cos\theta$. Figures 1(c) and 1(d) show that the resulting lattice potential has a small, state-dependent offset in energy between sites A and B.

To characterize this lattice using matter waves, we create a nearly pure, optically trapped Bose-Einstein condensate of 3×10^5 ^{87}Rb atoms that is spin polarized in the $|F = 1, m_F = -1\rangle$ state along the axis defined by a $\sim$0.5 G applied magnetic field. We then introduce a three-beam lattice potential with $|V_s(\mathbf{r})|_{max} = h \times 87 \pm 4$ kHz for a pulse time τ between 10 and 100 μs. This lattice depth is calibrated with independent measurements of the diffraction produced

by the one-dimensional lattices formed by pairs of the lattice beams [15]. After the pulse, we simultaneously switch off the optical lattice and optical trapping potentials and allow the atoms to expand freely for a 20-ms time of flight. We finally take an image of the density distribution in which the various diffraction orders, generated at the reciprocal lattice vectors by exposure to the lattice potential, are seen as separate peaks.

The first-order diffraction peaks in Figs. 2(a) and 2(c) show a pronounced inversion asymmetry. To quantify this asymmetry, we identify three reciprocal lattice vectors that describe first-order diffraction as $\mathbf{G}_1 = \mathbf{k}_3 - \mathbf{k}_2$ and its cyclic permutations, where $\mathbf{k}_{1,2,3}$ are the wave vectors of the incident beams that form the lattice. We define an asymmetry parameter $\mathcal{A}$ as

$$\mathcal{A} = \frac{\sum_i (P_{\mathbf{G}_i} - P_{-\mathbf{G}_i})}{\sum_i (P_{\mathbf{G}_i} + P_{-\mathbf{G}_i})}, \tag{1}$$

i.e., as the contrast between the diffraction intensities at wave vectors $\mathbf{G}_i$ and $-\mathbf{G}_i$, the two sets of wave vectors being related by inversion. This measure is robust against variations in the total atom number and against residual center-of-mass motion of the condensed atoms with respect to the lattice potential. We note that imaging aberrations introduce a slight offset in $\mathcal{A}$ (of about 0.1) in our experiment, seen in Figs. 2 and 3.

We confirm that the momentum-space inversion asymmetry is caused by the real-space inversion asymmetry of the lattice potential by varying the magnitude and sign of the inversion-symmetry-breaking potential $V_a(\mathbf{r})$. We tune $V_a(\mathbf{r})$ by rotating the orientation of the magnetic field from the vertical axis by the polar angle θ before exposing the condensate to the lattice potential.

Our data emphasize the fact that even an asymmetry in the lattice potential of $\leqslant 2.3\%$ can lead to highly visible asymmetry in the matter-wave diffraction pattern. The evolution of the momentum-space asymmetry $\mathcal{A}$ vs pulse time is portrayed in
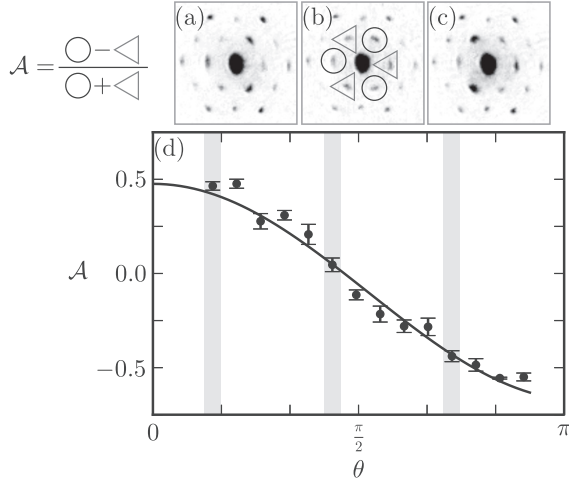
FIG. 2. An asymmetry parameter $\mathcal{A}$ is defined as the first-order population imbalance and measured for data taken as a function of θ with a pulse time of 50 μs. (a) Time-of-flight image for $\theta = 0.44$ shows an asymmetry in the first-order diffraction peaks. (b) We highlight the first-order peaks with circles (at $\mathbf{G}_i$) and triangles (at $-\mathbf{G}_i$). (c) Time-of-flight image for $\theta = 2.2$ shows reversal of the observed asymmetry. (d) $\mathcal{A}$ is computed for each of five images and the mean and standard error of these data are plotted. The solid line shows the expected dependence on θ.

Fig. 3. The asymmetry grows from small values at early times to over 50% at $\tau \sim 50$ μs, and also displays clear modulation in time reflecting the coherent dynamics of matter waves within the imposed lattice potential. Throughout these dynamics, reversing the sign of the inversion asymmetry of the lattice reverses the observed inversion asymmetry of the diffracted atoms.

We present two physical pictures that explain the origin of the observed momentum-space inversion asymmetry. First, we consider how the momentum-space asymmetry originates from low-order diffraction in the lattice. This description, shown schematically in Figs. 4(a) and 4(b), is valid in the limit of a shallow optical lattice and in the Raman-Nath regime, where we can ignore the kinetic energy of the diffracting atoms [16]. Both the scalar and vector Stark shift optical lattice potentials, $V_s(\mathbf{r})$ and $V_a(\mathbf{r})$, can be characterized in momentum space by their Fourier transforms $V_{s,a}(\pm\mathbf{G}_i)$ at the wave vectors $\pm\mathbf{G}_i$, where the relation $V_{s,a}(\mathbf{G}_i) = V_{s,a}^*(-\mathbf{G}_i)$ is valid because both potentials are real. Considering the C_3 rotational symmetry of both lattices and their respective inversion symmetries we have $V_s(\pm\mathbf{G}_i) = \beta_s$ and $V_a(\pm\mathbf{G}_i) = \pm i\beta_a$, where β_s and β_a are both real.

We now consider the probability amplitudes $p(\pm\mathbf{G}_i)$ for atoms diffracting from their initial zero momentum state to a final wave vector $\pm\mathbf{G}_i$ within a time τ. Figure 4(a) illustrates that such diffraction can be achieved by one first-order process, with amplitude $-i(\beta_s \mp i\beta_a)\tau/\hbar$, and by two second-order processes, which sum to an amplitude $(-i)^2(\beta_s \pm i\beta_a)^2\tau^2/\hbar^2$. We ignore higher order terms. Interference between the first- and second-order scattering amplitudes results in an imbalance of probability for diffraction into opposite wave vectors.
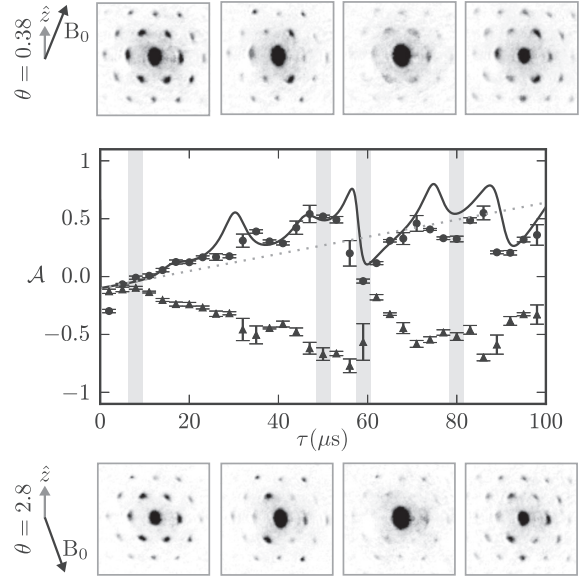

FIG. 3. Oscillations in $\mathcal{A}$ as a function of the Kapitza-Dirac pulse time τ, shown for $\theta = 0.38$ radians (circles) and $\theta = 2.8$ radians (triangles). The data represent the mean and standard error of five experimental runs at each pulse time. A numerical calculation (solid line) with no free parameters closely reproduces the time dependence of $\mathcal{A}$, while perturbation theory (dashed line) captures the short time behavior. Inset time-of-flight images for τ of 8, 50, 59, and 77 μs show directly the evolution of the first-order asymmetry. We note that discrepancies between theory and experiment, e.g., at times around 30, 60, and 80 μs, appear when the total population in the first-order peaks is small, causing a systematic reduction in the measured magnitude of $\mathcal{A}$.

Calculating the asymmetry parameter $\mathcal{A}$ at short times and for small lattice asymmetry ($|\beta_a| \ll |\beta_s|$) we obtain $\mathcal{A} \simeq 6\beta_a t/\hbar$, which is plotted as a gray dotted line in Fig. 3 and describes the data well for small τ.

While the model above provides a simple analytic expression for $\mathcal{A}$, its assumptions are violated under the conditions of our experiment. For one, our experiments are performed with a deep lattice that leads to diffraction to high order, as exemplified by the many diffraction peaks in our images. Second, the measurements are performed with pulse times that are long enough to be outside the Raman-Nath regime, which is shown by the high kinetic energy of the large momentum states produced in our experiment. Therefore, the diffraction pattern produced in our measurement is better described as resulting from coherent dynamics governed by the band structure of the optical lattice.

We performed numerical calculations that trace the evolution of a noninteracting gas, produced initially at zero momentum, within the lattice band structure. The numerical results shown in Fig. 3 are for $\theta = 0.44$ radians and a lattice depth of 87 kHz with no free parameters. The calculation matches well with the observed time dependence of the diffraction asymmetry.

To provide an intuitive description of the coherent dynamics in $\mathcal{A}$ that we both observe and calculate, we consider the
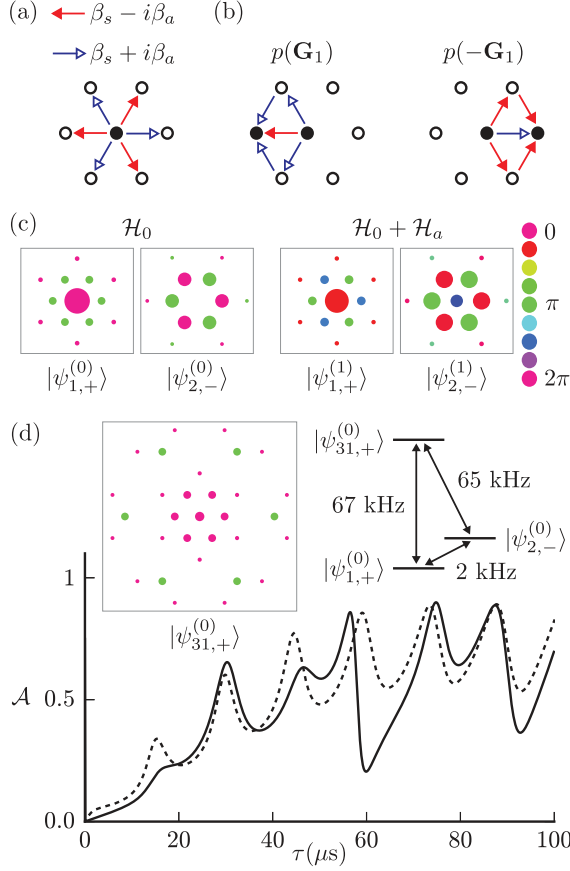
FIG. 4. (a) Atoms at zero momentum are coupled to wave vectors $\pm\mathbf{G}_i$ by the asymmetric Fourier components of the potential. (b) Interference between first- and second-order processes creates a population imbalance at $\pm\mathbf{G}_i$. (c) We treat the inversion asymmetric potential as a perturbation $\mathcal{H}_a$ on the inversion-symmetric lattice Hamiltonian $\mathcal{H}_0$ and show momentum-space amplitudes (spot size) and phases (color) of the two lowest energy eigenstates. In our experiment $\alpha_{2,1}$ is large and $\mathcal{H}_a$ strongly mixes the symmetric ground state $|\psi_{1,+}^{(0)}\rangle$ and the antisymmetric excited state $|\psi_{2,-}^{(0)}\rangle$. Both perturbed states are asymmetric and overlap with a stationary condensate. (d) Much of the oscillatory behavior observed in $\mathcal{A}$ can be attributed to the beating of three states, identified in the eigenspectrum of $\mathcal{H}_0$ as $|\psi_{1,+}^{(0)}\rangle$, $|\psi_{2,-}^{(0)}\rangle$, and $|\psi_{31,+}^{(0)}\rangle$. We show state $|\psi_{31,+}^{(0)}\rangle$, which is the excited state that best satisfies the criteria described in the first scenario of the text. The energy differences among these states define three frequencies (2, 65, and 67 kHz) that dominate the signal of $\mathcal{A}$. Our numerical calculations show that this three-state description (dotted line) captures most of the physics in the full signal of $\mathcal{A}$ (solid line).

effect of a small inversion-symmetry-breaking perturbation to the band structure of an inversion-symmetric lattice potential. The unperturbed Hamiltonian $\mathcal{H}_0$, which includes the kinetic energy and the inversion-symmetric lattice potential $V_s(\mathbf{r})$, has eigenstates $|\psi_{i,\pm}^{(0)}\rangle$ that are either even (labeled by $+$) or odd (labeled by $-$) under the action of the spatial inversion. The perturbation $\mathcal{H}_a$ results from the small antisymmetric lattice

potential $V_a(\mathbf{r})$ and mixes the even and odd eigenstates. To first order in $\mathcal{H}_a$, the zero quasimomentum eigenstates become

$$\left|\psi_{i,+}^{(1)}\right\rangle \approx \left|\psi_{i,+}^{(0)}\right\rangle + \sum_j \alpha_{j,i}\left|\psi_{j,-}^{(0)}\right\rangle, \qquad (2)$$

$$\left|\psi_{j,-}^{(1)}\right\rangle \approx \left|\psi_{j,-}^{(0)}\right\rangle + \sum_i -\alpha_{j,i}^*\left|\psi_{i,+}^{(0)}\right\rangle, \qquad (3)$$

where $\alpha_{j,i} = \frac{\langle\psi_{j,-}^{(0)}|\mathcal{H}_a|\psi_{i,+}^{(0)}\rangle}{E_{j,-}^{(0)}-E_{i,+}^{(0)}}$.

The initial state is a zero-momentum condensate that can be written in the basis of inversion-even eigenstates as $|\psi(0)\rangle = \sum_i c_i|\psi_{i,+}^{(0)}\rangle$. During the lattice pulse time τ this initial state evolves in time as

$$|\psi(t)\rangle = \sum_i c_i e^{-i\omega_{i,+}t}\left(\left|\psi_{i,+}^{(0)}\right\rangle + \sum_j \alpha_{j,i}\left|\psi_{j,-}^{(0)}\right\rangle\right)$$
$$+ \sum_{j,k} -\alpha_{j,k}c_k e^{-i\omega_{j,-}t}\left|\psi_{j,-}^{(0)}\right\rangle, \qquad (4)$$

where $\omega_{i,+} = E_{i,+}/\hbar$ and $\omega_{j,-} = E_{j,-}/\hbar$.

The first term of Eq. (4) represents the incorporation of inversion antisymmetry into the initially even eigenstates, and the second term represents fully antisymmetric states for which the perturbation introduces population at zero momentum. Figure 4(c) illustrates each of these effects on two states at zero quasimomentum that are heavily influenced by the perturbation $\mathcal{H}_a$: the initially symmetric ground state and antisymmetric first excited state.

The numerator of the inversion-asymmetry parameter $\mathcal{A}$ is the expectation value of an inversion-odd operator M that is diagonal in the basis of reciprocal lattice momenta, with matrix element ± 1 for the wave vectors $\pm\mathbf{G}_i$. Using the first-order expression above for $|\psi(t)\rangle$, we obtain $\langle M\rangle = M_1(t) + M_2(t)$ with

$$M_1(t) = \sum_{i,j,k}(c_i^* c_k e^{-i(\omega_{k,+}-\omega_{i,+})t}\alpha_{j,i}^* M_{j,k} + \text{c.c.}),$$
$$\qquad\qquad\qquad\qquad\qquad (5)$$
$$M_2(t) = \sum_{i,j,k}(c_k^* c_i e^{-i(\omega_{j,-}-\omega_{k,+})t}(-\alpha_{j,i})M_{j,k}^* + \text{c.c.}),$$

and $M_{j,i} = \langle\psi_{j,-}^{(0)}|M|\psi_{i,+}^{(0)}\rangle$.

These expressions identify two generic scenarios that lead to a large momentum-space asymmetry. The first results in oscillations described by both $M_1(t)$ and $M_2(t)$ and involves a trio of eigenstates of the unperturbed Hamiltonian $\mathcal{H}_0$ at zero quasimomentum: two inversion symmetric, $|\psi_{i,+}^{(0)}\rangle$ and $|\psi_{k,+}^{(0)}\rangle$, and one inversion antisymmetric, $|\psi_{j,-}^{(0)}\rangle$. These states can be identified by three key features. First, the symmetric states have significant population at zero momentum so as to overlap with the stationary condensate, giving large c_i and c_k. Second, the inversion-antisymmetric state is close in energy to one of the inversion-symmetric states, say $|\psi_{i,+}^{(0)}\rangle$, so that $\alpha_{j,i}$ is large and they are strongly mixed by the perturbation $\mathcal{H}_a$. Finally, the inversion-antisymmetric state and at least one of the inversion-symmetric states, say $|\psi_{k,+}^{(0)}\rangle$, have large population in the first-order diffraction momenta, so that $M_{j,k}$ is large. When these criteria are satisfied, we expect modulations of equal strength in M (and thus in $\mathcal{A}$) at frequencies $\omega_{k,+} - \omega_{i,+}$ and

$\omega_{j,-} - \omega_{k,+}$. The second scenario is described by $M_2(t)$ when $k = i$ and involves just two states – $|\psi_{i,+}^{(0)}\rangle$ and $|\psi_{j,-}^{(0)}\rangle$. These states are again characterized by large c_i and $\alpha_{j,i}$, and must both have large population in the first-order diffraction momenta so that $M_{j,i}$ is large. This scenario results in a modulation of $\mathcal{A}$ at frequency $\omega_{j,-} - \omega_{i,+}$.

In Fig. 4(d) we show that just one trio of states in this perturbation picture explains most of the dynamical variation in $\mathcal{A}$. Figure 4(c) shows that the state $|\psi_{1,+}^{(0)}\rangle$ has large population in the zero and first-order diffracted momenta, that $|\psi_{2,-}^{(0)}\rangle$ has large population in the first-order momenta, and that these states are heavily mixed by the perturbation, i.e., that $\alpha_{2,1}$ is large. As a result, these two states are dominant contributors to oscillation in $\mathcal{A}$ as in the second scenario described, and also couple with a third state $|\psi_{k,+}^{(0)}\rangle$ as in the first scenario. In Fig. 4(d) we isolate the symmetric excited state with the largest population in the zero and first-order diffracted momenta, $|\psi_{31,+}^{(0)}\rangle$. The energy of these three states define three frequencies that dominate the time evolution of $\mathcal{A}$. The large momentum-space asymmetry is observed when the Kapitza-Dirac pulse time is tuned so that these temporal oscillations interfere constructively. We note that there are several other symmetric excited states besides $|\psi_{31,+}^{(0)}\rangle$ that also play the role of $|\psi_{k,+}^{(0)}\rangle$ in the scenario we have outlined, and provide somewhat smaller contributions to the overall dynamics.

The observations and theoretical descriptions offered in this work illustrate how matter-wave diffraction can be made highly sensitive to, and strongly manipulated by, fine features of an optical lattice. Our work also suggests an explanation for the momentum-space asymmetry observed in the diffraction of a Bose-Einstein condensate of two spin states of ^{87}Rb and released from a spin-dependent optical lattice reported in Ref. [17] (see also Ref. [18]). The asymmetry was interpreted as evidence of a ground-state superfluid that forms with a spatially dependent phase in the superfluid order parameter. A later theoretical study [19] found no evidence for such a "twisted superfluid" state, which is consistent with naive expectations given that the optical lattice and mean-field interaction potentials experienced by the atoms are both real valued.

We suggest that the inversion-asymmetric diffraction patterns observed in the experiment [17] may have resulted from matter-wave diffraction from the inversion-asymmetric transient honeycomb lattice that repulsion from one atomic spin state creates for the second spin state. Such a transient lattice potential would have an interaction-energy asymmetry between the A and B sites of the honeycomb lattice that is on the order of the superfluid chemical potential (around $h \times 1$ kHz). This potential would persist for a time somewhat less than the recoil time (i.e., around 100 μs). The strength and duration of this asymmetric potential are comparable to those studied in the present work. The interaction-driven diffraction of one matter wave off another can be described equivalently as nonlinear coherent wave mixing induced by interatomic interactions [20]. The observation in Ref. [17] that the sign of the asymmetry parameter $\mathcal{A}$ was consistent between experimental repetitions supports our view that the asymmetry resulted from deterministic matter-wave dynamics rather than by spontaneous symmetry breaking at a phase transition. Moreover, in a recent experiment with the same system as in Ref. [17], the diffraction was modified by eliminating one spin population from the lattice just before the atoms were released [21]. The consequent elimination of the asymmetry signal is consistent with our suggested explanation.

[1] K. I. Petsas, A. B. Coates, and G. Grynberg, Phys. Rev. A **50**, 5173 (1994).

[2] I. Bloch, Nat. Phys. **1**, 23 (2005).

[3] I. Bloch, J. Dalibard, and S. Nascimbene, Nat. Phys. **8**, 267 (2012).

[4] J. Sebby-Strabley, M. Anderlini, P. S. Jessen, and J. V. Porto, Phys. Rev. A **73**, 033605 (2006).

[5] M. Ladd and R. Palmer, *Structure Determination by X-ray Crystallography: Analysis by X-rays and Neutrons* (Springer, New York, 2013), 5th ed.

[6] P. Soltan-Panahi, J. Struck, P. Hauke, A. Bick, W. Plenkers, G. Meineke, C. Becker, P. Windpassinger, M. Lewenstein, and K. Sengstock, Nat. Phys. **7**, 434 (2011).

[7] A. Wicht, J. M. Hensley, E. Sarajlic, and S. Chu, Phys. Scr. **2002**, 82 (2002).

[8] M. Kasevich and S. Chu, Appl. Phys. B **54**, 321 (1992).

[9] P. E. Moskowitz, P. L. Gould, S. R. Atlas, and D. E. Pritchard, Phys. Rev. Lett. **51**, 370 (1983).

[10] Yu. B. Ovchinnikov, J. H. Müller, M. R. Doery, E. J. D. Vredenbregt, K. Helmerson, S. L. Rolston, and W. D. Phillips, Phys. Rev. Lett. **83**, 284 (1999).

[11] P. J. Martin, B. G. Oldaker, A. H. Miklich, and D. E. Pritchard, Phys. Rev. Lett. **60**, 515 (1988).

[12] S. Wu, Y.-J. Wang, Q. Diot, and M. Prentiss, Phys. Rev. A **71**, 043602 (2005).

[13] G.-B. Jo, J. Guzman, C. K. Thomas, P. Hosur, A. Vishwanath, and D. M. Stamper-Kurn, Phys. Rev. Lett. **108**, 045305 (2012).

[14] C. Cohen-Tannoudji and J. Dupont-Roc, Phys. Rev. A **5**, 968 (1972).

[15] O. Morsch and M. Oberthaler, Rev. Mod. Phys. **78**, 179 (2006).

[16] B. Gadway, D. Pertot, R. Reimann, M. G. Cohen, and D. Schneble, Opt. Express **17**, 19173 (2009).

[17] P. Soltan-Panahi, D. S. Luhmann, J. Struck, P. Windpassinger, and K. Sengstock, Nat. Phys. **8**, 71 (2012).

[18] O. Jürgensen, K. Sengstock, and D.-S. Lühmann, Sci. Rep. **5**, 12912 (2015).

[19] S. Choudhury and E. J. Mueller, Phys. Rev. A **87**, 033621 (2013).

[20] D. Pertot, B. Gadway, and D. Schneble, Phys. Rev. Lett. **104**, 200402 (2010).

[21] M. Weinberg, O. Jürgensen, C. Ölschläger, D.-S. Lühmann, K. Sengstock, and J. Simonet, Phys. Rev. A **93**, 033625 (2016).

Appendix C

Mean-field scaling of the superfluid to Mott insulator transition in a 2D optical superlattice

This appendix includes the following manuscript, discussed in Chapter 5:

- *C. K. Thomas, T. H. Barter, T.-H. Leung, M. Okano, G. B. Jo, J. Guzman, I. Kimchi, A. Vishwanath and D. M. Stamper-Kurn,* "Mean-field scaling of the superfluid to Mott insulator transition in a 2D optical superlattice," arXiv: 1702.04433 (2017).

Mean-field scaling of the superfluid to Mott insulator transition in a 2D optical superlattice

Claire K. Thomas,[1] Thomas H. Barter,[1] Tsz-Him Leung,[1] Masayuki Okano,[1] Gyu-Boong Jo,[2]
Jennie Guzman,[3,4] Itamar Kimchi,[5] Ashvin Vishwanath,[1,6] and Dan M. Stamper-Kurn[1,7]

[1]*Department of Physics, University of California, Berkeley, California 94720, USA*
[2]*Department of Physics, Hong Kong University of Science and Technology, Clear Water Bay, Kowloon Hong Kong*
[3]*Sandia National Laboratories, Livermore, California 94550, USA*
[4]*Department of Physics, California State University, Hayward, California 94542, USA*
[5]*Department of Physics, Massachusetts Institute of Technology, Cambridge, Massachusetts 02139, USA*
[6]*Department of Physics, Harvard University, Cambridge, Massachusetts 02138, USA*
[7]*Materials Sciences Division, Lawrence Berkeley National Laboratory, Berkeley, California 94720, USA*
(Dated: February 25, 2017)

The mean-field treatment of the Bose-Hubbard model predicts properties of non-zero temperature lattice-trapped gases to be insensitive to the specific lattice geometry once system energies are scaled by the lattice coordination number z. We test this scaling hypothesis directly by driving identically-prepared ^{87}Rb gases through the superfluid–Mott insulator phase transition in two-dimensional lattices of either kagome ($z_{\text{kag}} = 4$) or triangular ($z_{\text{tri}} = 6$) geometry. At comparable interaction and tunneling energies throughout the transition, the measured coherent fraction of atoms is lower in the kagome lattice than in the triangular lattice and this difference is accounted for quantitatively by the scaling hypothesis. We also study the response of the gas to a change in lattice geometry, and observe out-of-equilibrium dynamics when the kagome-lattice Mott insulator is suddenly "hole-doped" by introducing the additional sites of the triangular lattice.

The Bose-Hubbard model describes bosons confined to a lattice, which undergo a low-temperature phase transition between superfluid and Mott insulating states that is driven by strong on-site interactions [1]. A mean-field treatment of this model neglects non-local correlations and predicts that system properties such as particle number, n, superfluid number, n_{sf}, and entropy, s, per lattice site depend on the values of the system's characteristic energies – the chemical potential, μ; on-site interaction energy, U; and thermal energy, $\tau = k_B T$ – once they are scaled by the product zJ, where z is the number of nearest neighbors or coordination number of the lattice and J is the tunneling energy. Aside from the inclusion of z, the mean-field theory is insensitive to the geometric structure of the lattice. More sophisticated treatments consider non-local correlations and account for the specific lattice geometry and find deviations from mean-field predictions, particularly in low-dimensional systems [2–9].

Ultracold atomic gases trapped in optical lattices experimentally realize the Bose-Hubbard Hamiltonian [10, 11] and have allowed for quantum simulations that identify the zero-temperature critical point with moderate precision by measuring either the fraction of atoms at zero quasimomentum [12, 13] or the closing of the Higgs-mode energy gap [14] in two-dimensional square lattices. The observed critical interaction strengths range between the mean-field prediction and the higher value predicted by a Quantum Monte Carlo calculation [2]. Interpretation of these measurements is complicated by the non-zero temperature and external harmonic confinement of the gases [15].

Here, we propose and pursue a direct test of the mean-field scaling prediction that does not require identifying the precise critical point and applies regardless of the non-zero temperature or external confinement of the sample. This test compares properties of trapped gases that are prepared identically, with the same total number N and entropy S, and loaded into optical lattices with different coordination numbers. Under the hypothesis that system properties are determined locally, i.e., using both the local density and mean-field approximations, global system properties such as the total particle number N, total superfluid population N_{sf}, and total entropy S are determined by integrating over a three-dimensional harmonically trapped sample as

$$F = K \int_{-\infty}^{\tilde{\mu}} d\tilde{\mu}' \, f(\tilde{\mu}', \tilde{U}, \tilde{\tau}). \tag{1}$$

Where $F \in \{N, N_{\text{sf}}, S\}$, $f \in \{n, n_{\text{sf}}, s\}$ and the tilde indicates an energy scaled by zJ. The effective number of occupied lattice sites is given by

$$K = \frac{\pi \alpha}{v} \left(\frac{2zJ}{m\bar{\omega}^2} \right)^{3/2} \tag{2}$$

where α is the number of equivalent sites in the unit cell, v is the unit cell volume, m is the atomic mass, and $\bar{\omega}$ is the geometric mean trapping frequency. The quantity N/K generalizes the "characteristic density," as defined by Rigol *et al.* [15], to non-square lattices.

According to the equations above, if samples prepared with the same total atom number and entropy are confined to lattices that differ in z, but have the same K and

$\tilde{U}$, then they will have the same $\tilde{\mu}$, $\tilde{\tau}$, and, consequently, N_{sf}. This statement is insensitive to the specific form of $f(\tilde{\mu}', \tilde{U}, \tilde{\tau})$, so that it is valid both at zero and non-zero temperature.

We test this prediction by preparing quantum degenerate gases of ^{87}Rb with a constant total atom number and entropy, and exploring the phase transition between the superfluid and Mott insulating states in the triangular and kagome geometries, which have coordination numbers $z_{tri} = 6$ and $z_{kag} = 4$. We quantify N_{sf} with measurements of the coherent fraction of atoms in each lattice and test the scaling hypothesis by comparing these measurements over a range of identical $\tilde{U}$. In this test, the phase diagram of the Bose-Hubbard model for different lattice geometries is compared not just at a critical point, but along a line in the $\tilde{\mu} - \tilde{\tau}$ plane. Our results agree quantitatively with the mean-field scaling prediction at all values of $\tilde{U}$.

Finally, in this work we explore the response of the quantum gas to a change in lattice geometry. We prepare a Mott insulator in the kagome lattice and then change the lattice structure to the triangular lattice while holding U and J constant. Slow changes induce a near-equilibrium phase transition from the Mott insulator in the kagome lattice to superfluid in the triangular lattice. Rapid changes, in which the insulator is suddenly "hole-doped" by the introduction of vacant lattice sites, result in transient oscillations of the strongly-interacting superfluid that damp out and lead to heating.

We create an optical superlattice by overlaying two triangular lattices of intensity minima, each formed at the intersection of three beams of light of equal intensity that propagate horizontally with in-plane polarization and intersect at equal angles [16]. We use light at wavelengths 532 nm and 1064 nm, resulting in lattices with spacings $a = 355$ nm and $2a$, respectively. A unit cell of the 1064-nm lattice contains four sites of the 532-nm lattice, labeled A – D in Fig. 1. The 532-nm lattice, formed with light that is blue-detuned from the principal ^{87}Rb atomic transitions, attracts atoms to its intensity minima. The resulting triangular lattice potential has a depth V_{532} that determines the atomic interaction and tunneling energies, U and J, where U also depends on the depth $V_{\perp}$ of an additional vertical lattice.

The overlapping 1064-nm lattice primarily introduces an energy offset $V_{A,B,C,D}$ among the four sites in the unit cell and has little influence on U or J [17]. Positioning the 1064-nm intensity minima to coincide with 532-nm intensity minima (sites D in Fig. 1) raises the D-site energy by $\Delta V = V_D - V_{A,B,C} = 8/9 \times V_{1064}$ and leaves a unit cell with three degenerate low-energy sites. When ΔV exceeds the relevant energies of low-temperature atoms in the ground band of the lattice (μ and J), the atoms become restricted to the kagome lattice. In this work, kagome lattice data were taken with $\Delta V/h = 13$ kHz, which satisfies the stated criteria as the chemical poten-
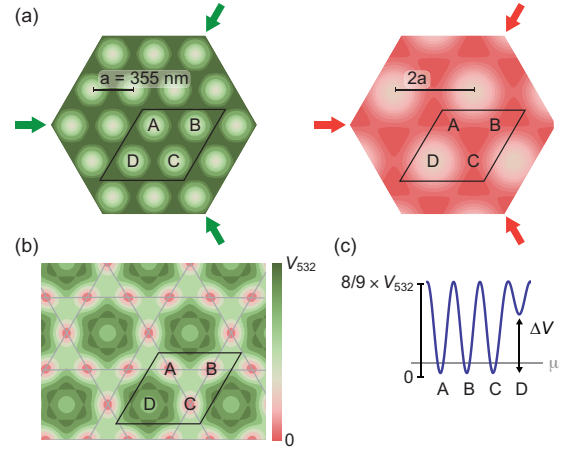

FIG. 1: Method for producing triangular and kagome optical lattices. (a) Triangular lattices created by light at wavelengths 532 nm (left) and 1064 nm (right) whose intensity – indicated by color saturation – has minima separated by lattice spacings $a = 355$ nm and $2a$, respectively. (b) The kagome lattice potential results when the the two lattices are overlapped such that the 1064-nm optical intensity minimum coincides with a minimum of the 532-nm lattice, as in the D-site here. (c) A one-dimensional slice through the sites of a unit cell, where atoms are trapped in the 532-nm triangular lattice potential and the effect of the 1064-nm lattice is to raise the potential at site D by an amount ΔV. The atoms are confined to the kagome geometry when $\Delta V > \mu, J$, the chemical potential and tunneling energies.

tial ranges between $\mu/h = 1.5$ and 2.9 kHz, and superfluid diffraction from this lattice showed the distinct signature of coherent atoms released from the kagome geometry [16]. The relative position of the commensurate lattices is measured interferometrically and stabilized actively [18].

For our experiments, we prepare nearly pure ^{87}Rb Bose-Einstein condensates of between 0.5 and 3×10^5 atoms in the $|F = 1, m_F = -1\rangle$ hyperfine state in a red-detuned crossed optical dipole trap, characterized by trap frequencies of $(\omega_x, \omega_y, \omega_z) = 2\pi \times (34, 64, 49)$ Hz. We then impose a one-dimensional lattice with potential depth $V_{\perp}/h = 41$ kHz formed by a retroreflected 1064-nm-wavelength beam propagating vertically. The gas is thus divided among approximately 17 two-dimensional planes that are effectively decoupled (with a single-atom tunneling rate of 5 Hz). Finally, we adiabatically load the atoms into the two-dimensional triangular superlattice with a simultaneous increase of the in-plane lattice beam intensities to the final trap depths [19]. All lattice potential depths are calibrated independently at regular intervals using lattice-modulation spectroscopy in the superfluid regime [18, 20].

After allowing 30 ms for the lattice-trapped gas to equilibrate [21], we release the atoms from the lattice into a
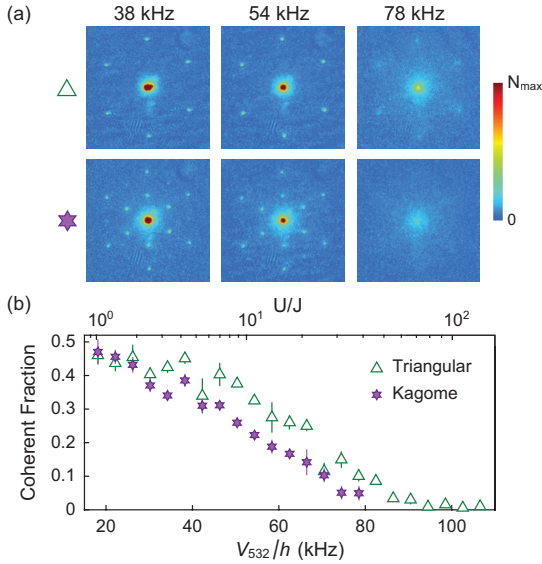
FIG. 2: The phase transition between the superfluid and Mott insulating states in two lattices with the same values of U and J and different coordination numbers, z. (a) Images of atoms released from the triangular (upper panel) and kagome (lower panel) lattices for $V_{532}/h = 38, 54$ and 78 kHz show correlations in the lattice-trapped gas. The superfluid portion of a gas coherently diffracts during expansion, resulting in sharp peaks at the reciprocal lattice vectors. The inner peaks in the kagome-lattice images indicate the larger primitive unit cell, and their rotational symmetry and relative population compared to the peak at $k = 0$ indicates proper alignment of the superlattice. On-site interactions drive the phase transition from the superfluid to the Mott insulating states, as indicated by loss of coherence with increasing lattice depth. (b) We measure coherent fraction by summing the number of coherent atoms at all peaks and dividing by the total number of atoms in an image. Data is shown as a function of 532-nm lattice depth (lower axis) and U/J (upper axis). Each data-point represents 3-5 iterations of the experiment and standard error is shown.

loosely horizontally confining magnetic potential in which they undergo a quarter-cycle of motion before we probe them by absorption imaging in the horizontal plane for a momentum-space characterization of the lattice-trapped gas [22]. The vertical lattice is ramped off about 150 μs prior to the turn-off of the superlattice and optical traps in order to reduce the rate of vertical expansion of the gas and thereby reduce the collisional transfer of vertical to transverse momentum.

Figure 2(a) shows typical momentum-space distributions for atoms expanding from the triangular and kagome lattices at several values of V_{532}. In the super-fluid regime, at low V_{532}, the distribution of atoms in the kagome lattice shows the additional diffraction peaks associated with the larger unit cell of the 1064-nm lattice. As either lattice is deepened, coherent diffraction

peaks diminish in strength and give way to a diffuse momentum-space distribution that represents both the incoherent portion of the gas and the incoherent momentum transferred by elastic scattering during expansion. We quantify the coherent fraction by counting the number of atoms in each sharp diffraction peak above the diffuse background and dividing by the total number of atoms in an image and show the results in Fig. 2(b).

The momentum-space images and resulting coherent fraction measurements show the influence of lattice geometry on the lattice-trapped Bose gas. At all lattice depths, the superfluid is less robust in the kagome lattice than in the triangular lattice, as expected owing to the lower coordination number. We found that the suppression of coherence upon increasing ΔV was reversible, i.e. that increasing and decreasing ΔV back to zero caused the coherent fraction to return nearly to the value observed with atoms loaded only into the 532-nm lattice. This finding confirms that any extraneous heating of the gas from the addition of the 1064-nm lattice was negligible.

Given our experimental parameters, we expect to form an $n = 2$ Mott insulator at the center of our gas. We observe the coherent fraction becoming negligible near $U/J = 60$ for the triangular lattice and $U/J = 40$ for the kagome lattice, consistent with the mean-field prediction that the $n = 2$ Mott lobe of a low-entropy sample forms at $\tilde{U} = 9.9$. However, as in previous studies, trap inhomogeneity and non-zero temperature influence measurements of the critical point, making these measurements difficult to interpret as precise tests of theoretical models.

By performing the same experiment in lattices that differ only in their geometry, we circumvent the need to isolate a transition point and instead use our measurements for a quantitative test of the mean-field scaling hypothesis. In Fig. 3 we compare the coherent fraction of atoms in the triangular and the kagome geometries with identical $\tilde{U}$. We observe that scaling the experimental U/J by z^{-1} leads to very good overlap between the two datasets.

To test the scaling hypothesis quantitatively, we apply a simultaneous spline fit to the two datasets and then determine the factor ζ by which the U/J axis of the kagome-lattice dataset should be scaled to best fit the triangular-lattice dataset by a least-squares measure. We obtain the optimal scaling factor $\zeta = 1.6 \pm 0.1$, where the mean-field prediction is $\zeta = z_{\text{tri}}/z_{\text{kag}} = 1.5$. Our results are consistent with mean-field scaling for all $\tilde{U}$, but how a more sophisticated treatment would affect the predicted scaling and functional form of these data remains an open question.

We note two imperfections in our approach. First, for technical reasons our experiments were performed with a constant harmonic trapping frequency $\bar{\omega}$. As a result, the relative effective site number K in the two lattices was around $K_{\text{tri}}/K_{\text{kag}} \simeq 1.4$. Therefore, the triangular-
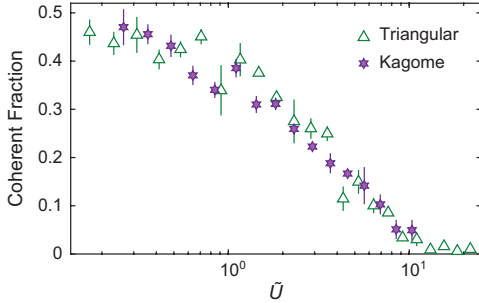
FIG. 3: A test of the mean-field scaling hypothesis in which the coherent fraction of atoms measured in the triangular and kagome lattices under the same conditions (Fig. 2(b)) are plotted against the scaled interaction energy $\tilde{U} = U/zJ$. The overlap of the two data sets at all $\tilde{U}$ indicates agreement with the mean-field scaling prediction.

lattice experiments were performed with lower $\tilde{\mu}$ and $\tilde{\tau}$ than the kagome-lattice experiments. In the mean-field picture, data for different K can be described as experiments performed in the same lattice geometry, but with N and S both scaled by K^{-1}, i.e. at the same total entropy per particle. We performed numerical calculations based on the mean-field and local density approximations, and found that scaling both N and S by this amount produced only negligible changes in the superfluid fraction for gases with small S/N as are used in this experiment.

Second, owing to collisions between atoms after their release from the lattice, and also to the challenge of quantifying the population in coherent peaks above their incoherent backgrounds, the coherent fraction determined from our images is an imperfect measure of the superfluid fraction of the gas. For example, the measured coherent fraction of $\simeq 0.4$ at low lattice depths is much lower than expected given the high condensate fraction of the gas before the lattice potentials are imposed, and given the agreement with mean-field theory for the appearance of the $n = 2$ Mott lobe. Our test of the mean-field scaling hypothesis is predicated on the assumption that the systematic underestimation of the coherent fraction from absorption images is identical for diffraction out of the two different lattice geometries.

Finally, we study the evolution of our lattice-trapped gas in response to changes in the structure of the optical lattice while U and J remain constant [17]. We create a Mott insulator in the kagome lattice, with $V_{532}/h = 55$ kHz and $\Delta V/h = 15$ kHz, so that $J/h \sim 106$ Hz and $U/h \sim 1.2$ kHz. We then deform the lattice into the triangular geometry by reducing $\Delta V/h$ to a minimal value of 0.5 kHz in a ramp time T_{ramp}. We allow the atoms to equilibrate in the triangular lattice before releasing them from their optical confinement and measuring the coherent fraction. The experimental sequence and data

are shown in Figs. 4(a) and 4(b). All data presented in Fig. 4 were taken under the same experimental conditions, but with longer hold time, lower image quality, and higher temperature than those in Figs. 2 and 3.

Figure 4 shows that introducing the additional lattice sites in a time that is long compared to $h/6J \sim 1.6$ ms restores coherent fraction nearly to the value reached in an adiabatically prepared triangular lattice, despite the non-zero final value of ΔV. As such, the gas undergoes a phase transition between the Mott insulating and superfluid states that is driven not by variations of U/J as in most previous works, but by a structural change of the lattice potential.

More rapid ramps result in a lower asymptotic coherent fraction after equilibration. Quenching from one lattice geometry to the other initiates transient dynamics in the newly formed superfluid that are damped and lead to a higher-temperature, lower-coherence gas after allowing for equilibration. Through band mapping measurements [23], we determined that these dynamics arise not from excitation to higher bands, but from excitation of the strongly interacting superfluid within the ground band of the triangular lattice. Such non-equilibrium dynamics
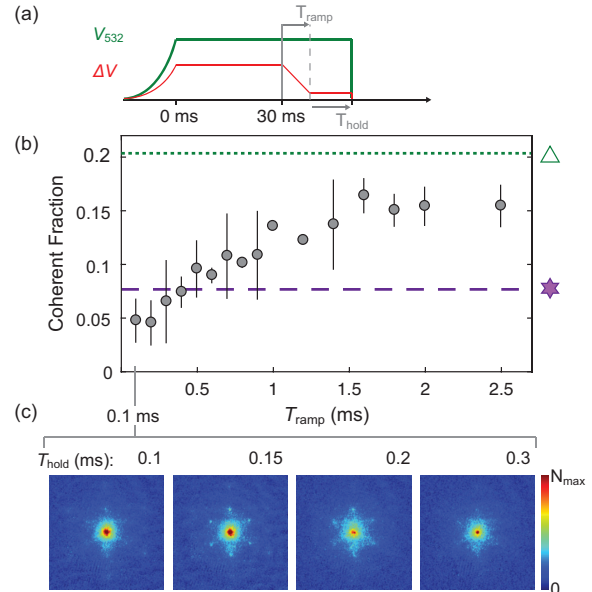
FIG. 4: Response of a degenerate Bose gas to a structural lattice change. (a) The experimental sequence. (b) Coherent fraction as a function of ramp time after the gas equilibrates in the final lattice. The coherence increases to nearly that of the adiabatically loaded triangular lattice when $T_{\text{ramp}} \sim h/6J$. Faster ramps lead to heating. (c) Images of the gas at short times after the fastest ramp show a rise of the coherent inner peak population at 0.15 ms. This rapid momentum-space redistribution indicates motion of the strongly-interacting superfluid within the unit cell. This signal decays and by 0.3 ms the total coherent fraction is reduced.

due to rapid "hole-doping" by the addition of one lattice site per unit cell are analogous to investigations of phase transitions triggered in solid-state systems by ultrafast optical pulses, where the evolution on differing timescales helps one disentangle the separate effects of electronic and structural phase transitions [24].

Images in Fig. 4(c) show the state of the gas at short times after the quench. We observe an increase in coherent population of the inner-peaks after 0.15 ms, while the total coherent fraction remains near-constant. This inner-peak population decays, and by 0.3 ms after the quench the total coherent fraction is significantly reduced. The rapid redistribution of strongly-interacting superfluid indicates motion of coherent atoms within the unit cell that is much faster than the tunneling rate. Future experiments might focus on manipulating the superlattice potential to characterize these non-equilibrium dynamics spectroscopically, or on exploring possible new phases in this superlattice at fractional fillings per lattice site [25–27].

[1] M. P. A. Fisher, P. B. Weichman, G. Grinstein, and D. S. Fisher, Phys. Rev. B **40**, 546 (1989).

[2] B. Capogrosso-Sansone, N. V. Prokof'ev, and B. V. Svistunov, Phys. Rev. B **75**, 134302 (2007).

[3] K. Sheshadri, H. R. Krishnamurthy, R. Pandit, and T. V. Ramakrishnan, Phys. Rev. Lett. **75**, 4075 (1995).

[4] F. E. A. dos Santos and A. Pelster, Phys. Rev. A **79**, 013614 (2009).

[5] R. V. Pai, J. M. Kurdestany, K. Sheshadri, and R. Pandit, Phys. Rev. B **85**, 214524 (2012).

[6] L. Zhi, J. Zhang, and Y. Jiang, Phys. Rev. A **85**, 023619 (2012).

[7] F. Wei, J. Zhang, and Y. Jiang, Eur. Lett. **113**, 16004 (2016).

[8] J. K. Freericks and H. Monien, Phys. Rev. B **53**, 2691 (1996).

[9] Y. Li, M. R. Bakhtiari, L. He, and W. Hofstetter, Phys. Rev. A **85**, 023624 (2012).

[10] D. Jaksch, C. Bruder, J. I. Cirac, C. W. Gardiner, and P. Zoller, Phys. Rev. Lett. **81**, 3108 (1998).

[11] M. Greiner, O. Mandel, T. Esslinger, T. W. Hänsch, and I. Bloch, Nature **415**, 39 (2002).

[12] I. B. Spielman, W. D. Phillips, and J. V. Porto, Phys. Rev. Lett. **100**, 120402 (2008).

[13] K. Jiménez-García, R. L. Compton, Y. J. Lin, W. D. Phillips, J. V. Porto, and I. B. Spielman, Phys. Rev. Lett. **105**, 110401 (2010).

[14] M. Endres, T. Fukuhara, D. Pekker, M. Cheneau, P. Schauss, C. Gross, E. Demler, S. Kuhr, and I. Bloch, Nature **487**, 454 (2012).

[15] M. Rigol, G. G. Batrouni, V. G. Rousseau, and R. T. Scalettar, Phys. Rev. A **79**, 053605 (2009).

[16] G.-B. Jo, J. Guzman, C. K. Thomas, P. Hosur, A. Vishwanath, and D. M. Stamper-Kurn, Phys. Rev. Lett. **108**, 045305 (2012).

[17] We used two methods to calculate Wannier functions and determine U and J. First, we assumed real-valued Wannier functions and considered the Fourier transform of the Bloch states in the single-particle band structure. Second, we used the steepest-descent minimization algorithm to generate maximally localized generalized Wannier states [28]. These two methods yield the same ground-state results and both show that U and J are the same within a few percent in our triangular and kagome lattices.

[18] The 532-nm (1064-nm) lattice depths were stable within 1% (6%) rms over several hours of data taking. Relative positions of the lattices were stable to within 18 nm rms in each horizontal direction.

[19] The lattice is loaded at a constant exponential rate of the 532-nm lattice so that the total load-time is determined by V_{532}.

[20] T. Stöferle, H. Moritz, C. Schori, M. Köhl, and T. Esslinger, Phys. Rev. Lett. **92**, 130403 (2004).

[21] Momentum-space images of superfluid samples showed that after 30 ms the diffraction represented the ground state of the lattice with negligible heating.

[22] S. Tung, G. Lamporesi, D. Lobser, L. Xia, and E. A. Cornell, Phys. Rev. Lett. **105**, 230408 (2010).

[23] M. Greiner, I. Bloch, O. Mandel, T. Hänsch, and T. Esslinger, App. Phys. B **73**, 769 (2001).

[24] C. Kübler, H. Ehrke, R. Huber, R. Lopez, A. Halabica, R. F. Haglund, and A. Leitenstorfer, Phys. Rev. Lett. **99**, 116401 (2007).

[25] P. Buonsante, V. Penna, and A. Vezzani, Phys. Rev. A **72**, 031602 (2005).

[26] K. Sengupta, S. V. Isakov, and Y. B. Kim, Phys. Rev. B **73**, 245103 (2006).

[27] S. A. Parameswaran, I. Kimchi, A. M. Turner, D. M. Stamper-Kurn, and A. Vishwanath, Phys. Rev. Lett. **110**, 125301 (2013).

[28] R. Walters, G. Cotugno, T. H. Johnson, S. R. Clark, and D. Jaksch, Phys. Rev. A **87**, 043613 (2013).

Appendix D

Replacing the Oven in E5

Refilling rubidium in the oven chamber involves removing the oven, placing a fresh vacuum sealed ampule containing 5 grams of rubidium. Opening the oven must be done with care, as contaminants in the chamber could damage the effectiveness of the machine. First, all parts needed should be collected and cleaned to UHV standards.

D.1 Supplies

1. Main Supplies

    a) ion pump

    b) roughing pump

    c) two turbo pumps

    d) new oven

    e) new oven nozzle

    f) Rb and K ampules for new oven

    g) heater strips

    h) heating clamps for oven

    i) micromega temperature controllers

    j) cylinder of nitrogen

    k) clean tubing for dry nitrogen

    l) dewar of liquid nitrogen

    m) RGA: residual gas analyzer

    n) vacuum tubes and valves for connecting pumps to machine

    o) pressure monitor

2. Replacements

   a) any new vacuum parts, cleaned to UHV standards

   b) spare blank flanges, these are used in place of parts that must be cleaned during process

   c) new ion gauge

3. Safety Supplies

   a) mineral oil

   b) many glass or metal containers for mineral oil

   c) lame-resistant lab coats

   d) flame-resistant gloves

   e) goggles

   f) face mask

4. Cleaning Supplies

   a) instructions on cleaning UHV parts

   b) simple green

   c) acetone, methanol

   d) deionized water

D.2 Replace rubidium

D.2.1 Prepare chamber

1. Turn off oven (6 hours before breaking vacuum)

2. Turn off cold catcher (30 minutes before breaking vacuum)

3. Make sure the gate valve to main chamber is securely closed

4. Move cold catcher thermistor setup upwards away from the oven. Clean the thermal goop extremely well so that it does not fall into the chamber when we open the 6 in valve.

5. Turn off ion pump (10 minutes before)

6. Pump new arm down with roughing pump, to ~ 1 mTorr

7. Flush new arm and tubing with dry nitrogen. This cleans out the new region. The nitrogen flows from a cylinder, through a regulator, through a vat of liquid nitrogen to condense any water and finally through the turbo pump inlet. The gauge on nitrogen regulator should be lower than 5 psi.

8. Stop nitrogen flow and pump down with roughing pump and turbo pump. Should take 20 minutes to get down to vacuum pressure. In that time, make sure the thermistor setup is well out of the way and the exterior of the oven chamber is as clean as possible.

9. Open valve

10. Flush oven chamber with nitrogen

11. Monitor main chamber pressure, an increase in pressure would indicate gate valve malfunction.

D.2.2   Remove parts from chamber

1. Close valve to roughing pump

2. Turn off the turbo pump, continue to vent dry N at slightly above 0 psi (don't over pressurize the chamber)

3. Fill the glass or metal buckets with mineral oil

4. Remove the oven cup. Dump contents into mineral oil. Spray methanol into the cup while holding the oven with fire-resistant glove over the vat of mineral oil.

5. The copper cold catcher is likely coated in Rb and appears white. Clean it by spraying small amounts of methanol onto the cold catcher. This will react with the Rb and you will be able to clean off the cold catcher and most of the inside of the chamber in this way.

6. Remove the 6 inch flange. Wrap in UHV foil to be cleaned. Replace with a cleaned blank

7. Remove the ion pump.

8. Install the new ion pump while all of the parts that were removed and dunked in oil are cleaned to UHV standards.

9. Continue cleaning inside the chamber with the new hole you just made, now you can reach more parts of Rb covered cold catcher. Spray.

10. Remove the lower flange and the oven shutter feedthrough. As always, have a piece of UHV foil ready to wrap the part in when it comes out.

11. Remove the cold catcher. Submerge into mineral oil.

D.2.3 Replace vacuum parts

All vacuum flanges should be bolted down in a star pattern to ensure that the copper gasket is uniformly compressed for an effective vacuum seal.

1. Remove the flange that is below the oven shutter and cold catcher.

2. Cover the opening with a clean closure (UHV foil)

3. Continue flowing nitrogen while cleaning the chamber with wipes and methanol. The wipes should go directly into mineral oil. There should be many containers of mineral oil in which to put the Rb covered wipes.

4. Install the rotary feedthrough.

5. Install the clean oven shutter.

6. Install the new cold catcher.

7. Wipe clean an ampule of Rb using methanol. Put it in the oven with the magnetic ball on top.

8. Install the new oven. Be sure the magnet will be on top of the ampule when it is installed.

9. Replace the ion pump. When you remove the one that is there nitrogen will flow through. The pump will be very heavy- have a plan for that. Put the new ion pump into place.

10. Pump down.

D.2.4 Bake the chamber

1. Put thermocouples on selected regions of the chamber. Label the ends.

2. Wrap everything that will be baked in one layer of light weight foil (not UHV foil)

3. Wearing appropriate safety gear (including masks to protect from fiberglass), wrap the chamber with fiberglass-filled heater strips. We use 3 for the oven area and 1 on the main chamber addition. They should not cross over themselves. Label them.

4. Wrap that with 2-3 more layers of foil

5. Plug the thermal tapes into voltage transformers.

6. Slowly ramp up the voltage and monitor the temperature until you get to 150°C

7. Pump until pressure is low enough to turn on RGA

8. Monitor water and nitrogen in chamber as they are pumped out

9. After reaching desired pressure, slowly decrease temperature of chamber

10. Wearing appropriate safety gear, unplug and remove heater strips and foil

Appendix E

Circuit designs and tips

The best advice I ever got about debugging circuits is that when your circuit doesn't work, there are three potential reasons:

1. It was incorrectly soldered

2. One of the elements is broken

3. The design is flawed

The potential culprits should be checked in that order. This sounds like obvious advice, but over the years I've returned to the list with many students. Pro-tip: it's almost always the first one. There is most likely a cold solder joint or missed connection. I've never made it to the third item on the list; it turns out the designer has put a lot of thought into it before sending it off to to be printed and in our years of experience with Sunstone Circuits, we have never had a print error.

In this appendix I'll describe the circuits that I've designed and how they can be used and tuned for various purposes. I'll also share some warnings and tips I've learned along the way. Before designing a new circuit, I recommend leafing through Texas Instruments technical notes SLLA057: *A Survey of Common-Mode Noise* and SLOA035B: *Amplifiers and Bits*.

E.1   Logarithmic photodiode

We use a Hamamatsu IR-enhanced Si PIN photodiode (S11499-01) for our photodioes. The enhanced signal of these photodiodes is sufficient at 1064 nm for stabilization. The photodiode outputs $\rho = 0.6$ Amps/Watt, so that the photodiode current is $I_{PD} = \rho P_{opt}$, where P_{opt} is the optical power into the diode.

A bipolar transistor can be used as a logarithmic converter, with $V_{out} = V_T \log_{10}(I_c/I_s)$, where $V_T = kT/q$ and I_s is a saturation current that is process and device-dependent. In the

logarithmic converter chip AD8304, the bipolar transistor has $V_T = 25.69$ mV at 25° C. The temperature-dependence is problematic if the chip is to be used as a consistent logarithmic converter.

In the AD8304, a second bipolar transistor is used as a reference, and the resulting signal, $V_{out} = V_y \log_{10}(I_{pd}/I_z)$, is temperature-stable. Here, V_y is a slope that defaults to 200 mV/decade = 10 mV/dB and I_z is the intercept at 100 picoamps. Both of these parameters are tunable with external resistors in the circuit design shown in Fig. E.1.

Combining the Hamamantsu photodiode with the factory settings of the AD8304, we have an output signal

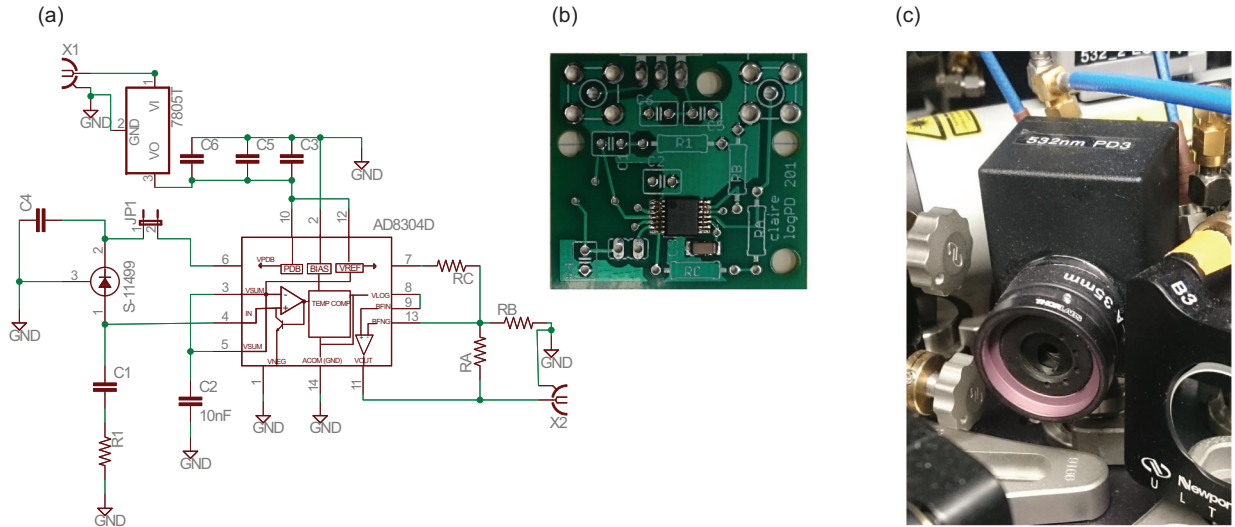$$V_{out} = 0.2 \log_{10}(P_{opt}/178 \text{ pW}) \tag{E.1}$$

Figure E.1: Logarithmic photodiode. (a) Circuit design (b) PCB by Sunstone Circuits, after soldering surface mount components in a toaster oven. (c) Completed photodiode in use.

E.1.1   Modifying slope and intercept

Increasing the slope of the response helps with precision, but comes at the cost of reducing the output range of the converter. The default output range is over 7 orders of magnitude, and we aim to stabilize power over at least 3 orders of magnitude. As such, the circuit is designed increase of the slope of the response. To increase the slope of the signal, one uses the internal buffer amplifier shown in the lower right of the circuit diagram within the AD8306 chip. Resistors R_A and R_B are used to increase the gain, where $G = R_A/R_B$. In our experiment we use $G = 2$, resulting in a slope of 400 mV/decade.

To reduce the slope, one would a shunt resistor, R_s, between V_{log} (pin 8) and ground. The pin is trimmed to 5 $k\Omega$, so $V_y = V_y R_s/(R_s + 5 \; k\Omega)$. For example, if $R_s = 3k\Omega$, then $V_y = 86$ mV/decade. Our PCB is not designed to reduce the slope.

The intercept is set by a reference voltage, V_{ref}, on pin 12 of the chip.

E.1.2   Adaptive biasing

The AD8304 chip has an option to adaptively bias the photodiode based on how much light is on the photodiode. The voltage on pin 6, 'VPDB,' varies from 0.6 V when $I_{PD} = 100$ pA (applying a reverse bias of 0.1 V), to 2.6 V when $I_{PD} = 10$ mA (applying a reverse bias of 1V).

E.1.3   Board design

The AD8304 is a surface mounted chip. Sunstone circuits offers an option to surface mount components. We opted to follow instructions from a Youtube video on soldering surface mount components in a toaster oven. The most important thing I learned in the design of the circuit is that it is incredibly important to get filtering capacitors as close as possible to the active element in the circuit, here the AD8304. This allows for the effective reduction of noise on the input signal. Figure E.1(b) shows that we surface mount both the chip and the 0.1 μF filtering capacitor C_3.

Table E.1: Elements in our photodiode circuit (Fig. E.1)

C_1	1 nF
C_2	10 nF
C_3	0.1 μF
C_4	100 nF
C_5	10 nF
C_6	10 μF
R_1	750 Ω
R_A	20.4 kΩ
R_B	10.2 kΩ
R_C	open

Capacitor and resistor values used in our photodiodes. The capacitor C_3 is surface mounted to improve filtering of the voltage that powers the chip. Note that R_A and R_B should be tuned to modify the slope of the response.

E.1.4 Possible improvements

Analog Devices also produces a high side current mirror chip, the ADL5315, which can be used to further reduce the noise of the logarithmic photodiode signal. We have found it to be unnecessary for our purposes thus far, but it may be useful in the future. Analog Devices Circuit Note CN-0056, entitled *Interfacing the ADL5315 High Side Current Mirror to a Translinear Logarithmic Amplifier in a Photodiode Power Detector Application* describes its use.

E.1.5 Exponential amplifier

The logarithmic current amplifier circuit is a part of a feedback loop, and is used in series with an exponential RF power amplifier. There is an element between them that responds quadratically in voltage. The output voltage of the three elements is linearly related to the input voltage. For our exponential amplifier we use the eval board of the Analog Devices element ADL5331. It has an internal temperature reference for stability, just as the AD8304 does.

E.2 Analog feedback in the log photodiode system

There are many helpful resources to learning about analog feedback systems. I strongly recommend the Review of Modern physics entitled *Feedback for physicists: A tutorial essay on control* [75], and a more technical review, *Schaum's Outline of Theory and Problems of Feedback and Control Systems* [76]. Here I will just describe the particulars of the feedback circuit that we use in this experiment.

There are three stages to the analog feedback board, shown on the following page. The first is a buffer stage. It is *not* an instrumentation amplifier or a subtractor circuit. Conventional wisdom would suggest that subtracting the input signal from the input ground would be ideal as an input to the feedback electronics. However, we found that this increased the noise in the system because the ground of the photodiode differs from the ground of the feedback board. This was the case even when we tried to ground the two to the same optics table. The problem is at least partially because the feedback electronics are spatially distant from the photodiode (by 1-3 meters), which is a limit of our experiment. We find that grounding the input SMA cable ground to the stabilization board ground solves this problem and doesn't introduce further complications.

The second stage is the integrator stage. The buffer output, which is $-V_{in}$, is added to the setpoint to produce an error signal. This feedback stage determines the voltage that should be sent to the control system so that the input voltage and setpoint voltage are equal.

There is a manual switch on the integrator portion of the circuit that allows switching between a few capacitors. The integrator feedback is maximum at DC, and decreases in voltage by 20 dB/decade. The point at which the integrator gain is zero is determined by the capacitor. When building the board, you first measure the open loop response of the

system to which you'll be applying feedback and choose a range of appropriate capacitors. This is a useful option, as we find that it is often necessary to change the feedback parameters when optimizing the system using the response of atoms.

The integral gain also has a bypass switch, which enables us to turn it off so that the DC gain is determined by the proportional feedback. The proportional gain is determined by the values of R_3 and $R_I = R_{13} = R_{11}$ as $|G| = R_3/R_I$. The switch is necessary to enable smooth switching of the laser light. If the integrator is on while there is no light on the photodiode, then the capacitors are charged and will output maximum gain as soon as there is a small signal. The circuit will quickly correct for this spike, but it can still be harmful in an optical lattice, where beam intensities must be carefully controlled even at low optical power. The switch enables us to bypass the integrator whenever the lasers are off, and switch it on when the beams are on. The switch has also enabled us to adapt the board for other purposes.

The final stage is a rectifier, which limits the output voltage of the feedback circuit. The exponential amplifier accepts a limited range of input voltages, between 0 and 1.4 Volts. Voltages outside of that range will damage the sensitive circuitry that allows for appropriate stability and base of the exponential. Here we limit the voltage to between 0 and 1.2 V.

The board shown is connected to a second board that is not shown, which contains basic circuitry to power the board, buffer the setpoint, and enable override of the entire feedback circuit, so that the setpoint is sent directly to the exponential amplifier. This last option is useful when we need to work on optics, block beam paths and measure optical powers. We use Texas Instruments part number REF102 as a voltage reference to power the board with regulated 10 V. When building a circuit board, always be sure to use the appropriate regulator, and don't ever try to reduce it with a voltage divider.
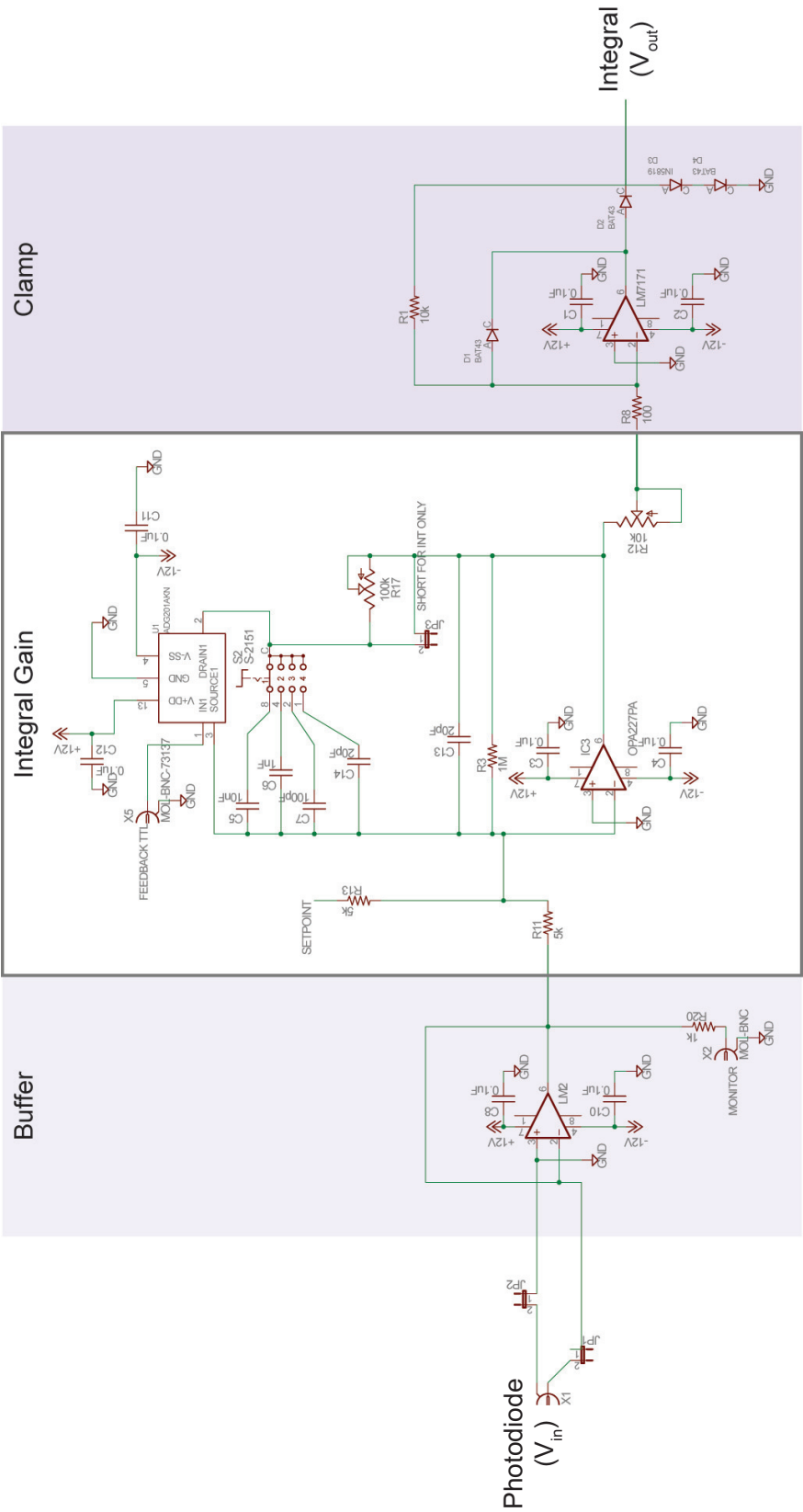
Bibliography

[1]   J. Sebby-Strabley et al. "Lattice of double wells for manipulating pairs of cold atoms". In: *Phys. Rev. A - At. Mol. Opt. Phys.* 73.3 (2006), p. 33605.

[2]   M. Ladd and R. Palmer. *Structure Determination by X-ray Crystallography: Analysis by X-rays and Neutrons.* Fifth. New York: Springer US, 2013.

[3]   D Jaksch et al. "Cold bosonic atoms in optical lattices". In: *Phys. Rev. Lett.* 81 (1998), p. 3108.

[4]   M. Greiner et al. "Quantum phase transition from a superfluid to a Mott insulator in a gas of ultracold atoms". In: *Nature* 415 (2002), p. 39.

[5]   I. B. Spielman, W. D. Phillips, and J. V. Porto. "Condensate Fraction in a 2D Bose Gas Measured across the Mott-Insulator Transition". In: *Phys. Rev. Lett.* 100.12 (2008), p. 120402.

[6]   K. Jiménez-García et al. "Phases of a two-dimensional bose gas in an optical lattice". In: *Phys. Rev. Lett.* 105.11 (2010), pp. 20–23.

[7]   M Endres et al. "The 'Higgs' amplitude mode at the two-dimensional superfluid/Mott insulator transition". In: *Nature* 487 (2012), p. 454.

[8]   W. Ketterle. "Happy birthday BEC". In: *Nat Phys* 11.12 (2015), pp. 982–983.

[9]   Y.-J. J Lin et al. "Rapid production of Rb-87 Bose-Einstein condensates in a combined magnetic and optical potential". In: *Phys. Rev. A* 79.6 (2009), p. 63631.

[10] T. Stöferle et al. "Transition from a Strongly Interacting 1D Superfluid to a Mott Insulator". In: *Phys. Rev. Lett.* 92.13 (2004), p. 130403.

[11] G. Wirth, M. Olschlager, and A. Hemmerich. "Evidence for orbital superfluidity in the P-band of a bipartite optical square lattice". In: *Nat Phys* 7 (2011), pp. 147–153.

[12] J Guzman et al. "Long-time-scale dynamics of spin textures in a degenerate F=1 (87)Rb spinor Bose gas". In: *Phys. Rev. A* 84 (2011), p. 63625.

[13] G.-B. Jo et al. "Ultracold Atoms in a Tunable Optical Kagome Lattice". In: *Phys. Rev. Lett.* 108.4 (2012), p. 45305.

[14] M Greiner et al. "Bose-Einstein condensates in 1D- and 2D optical lattices". In: *App. Phys. B* 73 (2001), p. 769.

[15] P. S. Julienne et al. "Collisional stability of double Bose condensates". In: *Phys. Rev. Lett.* 78 (1997), p. 1880.

[16] R. Walters et al. "Ab initio derivation of Hubbard models for cold atoms in optical lattices". In: *Phys. Rev. A* 87.4 (2013), pp. 1–13.

[17] R. Olf et al. "Thermometry and cooling of a Bose gas to 0.02 times the condensation temperature". In: *Nat Phys* 11.9 (2015), pp. 720–723.

[18] P. Soltan-Panahi et al. "Quantum phase transition to unconventional multi-orbital superfluidity in optical lattices". In: *Nat. Phys.* 8.1 (2012), p. 71.

[19] O. Jürgensen, K. Sengstock, and D.-S. Lühmann. "Twisted complex superfluids in optical lattices." In: *Sci. Rep.* 5 (2015), p. 12912.

[20] C. Cohen-Tannoudji and J. Dupont-Roc. "Experimental study of Zeeman light shifts in weak magnetic fields". In: *Phys. Rev. A* 5.2 (1972), pp. 968–984.

[21] R Grimm, M Weidemüller, and Y. Ovchinnikov. "Optical Dipole Traps for Neutral Atoms". In: *Adv. At. Mol. Opt. Phys.* 42 (2000), pp. 95–170.

[22] M. Rigol et al. "State diagrams for harmonically trapped bosons in optical lattices". In: *Phys. Rev. A* 79.5 (2009), pp. 1–9.

[23] M. P. A. Fisher et al. "Boson localization". In: *Phys. Rev. B* 40.1 (1989).

[24] K. Sheshadri et al. "Percolation-enhanced localization in the disordered bosonic Hubbard model". In: *Phys. Rev. Lett.* 75.22 (1995), pp. 4075–4078.

[25] F. E. A. dos Santos and A Pelster. "Quantum phase diagram of bosons in optical lattices". In: *Phys. Rev. A* 79 (2009), p. 13614.

[26] T.-L. Ho and Q. Zhou. "Intrinsic Heating and Cooling in Adiabatic Processes for Bosons in Optical Lattices". In: *Phys. Rev. Lett.* 99.12 (2007), p. 120404.

[27] F. Gerbier. "Boson Mott Insulators at Finite Temperatures". In: *Phys. Rev. Lett.* 99.12 (2007), p. 120405.

[28] D. McKay et al. "Metastable Bose-Einstein condensation in a strongly correlated optical lattice". In: *Phys. Rev. A* 91.2 (2015), pp. 1–12.

[29] Y. B. Band et al. "Elastic Scattering Loss of Atoms from Colliding Bose-Einstein Condensate Wave Packets". In: *Phys. Rev. Lett.* 84.24 (2000), pp. 5462–5465.

[30] A. M. Rey et al. "Bogoliubov approach to superfluidity of atoms in an optical lattice". In: *J. Phys. B* 36.5 (2003), p. 825.

[31] S Tung et al. "Observation of the Presuperfluid Regime in a Two-Dimensional Bose Gas". In: *Phys. Rev. Lett.* 105.23 (2010), p. 230408.

[32] J. Szczepkowski et al. "Analysis and calibration of absorptive images of Bose-Einstein condensate at nonzero temperatures". In: *Rev. Sci. Instrum.* 80.5 (2009).

[33] F. Gerbier et al. "Phase coherence of an atomic Mott insulator". In: *Phys. Rev. Lett.* 95.5 (2005), pp. 1–4.

[34] S. Trotzky et al. "Suppression of the critical temperature for superfluidity near the Mott transition". In: *Nat. Phys.* 6.12 (2010), pp. 998–1004.

[35] M Endres et al. "Observation of Correlated Particle-Hole". In: *Science (80-.).* 334 (2011), p. 200.

[36] B. Capogrosso-Sansone et al. "Monte Carlo study of the two-dimensional Bose-Hubbard model". In: *Phys. Rev. A* 77 (2008), p. 15602.

[37] L. Zhi, J. Zhang, and Y. Jiang. "Quantum phase transitions of ultracold Bose systems in nonrectangular optical lattices". In: *Phys. Rev. A* 85.2 (2012), p. 23619.

[38] F. Wei, J. Zhang, and Y. Jiang. "Quantum phase diagram and time-of-flight absorption pictures of an ultracold Bose system in a square optical superlattice". In: *Eur. Lett.* 113.1 (2016), p. 16004.

[39] J. K. Freericks and H Monien. "Strong-coupling expansions for the pure and disordered Bose-Hubbard model". In: *Phys. Rev. B* 53.5 (1996), pp. 2691–2700.

[40] N. Teichmann et al. "Bose-Hubbard phase diagram with arbitrary integer filling". In: *Phys. Rev. B* 79 (2009), p. 100503.

[41] N. Teichmann, D. Hinrichs, and M. Holthaus. "Reference data for phase diagrams of triangular and hexagonal bosonic lattices". In: *Eur. Lett.* 91.1 (2010), p. 6.

[42] J. F. Scott. "Soft-mode spectroscopy: Experimental studies of structural phase transitions". In: *Rev. Mod. Phys.* 46 (1974), pp. 83–128.

[43] J. B. Goodenough. "Direct Cation- -Cation Interactions in Several Oxides". In: *Phys. Rev.* 117 (1960), pp. 1442–1451.

[44] M Marezio et al. "Structural Aspects of the Metal-Insulator Transitions in Cr-Doped VO_2". In: *Phys. Rev. B* 5 (1972), p. 2541.

[45] M. M. Qazilbash et al. "Infrared spectroscopy and nano-imaging of the insulator-to-metal transition in vanadium dioxide". In: *Phys. Rev. B* 79 (2009), p. 75107.

[46] J. M. Booth and P. S. Casey. "Production of VO2 M-1 and M-2 Nanoparticles and Composites and the Influence of the Substrate on the Structural Phase Transition". In: *Acs Appl Mater Inter* 1 (2009), p. 1899.

[47] I Bloch, J Dalibard, and W Zwerger. "Many-body physics with ultracold gases". In: *Rev. Mod. Phys.* 80.3 (2008), pp. 885–964.

[48] M. Lewenstein et al. "Ultracold atomic gases in optical lattices: mimicking condensed matter physics and beyond". In: *Adv Phys* 56.2 (2007), pp. 243–379.

[49] L Santos et al. "Atomic Quantum Gases in Kagome Lattices". In: *Phys. Rev. Lett.* 93 (2004), p. 30601.

[50] J Ruostekoski. "Optical Kagome Lattice for Ultracold Atoms with Nearest Neighbor Interactions". In: *Phys. Rev. Lett.* 103 (2009), p. 80406.

[51] V. Elser. "Nuclear antiferromagnetism in a registered ^{3}He solid". In: *Phys. Rev. Lett.* 62 (1989), p. 2405.

[52] J. B. Marston and C Zeng. "Spin-peierls and spin-liquid phases of kagome quantum antiferromagnets". In: *J. Appl. Phys.* 69 (1991), pp. 5962–5964.

[53] S Sachdev. "Kagomé- and triangular-lattice Heisenberg antiferromagnets: Ordering from quantum fluctuations and quantum-disordered ground states with unconfined bosonic spinons". In: *Phys. Rev. B* 45 (1992), p. 12377.

[54] P Nikolic and T Senthil. "Physics of low-energy singlet states of the Kagome lattice quantum Heisenberg antiferromagnet". In: *Phys. Rev. B* 68 (2003), p. 214415.

[55] F Wang and A Vishwanath. "Spin-liquid states on the triangular and Kagome lattices: A projective-symmetry-group analysis of Schwinger boson states". In: *Phys. Rev. B* 74 (2006), p. 174423.

[56] Y Ran et al. "Projected-wave-function study of the spin-1/2 Heisenberg model on the kagome lattice". In: *Phys. Rev. Lett.* 98 (2007), p. 117205.

[57] R. R. P. Singh and D. A. Huse. "Ground state of the spin-1/2 kagome-lattice Heisenberg antiferromagnet". In: *Phys. Rev. B* 76 (2007), p. 180407.

[58] S. Yan, D. A. Huse, and S. R. White. "Spin-Liquid Ground State of the S = 1/2 Kagome Heisenberg Antiferromagnet". In: *Science (80-.).* 332 (2011), pp. 1173–1176.

[59] C. J. Wu et al. "Flat bands and Wigner crystallization in the Honeycomb optical lattice". In: *Phys. Rev. Lett.* 99 (2007), p. 70401.

[60] S. D. Huber and E. Altman. "Bose condensation in flat bands". In: *Phys. Rev. B* 82 (2010), p. 184502.

[61] H. Tasaki. "Ferromagnetism in the Hubbard models with degenerate single-electron ground states". In: *Phys. Rev. Lett.* 69 (1992), p. 1608.

[62] M. P. Shores et al. "A Structurally Perfect S = 1/2 Kagomé Antiferromagnet". In: *J Am Chem Soc* 127 (2005), pp. 13462–13463.

[63] Z Hiroi et al. "Spin-1/2 kagome-like lattice in Volborthite $Cu_3V_2O_7(OH)_{(2)}\cdot 2 H_2O$". In: *J. Phys. Soc. Jpn.* 70 (2001), pp. 3377–3384.

[64] S. Taie et al. "Coherent driving and freezing of bosonic matter wave in an optical Lieb lattice". In: *Sci. Adv.* 1.10 (2015).

[65] H. Ozawa et al. "Interaction-Driven Shift and Distortion of a Flat Band in an Optical Lieb Lattice". In: *Phys. Rev. Lett.* 118.17 (2017), p. 175301.

[66] S. Mukherjee et al. "Observation of a Localized Flat-Band State in a Photonic Lieb Lattice". In: *Phys. Rev. Lett.* 114.24 (2015), p. 245504.

[67] M Lohse et al. "A Thouless quantum pump with ultracold bosonic atoms in an optical superlattice". In: *Nat Phys* 12.4 (2016), pp. 350–354.

[68] I. Bloch, J. Dalibard, and S. Nascimbène. "Quantum simulations with ultracold quantum gases". In: *Nat. Phys.* 8.4 (2012), pp. 267–276.

[69] M Aidelsburger et al. "Measuring the Chern number of Hofstadter bands with ultracold bosonic atoms". In: *Nat Phys* 11.2 (2015), pp. 162–166.

[70] D. A. Abanin et al. "Interferometric Approach to Measuring Band Topology in 2D Optical Lattices". In: *Phys. Rev. Lett.* 110.16 (2013), p. 165304.

[71] G. Jotzu et al. "Experimental realization of the topological Haldane model with ultracold fermions". In: *Nature* 515.7526 (2014), pp. 237–240.

[72] F. Gerbier and J. Dalibard. "Gauge fields for ultracold atoms in optical superlattices". In: *New J. Phys.* 12.3 (2010), p. 33007.

[73] M. P. Zaletel et al. "Chiral bosonic Mott insulator on the frustrated triangular lattice". In: *Phys. Rev. B* 89.15 (2014), pp. 1–8.

[74] C. K. Thomas et al. "Signatures of spatial inversion asymmetry of an optical lattice observed in matter-wave diffraction". In: *Phys. Rev. A* 93.6 (2016), p. 63613.

[75] J. Bechhoefer. "Feedback for physicists: A tutorial essay on control". In: *Rev. Mod. Phys.* 77.3 (2005), pp. 783–836.

[76] J. J. DiStefano III, A. Stubberud, and I. J Williams. *Schaum's Outline of Theory and Problems of Feedback and Control Systems*. McGraw-Hill, 1990.